Title

On the emergence of attractive load-bearing forces in vibration-induced squeeze-film gas lubrication

Permalink

https://escholarship.org/uc/item/8gv9897w

Author

Ramanarayanan, Sankaran

Publication Date

2024

UNIVERSITY OF CALIFORNIA SAN DIEGO

On the emergence of attractive load-bearing forces in vibration-induced squeeze-film gas lubrication

A dissertation submitted in partial satisfaction of the
requirements for the degree Doctor of Philosophy

in

Engineering Sciences (Aerospace Engineering)

by

Sankaran Ramanarayanan

Committee in charge:

Professor Antonio L. Sánchez, Chair
Professor Stefan G. Llewellyn Smith
Professor David Saintillan
Professor Michael T. Tolley
Professor William R. Young

2024

The Dissertation of Sankaran Ramanarayanan is approved, and it is acceptable in quality and form for publication on microfilm and electronically.

University of California San Diego

2024

DEDICATION

This thesis is dedicated to all my loved ones.

“After telling Claude that I didn’t want to be disturbed, I lay down in bed
and fell into what I thought would be the welcome oblivion of sleep.

Sleep came, but the witness continued, witnessing
sleep from its position behind the body.

This was the oddest experience.
The mind was definitely asleep,
but something was simultaneously awake.”

Suzanne Segal
Collision with the infinite:
A life beyond the personal self

TABLE OF CONTENTS

LIST OF FIGURES

LIST OF TABLES

ACKNOWLEDGEMENTS

I must begin by acknowledging my wonderful family, without whom I would have never been able to pursue my passions in engineering sciences.

I would like to also acknowledge my advisor and mentor in myriad respects, Professor Antonio L. Sánchez, for training me patiently in the elegant discipline of perturbation methods as it applies to the study of fluid dynamics, for guiding me with incredible dedication in my pursuit of excellence in scientific research, and most of all, for reminding me repeatedly *not* to spell the word “straightforward” with a hyphen, an error that I hope has not occurred in this dissertation.

I am grateful to have been surrounded by passionate colleagues both inside and outside my research group, including Edward, Sombuddha, Brandon, Javier, Guillermo, Stephanie, Obed and many more. I would like to sincerely thank Dr. Wilfried Coenen for providing me with invaluable training in computation fluid dynamics, a subject that I have always found challenging. The finite-element fluid-flow simulations included in this dissertation would not have been remotely possible without his initiative and frequent guidance. I would also like to acknowledge my colleague and close friend, Ian Frankel, for valuable conversations regarding the dynamic bending of solid structures as well as exciting rallies of ping-pong in the graduate lounge (once using a tennis ball due to lack of proper equipment).

The theoretical investigations outlined in the following text were primarily inspired by experiments conducted by Dr. William Hakes Weston-Dawkes and Mr. Chengze-Jia (Jay) in the Bioinspired Robotics and Design Lab here at UC San Diego, under the direction of Professor Michael Tolley and Mr. Mike Everman. I gratefully acknowledge the four of them for valuable conversations regarding practical aspects of squeeze-film levitation.

I learned from Jay that, prior to the studies conducted by the Design lab, Dr. David Colasante performed experiments of his own where he demonstrated very impressive attractive load-bearing capacities with use of large-scale squeeze-film levitators. When I reached out to Dr. Colasante personally, he provided a wealth of information regarding his experiments, which helped contextualize the results of my theoretical investigations and substantially enriched the discussions contained in this dissertation. I must thank him sincerely for his invaluable contributions.

Chapter 2, in part, has been published in the *Journal of Fluid Mechanics* under the title "Viscoacoustic squeeze film force on a rigid disk undergoing small axial oscillations", by S. Ramanarayanan, W. Coenen and A. L. Sánchez, 933, A15, (2022). The dissertation author and his doctoral advisor were the primary authors and investigators of this paper.

Chapter 3 has been published in *AIP Advances* under the title "On the enhanced attractive load capacity of resonant flexural squeeze-film levitators", by S. Ramanarayanan and A. L. Sánchez, 12(10), 105126, (2022). The dissertation author was the primary investigator and author of this paper.

Chapter 4 is currently being prepared for submission for publication along with A. L. Sánchez, under the title "The role of fluid–structure coupling in the generation of attractive squeeze-film forces". The dissertation author was the primary investigator and author of this draft.

Chapter 5 has been published in *Flow* under the title "Benefits of controlled inclination for contactless transport by squeeze-film levitation", by S. Ramanarayanan and A. L. Sánchez, 3, E26, (2023). The dissertation author was the primary investigator and author of this paper.

Finally, I must thank the Charles Lee Powell foundation for kindly supporting my Masters studies through the Powell/Bundle fellowship, as well as the ARCS foundation (Achievement Reward for College Scientists) for their generous support of my doctoral research by way of an annual financial award.

VITA

2019	B. S. in Aerospace Engineering, University of California San Diego
2020	M. S. in Engineering Sciences (Aerospace Engineering), University of California San Diego
2024	Ph. D. in Engineering Sciences (Aerospace Engineering), University of California San Diego

PUBLICATIONS

S. Ramanarayanan, W. Coenen, A. L. Sánchez, “Viscoacoustic squeeze film force on a rigid disk undergoing small axial oscillations”, *Journal of Fluid Mechanics*, 933, A15, 2022.

S. Ramanarayanan, A. L. Sánchez, “On the enhanced attractive load capacity of resonant flexural squeeze-film levitators”, *AIP Advances*, 12(10), 105126, 2022.

L. L. Becerra, T. Rafeedi, S. Ramanarayanan, I. Frankel, J. Miller, A. X. Chen, Y. Qie, D. J. Lipomi, H. Garudadri, T. N. Ng. “Bidirectional Venturi Flowmeter Based on Capacitive Sensors for Spirometry”, *Advanced Materials Technologies*, 2300627, 2023.

S. Ramanarayanan, A. L. Sánchez, “Benefits of controlled inclination for contactless transport by squeeze-film levitation”, *Flow*, 3, E26, 2023.

C. Jia, S. Ramanarayanan, A. L. Sánchez, M. Tolley, “Controlling the Motion of Gas-Lubricated Adhesive Disks using Multiple Vibration Sources”, *Frontiers in Robotics and AI*, 10, 1231976, 2023.

S. Ramanarayanan, A. L. Sánchez, “The role of fluid–structure coupling in the generation of attractive squeeze-film forces”, *in preparation*.

ABSTRACT OF THE DISSERTATION

On the emergence of attractive load-bearing forces in vibration-induced squeeze-film gas lubrication

by

Sankaran Ramanarayanan

Doctor of Philosophy in Engineering Sciences (Aerospace Engineering)

University of California San Diego, 2024

Professor Antonio L. Sánchez, Chair

This dissertation investigates the fluid–structure dynamics involved in squeeze-film levitation, in pursuit of a theoretical explanation for the anomalously large, attractive load-bearing forces observed in recent experiments.

Consider a rigid disk vibrating rapidly along its axis of symmetry near a parallel wall, inducing oscillatory airflow in the thin film of air separating the disk and the wall as well as its periphery. Due to the nonlinear effects of fluid inertia and compressibility, the air pressure within the film varies in time asymmetrically about its ambient value, providing a nonzero *time-averaged* pressure force on the disk. Prior studies of this “squeeze-film” effect report that the time-averaged force typically repels the disk from the wall, making it a suitable mechanism for bearing lubrication. The strong attractive forces reported recently thus constitute a radical departure from this historical norm, expanding the range of possible applications to include wall-climbing robots and versatile contactless grippers. This dissertation aims to understand the fluid–structure physics underlying the emergence of strong attraction, through the derivation of reduced mathematical formulations that may ultimately aid the development of such novel systems.

Gas-lubricated systems represent an exceptional family of slender fluid flows for which the effects of compressibility and viscous shear enter simultaneously while maintaining small values of the Knudsen number, thereby guaranteeing applicability of the continuum hypothesis in describing the flow. Thus, the classical Navier–Stokes equations are used here to investigate the gas dynamics in the thin film as well as the effectively incompressible discharge and entrainment of air across a small region surrounding its edge. An approximate solution obtained using the method of matched asymptotic expansions indicates that the augmented attractive forces observed in recent experiments can be attributed to the pronounced dynamic bending of the highly flexible disks utilized. The theoretical formulation is then generalized to describe two-way fluid–structure coupling between the undulating disk and the thin-film airflow, thereby yielding predictions of system behavior that exhibit greatly improved agreement with experimental data. The canonical problems outlined herein can be readily extended to describe more complex configurations of practical interest—in particular, those involving transportation of the levitated object.

Chapter 1

Introduction

1.1 Executive summary

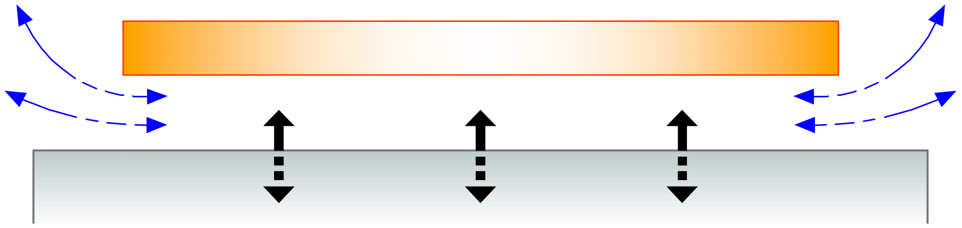

Figure 1.1. Diagram of a typical ‘squeeze-film levitation’ system, involving two objects with parallel surfaces whose separation distance varies in time due to normal oscillations of, in this case, the lower object. The blue arrows depict pulsatile airflow between the slender air layer and the stagnant surroundings.

A typical ‘squeeze-film levitation’ (SFL) system, as depicted in figure 1.1, involves two objects whose parallel surfaces are separated by a thin layer of air, the so-called ‘squeeze film’. One of the objects performs high-frequency oscillations along an axis perpendicular to the surfaces, inducing oscillatory airflow in the slender film and its outer periphery. Since the dynamics of this airflow is inherently nonlinear, owing to effects of fluid inertia and gaseous compressibility, the periodic variation with time of the fluid pressure in the film can be expected to be non-sinusoidal even if the object oscillates sinusoidally. Thus, the *cycle-averaged* value of the pressure acting on the film-adjacent surface of each object differs from the ambient value found in the unperturbed air sufficiently far from the film, providing a time-averaged normal force on each object. This force has been observed to be typically repulsive [7], and is referred to in this dissertation as the steady squeeze-film force (SSF).

It is useful to explore from the perspective of fundamental fluid mechanics the source of this cycle-averaged overpressure. The asymmetrical rise and drop of pressure within the thin air film in response to symmetrical oscillations of a bounding surface may be attributed to at least two factors: (i) the nature of fluid acceleration and (ii) the dependence of gaseous density on pressure variations. To understand conceptually the first factor, imagine the following thought experiment. Drop a handful of small, buoyant particles in a tray filled with a viscous fluid such as syrup, press a plastic card against the surface of the tray and excite the fluid by oscillating the card back and forth near one of the walls of the tray. Due to the suppression of fluid acceleration by strong viscous stresses, the motion of the fluid will be primarily dictated by the time-symmetrical motion of the card. Now repeat the thought experiment with a less viscous fluid such as water, which would give rise to much more complex flow patterns. Even when the card is momentarily brought to a stop, the flow continues to evolve. It does so in a manner such that the flow velocity at any point in the flow field—and, correspondingly, also the associated pressure—varies asymmetrically during the closing and opening oscillation strokes. As an illustrative example of the second factor, consider the classical problem of the adiabatic compression and expansion of a gas in an insulated cylinder by an oscillating piston. For sufficiently low frequencies, i.e. quasistatic operation, the laws of thermodynamics for an ideal gas state that there is a nonlinear relationship between the volume and pressure of the gas contained within the cylinder. Thus, the rise in gas pressure due to a certain inward displacement of the piston is not equal in magnitude to the drop in pressure due to an *equal* outward displacement.

While the conceptual arguments outlined above justify the presence of a time-averaged pressure deviation inside the film, they do not clarify why the resulting force is typically repulsive and not attractive, warranting a detailed analysis of the relevant aerodynamics. Furthermore, the assumption of time-symmetrical surface oscillations may be invalid for systems where the oscillator’s inertia is sufficiently low for its motion to be affected by the very pressure variations

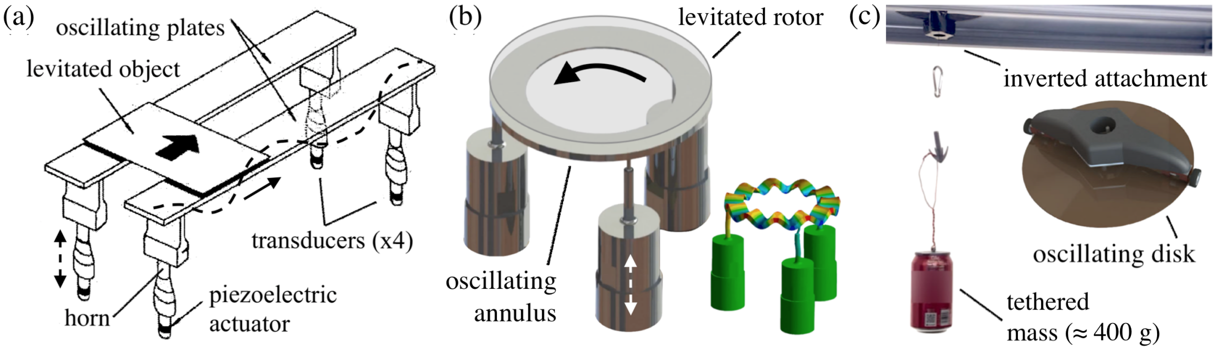

Figure 1.2. Contactless (a) transport [1] and (b) rotation [2] of objects levitating above platforms that are oscillated flexurally by piezoelectric transducers, and (c) attachment below a horizontal wall of a load-carrying robot equipped with a flexurally oscillating disk [3].

that it generates, warranting additionally the consideration of two-way-coupled fluid–structure interactions.

The phenomenon of SFL, first implemented within the context of gaseous lubrication [8–10], has been applied in recent decades to the design of contactless levitators that can suspend and transport sensitive objects such as microelectronic components and glass substrates [1,11–14]. The three panels of figure 1.2 show illustrative examples of different systems that achieve contactless levitation by oscillating a flat object along its normal axis in the close vicinity of a parallel surface. Researchers have also demonstrated that generating traveling-wave oscillations on the flat object gives rise to steady fluid shear stresses in the air layer, allowing transportation [1] and manipulation [2] of the levitated object, as depicted respectively in panels 1.2(a) and (b). Interestingly, under certain operating conditions the time-averaged force has been observed to transition from repulsion to attraction, allowing attractive suspension of objects several hundred grams in mass [3], as shown in panel 1.2(c). Elucidating the physics behind this anomalous emergence of an attractive SSF is the primary objective of the following dissertation.

Provided below in § 1.2 is a brief historical overview of the squeeze-film effect, including its inception and various relevant applications. Reports of the transition to attractive levitation are detailed in § 1.3 and motivations for the present work are provided in § 1.4. The present chapter is concluded in § 1.5 with an itemized overview of the remaining content in this dissertation.

1.2 History and applications of the squeeze-film effect

The discipline of squeeze-film levitation was largely inspired, albeit unintentionally, by an experimental investigation of the non-Newtonian properties of air.

In September of 1956, at the 9th International Congress of Applied Mechanics held at the University of Brussels, Belgium, Professor M. Reiner of the Israel Institute of Technology presented a demonstration [15] where a disk of diameter $2a = 6.7$ centimeters was spun at a speed of approximately $\omega = 7000$ rotations per minute near a larger, coaxially aligned disk, their parallel surfaces separated by a thin film of air. The distance between the disk surfaces was gradually reduced, and a slight decrease in air pressure was observed near the center of the film. For a distance of $h_o \approx 0.5$ millimeters, the central gauge pressure was measured to be $\Delta p \approx -9.7 \times 10^{-4}$ atm (atmospheres). When h_o was reduced below a critical value of around twenty micrometers, the suction disappeared and a sharp rise in pressure was observed. An immense central overpressure of $\Delta p \approx 0.5$ atm was reached before physical contact occurred between the disks!

Since $h_o/a \lesssim 0.015 \ll 1$ in this experiment, the thin-film approximation [16] may be drawn to describe the airflow between the disks, whence transverse variations of pressure across the air film are negligibly smaller (by a factor of order h_o^2/a^2) than radial deviations from the ambient value found in the unperturbed air outside the film. Since the lubrication Reynolds number of the flow (≈ 12.4) is of order unity, the magnitude of the radial deviations Δp may be approximated using the formulas derived by K. Stewartson [17], which provide $\Delta p \approx -1.1 \times 10^{-3}$ atm, as explained in [5]. This prediction agrees well, in sign and magnitude, with the reported suction in Reiner's experiment, but not with the subsequently observed large overpressures.

Reiner postulated that the anomalous rise in central pressure must be attributed to the so-called 'Weissenberg' effect [18], the tendency of a non-Newtonian fluid to flow toward the axis of rotation. While this behavior had been conclusively demonstrated for colloidal and polymeric liquids with high viscosities, the emergence of such viscoelastic behavior in this gaseous shear flow would have required that the separation distance h_o be of order 4×10^{-9} m, smaller in fact than the mean free path of air [5].

In a seminal communication published less than a year following this demonstration, Sir Geoffrey Taylor and Phillip Saffman [5] proposed that the enormous pressure generated in the air layer may be completely unrelated to the rotation of the fluid, and may instead owe to vibrations of the spinning disk arising from dynamic imbalances. Using an appropriately reduced form of the Navier–Stokes conservation equations for a viscous, *variable-density* fluid, Taylor and Saffman proved that sinusoidal perpendicular oscillations with an amplitude of just $b = 2.5$ micrometers would give rise to a time-averaged central overpressure of 0.31 atm when the gap width is reduced to $h_o = 2b = 5$ micrometers. This overpressure would continue to grow with the inverse square of h_o as the latter is further reduced.

In the following years, interest grew rapidly in potential applications of this phenomenon of wall-vibration-induced overpressure in thin, wall-bounded gas layers—the so-called compressible squeeze-film effect. The most prominent of these applications are discussed below.

1.2.1 Bearing lubrication

Gaseous lubrication involves the generation of super-ambient pressures inside a thin film of gas between two close surfaces, providing substantial repulsive load capacity while allowing relative translational motion with remarkably low skin friction. These pressures are typically generated by (i) using surface translation to shear and channel the gas into a convergent geometrical region, providing an *aerodynamic* bearing whose load capacity depends critically on the translational speed, or (ii) actively pumping gas into the film through an orifice or pores on the surface(s), providing a so-called *aerostatic* bearing that acts as a spring-damper even under static conditions. While the former is best suited for high-speed applications, such as foil bearings in aeronautical turbomachinery, the latter has been successfully exploited in a variety of avenues that require precision, ranging from measuring instruments to machine tools [7, 19]. (Further details regarding the history and applications of gaseous lubrication can be found in [20–22].)

Such overpressures can also be achieved, as Taylor and Saffman [5] proved, using the so-called 'squeeze-film' effect, i.e. by rapidly oscillating either surface along its normal axis [9]. At sufficiently high frequencies, cyclical compression and expansion of the gas effectively entrapped in the interior of the film produces a super-ambient *time-averaged* pressure that provides a significant, *steady*, repulsive force on the two bounding objects [5].

When compared to conventional gas-lubricated bearings, these so-called *squeeze-film air bearings* (SFABs) have been reported to display superior stability and controllability [7]. Conventional bearings exhibit certain disadvantages due to the high flow speeds required to achieve practically applicable load capacities using gas, rather than liquid, as the lubricant. For instance, aerodynamic bearings may experience (i) gradual surface wear due to contact friction experienced during start-up and stoppage [7] or (ii) self-excited vibrations, such as "whirl" in rotor-bearing systems, due to hydrodynamic instabilities [23, 24]. On the other hand, externally pressurized aerostatic bearings may experience (i) so-called "micro-vibrations" of a free bounding surface, caused by turbulent vortex shedding downstream of the inlet [25], or (ii) a substantial net reduction in load capacity due to "pressure depression"—the expansion of transonic inflow to supersonic conditions within the gas film follow by complex shock wave–boundary layer interactions [26, 27]. Provided that the operating parameters are chosen carefully, SFABs may, in principle, be able to achieve load capacities comparable to those of conventional bearings while avoiding the operational issues associated with turbulence, hydrodynamic instability and transonic airflow, a proposition that must be studied rigorously in the future (see § 6).

Twentieth-century innovations in the generation of high-frequency oscillation—in particular, piezoelectric actuators—prompted integration of the squeeze-film effect into existing aerodynamic bearings [7]. According to a dissertation from 1980 [10], such 'hybrid' bearings were of practical interest primarily in "support of gyroscope gimbals and slider bearings for the computer industry".

1.2.2 Levitation and transportation

In the 1990s, the ability to sustain loads with use of gaseous lubrication came into interest in applications involving the contactless handling of sensitive items, i.e. *squeeze-film levitation* (SFL). This technique was initially interpreted as a limiting form of acoustic levitation, which allows aerial suspension of matter using a non-uniform, time-averaged pressure field generated by the interaction of sound waves between vibrating and reflecting surfaces [28], although the underlying physics has been shown to differ fundamentally [29]. When the mean separation distance between an oscillating 'radiator' and a parallel reflector is reduced well below the local acoustic wavelength, the pressure waves generated by the oscillator travel effectively laterally outward between the two surfaces, subject to non-negligible viscous attenuation, and the resulting time-averaged pressure distribution in the squeeze film yields a large, steady, repulsive force that is felt by both objects [11].

While items suspended using conventional acoustic levitation typically scale centimetrically and weigh a few grams at best [30, 31], SFL has been proven to be capable of sustaining much heavier repulsive loads with substantially larger surface areas. Use of the piezoelectric 'Bolt-clamped Langevin Transducer', pictured in figures 1.2(a) and (b), has allowed stable levitation of objects with masses ranging from a few grams to several kilograms, over planar surfaces with areas ≈ 50 cm^2 [1, 2, 6, 7, 11–14, 19, 32–43]. SFL is not restricted to configurations that involve planar surfaces; for instance, spherical rotors weighing several hundred grams have been successfully levitated above a socket-shaped oscillator, while performing several thousand revolutions per minute (rpm) due to low skin friction [44].

A natural application of this phenomenon—the ability to suspend, manipulate and transport sensitive objects without physical contact—is assembly line manufacturing. SFL is particularly preferable for handling microelectronic components, such as surface-mount devices to be soldered to a circuit board, in place of contact-based, soft grippers that may deposit residual materials or produce electrostatic adhesion that prevents reliable detachment [6]. Transportation of levitated objects has been achieved using, predominantly, two distinct methods: (i) tilting the levitated object, which yields a steady pressure force with a propulsive component [45], or (ii) exciting traveling waves on the oscillating platform using multiple vibration sources, to produce steady, propulsive shear stresses on the levitated object [1, 13, 14]. Using the latter method, objects with masses of order 10 g have been transported at speeds of order 10 cm/s [1]. Additionally, piezoelectric transducers have been attached to the levitated object itself, to produce controllable, self-levitating, traveling-wave-driven mobile robots [32–34]. Analogously, annular oscillators that are (i) fragmented into tilted sections (similar to a tilting-pad thrust bearing) [46] or (ii) excited to exhibit azimuthal traveling-wave oscillations [1, 2, 35, 47] have been used to rotate levitated objects at speeds of $\approx$ 1000 rpm (see figure 1.2(b)).

1.3 Transition from repulsive to attractive forces

While most squeeze-film levitators generate strong repulsive forces, a remarkable transition to attraction was reported in 2002 [37], albeit producing comparatively weak forces. Only under a limited range of operating conditions, namely, for surfaces with millimetric characteristic dimensions and/or oscillation frequencies as low as several hundred Hz, this transition was observed when the separation distance between the two objects was increased beyond a critical value [4, 6, 36, 48]. The relatively small attractive forces, corresponding to average stresses smaller than 1 gf/cm^2 (grams-force per square centimeter), have since been of limited practical interest.

However, as reported in a 2015 U.S. patent [49] by David Colasante, M.D., and confirmed independently in a 2021 experimental study by the Bioinspired Robotics and Design (BRD) Lab at the University of California San Diego [3], this minor attractive load capacity may be magnified a thousandfold if the stiffness of the oscillator is reduced deliberately to provide pronounced flexural deformations. In illustrating the extent of the magnification seen in [3], it is useful to draw a comparison against the data reported in the aforementioned, seminal communication from 2002 where attraction in air was first reported [37]. The two experiments involved comparable operating parameters, including similar object surface areas and forcing frequencies. The key difference is that the original experiments [37] involved a 10-mm-thick aluminum cylinder oscillating, allegedly, with effectively uniform amplitude, while the recent study [3] was conducted using centrally excited plastic disks, each with a thickness of less than one millimeter, reportedly undergoing substantial flexure. While the first paper reports a maximum attractive SSF of approximately 0.52 gf for a 7-cm-diameter surface, well in agreement with other experimental and computational studies that investigated effectively rigid-body systems [4, 6, 12, 36], the recent study claims to have achieved forces of over 400 gf using a disk of diameter 4.9 cm. The primary goal of this dissertation is to investigate the underlying fluid dynamics giving rise to this thousandfold magnification of attractive load capacity.

Attractive SFL may be of practical interest due not only to the recently improved load capacity but also to remarkable energy efficiency. In his experiments, by oscillating a 12" x 6", 0.4-mm-thick aluminum plate at 83 Hz using two audio exciters, Dr. Colasante demonstrated steady attractive levitation of a ≈ 2.6 kg payload (5.72 lb) with just 3 W (watts) of supplied power [50]. While this force is notably weaker than the repulsive load-bearing forces observed in the history of SFL, e.g. 11.7 kgf [19], we see a remarkable improvement in energy efficiency. The cited experiment [19] required 50 W of input, yielding an efficiency (defined here as the levitated mass per unit power input) of approximately 235 g/W. In contrast, efficiencies of the order of 1000 and 2000 g/W were achieved respectively in the experiments by Dr. Colasante [51] and the BRD lab [3]. For context, note that a very efficient multicopter motor [52] equipped with a 16-inch-diameter propeller produces about 2.1 kgf of thrust while consuming close to 333 W (≈ 6.3 g/W).

It must be noted here that, in more recent experiments, Dr. Colasante appears to have achieved much greater attractive load capacities while maintaining the high efficiency. By oscillating larger metal plates with more powerful audio exciters, he has recorded attractive forces ranging from ≈ 19 kgf (41 lbf) with 25 W of power [53] to ≈ 200 kgf (440 lbf) with 200 W [54]!

The BRD lab [3] reports that the light, flexible plastic oscillators utilized in their experiments were subject to substantial aerodynamic coupling; in other words, the dynamic deformations of the oscillator were measurably influenced by aerodynamic forces arising from the oscillatory airflow in the squeeze film. Describing such ‘two-way-coupled’ fluid–structure interactions can be anticipated to be integral in predicting accurately the attractive levitation forces generated by SFL systems driven by oscillators with low inertia and structural stiffness.

1.4 Motivation for the present theoretical modeling

Due to the recent developments in squeeze-film levitation outlined above, it may be envisioned that contemporary SFL devices will exhibit practical utility, for instance, in connection with wall-climbing robots or assembly line applications such as material-processing equipment and pick-and-place machinery. Applications involving larger loads can also be envisioned, such as those emerging in warehouse fulfillment and in-home automation, provided that scalability issues—such as hydrodynamic instabilities—can be adequately addressed (see § 6).

Pursuant of realizing practical systems that may enable such applications, the principal objective of the present dissertation is to approach a better understanding of the fundamental physics underlying repulsive and attractive SFL, by means of developing simplified theoretical descriptions of the relevant fluid–structure dynamics. Perturbation methods are employed as the primary tool of investigation, and results are verified either by numerical methods or by comparison to prior experiments and simulations.

While prior theoretical analyses have deeply investigated the physics surrounding SFL and inspired substantial practical development, much remains to be understood about SFL before it can be practically implemented—in a controlled manner—outside of spheres of academic research. The most advanced analyses to date have involved high-fidelity numerical simulations that yield accurate, experimentally verified results, albeit incurring large computational costs and thus affording physical insights only for a restrictively small range of the relevant operating parameters. On the other hand, simplified quasi-analytical models that provide a wider view of the parametric domain have typically relied on assumptions that involve neglecting fundamental physical factors, such as fluid inertia, gaseous compressibility, pressure variations near the periphery of the squeeze film, structural deformations of the oscillator and fluid–structure coupling. (An overview of relevant literature can be found in § 2.2.1.)

The theoretical descriptions outlined in this document constitute in no way a comprehensive treatment of the complex problems posed by the various contemporary applications of bidirectional squeeze-film levitation. Rather, they are designed to rigorously address fundamental, previously unanswered questions that the author believes to be important in an approach to a better physical understanding of this intriguing phenomenon—one that eludes simplistic, intuitive characterization.

1.5 Organization of the dissertation

The remainder of this document is divided into five chapters, each of which addresses a distinct class of questions regarding the fluid dynamics of bidirectional squeeze-film levitation. Summarized below are the questions asked and the insights gained as part of each chapter.

Chapter 2) Why has the attractive load capacity of squeeze-film levitators been substantially lower than their repulsive capacity, until very recently? What are the most significant physical parameters governing the canonical squeeze-film effect, and under what precise conditions does the transition to attractive forces occur?

The majority of prior experimentation with attractive levitation has been conducted using bulky oscillators undergoing limited elastic flexure. When attractive forces are produced by an ideal rigid-body system, the time-averaged pressure is known to drop from a super-ambient value near the center of the squeeze film to a sub-ambient value of comparable magnitude at its outer edge, before sharply rising back to the ambient value across a small peripheral region surrounding the film. In this chapter, the method of matched asymptotic expansions is applied to rigid-body systems to analyze and relate the flow in the film and the periphery, producing a rigorous description of canonical squeeze-film levitation that unifies prior reduced analyses and agrees quantitatively with the results of recent CFD (computational fluid dynamics) simulations. The powerful repulsive force generated by rigid oscillators has been known to grow with the inverse square of the separation distance as the latter is reduced, bounded only by the finiteness of the oscillation amplitude. The present theory reveals that the transition to attraction occurs for relatively small values of the product of the oscillation frequency and film surface area, below which the generated attractive forces are comparatively diminutive. The attractive SSF achieves a small extremum for a critical value of the separation distance, both of which can be calculated efficiently using the derived formulae.

Chapter 3) How does the flexibility of an SFL oscillator affect the system's attractive load capacity? How do the physical mechanisms governing the transition to attraction differ between flexural and rigid-body systems?

The objective of this chapter is to explain the physical mechanisms that underly the thousandfold improvement in attractive load capacity observed in recent experiments involving thin, highly flexible oscillators. For this purpose, the matched-asymptotic formulation developed in Chapter 2 is extended here to account for resonant flexural oscillations of a thin disk. In contrast with the results of prior literature that investigated high-frequency elastic deformations of thicker oscillators, it is found here that incorporation of resonant, low-frequency thin-plate dynamics successfully reproduces the observed magnification of attractive load capacity. While the transition to attraction for rigid-body systems occurs solely due to a drop in steady pressure near the outer edge of the squeeze film, that for flexural systems is found to stem from valleys of pressure inside the film that occur near the nodal circles of the standing wave exhibited by the flexible oscillator. Furthermore, the transition is found to occur for a much wider range of the critical operating parameters—oscillation frequency and film surface area. Both the extent of this favorable parametric region and the scale of the associated attractive forces are found to grow substantially for rising values of the elastic wavenumber, i.e. for disks with increasing flexibility.

Chapter 4) How do fluid–structure interactions affect the motion of a flexible oscillator, the associated gas flow in the squeeze film, and the resulting load capacity?

While the results from Chapter 3 successfully reproduced the tremendous scale of attractive forces observed in the recent experiments, other aspects of the experimental data exhibit glaring disagreement with the theoretical predictions, primarily due to effects of fluid–structure coupling. In this chapter, the dynamic Kirchoff–Love equation describing the flexural oscillations of a thin disk is coupled with the Reynolds equation describing compressible gas flow in the slender film, yielding a problem involving two-way-coupled fluid–structure interactions. The formulation allows characterization of the disk motion under the simultaneous action of a localized, time-harmonic excitation force with a known force amplitude and the reactive forces caused by structural bending and squeeze-film overpressure. The nonlinear problem is solved with use of asymptotic methods to provide an analytical expression specifying the attractive levitation force as a function of the excitation force amplitude. Accounting for two-way coupling is found to give rise to a distinct dimensionless parameter, C, which measures the degree to which the dynamic disk flexure is dampened by oscillatory pressure variations in the squeeze film associated with the viscous gas flow. For increasing values of C, successive resonant modes of the disk are suppressed by viscous attenuation and, for very large values $C \gg 1$, the system exhibits an interesting universal behavior that gives rise to a parameter-independent levitation force. Asymptotic predictions for sufficiently large values of C yield promising agreement with experimental measurements of the levitation force, the causal time-averaged squeeze-film pressure distribution and the associated time-averaged disk deformation. In particular, increasing the disk radius beyond a critical value is found to yield no benefit for the attractive load capacity, justifying the development of large-scale SFL systems with multiple small oscillators. The chapter ends with suggestions for advanced theoretical formulations that may be developed in the future to provide greater accuracy in describing practical SFL systems.

Chapter 5) Can levitation systems that operate using the attractive squeeze-film force be modified to also provide transportation of the suspended object? Among the techniques that exist for transporting objects suspended repulsively, which method—or combination of methods—may be adapted for this purpose?

Considered in this chapter are two prominent methods of squeeze-film transportation: (i) forcing the oscillator to exhibit laterally asymmetrical dynamic flexure, such as traveling-wave oscillations, and (ii) simply tilting the oscillated object in the desired direction of motion. A reduced theoretical description of the relevant flow problem is developed, using the compressible-flow Reynolds equation, allowing straightforward asymptotic computation of the levitation and (quasistatic) thrust forces produced in a planar, asymmetrical squeeze-film system. Tilting the oscillation axis of a rigid-body system provides a substantial thrust force, making it a suitable transport mechanism for repulsively levitated objects, but reduces significantly the maximum repulsive load capacity. On the other hand, for flexural oscillation systems, appropriate inclination is found to increase both the thrust and the associated attractive load capacity, with greater benefits obtained for flexural oscillation modes that exhibit higher lateral asymmetry.

Chapter 6) Why is the squeeze-film effect not as ubiquitous in real-world applications as other methods of levitation and gaseous lubrication? Which specific aspects of this phenomenon require further investigation and/or innovation?

Provided in this final chapter are recommendations for future work in the study of squeeze-film levitation, split into two main categories: open practical challenges that currently deter commercial implementation of this technology and viable extensions of the present theoretical work that may provide improved accuracy, generality and versatility. A third section of this chapter explores other techniques for vibration-induced attraction found in literature.

Chapter 2

Viscoacoustic theory of rigid-body squeeze-film levitation

2.1 Executive summary

In this chapter, we investigate the air flow induced by a rigid circular disk or piston vibrating harmonically along its axis of symmetry in the immediate vicinity of a parallel surface.

Previous attempts to characterize these so-called "squeeze-film" systems largely relied on simplifications afforded by neglecting either fluid acceleration or viscous forces inside the thin enclosed gas layer. The present viscoacoustic analysis employs the asymptotic limit of small vibration amplitudes to investigate the flow by systematic reduction of the Navier–Stokes equations in two distinct flow regions, namely, the inner gaseous film where streamlines are nearly parallel to the confining walls and the near-edge region of non-slender flow that features gas exchange with the surrounding stagnant atmosphere.

The flow in the gaseous film depends on the relevant Stokes number, defined as the ratio of the characteristic viscous time across the film to the characteristic oscillation time, and on a compressibility parameter, defined as the square of the ratio of the acoustic time for radial pressure equilibration to the oscillation time. A Strouhal number based on the local residence time emerges as an additional governing parameter for the near-edge region, which is incompressible at leading order. The method of matched asymptotic expansions is used to describe the solution in both regions, across which the time-averaged pressure exhibits comparable variations that give

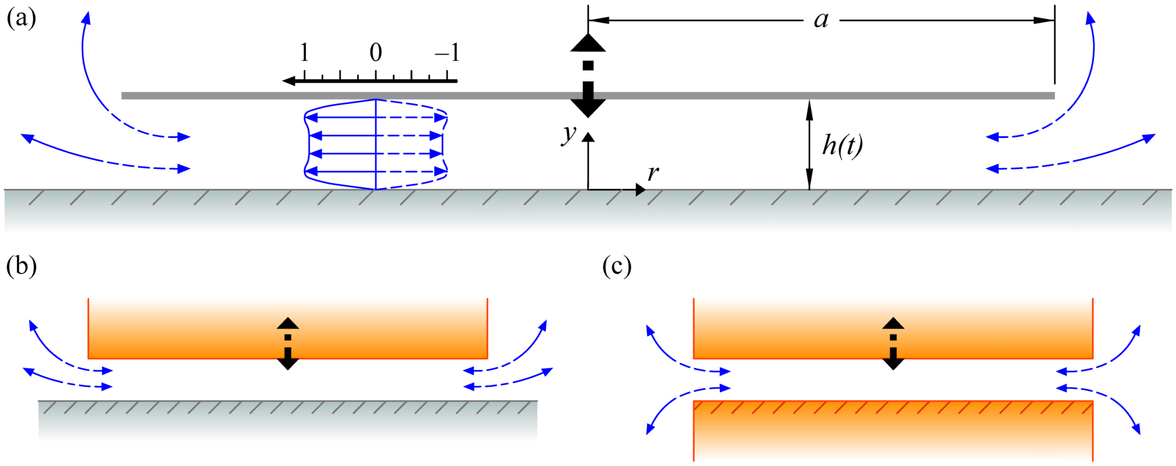

Figure 2.1. Schematic illustration of the three axisymmetric flow configurations examined in this study, including (a) a disk or (b) a piston vibrating close to an infinite wall, and (c) a piston vibrating close to another piston. The curved arrows in each case represent airflow in the near-edge region, extending over radial distances $r - a \sim h_o$. The velocity profile pictured inside the slender inner region $a \geq a - r \gg h_o$ of the disk–wall configuration in panel (a) corresponds to the leading-order flow (2.35) generated for a Stokes number of $\alpha^2 = 300$.

opposing contributions to the resulting time-averaged force experienced by the disk or piston. A diagram structured with the Stokes number and compressibility parameter as coordinates reveals that this steady squeeze-film force, typically repulsive for small values of the Stokes number, alternates to attraction across a critical separation contour in the parametric domain that exists for all Strouhal numbers.

To the best of our knowledge, this analysis provides, for the first time, a unifying viscoacoustic theory of axisymmetric squeeze films, which yields a reduced parametric description for the time-averaged repulsion/attraction force that is potentially useful in applications including non-contact fluid bearings and robot locomotion.

2.2 Introduction

This chapter concerns the fluid motion induced by a rigid circular disk (or piston) of radius a vibrating along its axis in the vicinity of a stationary parallel surface. The three specific geometrical configurations to be analyzed are represented in figure 2.1. The width of the gap separating the two parallel surfaces is assumed to vary harmonically in time according to

$$h(t) = h_o + b\cos(\omega t) \tag{2.1}$$

or, equivalently,

$$\frac{h(t)}{h_o} = 1 + \varepsilon\cos(\omega t), \tag{2.2}$$

where $h_o \ll a$ is the mean separation distance, ω is the angular frequency, b is the oscillation amplitude, and $\varepsilon = b/h_o$ is the relevant relative amplitude. Such slender-flow systems, commonly referred to as "squeeze-film" systems, are of great interest in the context of gas lubricated bearings present in high-speed rotary machinery and also in contactless levitation devices used in assembly line transport of microelectronics [7]. In the former case of squeeze-film air bearings, there is great demand for predicting the load capacity, while in the latter, referred to as "squeeze-film levitation" (SFL), the sensitivity of transported items additionally warrants comprehension of radial pressure departures $p(r) - p_a$ from the outer ambient value p_a.

It must be noted that, in applications of SFL, the oscillator is typically situated below the levitated object, in contrast to the illustrations in the figure. In that case, one may question whether it is appropriate to prescribe the variation of the gap width $h(t)$ since the unconstrained, levitated object would be free to oscillate in response to the transient overpressures beneath. However, due to the high forcing frequencies involved in practical applications, such induced vibrations are seen to be relatively small, and can be virtually eliminated with use of a suitable damping mechanism [3, 39]. The results derived in this chapter are thus, in principle, applicable to such configurations as well.

A key aspect of the flow problem is that, although the disk motion is harmonic, the resulting overpressure $p - p_a$ displays, in general, a nonzero time-averaged value at any given location, that being a consequence of the systemic nonlinearities introduced by convection and gaseous compressibility. As a result, the disk or piston experiences a steady perpendicular force, hereafter referred to as the time-averaged or steady squeeze-film force (SSF). In principle, the SSF may act to either repel or attract two objects with parallel surfaces, but decades worth of experiments demonstrate that repulsive forces are typically thousands of times stronger, and occur for a much wider range of operating conditions [1, 19, 37]. (In recent years, a dramatic increase in the attractive load capacity of SFL systems has been demonstrated with use of highly flexible oscillators, a development that is discussed at length in Chapters 3 and 4 of this dissertation).

2.2.1 Modeling considerations

Analysis of the fluid flow induced by the disk oscillations must consider the existence of two different regions, namely, the slender film separating the disk from the planar wall at radial distances r in the range $a \geq a - r \gg h_o$, where streamlines are aligned with the parallel surfaces, and the non-slender peripheral region that extends over distances of order h_o from the disk edge, which controls the exchange of fluid with the surrounding stagnant atmosphere and its associated pressure drop. We shall see that the behavior of the flow in the slender film depends on the relative magnitude of the characteristic oscillation time ω^{-1}, when compared with the two principal mechanical timescales, namely, that for viscous diffusion of momentum across the gas layer $t_v = h_o^2/(\mu_a/\rho_a)$, where μ_a and ρ_a are the values of the viscosity and density in the surrounding atmosphere, and the characteristic acoustic timescale for radial pressure equilibration $t_a = a/(p_a/\rho_a)^{1/2}$, where $(p_a/\rho_a)^{1/2}$ is, aside from a factor $\gamma^{1/2}$, the ambient value of the sound speed, with γ denoting the ratio of specific heats. The analysis that follows assumes all three times to be comparable, yielding order-unity values of the relevant Stokes number

$$\alpha^2 = \frac{t_v}{\omega^{-1}} = \frac{\omega h_o^2}{\mu_a/\rho_a} \tag{2.3}$$

and of the relevant compressibility parameter

$$\Lambda = \left(\frac{t_a}{\omega^{-1}}\right)^2 = \frac{\omega^2 a^2}{p_a/\rho_a}. \tag{2.4}$$

The three length scales present in the problem (i.e. the disk radius a, the mean separation distance h_o, and the oscillation amplitude εh_o) introduce two additional operational parameters – the relative oscillation amplitude ε and the slenderness ratio $\delta = h_o/a \ll 1$.

It will be shown in the following analysis that the time-averaged pressure drop across the slender film, identical for all three geometrical configurations shown in figure 2.1, depends solely on α^2 and Λ, while that across the peripheral region, different for each geometrical configuration, depends additionally on a third controlling parameter, the local Strouhal number

$$St = \frac{t_c}{\omega^{-1}} = \frac{\delta}{\varepsilon}, \tag{2.5}$$

where $t_c = h_o/(\varepsilon\omega a)$ is the characteristic residence time in the pulsatile peripheral flow. (Note that the characteristic radial flow speed at the film edge induced by disk motion and used to define t_c is $(b/h_o)\omega a$, as follows from the conservation of mass in the film.) The majority of previous analyses of squeeze-film systems $\delta \ll 1$ have been restricted to specific limiting cases of the slender gas-film problem, arising for extreme values of α^2 and Λ, namely, incompressible flow for $\Lambda \to 0$, inviscid flow for $\alpha^2 \gg 1$, and lubrication flow for $\alpha^2 \ll 1$.

A unifying viscoacoustic theory of squeeze-film systems, that embodies all of these specific cases and accounts for the pressure variation across the peripheral region, is to be developed here by considering the regime $\alpha^2 \sim 1$ and $\Lambda \sim 1$ for asymptotically small values of the relative oscillation amplitude $\varepsilon = b/h_o \ll 1$ and the slenderness ratio $\delta \ll 1$ in the distinguished limit $\varepsilon \sim \delta$ (or, equivalently, $St \sim 1$). While the assumption that $\varepsilon \ll 1$ inevitably limits the accuracy of the following theoretical description for gap widths that are comparable to the operating amplitude, $h_o \sim b$, it will be shown to allow efficient mathematical reduction of the problem and yield practically relevant insights into the physics of rigid-body squeeze-film systems. It must finally be noted that, since the mean free path is of order $\ell \sim (\mu_a/\rho_a)/(p_a/\rho_a)^{1/2}$, in the limit investigated here, the relevant Knudsen number in the gas layer is $Kn = \ell/h_o \sim (\Lambda^{1/2}/\alpha^2)(h_o/a) \sim \delta \ll 1$, thereby guaranteeing applicability of the continuum hypothesis to the description of the flow.

A note on the emergence of compressibility in gaseous lubrication flows

It is natural to question the relevance to squeeze-film levitation of gaseous compressibility, a phenomenon that is most commonly associated with high-speed aerodynamics and air-breathing propulsion systems. Experiments conducted in the 1890's by Albert Kingsbury [55] revealed that the performance of air-lubricated journal bearings differed distinctly from those lubricated using liquids, and could not be explained with use of the theory of hydrodynamic lubrication developed earlier by Osborne Reynolds [56]. Promising agreement with the experimental data was obtained later in 1913 by W. J. Harrison [57], who generalized the theory of Reynolds to account for compressibility and integrated numerically the resulting nonlinear differential equation.

In conventional aerodynamics, such as the study of external airflow around a submerged body, the importance of compressibility—the variability of air density in response to pressure differences—is determined by the relevant Mach number $M = u_c/c_a$, the ratio of the characteristic flow speed u_c to the local ambient sound speed c_a. Since variations of pressure p around the body are dominantly balanced by convective acceleration of the air, the characteristic scale of relative density variations can be estimated as $\Delta\rho/\rho_a = \gamma M^2$, where we have deduced from the thermal equation of state the fact that $\Delta\rho/\rho \sim \Delta p/p$. Under the assumption of adiabatic, inviscid flow, relative density variations will be of order 0.05 for $M \lesssim 0.3$, whence effects of compressibility can be safely disregarded in a theoretical description of the salient flow dynamics [58].

In contrast, for the wall-bounded slender flow geometries found in lubricated bearings (see § 1.2), compressibility may arise even at low Mach numbers due to a dominant balance between pressure forces and strong viscous shear stresses, provided that the relevant Reynolds number Re is small. For such a layer having characteristic thickness h_o and length a, it follows that $\Delta\rho/\rho_a = \gamma M^2/(Re\, h_o/a)$, whence density variations may be non-negligible if either $Re = u_c h_o/(\mu_a/\rho_a)$ or the aspect ratio h_o/a is sufficiently small relative to the square of the Mach number. Note further that the associated Knudsen number in the gas layer scales as $Kn = M/Re$. Thus, for slender flows with $M \ll 1$, $Re \sim 1$ and sufficiently small aspect ratio h_o/a, effects of compressibility and viscous shear may enter simultaneously while preserving small values of Kn, whence the airflow can be analyzed with use of a conventional continuum description.

Even among such slender-flow systems, squeeze-film lubrication presents an interesting configuration where compressibility may arise also due to small-amplitude normal oscillations of the bounding wall. Consider an operating condition where the relevant Stokes number $\alpha^2 = \omega h_o^2/(\mu_a/\rho_a)$ is large, i.e. the flow can be considered effectively inviscid outside near-wall boundary layers, and the oscillation amplitude b is small compared to the mean film width h_o. Pressure variations are then balanced prominently by local acceleration of the air (since the associated Strouhal number h_o/b is large), giving $\Delta\rho/\rho_a = \gamma M^2 h_o/b$. Even in the case of low-speed flow $M \ll 1$, relative density variations may be non-negligible for sufficiently small values of the relative amplitude b/h_o.

Historical theoretical approaches

The classical lubrication (or Stokes) limit $\alpha^2 \ll 1$, describing compressible flow with negligible fluid acceleration, has been widely studied throughout the twentieth century by way of the isothermal squeeze-film equation [8], a modified form of the well-known Reynolds lubrication equation [56]. Specific interest in the role of compressibility in the slender gas layer was piqued by an experiment demonstrated in 1956 at the 9th International Congress of Applied Mechanics at Brussels [15], where a disk rotating around its axis in close proximity to a parallel wall was reported to experience a perpendicular suction force that transitioned to growing repulsion as the gap between the disk and the wall was reduced. In a subsequent clarifying analysis, Taylor and Saffman [5] proved that the observed repulsive squeeze-film force could be explained by effects of compressibility arising from imperfections in the operation of the rotor such as off-axis rotation or normal vibrations. They demonstrated using perturbation methods that the steady overpressure resulting from the latter case scales with the square of the dimensionless vibration amplitude ε and depends on a single parameter—the squeeze number $\sigma = 12\Lambda/\alpha^2$. These results were formalized by [8] with use of the isothermal squeeze-film equation for planar and axisymmetric geometries. Finite-difference solutions of the axisymmetric squeeze-film equation were experimentally verified by [9], who noted the presence of a central region dominated by viscous damping, where the film pressure varies gradually, and a near-edge region where the pressure drops rapidly toward ambient conditions, the latter of which was treated by [59] as a mathematical boundary layer of thickness $O(\sigma^{-1/2})$. It must be noted that, in the ideal lubrication limit $\alpha^2 \to 0$, the scale of pressure variations across the small peripheral region surrounding the film edge is sufficiently small such that the steady pressure in the film can be assumed to reach the ambient value p_a immediately at the edge $r = a$ [60].

On the other hand, the limit of large Stokes numbers $\alpha^2 \gg 1$, where the flow is nearly inviscid outside thin, near-wall (Stokes) boundary layers, has been treated by some as a limiting form of *acoustic levitation*, which conventionally involves the suspension of light objects in the antinodes of standing pressure waves between a vibrating piston and a reflector plate separated by an integral multiple of the half-wavelength of sound [7]. When the mean separation distance is made much smaller than the acoustic wavelength, i.e. $h_o \ll a$ with $\Lambda \sim 1$, the reflector plate itself experiences an immense, repulsive SFL force. In 1902, Lord Rayleigh presented a foundational formulation of acoustic radiation inside a cylindrical piston of air undergoing transverse vibrations, expressing the overpressure in terms of the volumetric energy density [61]. After several years of disagreement over the application of Rayleigh's theory to acoustic levitation, [62] detailed the one-dimensional Rayleigh and Langevin radiation pressures—for flows with and without circumferential confinement—imposed by a vibrating piston on a perfectly reflecting parallel surface for arbitrary mean separation width. Clarifications were provided regarding distinctions between the Eulerian and Lagrangian definitions of the time average, the role played by second-order acoustic straining in reducing the mean pressure, and the additional hydrostatic pressure contributed by flow confinement. Surprisingly, this 1D theory has been shown to exhibit reasonable agreement with experimental measurements of controlled, ultrasonic squeeze-film systems for sufficiently large separation distances h_o (for which $5 \lesssim \alpha^2 \lesssim 100$), where the generated levitation forces were of order 0.1–1.5 kgf [1, 19].

Recent improvements in theoretical modeling

The two theoretical approaches described above (i.e. nonlinear acoustics and lubrication theory) break down beyond their respective ranges of validity, defined by the magnitude of the mean gap width h_o relative to the characteristic thickness of the Stokes layers that develop on the parallel surfaces $\delta_{SL} = \sqrt{\mu_a/(\rho_a \omega)}$. For systems where $h_o \gg \delta_{SL}$, viscous effects are confined to thin Stokes layers, so that the 1D inviscid formulation based on nonlinear acoustics proves to be fairly accurate, although validity is limited in principle by the fact that radial pressure variations are entirely neglected. In contrast, viscous forces are dominant everywhere in the opposite limit $h_o \ll \delta_{SL}$, in which lubrication theory displays excellent agreement with experimental observations [19], while the inviscid theory is seen to severely undershoot the experimentally measured SSF. The predictive capability of lubrication theory deteriorates rapidly for increasing values of h_o, as shown by comparisons with Navier–Stokes computations [63], the latter revealing that variations of the steady pressure across the peripheral region become comparable in magnitude to those along the film at sufficiently low oscillation frequencies, thereby invalidating the aforementioned assumption regarding the value of the edge pressure ($p = p_a$ at $r = a$). Indeed, in a seminal analysis of the squeeze-film effect in 1970 [64], C. H. T. Pan concludes that, for finite squeeze numbers σ, “the weakest link in the lubrication theory ... is the omission of the convective inertia in the edge region”.

Applicability of either theory for real-life squeeze-film levitation systems is further complicated by the fact that the equilibrium levitation distance h_o is typically unknown prior to operation, yielding uncertainty in the choice of the needed analytical framework. Furthermore, there exists a non-negligible intermediate range of levitation heights $h_o \sim \delta_{SL}$, describing the

.

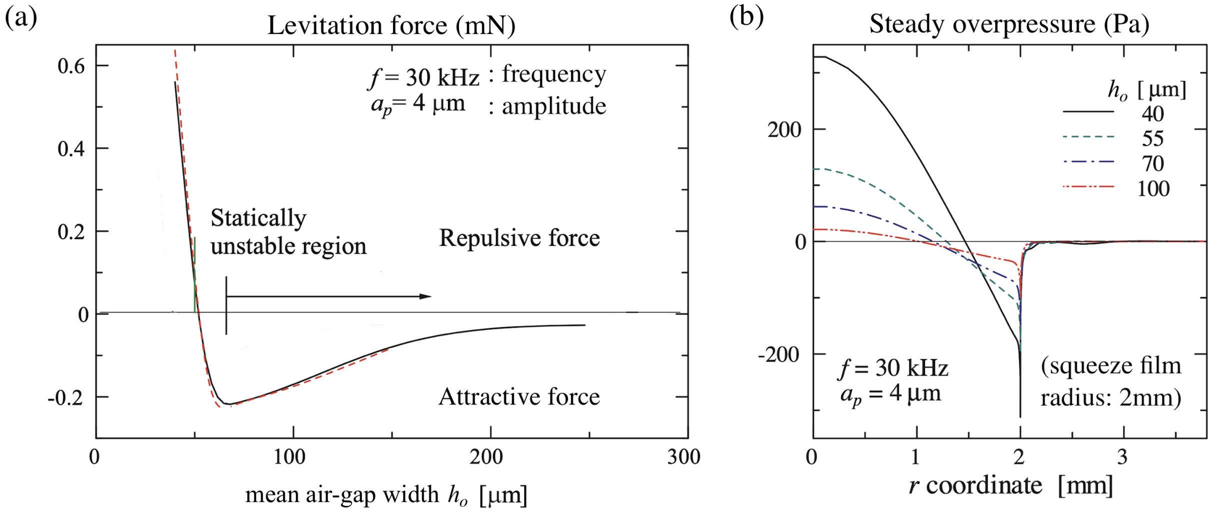

Figure 2.2. Results of direct numerical simulations by Yoshimoto, Shou and Somaya [4], reproduced with simplifications from figures 10 and 11 in [4]. Displayed are (b) sample profiles of the steady overpressure in the squeeze film under operating conditions for which an increase in the mean air-gap width h_o causes a transition from repulsive to attractive levitation forces. The variation of the force with separation distance (a) is strikingly similar to that found for a Bernoulli gripper, but the causal distribution of pressure (b) is highly different [65].

operating conditions of many practical systems [1, 19], where effects of neither fluid inertia nor viscous shear can be neglected. Recent efforts to develop more sophisticated formulations have thus faced two principal challenges: (i) derivation of a comprehensive *viscoacoustic* theory that considers simultaneous effects of fluid inertia, viscosity and gaseous compressibility and (ii) development of an accurate boundary condition for the pressure at the edge of the film.

With regard to the first, inertial corrections to viscous-flow solutions have been proposed, either through iteration schemes [66] and perturbation methods [67] for small Reynolds numbers $\varepsilon(h_o/\delta_{SL})^2 \ll 1$, or through averaging of the acceleration terms in the Navier–Stokes momentum equation across the slender film [68]. Both of the cited studies demonstrated greatly improved agreement with experimental measurements in their respective regimes of validity [66, 68], but neglected gaseous compressibility. With regard to the question of the edge pressure, some have correctly argued that, for very large Reynolds numbers, the flow exiting the film is a jet with uniform ambient pressure, whereas that entering is entrained due to a quasi-steady decrease in pressure from the quiescent surroundings to the edge [69]. Turns [70] proposed an empirical correction to represent this entrance pressure drop while, in a later publication, Li, Cao, Liu and Ding [68] applied integral conservation laws to an arbitrary control volume in the periphery of the film, the latter yielding significant agreement with experimental data. Several numerical studies of the flow in the film [38, 63, 71] have adopted an artificial "radiation boundary condition" that minimizes the reflection of acoustic waves at its edge [72, 73]. In a recent study [74], perturbation theory was applied to reduce the Navier–Stokes equations in both the film and the peripheral region, the latter of which was assumed to be inviscid, allowing imposition of an approximate analytical radiation boundary condition [75] for the oscillatory film pressure in the first approximation. The resulting system of linear, time-independent partial differential equations was solved computationally, yielding a reduced-order, viscoacoustic, adiabatic model that demonstrated reasonable accuracy for a fairly wide range of h_o [74]. On the other hand, brute-force numerical simulations have been conducted in expanded spatial domains that explicitly model the peripheral flow, successfully reproducing the transition to weak, attractive SSFs that has been experimentally observed [4, 6]. In particular, Yoshimoto, Shou and Somaya [4] provide numerical results (copied above in figure 2.2) that demonstrate clearly how, under operating conditions that give rise to attractive levitation forces, spatial variations of the steady pressure exhibit comparable magnitude along the film and across a smaller region surrounding its edge. Such models display excellent qualitative agreement with experimental data for substantial ranges of h_o, albeit at the expense of computational speed.

Further details regarding the history of the theoretical modeling of squeeze-film systems can be found in Da Silva's dissertation from 1980 [10] and a recent review article [7].

Novelty of the present formulation

The purpose of this chapter is to develop an efficient viscoacoustic theory that synthesizes rigorous quantification of the time-averaged peripheral pressure variations with analytical reduction of the equations governing film flow. Such a formulation is necessary to (i) accurately predict *a priori* the levitation characteristics of arbitrary SFL systems and (ii) understand the physical principles that underly the anomalous transition to weak attractive forces [37]. The limit $\Lambda \sim 1$, $\alpha^2 \sim 1$, and $\varepsilon \sim \delta \ll 1$ addressed below enables the analysis of effects of viscosity, local acceleration, thermal diffusion, acoustic wave propagation and the nonlinearities introduced by convection and compressibility, while encompassing the specific cases investigated in the past as limiting solutions for extreme values of the controlling parameters Λ and α^2. The method of matched asymptotic expansions will be used to relate the solution in the two distinct flow regions, ultimately providing quantitative information regarding the dependence of the time-averaged force on the governing parameters Λ, α^2 and $St = \delta/\varepsilon$, and the specific edge geometry (see figure 2.1). The squeeze-film force will be shown to involve two comparable contributions—the first accounting for variations of the pressure along the slender gas layer relative to its value at the edge $r = a$, and the second involving the relaxation of pressure across the near-edge region from said value to ambient conditions—the latter of which is found to be responsible for the transition to attractive forces for rigid-body systems.

2.2.2 Organization of the chapter

The remainder of this chapter is organized as follows. The reduced conservation equations governing each of the two distinct flow regions are presented in § 2.3 in dimensional form, accompanied by justificatory discussions of the associated characteristic scales. The dimensionless conservation equations pertaining to the slender film are written in § 2.4 and their leading-order time-harmonic solution is presented in § 2.5. Associated first-order corrections to the film pressure are computed in § 2.6 and used to determine the first contribution to the time-averaged levitation force, along with simplified expressions of both for limiting values of the Stokes number and the compressibility parameter. The dimensionless conservation equations describing flow in the peripheral region of the squeeze film are written in § 2.7, supplemented by a boundary condition that accounts for the driving radial velocity present at the edge of the slender gas film, obtained by asymptotically matching with the leading-order solution from the film. Numerical computations of the time-averaged pressure drop across the peripheral region are presented, along with predictions of its behavior for limiting values of the Stokes number and the peripheral Strouhal number. The dependence on the three governing parameters of the steady squeeze-film force acting on the oscillating body, which accounts for comparable pressure contributions from the two distinct flow regions, is discussed in § 2.8 with specific attention dedicated to the criteria required for a transition between repulsive and attractive forces. The force predicted by our asymptotic analysis is compared with that determined in recent CFD (computational fluid dynamics) simulations [6]. Concluding remarks are given in § 2.9, and finally, explicit expressions needed for the asymptotic computation of the steady film pressure and squeeze-film force are provided in § 2.10.

Our asymptotic analysis: (i) reveals that the time-averaged pressure drop across the near-edge region—from the unperturbed, ambient air to the edge of the squeeze-film—is comparable in magnitude and *necessarily* opposite in sign to that found along the wall-bounded gas layer—from its edge to its center; (ii) leads to simplified expressions that expedite the evaluation of the steady squeeze-film force over a wide range of conditions of practical interest, potentially facilitating the operation and control of high-frequency systems; (iii) unveils a boundary on the α^2–Λ parametric plane across which the force switches from repulsion to attraction; (iv) demonstrates numerically that the force is only weakly dependent on the precise geometric configuration of the near-edge region, under the present assumptions, and (v) compares favorably with recently published computational results [6].

2.3 Distinct regions and characteristic scales

An asymptotic analysis of the flow induced by the harmonic disk oscillations defined in (2.2) is to be given for $\alpha^2 \sim 1$ and $\Lambda \sim 1$ in the distinguished double limit $\varepsilon \ll 1$ and $\delta = h_o/a \ll 1$ with $\varepsilon \sim \delta$. The axisymmetric periodic motion will be described in terms of the radial and axial velocity components $u(r,y,t)$ and $v(r,y,t)$, with y and r denoting the axial distance from the wall and the radial distance from the disk center, as indicated in figure 2.1. The description must account for the variations of the pressure p, density ρ, and temperature T of the gas from their ambient values p_a, ρ_a, and T_a. The analysis must consider the existence of two distinct regions, namely, the slender gas layer separating the disk from the planar wall, where the streamlines are nearly parallel to the bounding solid surfaces, and the boundary region of non-slender flow extending over distances of order h_o from the disk edge. We shall give below the reduced conservation equations and the associated scales for the flow in these two regions.

The full compressible Navier–Stokes equations governing the axisymmetric flow investigated here can be found in [76] in cylindrical form. In the slender gas film separating the two parallel solid surfaces, where $r \sim a$ and $y \sim h_0 \ll a$, these conservation equations can be simplified to the boundary-layer form

$$\frac{\partial \rho}{\partial t} + \frac{1}{r}\frac{\partial}{\partial r}(\rho r u) + \frac{\partial}{\partial y}(\rho v) = 0, \tag{2.6}$$

$$\frac{\partial p}{\partial y} = 0, \tag{2.7}$$

$$\rho\left(\frac{\partial u}{\partial t} + u\frac{\partial u}{\partial r} + v\frac{\partial u}{\partial y}\right) = -\frac{\partial p}{\partial r} + \frac{\partial}{\partial y}\left(\mu\frac{\partial u}{\partial y}\right), \tag{2.8}$$

$$\rho c_p\left(\frac{\partial T}{\partial t} + u\frac{\partial T}{\partial r} + v\frac{\partial T}{\partial y}\right) - \left(\frac{\partial p}{\partial t} + u\frac{\partial p}{\partial r}\right) = \mu\left(\frac{\partial u}{\partial y}\right)^2 + \frac{\partial}{\partial y}\left(\kappa\frac{\partial T}{\partial y}\right). \tag{2.9}$$

For the slender flow analyzed here, molecular-transport terms involving radial derivatives are a factor $(h_o/a)^2 = \delta^2 \ll 1$ smaller than those involving transverse derivatives, so that only the latter have been retained in writing the viscous force per unit volume in (2.8) and the heat-conduction and viscous-dissipation terms in (2.9). At the same level of approximation (i.e. with small relative errors of order $\delta^2 \ll 1$), the analysis neglects the variations of the pressure across the gas layer, as reflected by the reduced equation (2.7). In the proceeding analysis, the specific heat at constant pressure c_p is assumed to be constant, while the viscosity coefficient μ and the thermal conductivity κ are assumed to vary from their ambient values according to

$(\mu/\mu_a) = (\kappa/\kappa_a) = (T/T_a)^\nu$ with $\nu \approx 0.77$, an excellent approximation for air [77], for which the Prandtl number takes the value $Pr = c_p\mu/\kappa = 0.7$ and the ratio of specific heats takes the value $\gamma = 1.4$. The above equations must be supplemented with the equation of state

$$\frac{p}{p_a} = \frac{\rho}{\rho_a}\frac{T}{T_a}. \tag{2.10}$$

In the slender gas layer the axial velocities induced by the displacement rate $\mathrm{d}h/\mathrm{d}t = -\varepsilon\omega h_o \sin(\omega t)$ of the moving surface are of order $v_c = \varepsilon\omega h_o$. The associated radial velocities are much larger, of order $u_c = v_c/\delta = \varepsilon\omega a$, as follows from the straightforward order-of-magnitude balance $u_c/a \sim v_c/h_o$ stemming from (2.6). Since it is assumed that the characteristic time for the oscillatory motion ω^{-1} is comparable to the characteristic viscous and heat conduction times across the gaseous film $t_v = h_o^2/(\mu_a/\rho_a)$ and $t_h = Pr\, t_v \sim t_v$, viscous stresses and heat conduction can be expected to have, in principle, a significant effect on the oscillatory flow. In contrast, convective acceleration has a negligible effect at leading order in the limit $\varepsilon \ll 1$, because the associated Strouhal number is $\varepsilon^{-1} \gg 1$, as can be seen by comparing the orders of magnitude of the local acceleration $\partial u/\partial t \sim \omega u_c$ and the convective acceleration $u\, \partial u/\partial r \sim u_c^2/a$ in (2.8). A similar order-of-magnitude analysis in the energy equation (2.9) provides $(u\partial T/\partial r)/(\partial T/\partial t) \sim \varepsilon$, indicating that convective heat transport is also negligible at leading order. Note that, since the characteristic value of the radial pressure variations $p - p_a$ needed to produce velocity changes of order $u_c = \varepsilon\omega a$ in times of order ω^{-1} is $\Delta p = \rho_a \varepsilon \omega^2 a^2$, as follows from the balance $\partial p/\partial r \sim \rho\, \partial u/\partial t$, the resulting instantaneous levitation force acting on the disk is expected to be of order $\langle \mathcal{F}_L \rangle \sim \Delta p\, a^2 = \rho_a \varepsilon \omega^2 a^4$.

In the limit $\Lambda \sim 1$ considered here, the pressure variations $p - p_a \sim \Delta p$ induced in the gap are small compared with the ambient pressure, as can be seen by writing $\Delta p/p_a \sim \varepsilon(\omega^2 a^2)/(p_a/\rho_a) = \varepsilon\Lambda$. Correspondingly, the relative density and temperature variations from their respective ambient values are also small, of order $(\rho - \rho_a)/\rho_a \sim (T - T_a)/T_a \sim \varepsilon\Lambda$, as follows from the equation of state (2.10). The conservation equations (2.6)–(2.10) at leading order will be shown to reduce to a linear problem describing compressible unsteady lubrication flow, which will be solved analytically in closed-form. The leading-order flow variables will be shown to vary harmonically with time, thus yielding no time-averaged contributions over a period of the driving oscillations, with the time-averaging operator formally defined by

$$\langle\cdot\rangle = \frac{\omega}{2\pi}\int_t^{t+2\pi/\omega} \cdot \, \mathrm{d}t \,. \tag{2.11}$$

We shall see that, since the pressure distribution at leading order has a zero time-averaged value, the computation of the time-averaged levitation force $\langle\mathcal{F}_L\rangle$ requires quantification of higher-order corrections associated with nonlinear convective and compressibility effects, involving time-averaged pressure differences $\langle p - p_a\rangle$ of order $\rho_a\varepsilon^2\omega^2a^2 = \varepsilon\Delta p$. The associated time-averaged levitation force $\langle\mathcal{F}_L\rangle \sim \varepsilon\Delta p\, a^2 = \varepsilon^2\rho_a\omega^2a^4$ can be expressed conveniently in the dimensionless form

$$\frac{\langle\mathcal{F}_L\rangle}{\varepsilon^2\rho_a\omega^2\pi a^4} = \frac{2}{\varepsilon}\int_0^1 \frac{\langle p - p_a\rangle}{\Delta p}\frac{r}{a}\mathrm{d}\left(\frac{r}{a}\right). \tag{2.12}$$

The slender gas layer, where the radial velocity is of order $u \sim u_c$, connects with the ambient atmosphere through a non-slender near-edge boundary region where $r - a \sim y \sim h_o$ and $u \sim v \sim u_c$. The flow in this region involves small pressure variations of order $(p - p_a)/p_a \sim \varepsilon^2\Lambda$, as follows from a balance between the pressure force per unit mass $\rho^{-1}\nabla p \sim (p - p_a)/(\rho_a h_o)$ and the convective acceleration $\mathbf{v}\cdot\nabla\mathbf{v} \sim u_c^2/h_o$, with $\mathbf{v} = (u,v)$ and $\nabla = (\partial/\partial r, \partial/\partial y)$. As can be expected from the equation of state (2.10), the associated density and temperature variations in this region are also small, of order $(\rho - \rho_a)/\rho_a \sim (T - T_a)/T_a \sim (p - p_a)/p_a \sim \varepsilon^2\Lambda$, so that at leading order in the limit $\varepsilon \ll 1$, the flow is effectively incompressible and features constant transport properties. Also, since $r - a \sim y \sim h_o \ll a$, the leading-order flow is locally planar, with a velocity field determined from the familiar incompressible two-dimensional equations

$$\nabla\cdot\mathbf{v} = 0, \tag{2.13}$$

$$\frac{\partial\mathbf{v}}{\partial t} + u\frac{\partial\mathbf{v}}{\partial r} + v\frac{\partial\mathbf{v}}{\partial y} = -\frac{\nabla p}{\rho_a} + \frac{\mu_a}{\rho_a}\left(\frac{\partial^2\mathbf{v}}{\partial r^2} + \frac{\partial^2\mathbf{v}}{\partial y^2}\right). \tag{2.14}$$

Using $u \sim v \sim u_c = \varepsilon\omega a$ in (2.14) provides the orders of magnitude of the local acceleration $\partial\mathbf{v}/\partial t \sim \omega u_c$, convective acceleration $\mathbf{v}\cdot\nabla\mathbf{v} \sim u_c^2/h_o$ and viscous force per unit mass $(\mu_a/\rho_a)\nabla^2\mathbf{v} \sim (\mu_a/\rho_a)u_c/h_o^2$, giving values that are comparable in magnitude in the limit $\alpha^2 \sim 1$ considered here, so that all terms in (2.14) must, in general, be retained in the description. It will be shown that the pressure drop across this boundary region, of order $p - p_a \sim \rho_a\varepsilon\omega^2 a h_o = \delta\Delta p$, contains a nonzero time-averaged component. In the distinguished limit $\delta \sim \varepsilon$, this local pressure drop is comparable in magnitude to the *time-averaged* pressure differences $\langle p - p_a\rangle \sim \varepsilon\Delta p$ induced along the gas film, consistent with the results of [4] (see figure 2.2), and must therefore be accounted for in computing the steady levitation force, as done in the following.

The asymptotic analysis below will consider separate solutions in the slender gas layer and in the near-edge region. The scales identified above will be used in defining appropriate dimensionless variables of order unity in each region. Following standard practice [78], asymptotic expansions in increasing powers of ε will be introduced for the different flow variables, leading to a hierarchy of problems that will be solved sequentially with account taken of the matching conditions arising at each order. To compute the time-averaged levitation force (2.12) with small relative errors of order $\varepsilon \sim \delta$, the description must consider two terms in the expansions for the slender region, whereas only the leading-order terms are needed in the near-edge region.

2.4 Formulation of the problem in the slender gaseous film

The analysis uses the dimensionless time $\tau = \omega t$ and dimensionless gap width

$$H = \frac{h}{h_o} = 1 + \varepsilon \cos(\tau)\,. \tag{2.15}$$

Substitution of the appropriate order-unity variables $\xi = r/a$, $Y = y/h_o$, $U = u/u_c$, $V = v/v_c$, $P = (p - p_a)/\Delta p$, $R = (\rho - \rho_a)/(\varepsilon \Lambda \rho_a)$ and $\Theta = (T - T_a)/(\varepsilon \Lambda T_a)$ into the governing equations (2.6) and (2.8)–(2.10) gives, with errors of order $\delta^2 \sim \varepsilon^2$,

$$\Lambda \frac{\partial R}{\partial \tau} + \frac{1}{\xi}\frac{\partial}{\partial \xi}[(1+\varepsilon\Lambda R)\xi U] + \frac{\partial}{\partial Y}[(1+\varepsilon\Lambda R)V] = 0, \tag{2.16}$$

$$(1+\varepsilon\Lambda R)\left[\frac{\partial U}{\partial \tau} + \varepsilon\left(U\frac{\partial U}{\partial \xi} + V\frac{\partial U}{\partial Y}\right)\right] = -\frac{\partial P}{\partial \xi} + \frac{1}{\alpha^2}\frac{\partial}{\partial Y}\left[(1+\varepsilon\Lambda\Theta)^{\nu}\frac{\partial U}{\partial Y}\right], \tag{2.17}$$

$$(1+\varepsilon\Lambda R)\left[\frac{\partial \Theta}{\partial \tau} + \varepsilon\left(U\frac{\partial \Theta}{\partial \xi} + V\frac{\partial \Theta}{\partial Y}\right)\right] - \left(\frac{\gamma-1}{\gamma}\right)\left(\frac{\partial P}{\partial \tau} + \varepsilon U\frac{\partial P}{\partial \xi}\right) = \varepsilon\left(\frac{\gamma-1}{\gamma}\right)\frac{(1+\varepsilon\Lambda\Theta)^{\nu}}{\alpha^2}\left(\frac{\partial U}{\partial Y}\right)^2 + \frac{1}{Pr\,\alpha^2}\frac{\partial}{\partial Y}\left[(1+\varepsilon\Lambda\Theta)^{\nu}\frac{\partial \Theta}{\partial Y}\right], \tag{2.18}$$

$$P = R + \Theta + \varepsilon\Lambda R\Theta, \tag{2.19}$$

while the axial momentum equation (2.7) becomes $\partial P/\partial Y = 0$, whence $P = P(\xi,\tau)$. The present system of equations admits analytic periodic solutions that satisfy isothermal non-slip conditions at the bounding walls,

$$\begin{cases} U = V = \Theta = 0 & \text{at} \quad Y = 0 \\ U = V + \sin(\tau) = \Theta = 0 & \text{at} \quad Y = H(\tau), \end{cases} \tag{2.20}$$

together with the regularity condition at the axis of symmetry, which implies that

$$U = \frac{\partial P}{\partial \xi} = \frac{\partial R}{\partial \xi} = \frac{\partial \Theta}{\partial \xi} = 0 \quad \text{at} \quad \xi = 0\,. \tag{2.21}$$

The needed boundary condition for the pressure P at the edge of the gas layer (i.e. at $\xi = 1$) is to be obtained from matching with the near-edge solution, as described in the following analysis. Substitution of the scaled variables into (2.12) yields

$$\langle F_L \rangle = \frac{2}{\varepsilon} \int_0^1 \langle P \rangle \xi \mathrm{d}\xi \tag{2.22}$$

for the dimensionless levitation force $\langle F_L \rangle = \langle \mathcal{F}_L \rangle / (\varepsilon^2 \rho_a \omega^2 \pi a^4)$. For future reference, it is of interest to note that (2.16) can be integrated across the gas layer to give

$$\Lambda \frac{\partial}{\partial \tau} \left(\int_0^H R \mathrm{d}Y \right) + \frac{1}{\xi} \frac{\partial}{\partial \xi} \left(\xi \int_0^H (1 + \varepsilon \Lambda R) U \mathrm{d}Y \right) - \sin(\tau) = 0, \tag{2.23}$$

with use made of the well-known Leibniz integral rule to exchange the time derivative and spatial integral involved in the first term. Computing the time average of (2.23) and integrating the result in the radial direction gives

$$\left\langle \int_0^H (1 + \varepsilon \Lambda R) U \mathrm{d}Y \right\rangle = 0 \tag{2.24}$$

upon imposing the boundary condition $U = 0$ at $\xi = 0$.

2.5 Leading-order solution in the gaseous film

The above problem is to be solved for $\varepsilon \ll 1$ by substituting the expansions

$$\begin{cases} U = U_0 + \varepsilon U_1 + \cdots \\ V = V_0 + \varepsilon V_1 + \cdots \\ P = P_0 + \varepsilon P_1 + \cdots \\ R = R_0 + \varepsilon R_1 + \cdots \\ \Theta = \Theta_0 + \varepsilon \Theta_1 + \cdots \end{cases} \tag{2.25}$$

into (2.16)–(2.19) and solving sequentially the problems that arise at different orders in powers of ε. Only the first two terms are to be considered in our analysis, consistent with the accuracy of (2.16)–(2.19) (note that the terms of order $\delta^2 \sim \varepsilon^2$ and smaller that were neglected in writing those equations would need to be retained if the analysis were to be carried out to higher orders).

To simplify the development, the axial coordinate Y will be replaced in the conservation equations (2.16)–(2.18) by its normalized counterpart $\eta = Y/H(\tau)$, with use of the substitutions, each accurate to order ε,

$$\frac{\partial}{\partial Y} \to (1-\varepsilon\cos\tau)\frac{\partial}{\partial \eta} \qquad \text{and} \qquad \frac{\partial}{\partial \tau} \to \frac{\partial}{\partial \tau} + \varepsilon\eta\sin\tau\frac{\partial}{\partial \eta}\,. \tag{2.26}$$

At leading order, the problem reduces to the integration of the linear system of equations

$$\Lambda\frac{\partial R_0}{\partial \tau} + \frac{1}{\xi}\frac{\partial}{\partial \xi}(\xi U_0) + \frac{\partial V_0}{\partial \eta} = 0, \tag{2.27}$$

$$\frac{\partial U_0}{\partial \tau} = -\frac{\partial P_0}{\partial \xi} + \frac{1}{\alpha^2}\frac{\partial^2 U_0}{\partial \eta^2}, \tag{2.28}$$

$$\frac{\partial \Theta_0}{\partial \tau} - \frac{\gamma-1}{\gamma}\frac{\partial P_0}{\partial \tau} = \frac{1}{Pr\,\alpha^2}\frac{\partial^2 \Theta_0}{\partial \eta^2}, \tag{2.29}$$

$$P_0 = R_0 + \Theta_0, \tag{2.30}$$

subject to

$$\begin{cases} U_0 = V_0 = \Theta_0 = 0 & \text{at} \quad \eta = 0 \\ U_0 = V_0 + \sin(\tau) = \Theta_0 = 0 & \text{at} \quad \eta = 1 \\ U_0 = \dfrac{\partial P_0}{\partial \xi} = \dfrac{\partial R_0}{\partial \xi} = \dfrac{\partial \Theta_0}{\partial \xi} = 0 & \text{at} \quad \xi = 0\,. \end{cases} \tag{2.31}$$

Since the pressure variation across the near-edge region is of order $\delta\Delta p$, as described in the paragraph following (2.12), at leading order in the limit $\varepsilon \sim \delta \ll 1$, the pressure in the gap must satisfy

$$P_0 = 0 \quad \text{at} \quad \xi = 1. \tag{2.32}$$

We shall see that the pressure drop across the near-edge region enters when matching with the following term in the expansion of the inner pressure, producing a nonzero first-order correction $P_1 \neq 0$ at $\xi = 1$ that must be accounted for when computing the time-averaged levitation force.

We begin the solution process by integrating (2.27) in the transverse direction using $V_0(\eta = 0) = 0$, yielding

$$V_0(\eta) = -\int_0^\eta \left[\Lambda \frac{\partial R_0}{\partial \tau} + \frac{1}{\xi}\frac{\partial}{\partial \xi}(\xi U_0)\right] \mathrm{d}\eta\,, \tag{2.33}$$

which will be useful later. Evaluating (2.33) at $\eta = 1$ gives

$$\int_0^1 \left[\Lambda \frac{\partial R_0}{\partial \tau} + \frac{1}{\xi}\frac{\partial}{\partial \xi}(\xi U_0)\right] \mathrm{d}\eta = \sin\tau\,, \tag{2.34}$$

which, along with equations (2.28)–(2.30), forms a closed system from which the four constituent variables P_0, Θ_0, R_0 and U_0 can be fully determined. Since the leading-order problem in the gas layer (2.27)–(2.30) is linear and driven purely by time-harmonic boundary conditions (2.31), the five flow variables must necessarily vary harmonically with time. Additionally, it can be deduced from the discussion below (2.15) that the film pressure at this order does not vary in the transverse direction, that is, $P_0 = P_0(\xi, \tau)$. Upon consideration of these facts and close inspection of equations (2.28)–(2.30), we may anticipate that the solution can be expressed using separation of variables in the form

$$\begin{cases} P_0 = \mathrm{Re}\left[\mathrm{e}^{\mathrm{i}\tau}\Pi(\xi)\right] \\ \Theta_0 = \dfrac{\gamma-1}{\gamma}\mathrm{Re}\left[\mathrm{e}^{\mathrm{i}\tau}\Pi(\xi)\mathcal{G}'_\Theta(\eta)\right] \\ R_0 = \mathrm{Re}\left\{\mathrm{e}^{\mathrm{i}\tau}\Pi(\xi)\left[1 - \dfrac{\gamma-1}{\gamma}\mathcal{G}'_\Theta(\eta)\right]\right\} \\ U_0 = \mathrm{Re}\left[\mathrm{i}\mathrm{e}^{\mathrm{i}\tau}\Pi'\mathcal{G}'_U(\eta)\right]\,, \end{cases} \tag{2.35}$$

where the transverse functions $\mathcal{G}'_U(\eta) = \mathrm{d}\mathcal{G}_U/\mathrm{d}\eta$ and $\mathcal{G}'_\Theta(\eta) = \mathrm{d}\mathcal{G}_\Theta/\mathrm{d}\eta$ have been expressed as derivatives in anticipation of the integral in (2.33) necessary to determine V_0. Substituting (2.35) into (2.28) and (2.29) gives

$$-\frac{1}{\alpha^2 \mathrm{i}}\frac{\mathrm{d}^3\mathcal{G}_U}{\mathrm{d}\eta^3} + \frac{\mathrm{d}\mathcal{G}_U}{\mathrm{d}\eta} = 1 \qquad \text{and} \qquad -\frac{1}{Pr\alpha^2 \mathrm{i}}\frac{\mathrm{d}^3\mathcal{G}_\Theta}{\mathrm{d}\eta^3} + \frac{\mathrm{d}\mathcal{G}_\Theta}{\mathrm{d}\eta} = 1 \tag{2.36}$$

respectively. Since the functions $\mathcal{G}_U(\eta)$ and $\mathcal{G}_\Theta(\eta)$ satisfy identical boundary conditions $\mathcal{G}'_U = \mathcal{G}'_\Theta = 0$ at $\eta = 0, 1$, as follows from (2.31), it is convenient to recast the above equations in the consolidated form

$$-\frac{1}{4\beta^2}\frac{\mathrm{d}^3\mathcal{G}}{\mathrm{d}\eta^3} + \frac{\mathrm{d}\mathcal{G}}{\mathrm{d}\eta} = 1\,, \quad \text{with} \quad \beta_U = \frac{\alpha}{2}\frac{(1+\mathrm{i})}{\sqrt{2}} \quad \text{and} \quad \beta_\Theta = \sqrt{Pr}\frac{\alpha}{2}\frac{(1+\mathrm{i})}{\sqrt{2}}\,, \tag{2.37}$$

where the function $\mathcal{G}'(\eta;\beta) = \mathrm{d}\mathcal{G}/\mathrm{d}\eta$ describes the transverse variations $\mathcal{G}'_U(\eta) = \mathcal{G}'(\eta;\beta_U)$ and $\mathcal{G}'_\Theta(\eta) = \mathcal{G}'(\eta;\beta_\Theta)$ of the radial velocity component and temperature deviation, respectively. The constant-coefficient ordinary differential equation in (2.37) can be integrated using (2.31) to give

$$\mathcal{G} = \eta - \frac{\sinh[\beta(2\eta-1)] + \sinh\beta}{2\beta\cosh\beta} \qquad \text{and} \qquad \mathcal{G}' = 1 - \frac{\cosh[\beta(2\eta-1)]}{\cosh\beta}\,. \tag{2.38}$$

To determine the radial function $\Pi(\xi)$, we substitute (2.35) and (2.38) into (2.34), which yields the classical Bessel's equation

$$\frac{1}{\xi}\frac{\mathrm{d}}{\mathrm{d}\xi}\left(\xi\frac{\mathrm{d}\Pi}{\mathrm{d}\xi}\right) + \frac{1-\frac{\gamma-1}{\gamma}\mathcal{G}_\Theta(1)}{\mathcal{G}_U(1)}\Lambda\Pi = -\frac{1}{\mathcal{G}_U(1)}\,, \tag{2.39}$$

which can be integrated using the boundary conditions $\Pi(\xi=1) = \Pi'(\xi=0) = 0$, where $\Pi' = \mathrm{d}\Pi/\mathrm{d}\xi$, consistent with (2.31), to give

$$\Pi = \frac{J_0\left(\xi\sqrt{C\Lambda}\right)/J_0\left(\sqrt{C\Lambda}\right) - 1}{\mathcal{G}_U(1)C\Lambda} \quad \text{and} \quad \Pi' = -\frac{J_1\left(\xi\sqrt{C\Lambda}\right)/J_0\left(\sqrt{C\Lambda}\right)}{\mathcal{G}_U(1)\sqrt{C\Lambda}}\,, \tag{2.40}$$

where J_0 and J_1 represent the Bessel functions of the first kind of order 0 and 1, respectively, and the constant C is defined as

$$C = \frac{1 - \frac{\gamma-1}{\gamma}\mathcal{G}_\Theta(1)}{\mathcal{G}_U(1)}, \quad \text{with} \quad \mathcal{G}_U(1) = 1 - \frac{\tanh\beta_U}{\beta_U} \quad \text{and} \quad \mathcal{G}_\Theta(1) = 1 - \frac{\tanh\beta_\Theta}{\beta_\Theta}. \tag{2.41}$$

The final step of the solution process is to substitute the known forms of U_0 and R_0 into (2.33), which yields

$$V_0 = \mathrm{Re}\left\{ \mathrm{i}\mathrm{e}^{\mathrm{i}\tau} \left[\frac{\mathcal{G}_U(\eta)}{\mathcal{G}_U(1)} + \Lambda\Pi \left(C\mathcal{G}_U(\eta) + \frac{\gamma-1}{\gamma}\mathcal{G}_\Theta(\eta) - \eta \right) \right] \right\} \tag{2.42}$$

for the transverse velocity component.

The above results can be used to evaluate the limiting value of the radial velocity at the outer edge of the gaseous film

$$U_0(\xi = 1, \eta, \tau) = A\,\mathrm{Re}\left\{ \mathrm{i}\mathrm{e}^{\mathrm{i}(\tau+\varphi)} \left[1 - \frac{\cosh\left[\frac{\alpha(1+\mathrm{i})}{2\sqrt{2}}(2\eta - 1)\right]}{\cosh\left[\frac{\alpha(1+\mathrm{i})}{2\sqrt{2}}\right]} \right] \right\}, \tag{2.43}$$

where the boundary value of the pressure gradient

$$\Pi'(1) = -\frac{J_1\left(\sqrt{C\Lambda}\right)/J_0\left(\sqrt{C\Lambda}\right)}{\mathcal{G}_U(1)\sqrt{C\Lambda}} \tag{2.44}$$

has been written in terms of its modulus $A = |\Pi'(1)|$ and argument $\varphi = \arg[\Pi'(1)]$. Equation (2.43) will be needed later for computing the flow in the peripheral region (see § 2.7.1). The order-unity factor A is a measure of the stroke volume driven by the moving disk, as can be seen by writing, for example, $\int_\pi^{2\pi} \left[\int_0^1 U_0(\xi = 1, \eta, \tau)\, 2\pi\, \mathrm{d}\eta\right] \mathrm{d}\tau = 4\pi A\,\mathrm{Re}\left[\mathrm{e}^{\mathrm{i}\varphi}\mathcal{G}_U(1)\right]$. Its value will enter in the determination of the time-averaged levitation force (see § 2.6.2 and § 2.7.3). The dependence of $A = |\Pi'(1)|$ on α and Λ, which can be evaluated using (2.44), is visualized in figure 2.3(a), to be discussed later.

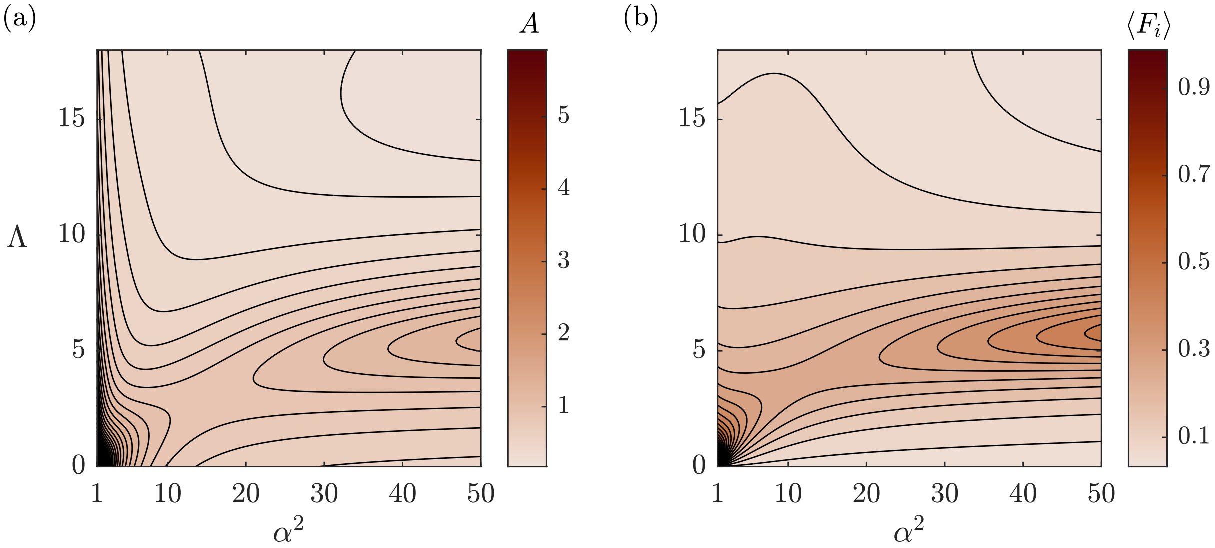

Figure 2.3. Variation with α^2 and Λ of (a) the stroke volume $A = |\Pi'(1)|$ evaluated with use of (2.44) and (b) the inner contribution to the levitation force $\langle F_i \rangle$ evaluated from (2.59). Computations were carried out using $\nu = 0.77$, $Pr = 0.7$ and $\gamma = 1.4$.

2.6 First-order correction for the pressure in the gas film

2.6.1 Time-averaged pressure distribution

Since the solution (2.35) is harmonic, the time-averaged values of all flow variables are identically zero (i.e. $\langle U_0 \rangle = 0$, $\langle P_0 \rangle = 0$, ...), so that the pressure at leading order does not contribute to the steady levitation force $\langle F_L \rangle$ exerted on the disk. As a result, the computation of $\langle F_L \rangle$ from (2.22) requires consideration of the time-averaged first-order correction $\langle P_1 \rangle(\xi)$ for the pressure, which yields

$$\langle F_L \rangle = 2 \int_0^1 \langle P_1 \rangle \xi \mathrm{d}\xi \,, \tag{2.45}$$

with small relative errors of order $\varepsilon \sim \delta$. To determine the steady pressure distribution $\langle P_1 \rangle(\xi)$, one may begin by noting that the associated time-averaged radial-velocity correction $\langle U_1 \rangle$ must satisfy

$$\int_0^1 \langle U_1 \rangle \mathrm{d}\eta = -\int_0^1 \langle \cos(\tau) U_0 \rangle \mathrm{d}\eta - \Lambda \int_0^1 \langle R_0 U_0 \rangle \mathrm{d}\eta, \tag{2.46}$$

obtained at order ε from (2.24). In addition, time-averaging the equation that results from collecting terms of order ε in the momentum equation (2.17) provides

$$f = -\frac{\mathrm{d}\langle P_1\rangle}{\mathrm{d}\xi} + \frac{1}{\alpha^2}\frac{\partial^2\langle U_1\rangle}{\partial\eta^2}, \tag{2.47}$$

where the known function

$$\begin{aligned} f(\xi,\eta) = \Bigg\langle \Lambda R_0\frac{\partial U_0}{\partial\tau} + U_0\frac{\partial U_0}{\partial\xi} + V_0\frac{\partial U_0}{\partial\eta} \\ + \eta\sin\tau\frac{\partial U_0}{\partial\eta} + \frac{1}{\alpha^2}\frac{\partial}{\partial\eta}\left[(2\cos(\tau) - \nu\Lambda\Theta_0)\frac{\partial U_0}{\partial\eta}\right]\Bigg\rangle \end{aligned} \tag{2.48}$$

can be re-expressed in ‘conservative’ form by adding to it the time average of the left-hand side of the order-unity continuity equation (2.27), giving

$$\begin{aligned} f(\xi,\eta) = \frac{1}{\xi}\frac{\partial}{\partial\xi}\left(\xi\left\langle U_0^2\right\rangle\right) + \frac{\partial}{\partial\eta}\langle V_0U_0\rangle \\ + \eta\left\langle\sin(\tau)\frac{\partial U_0}{\partial\eta}\right\rangle + \frac{2}{\alpha^2}\left\langle\cos(\tau)\frac{\partial^2U_0}{\partial\eta^2}\right\rangle - \frac{\Lambda\nu}{\alpha^2}\frac{\partial}{\partial\eta}\left\langle\Theta_0\frac{\partial U_0}{\partial\eta}\right\rangle, \end{aligned} \tag{2.49}$$

both of which can be evaluated in terms of the expressions given in (2.35). Note that the terms in the expressions for f that involve $\cos(\tau)$ and $\sin(\tau)$ stem from the change of variables described in (2.26). Integrating the reduced momentum equation (2.47) with the no-slip conditions $\langle U_1\rangle = 0$ at $\eta = 0,1$ gives

$$\frac{\langle U_1\rangle}{\alpha^2} = -\frac{\mathrm{d}\langle P_1\rangle}{\mathrm{d}\xi}\frac{(1-\eta)\eta}{2} + \eta\int_0^\eta f\,\mathrm{d}\tilde{\eta} - \int_0^\eta f\tilde{\eta}\,\mathrm{d}\tilde{\eta} - \eta\int_0^1 f(1-\tilde{\eta})\,\mathrm{d}\tilde{\eta}, \tag{2.50}$$

where $\tilde{\eta}$ is a dummy integration variable. The associated radial flux,

$$\frac{1}{\alpha^2}\int_0^1\langle U_1\rangle\mathrm{d}\eta = -\frac{1}{12}\frac{\mathrm{d}\langle P_1\rangle}{\mathrm{d}\xi} - \frac{1}{2}\int_0^1\eta(1-\eta)f\,\mathrm{d}\eta \tag{2.51}$$

can be substituted into (2.46) to give

$$\langle P_1\rangle' = \frac{12}{\alpha^2}\left[\int_0^1 \langle\cos(\tau)U_0\rangle \mathrm{d}\eta + \Lambda\int_0^1 \langle R_0 U_0\rangle \mathrm{d}\eta\right] - 6\int_0^1 \eta(1-\eta) f \,\mathrm{d}\eta \tag{2.52}$$

for the derivative of the time-averaged pressure $\langle P_1\rangle' = \mathrm{d}\langle P_1\rangle/\mathrm{d}\xi$. The above equation can be readily integrated to give

$$\langle P_1\rangle(\xi) - \langle P_1\rangle(1) = -\int_\xi^1 \langle P_1\rangle' \,\mathrm{d}\xi \tag{2.53}$$

for the pressure variation from the unknown boundary value $\langle P_1\rangle(1)$. The above integral can be evaluated with use of (2.52) along with the identity

$$\left\langle \mathrm{Re}\left(\mathrm{e}^{\mathrm{i}\tau}\mathcal{A}\right)\mathrm{Re}\left(\mathrm{e}^{\mathrm{i}\tau}\mathcal{B}\right)\right\rangle = \frac{1}{2}\mathrm{Re}(\mathcal{A}\mathcal{B}^*), \tag{2.54}$$

which applies to any generic time-independent complex functions $\mathcal{A}$ and $\mathcal{B}$, with the asterisk $*$ denoting complex conjugates. The resulting expression can be cast in the form

$$\begin{aligned}\langle P_1\rangle(\xi) - \langle P_1\rangle(1) = {} & 3\,\mathrm{Re}\Bigg\{ -\frac{2\mathrm{i}}{\alpha^2}(X_1^* + \Lambda X_2)\mathcal{H}_1 + \frac{\mathrm{i}(\gamma-1)\Lambda}{\gamma\alpha^2} X_2\,(2\mathcal{H}_2 + \nu\mathcal{H}_3) \\ & + X_3\mathcal{H}_4 + \left[\frac{X_1^*}{\mathcal{G}_U(1)} + C\Lambda X_2\right]\mathcal{H}_5 + \Lambda X_2\left(\frac{\gamma-1}{\gamma}\mathcal{H}_6 - \mathcal{H}_7\right) - X_1\mathcal{H}_8\Bigg\},\end{aligned} \tag{2.55}$$

involving the complex functions $X_i(\xi)$ and the complex constants $\mathcal{H}_j$ (with $i = 1-3$ and $j = 1-8$), whose expressions as functions of Λ and α^2 are given in § 2.10.

2.6.2 An expression for the steady squeeze-film force (SSF)

Substitution of (2.53) into (2.45) yields

$$\langle F_L\rangle = \langle F_i\rangle + \langle F_e\rangle, \tag{2.56}$$

where

$$\langle F_i \rangle = 2\int_0^1 [\langle P_1 \rangle - \langle P_1 \rangle(1)]\xi \, \mathrm{d}\xi \qquad \text{and} \qquad \langle F_e \rangle = \langle P_1 \rangle(1)\,. \tag{2.57a,b}$$

The first term on the right-hand side of (2.56), to be evaluated with use of

$$\langle F_i \rangle = -\int_0^1 \langle P_1 \rangle' \, \xi^2 \, \mathrm{d}\xi, \tag{2.58}$$

obtained from (2.57a) using integration by parts, is associated with the pressure increase in the gas film from its value at the disk edge. The integral in (2.58) can be expressed in the form

$$\begin{aligned} \langle F_i \rangle = 3\,\mathrm{Re}\Bigg\{ & -\frac{2\mathrm{i}}{\alpha^2}(\mathcal{X}_1^* + \Lambda \mathcal{X}_2)\mathcal{H}_1 + \frac{\mathrm{i}(\gamma-1)\Lambda}{\gamma\alpha^2}\mathcal{X}_2\,(2\mathcal{H}_2 + \nu\mathcal{H}_3) + \mathcal{X}_3\mathcal{H}_4 \\ & + \left[\frac{\mathcal{X}_1^*}{\mathcal{G}_U(1)} + C\Lambda\mathcal{X}_2\right]\mathcal{H}_5 + \Lambda\mathcal{X}_2\left(\frac{\gamma-1}{\gamma}\mathcal{H}_6 - \mathcal{H}_7\right) - \mathcal{X}_1\mathcal{H}_8 \Bigg\}, \end{aligned} \tag{2.59}$$

where the complex constants $\mathcal{X}_i = 2\int_0^1 X_i\,\xi \mathrm{d}\xi$ (with $i = 1-3$) are given in § 2.10. The associated variation of $\langle F_i \rangle$ with Λ and α^2 is depicted in figure 2.3(b). Limiting expressions for $\langle F_i \rangle$ are to be derived below for the cases $\Lambda \ll 1$, $\alpha^2 \ll 1$ and $\alpha^2 \gg 1$.

The second term $\langle F_e \rangle$ in (2.56), comparable in magnitude to $\langle F_i \rangle$, arises from the departure of the time-averaged pressure at the disk edge from its ambient value in the surrounding stagnant gas. The computation of this quantity requires consideration of the flow in the non-slender near-edge region, a problem to be addressed in § 2.7.

2.6.3 Limiting cases of interest

The spatial variation of steady pressure along the film, $\langle P_1 \rangle(\xi) - \langle P_1 \rangle(1)$, and its contribution $\langle F_i \rangle$ to the levitation force, given respectively in (2.55) and (2.59), admit simplified forms for limiting values of the two controlling parameters Λ and α^2, to be investigated below. Consistency between each limiting solution and the respective original expression was confirmed computationally.

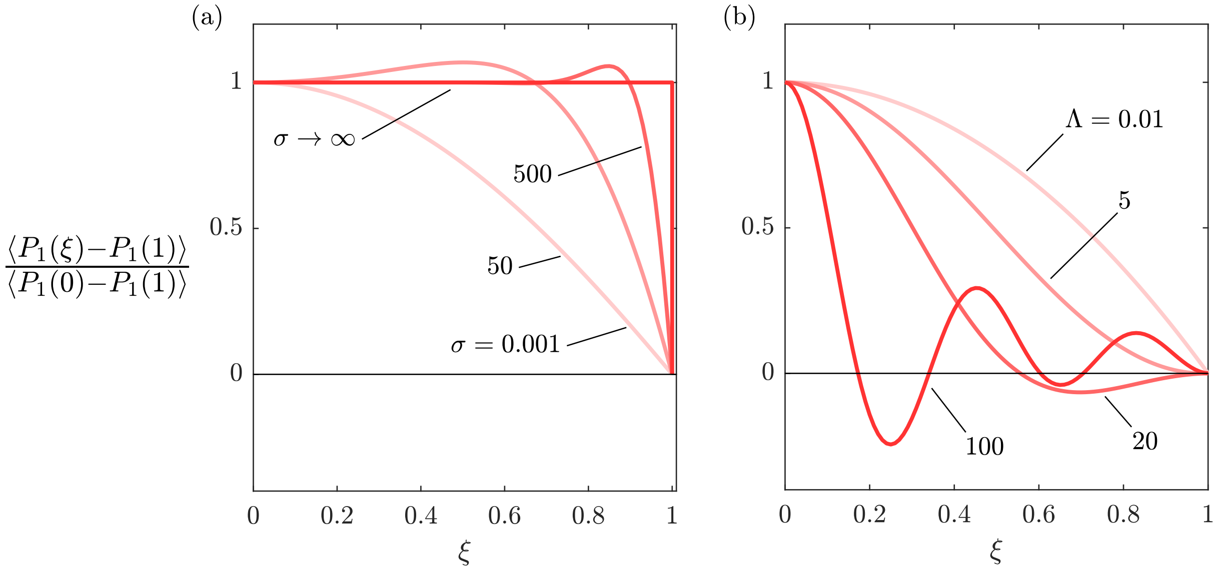

Figure 2.4. Normalized variation of the time-averaged pressure along the slender film with respect to its value at the edge. Curves are shown for (a) various values of $\sigma = 12\Lambda/\alpha^2$ under the lubrication limit and (b) various values of Λ under the inviscid limit (see § 2.6.3).

The incompressible limit $\Lambda \ll 1$

In the limit $\Lambda \ll 1$, the gas behaves effectively as incompressible, in that the motion is independent of the density variations, with the leading-order pressure and velocity distributions reducing to

$$P_0 = \frac{1-\xi^2}{4}\mathrm{Re}\left[\frac{\mathrm{e}^{\mathrm{i}\tau}}{\mathcal{G}_U(1)}\right], \quad U_0 = -\frac{\xi}{2}\mathrm{Re}\left[\mathrm{i}\mathrm{e}^{\mathrm{i}\tau}\frac{\mathcal{G}_U'(\eta)}{\mathcal{G}_U(1)}\right], \quad V_0 = \mathrm{Re}\left[\mathrm{i}\mathrm{e}^{\mathrm{i}\tau}\frac{\mathcal{G}_U(\eta)}{\mathcal{G}_U(1)}\right], \tag{2.60}$$

as follows from (2.35), whence the dimensionless stroke volume simplifies to

$$A = \frac{1}{2}\left|\frac{\beta_U}{\beta_U - \tanh\beta_U}\right| . \tag{2.61}$$

Using these expressions in (2.52) yields the parabolic steady overpressure distribution

$$\langle P_1\rangle(\xi) - \langle P_1\rangle(1) = \frac{3}{8}\left(\xi^2-1\right)\mathrm{Re}\left[\frac{|\mathcal{G}_U'|^2 - 2\mathcal{G}_U\mathcal{G}_U^{*\prime\prime}}{|\mathcal{G}_U(1)|^2} + \frac{2\eta\mathcal{G}_U'' - 4(1-\mathcal{G}_U')}{\mathcal{G}_U(1)}\right], \tag{2.62}$$

substitution of which in (2.57) gives

$$\langle F_i \rangle = \mathrm{Re}\left\{ \left[30\beta_U \tanh\beta_U \tan\beta_U - (24\beta_U^2 + 3)\tanh\beta_U \right.\right.$$
$$\left.\left. + (24\beta_U^2 - 105)\tan\beta_U + 4\beta_U^3 \right] \Big/ \left[128\beta_U(\beta_U - \tanh\beta_U)(\beta_U - \tan\beta_U) \right] \right\}, \tag{2.63}$$

which is found to depend purely on the Stokes number through $\beta_U = \alpha(1+\mathrm{i})/\sqrt{8}$.

The classical lubrication (Stokes) limit $\alpha^2 \ll 1$

When the Stokes number assumes small values $\alpha^2 \ll 1$, fluid acceleration driven by disk oscillations becomes negligibly small relative to viscous diffusion of momentum. To preserve nontrivial dominant balances in the momentum (2.17) and state (2.19) equations with $\alpha^2 \to 0$, the dimensionless pressure, temperature and density variables must be rescaled appropriately as

$$\frac{\bar{P}}{\alpha^2 P} = \frac{\bar{R}}{\alpha^2 R} = \frac{\bar{\Theta}}{\alpha^2 \Theta} = 1\,, \tag{2.64}$$

substitution of which into the energy equation (2.18) gives $\partial^2\bar{\Theta}/\partial Y^2 = 0$ for $\alpha^2 \to 0$, whence $\bar{\Theta} = 0$ due to the isothermal conditions on the bounding surfaces. It follows then from the state equation that $\bar{P} = \bar{R}$, and from the reduced momentum equation $\partial\bar{P}/\partial\xi = \partial^2 U/\partial Y^2$ that the radial velocity component varies across the gas layer in terms of the classical Poiseuille profile

$$U(\xi,Y,\tau) = -\frac{\partial\bar{P}}{\partial\xi}\frac{(H-Y)Y}{2}\,, \tag{2.65}$$

consistent with the non-slip conditions on the walls. Integrating the continuity equation (2.16) across the gas film using the known expressions for $\bar{R}$ and U yields

$$\sigma\frac{\partial(H\bar{P})}{\partial\tau} - \frac{H^3}{\xi}\frac{\partial}{\partial\xi}\left[\left(1+\varepsilon\frac{\sigma}{12}\bar{P}\right)\xi\frac{\partial\bar{P}}{\partial\xi}\right] - 12\sin\tau = 0\,, \tag{2.66}$$

the relevant isothermal squeeze-film equation, whence the radial pressure distribution can be determined solely in terms of

$$\sigma = \frac{12\Lambda}{\alpha^2} = \frac{12\mu_a \omega a^2}{p_a h_o^2}, \tag{2.67}$$

a similarity parameter unique to the lubrication limit known as the squeeze number [8]. Solving (2.66) using the truncated expansion $\bar{P} = \bar{P}_0 + \varepsilon \bar{P}_1$ yields

$$\alpha^2 A = 12 \left| \frac{J_1(\beta_\sigma)}{\beta_\sigma J_0(\beta_\sigma)} \right|, \qquad \text{where} \qquad \beta_\sigma = \sqrt{\sigma}\,\frac{(1+\mathrm{i})}{\sqrt{2}}, \tag{2.68}$$

for the characteristic value of the stroke volume and

$$\langle \bar{P}_1 \rangle(\xi) - \langle \bar{P}_1 \rangle(1) = \frac{3}{\sigma}\mathrm{Re}\left\{ \left[1 - \frac{J_0(\xi\beta_\sigma)}{J_0(\beta_\sigma)} \right] \left[\frac{J_0(\xi\beta_\sigma^*)}{J_0(\beta_\sigma^*)} + 5 \right] \right\} \tag{2.69}$$

for the time-averaged pressure distribution, the latter providing

$$\alpha^2 \langle F_i \rangle = \frac{15}{\sigma}\mathrm{Re}\left[1 - \frac{2J_1(\beta_\sigma)}{\beta_\sigma J_0(\beta_\sigma)} \right] \tag{2.70}$$

for the corresponding contribution to the levitation force. The limiting pressure distribution (2.69) is visualized in figure 2.4(a) for selected values of σ. Since, as shall be proven in § 2.7.4, the edge pressure $\langle \bar{P}_1 \rangle(1)$ is identically zero when $\alpha^2 = 0$, equation (2.69) recovers exactly the results found by Taylor and Saffman [5], and (2.70) provides the full levitation force $\langle F_L \rangle$ under the first approximation of the classical lubrication limit, as can be seen from (2.56) and (2.57*b*).

In the sub-limit $\sigma \ll 1$, representing gas flow with small density variations, (2.68) and (2.70) reduce to give

$$A \to 6/\alpha^2 \quad \text{and} \quad \langle F_i \rangle \to (15/4)\Lambda/\alpha^4, \tag{2.71}$$

signifying high relative stroke volumes and diminishing repulsive levitation forces. In the opposite limit $\sigma \gg 1$, the relative stroke volume A assumes diminishing values due to high gaseous compressibility while the dimensional repulsive force $\langle \mathcal{F}_L \rangle$ grows, in principle, unboundedly.

This can be seen by rewriting the corresponding limiting expression, $\alpha^2\langle F_i\rangle = \alpha^2\langle F_L\rangle \to 15/\sigma$, in the normalized form $\langle \mathcal{F}_L\rangle/(\varepsilon^2 p_a \pi a^2) \to 5/4$, whence it is apparent that $\langle \mathcal{F}_L\rangle$ grows with the inverse square of the reducing mean air-gap width h_o (recall from (2.2) that $\varepsilon = b/h_o$).

The inviscid limit $\alpha^2 \gg 1$

When $\alpha^2 \to \infty$, viscous diffusion, significantly outpaced by fluid acceleration, is confined to vanishingly thin near-wall (Stokes) boundary layers. Note that the interference of transverse acoustic waves in the gas film, of characteristic wavelength $\lambda_t = \omega^{-1}\sqrt{\gamma p_a/\rho_a}$, can be neglected under the limit of slender flow $h_o/a \ll 1$ because the relevant 'acoustic wavenumber' $K = \sqrt{\Lambda/\gamma}$ is of order unity (i.e. $h_o/\lambda_t = K h_o/a \ll 1$). Upon relaxation of the non-slip boundary conditions, the leading-order solution reduces to

$$P_0 = \Pi\cos(\tau), \qquad U_0 = -\Pi'\sin(\tau), \qquad V_0 = -\eta\sin(\tau), \tag{2.72}$$

where the reduced pressure Π and its gradient Π' have simplified to

$$\Pi(\xi) = \frac{J_0(K\xi)\Big/J_0(K) - 1}{K^2} \qquad \text{and} \qquad \Pi'(\xi) = -\frac{J_1(K\xi)\Big/J_0(K)}{K}, \tag{2.73}$$

yielding

$$A = \left|\frac{J_1(K)}{KJ_0(K)}\right|, \tag{2.74}$$

$$\langle P_1\rangle(\xi) - \langle P_1\rangle(1) = \frac{J_1^2(K) - J_1^2(K\xi) + \left[J_0^2(K) - J_0^2(K\xi)\right]^2}{4K^2J_0^2(K)} \tag{2.75}$$

and

$$\langle F_i\rangle = \frac{1}{4K^2}\left[1 + \frac{J_1(K)}{J_0(K)}\left(\frac{J_1(K)}{J_0(K)} - \frac{2}{K}\right)\right], \tag{2.76}$$

all of which depend solely on Λ through the acoustic wavenumber $K = \sqrt{\Lambda/\gamma}$. The limiting pressure distribution (2.75) is visualized in figure 2.4(b) for selected values of Λ. Note that the predicted values of A and $\langle F_i \rangle$ become unbounded for critical values of K that represent resonant states of inviscid gas dynamics. For example, for the value $\gamma = 1.4$ used in generating the results plotted in figure 2.3, the first singularity develops at $\Lambda = 8.096$, symptoms of which are visible in the form of local maxima of A and $\langle F_i \rangle$, observed in the figure near $\Lambda = 6$ for $\alpha^2 = 50$.

Unlike previous reduced descriptions of inviscid flow in rigid-body squeeze-film systems [1, 19], radial pressure variations are not neglected in the limiting solution above.

2.7 Leading-order solution in the peripheral region

2.7.1 Problem formulation

As previously discussed, the non-slender flow at distances of order h_o from the disk edge involves velocities of order $u \sim v \sim u_c = \varepsilon\omega a$ and spatial pressure differences of order $\delta\Delta p \sim \varepsilon\Delta p = \rho_a u_c^2$. The description below employs the local rescaled coordinates $X = (r-a)/h_o$ and $Y = y/h_o$. The velocity must match with that found at the edge of the slender gaseous film, given at leading order in (2.43). To facilitate the matching and reduce the parametric dependence of the solution, it is convenient to introduce a shifted time variable $\hat{\tau} = \tau + \varphi$ and use the local velocity Au_c in the definition of the dimensionless variables $\hat{\mathbf{V}} = (\hat{U}, \hat{V}) = [u/(Au_c), v/(Au_c)]$ and $\hat{P} = (p - p_a)/(\rho_a A^2 u_c^2)$. Substitution of these definitions into the reduced local conservation equations (2.13) and (2.14) gives, with errors of order $\varepsilon \sim \delta$,

$$\nabla \cdot \hat{\mathbf{V}} = 0, \tag{2.77}$$

$$\hat{St}\frac{\partial \hat{\mathbf{V}}}{\partial \hat{\tau}} + \hat{\mathbf{V}} \cdot \nabla \hat{\mathbf{V}} = -\nabla \hat{P} + \frac{\hat{St}}{\alpha^2}\nabla^2 \hat{\mathbf{V}}, \tag{2.78}$$

where $\nabla = (\partial/\partial X, \partial/\partial Y)$. As a result of the choice of velocity scale, the Strouhal number enters above in the normalized form

$$\hat{St} = \frac{h_o/(Au_c)}{\omega^{-1}} = \frac{\delta/\varepsilon}{A}. \tag{2.79}$$

This additional parameter is of order unity in the distinguished limit $\varepsilon \sim \delta$ considered here, with $\hat{Re} = \alpha^2/\hat{St} = \rho_a A u_c h_o/\mu_a$ being the corresponding Reynolds number.

Equations (2.77) and (2.78) must be integrated for each of the three geometric configurations of the edge (see figure 2.1), with the condition that the velocity must be zero on the walls:

$$\hat{\mathbf{V}} = 0 \quad \text{at} \quad \begin{cases} (X \le 0, Y = 1)\,; \quad Y = 0\,; \quad (X = 0, Y \ge 1) & \text{for piston–wall} \\ (X \le 0, Y = 0, 1)\,; \quad (X = 0, Y \le 0 \,|\, Y \ge 1) & \text{for piston–piston} \\ (X \le 0, Y = 1)\,; \quad Y = 0 & \text{for disk–wall,} \end{cases} \tag{2.80}$$

and must vanish in the open atmosphere, where the pressure must correspondingly approach its ambient value, so that

$$\hat{\mathbf{V}} \to 0 \quad \text{and} \quad \hat{P} \to 0 \quad \text{as} \quad X^2 + Y^2 \to \infty\,. \tag{2.81}$$

Matching with the velocity found at the edge of the slender gas layer, given at leading order in (2.43), provides the additional boundary condition (common to all three geometries)

$$\hat{U} - \mathrm{Re}\left\{ \mathrm{i}e^{\mathrm{i}\hat{\tau}} \left[1 - \frac{\cosh\left[\frac{\alpha(1+\mathrm{i})}{2\sqrt{2}}(2Y-1)\right]}{\cosh\left[\frac{\alpha(1+\mathrm{i})}{2\sqrt{2}}\right]} \right] \right\} = \hat{V} = 0 \text{ as } X \to -\infty \text{ for } 0 \le Y \le 1, \tag{2.82}$$

substitution of which into the horizontal component of the momentum equation (2.78) provides an accompanying pressure distribution of the general form

$$\hat{P} = \hat{St}\cos(\hat{\tau})X + \hat{P}_\infty(\hat{\tau}) \quad \text{as} \quad X \to -\infty \quad \text{for} \quad 0 \le Y \le 1, \tag{2.83}$$

involving, as a consequence of integration, a time-dependent pressure offset $\hat{P}_\infty(\hat{\tau})$. The time average of this offset, $\langle \hat{P}_\infty \rangle = \hat{P}_e$, will be seen to play a fundamental role in the final step of the asymptotic matching process required to close the computation of the levitation force.

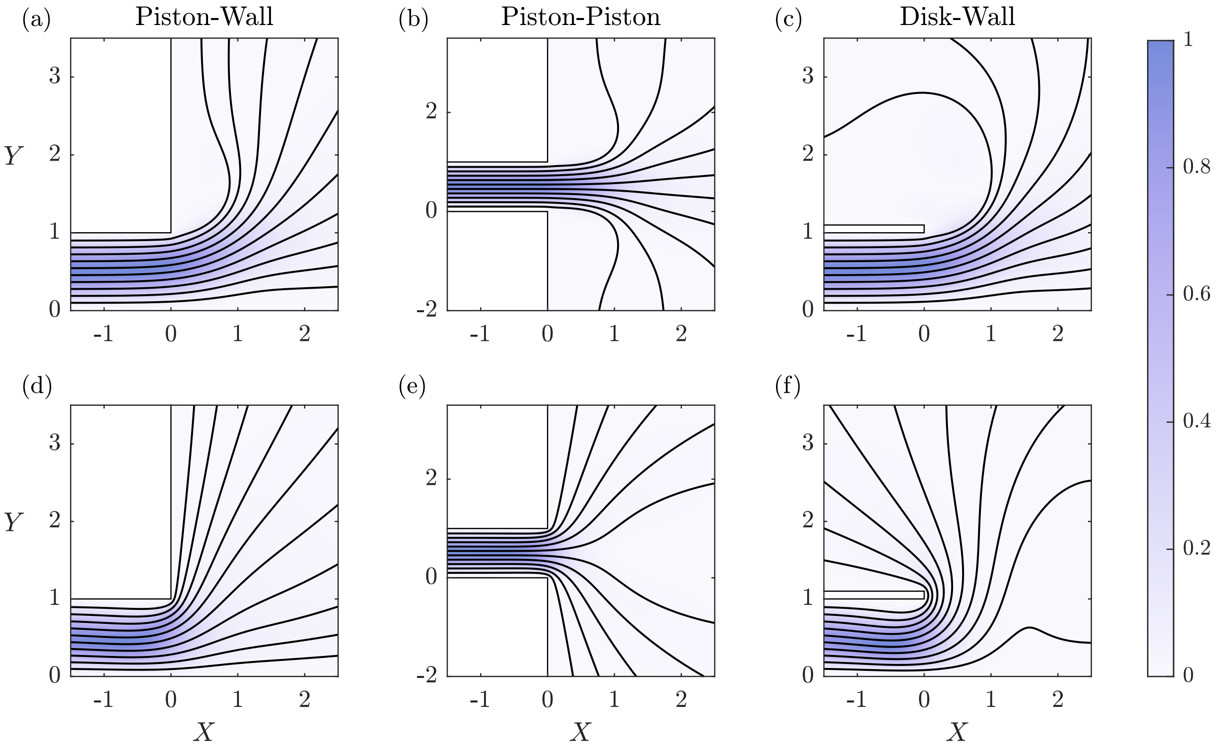

Figure 2.5. Streamlines for $\alpha^2 = 20, \hat{St} = 0.5\,(\hat{Re} = 40)$ in the peripheral flow regions of the three geometric configurations presented in figure 2.1, shaded to represent the flow speed $(\hat{U}^2 + \hat{V}^2)^{1/2}$. The images of outflow along the top row (a, b and c) correspond to values of time $\hat{\tau} = 2n\pi - \pi/2$ and those representing inflow (d, e and f) correspond to $\hat{\tau} = 2n\pi + \pi/2$, where $n \in \mathbb{N}$.

2.7.2 Selected numerical results

The solution in the near-edge region depends on two parameters, namely, the Strouhal number $\hat{St}$, which measures unsteady effects in (2.78), and the Stokes number α^2, which measures viscous forces in (2.78) and enters also through the boundary condition (2.82). The numerical integration was based on the weak formulation of the Navier–Stokes equations (2.77) and (2.78). A Lagrange-Galerkin second-order temporal finite difference scheme using the rescaled time variable $\hat{\tau}/\hat{St}$ was employed along with P2/P1 Taylor-Hood finite elements for velocity and pressure. The resulting system of partial difference equations was implemented in the open source software FreeFEM [79] in conjunction with the MUMPS framework (Multifrontal Massively Parallel sparse direct Solver). Further details regarding the numerical method are available in an exemplary analysis by Carpio, Prieto and Vera [80].

Three computational meshes were designed to represent the different geometrical configurations of the periphery (see figure 2.1), each consisting of non-slip boundaries representing the solid surfaces listed in (2.80), an inner boundary at $-X = \ell_n \gg 1$ for $0 \leq Y \leq 1$, where the matching velocity (2.82) was imposed, and a circular-arc outer boundary at $(X^2 + Y^2)^{1/2} = \ell_p \gg 1$ representing the unperturbed surroundings. The advective boundary condition $\hat{St}\,\partial \hat{\mathbf{V}}/\partial \tau + \hat{\mathbf{V}} \cdot \nabla \hat{\mathbf{V}} = 0$ was applied along this finite ambient boundary in place of the original condition (2.81) to assist numerical convergence. To ease constraints on spatial discretization, the disk in the disk–wall configuration was given a finite relative thickness of 0.1. Each triangulated grid was refined near the mouth of the gas film $X = 0$ to allow better characterization of the anticipated shedding of vorticity into the surroundings. Convergence tests were conducted to verify the validity of each mesh with regards to the choice of dimensions ℓ_n and ℓ_p and of spatial and temporal resolution.

Each computation was initialized with stagnant conditions ($\hat{\mathbf{V}} = 0, \hat{P} = 0$) and carried out until a 2π periodic solution was reached, the criterion for convergence being that the relative difference between the computed values of the constant $\hat{P}_e$ (see below (2.83)) be less than or approximately 0.5% over subsequent cycles. While the number of cycles necessary for convergence was found to vary weakly with the two governing parameters, the time step required for stability became restrictively small for large values of the Reynolds number, $\hat{Re} = O(100)$.

Illustrative results obtained for $\alpha^2 = 20$ and $\hat{St} = 0.5$ for the three geometrical configurations (piston–wall, piston–piston and disk–wall) are shown in figure 2.5. The plots represent distributions of flow speed and associated instantaneous streamlines at selected instants of time $\hat{\tau}$ differing by a semi-period of the driving oscillations (2.82). The results shown in panels (a)–(c) are for $\hat{\tau} = 2n\pi - \pi/2$, corresponding to outflow, while those in panels (d)–(f) are for $\hat{\tau} = 2n\pi + \pi/2$, corresponding to inflow (where n is any positive natural number).

Although the driving velocity (2.82) is time-harmonic, the nonlinearity induced by convective acceleration in (2.78) yields non-harmonic velocities $\hat{\mathbf{V}}$ and pressures $\hat{P}$ in the region of fluid exchange between the gaseous film and the stagnant surroundings. This non-harmonic periodicity, clearly noticeable for the Reynolds number $\hat{Re} = 40 \gg 1$ represented in figure 2.5, is evidenced by the asymmetry between the streamlines depicting outflow (panels (a)–(c)) and those depicting inflow (panels (d)–(f)), associated with a nontrivial distribution of the resulting time-averaged velocity $\langle \hat{\mathbf{V}} \rangle$. The degree of nonlinearity can also be anticipated to hold strong correlation with the magnitude of the time-averaged pressure $\langle \hat{P} \rangle$, which approaches the limiting value $\langle \hat{P} \rangle = \hat{P}_e$ in the gas film as $X \to -\infty$, as indicated below (2.83).

2.7.3 Pressure drop across the peripheral region

The constant $\hat{P}_e$, which represents the time-averaged pressure drop across the near-edge region, was determined as part of the numerical integration. Its value is related to the unknown boundary value $\langle P_1 \rangle(1)$ of the pressure distribution in the gaseous film, which determines the second contribution $\langle F_e \rangle = \langle P_1 \rangle(1)$ to the levitation force (2.56). Their relation can be established by noting that the variables P and $\hat{P}$ satisfy $P = \varepsilon A^2 \hat{P}$, as follows from their respective definitions. Substituting into this relation the two-term expansion for the film pressure $P = P_0 + \varepsilon P_1$, evaluated at $\xi = 1$, and the limiting form of the peripheral pressure distribution for $X \to -\infty$ (2.83) provides the general matching condition

$$P_0\Big|_{\xi=1} + \varepsilon P_1\Big|_{\xi=1} = \varepsilon A^2 \left[\hat{St}\cos(\hat{\tau})X + \hat{P}_\infty(\hat{\tau})\right], \tag{2.84}$$

valid up to $O(\varepsilon)$, whence we can deduce that matching the pressure fields in the slender film and in the near-edge region requires firstly that $P_0 = 0$ at $\xi = 1$, which is the boundary condition already imposed for the inner problem at leading order in (2.32), and additionally that

$$\langle F_e \rangle = \langle P_1 \rangle(1) = A^2 \hat{P}_e, \tag{2.85}$$

where $A = |\Pi'(1)|(\Lambda, \alpha^2)$ is the dimensionless stroke volume represented in figure 2.3(a). The computation of $\hat{P}_e$ is therefore essential to enable the evaluation of the force experienced by the

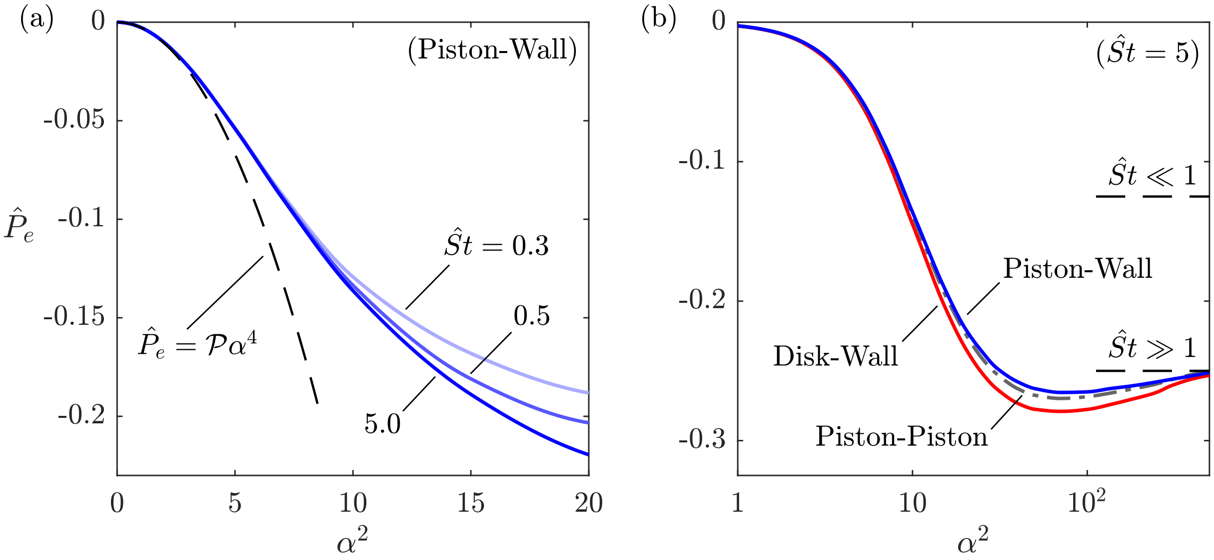

Figure 2.6. Variation of the steady peripheral pressure drop $\hat{P}_e$ with α^2 and (a) selected values of $\hat{S}t$, for the piston–wall configuration, and (b) the three geometrical configurations indicated in figure 2.1, for $\hat{S}t = 5$. The dashed curve in panel (a) corresponds to the asymptotic prediction given in (2.97) corresponding to $\alpha^2 \ll 1$, while the horizontal dashed lines in panel (b) correspond to the asymptotic predictions given in (2.101) and (2.106) for $\alpha^2 \gg 1$ and extreme values of $\hat{S}t$.

disk. It is worth noting that the expression for the steady squeeze-film force (2.56), originating from (2.12), does not account for the variations of $\langle \hat{P} \rangle$ from $\hat{P}_e$ that occur inside the film at distances $-X \sim 1$ from the edge (i.e. $a - r \sim h_o$). This higher-order effect, not considered here, could be incorporated into the analysis to provide a small relative correction, of order $\delta \sim \varepsilon$, to the steady force $\langle F_L \rangle$.

The variation of $\hat{P}_e$ with α^2 corresponding to the piston–wall geometry is represented in figure 2.6(a) for selected values of $\hat{S}t$. As can be seen, $\hat{P}_e$ is always negative, indicating that the time-averaged pressure near the entrance of the gas film is always smaller than the ambient value, with the magnitude of the pressure drop becoming larger for larger values of $\hat{S}t$. The variation of the curves $\hat{P}_e(\alpha^2)$ with $\hat{S}t$ diminishes rapidly as the latter parameter approaches values of $O(5)$. In such cases, it may be of practical interest to expedite the computation of $\hat{P}_e$ by considering the limit of large Strouhal numbers $\hat{S}t \to \infty$, as done in § 2.7.6 below.

As demonstrated by the results shown in figure 2.6(b) for $\hat{S}t = 5$, the dependence of

$\hat{P}_e$ on the geometrical configuration is fairly weak, well in qualitative accordance with the experimental observations of [38]. The curves corresponding to the piston–piston and piston–wall configurations are nearly indistinguishable, while that for the disk–wall geometry exhibits departures of little over 5% from the other two curves.

It is worth noting that the dependences of $\hat{P}_e$ on $\hat{S}t$ and on the geometrical configuration entirely disappear as the Stokes number becomes small, where all solution curves adopt an identical parabolic shape. Also of interest is that, as seen in figure 2.6(b), the variation of $\hat{P}_e$ with α^2 is in general non-monotonic, with the magnitude of the pressure drop reaching a maximum at an intermediate value of α^2 before reducing to approach a finite asymptotic value as $\alpha^2 \to \infty$. The limiting behaviors of the solution for $\alpha^2 \ll 1$ and $\alpha^2 \gg 1$ are to be further investigated below.

2.7.4 Creeping flow for $\alpha^2 \ll 1$

Since airflow in the peripheral region is driven by the radial flow emanating from the slender film, the analysis of the limit $\alpha^2 \ll 1$ begins by expressing the driving edge velocity profile (2.82) as a power-series expansion in terms of the small parameter α^2,

$$\hat{U} = \alpha^2 \left[\frac{1}{2} Y(Y-1)\cos\hat{\tau} + \alpha^2 \mathcal{S}_1(Y)\sin\hat{\tau} + \alpha^4 \mathcal{S}_2(Y)\cos\hat{\tau} + \cdots \right], \tag{2.86}$$

where $\mathcal{S}_1(Y)$, $\mathcal{S}_2(Y)$, $\cdots$ are polynomial functions of increasing degree. Since $\hat{U} \sim \alpha^2$ while $\hat{P} \sim 1$, the latter following from the balance between viscous and pressure forces in (2.78), it appears convenient to introduce perturbation expansions of the form

$$\begin{cases} \hat{\mathbf{V}} = \alpha^2(\hat{\mathbf{V}}_0 + \alpha^2\hat{\mathbf{V}}_1 + \alpha^4\hat{\mathbf{V}}_2 + \cdots) \\ \hat{P} = \hat{P}_0 + \alpha^2\hat{P}_1 + \alpha^4\hat{P}_2 + \cdots . \end{cases} \tag{2.87}$$

Substituting the above expressions into (2.77) and (2.78) and collecting terms in powers of α^2 leads to a hierarchy of problems that can be solved sequentially.

At leading order, both $\hat{\mathbf{V}}_0$ and $\hat{P}_0$ are linearly proportional to $\cos\hat{\tau}$. The solution can be simplified by introduction of the time-independent reduced variables

$$\tilde{\mathbf{V}}_0(X,Y) = \hat{\mathbf{V}}_0/\cos\hat{\tau} \quad \text{and} \quad \tilde{P}_0(X,Y) = \hat{P}_0/(\hat{S}t\cos\hat{\tau}), \tag{2.88}$$

which satisfy

$$\nabla\cdot\tilde{\mathbf{V}}_0 = 0, \quad 0 = -\nabla\tilde{P}_0 + \nabla^2\tilde{\mathbf{V}}_0, \tag{2.89}$$

with no-slip boundary conditions (2.80) at the walls, the stagnant-flow condition (2.81) in the ambient atmosphere, and

$$\tilde{\mathbf{V}}_0 \to \left[\tfrac{1}{2}Y(Y-1),0\right] \quad \text{as} \quad X \to -\infty \quad \text{for} \quad 0 \le Y \le 1, \tag{2.90}$$

the latter corresponding to a pressure gradient $\partial\tilde{P}_0/\partial X = 1$, consistent with the first term in (2.83). The parameter-free problem defined above, corresponding to steady Stokes flow at the mouth of a planar channel, was solved numerically to determine the function $\tilde{\mathbf{V}}_0(X,Y)$ for the three different geometries considered here. Note that the associated pressure $\hat{P}_0 = \hat{S}t\tilde{P}_0(X,Y)\cos\hat{\tau}$ has a vanishing time-averaged value $\langle\hat{P}_0\rangle = 0$, indicating that the pressure drop $\hat{P}_e$ is identically zero at this order.

At the following order (α^2), the conservation equations are

$$\nabla\cdot\hat{\mathbf{V}}_1 = 0, \quad \frac{\partial\hat{\mathbf{V}}_0}{\partial\hat{\tau}} = -\frac{1}{\hat{S}t}\nabla\hat{P}_1 + \nabla^2\hat{\mathbf{V}}_1, \tag{2.91}$$

with the first-order correction for the velocity satisfying

$$\hat{\mathbf{V}}_1 \to [\mathcal{S}_1(Y)\sin\hat{\tau},0] \quad \text{as} \quad X \to -\infty \quad \text{for} \quad 0 \le Y \le 1. \tag{2.92}$$

Inspection of the above equations reveals that $\hat{\mathbf{V}}_1$ and $\hat{P}_1$ are both linearly proportional to $\sin\hat{\tau}$, so that their time-averaged values are also identically zero. Hence, the computation of the pressure drop $\hat{P}_e$ requires consideration of the problem that arises at $O(\alpha^4)$, which comprises the conservation equations

$$\nabla \cdot \hat{\mathbf{V}}_2 = 0, \quad \hat{S}t \frac{\partial \hat{\mathbf{V}}_1}{\partial \hat{\tau}} + \hat{\mathbf{V}}_0 \cdot \nabla \hat{\mathbf{V}}_0 = -\nabla \hat{P}_2 + \hat{S}t \nabla^2 \hat{\mathbf{V}}_2, \tag{2.93}$$

with $\hat{\mathbf{V}}_2$ satisfying the matching condition

$$\hat{\mathbf{V}}_2 \to [\mathcal{S}_2(Y)\cos\hat{\tau}, 0] \quad \text{as} \quad X \to -\infty \quad \text{for} \quad 0 \le Y \le 1. \tag{2.94}$$

Since $\hat{\mathbf{V}}_0 = \tilde{\mathbf{V}}_0(X,Y)\cos\hat{\tau}$ and $\langle \cos^2 \hat{\tau} \rangle = 1/2$, the nonlinear convective acceleration yields a nonzero contribution $\langle \hat{\mathbf{V}}_0 \cdot \nabla \hat{\mathbf{V}}_0 \rangle = \frac{1}{2} \tilde{\mathbf{V}}_0 \cdot \nabla \tilde{\mathbf{V}}_0$ when taking the time average of the above problem, resulting in a steady-streaming motion with nonzero values of $\langle \hat{\mathbf{V}}_2 \rangle$ and $\langle \hat{P}_2 \rangle$. To emphasize the parameter-free nature of the resulting time-averaged pressure distribution, it is of interest to incorporate the Strouhal number in the definition of the steady-streaming velocity $\hat{\mathbf{V}}_{\text{ss}} = \hat{S}t \langle \hat{\mathbf{V}}_2 \rangle$, to be determined, along with the pressure $\hat{P}_{\text{ss}} = \langle \hat{P}_2 \rangle$, by integration of

$$\nabla \cdot \hat{\mathbf{V}}_{\text{ss}} = 0, \quad \frac{1}{2} \tilde{\mathbf{V}}_0 \cdot \nabla \tilde{\mathbf{V}}_0 = -\nabla \hat{P}_{\text{ss}} + \nabla^2 \hat{\mathbf{V}}_{\text{ss}}, \tag{2.95}$$

with boundary conditions $\hat{\mathbf{V}}_{\text{ss}} = 0$ at the solid boundaries, $\hat{\mathbf{V}}_{\text{ss}} = \hat{P}_{\text{ss}} = 0$ in the surrounding atmosphere, and

$$\hat{\mathbf{V}}_{\text{ss}} \to 0 \quad \text{as} \quad X \to -\infty \quad \text{for} \quad 0 \le Y \le 1. \tag{2.96}$$

Numerical integration of the above hierarchy of problems, with use of an advective condition at the finite outer boundary analogous to that described in § 2.7.2, determines, in particular, the (negative) value $\mathcal{P}$ of $\hat{P}_{\text{ss}}$ as $X \to -\infty$ for $0 \le Y \le 1$, which yields

$$\hat{P}_e = \mathcal{P} \alpha^4 \quad \text{for} \quad \alpha^2 \ll 1. \tag{2.97}$$

With $\tilde{\mathbf{V}}_0$ being also independent of $\hat{S}t$, the solution depends only on the geometrical configuration. The resulting values of $\mathcal{P}$ were found to be effectively identical for all three configurations, i.e.

$$\mathcal{P} = -(2.67803, 2.67815, 2.67714) \times 10^{-3}, \tag{2.98}$$

for the piston–wall, piston–piston, and disk–wall configurations, respectively, indicating that, for $\alpha^2 \ll 1$, the pressure drop across the peripheral region is fundamentally related to the flow between the two parallel surfaces, while the flow outside exerts a lesser influence. To illustrate the accuracy of the asymptotic results for $\alpha^2 \ll 1$, the parabolic prediction (2.97) is compared in figure 2.6(a) with the results of the numerical integrations of the complete incompressible Navier–Stokes equations (2.77) and (2.78).

2.7.5 Inviscid flow for $\alpha^2 \gg 1$

In the limit of large Stokes numbers, the conservation equations describing peripheral flow (2.77) and (2.78) reduce to the Euler equations

$$\nabla \cdot \hat{\mathbf{V}} = 0, \quad \hat{S}t \frac{\partial \hat{\mathbf{V}}}{\partial \hat{\tau}} + \hat{\mathbf{V}} \cdot \nabla \hat{\mathbf{V}} = -\nabla \hat{P}, \tag{2.99}$$

subject to the condition of no penetration along the solid boundaries and the oscillating plug-flow velocity

$$\hat{\mathbf{V}} \to [-\sin \hat{\tau}, 0] \quad \text{as} \quad X \to -\infty \quad \text{for} \quad 0 \le Y \le 1, \tag{2.100}$$

the latter following from (2.82) when $\alpha^2 \gg 1$. Vorticity is confined to thin layers of relative thickness α^{-1}, including near-wall (Stokes) boundary layers and a vortex sheet of evolving shape (two for the piston–piston geometry) originating at the rim of the disk/piston. In this limit $\alpha^2 \gg 1$, numerical integration of the associated time-dependent free-boundary problem, needed to determine the nearly inviscid value $\hat{P}_i(\hat{S}t)$ of $\hat{P}_e$, is a difficult task, not to be pursued below. Instead, we shall focus on the solutions arising in the two limiting cases $\hat{S}t \ll 1$ and $\hat{S}t \gg 1$, which are amenable to an analytical description.

In the quasi-steady limit $\hat{St} \ll 1$, the local acceleration term in (2.99) can be neglected in the first approximation, so that the familiar Bernoulli's equation $\hat{P} + |\hat{\mathbf{V}}|^2/2 = \text{constant}$ applies along streamlines. The solution that emerges can be anticipated to be drastically different for inflow (i.e. $0 < \hat{\tau} < \pi$) and outflow (i.e. $\pi < \hat{\tau} < 2\pi$). During the outflow semi-cycle, the stream along the gas film separates at the exit section to form a planar jet that discharges with parallel streamlines surrounded by nearly stagnant ambient fluid. In that case, the pressure along the film remains equal to the ambient pressure, i.e. $\hat{P} = 0$. For inflow, on the other hand, the ambient gas accelerates from rest along streamlines approaching the film edge from all directions. Conservation of stagnation pressure $\hat{P} + |\hat{\mathbf{V}}|^2/2 = 0$ yields $\hat{P} = -\sin^2(\hat{\tau})/2$ for the pressure along the film away from the entrance. Consequently, since $\hat{P} = 0$ in the gas film during outflow (i.e. for $\pi \le \hat{\tau} \le 2\pi$), the time-averaged pressure drop, obtained by taking the time average of the gas-film pressure over a period, reduces to

$$\hat{P}_i = -\frac{1}{2\pi}\int_0^{\pi} \frac{1}{2}\sin^2\hat{\tau}\,\mathrm{d}\hat{\tau} = -\frac{1}{8} \quad \text{for} \quad \hat{St} \ll 1. \tag{2.101}$$

In the opposite case, the nearly acoustic limit of large Strouhal numbers $\hat{St} \gg 1$, it is convenient to introduce perturbation expansions in integral powers of the inverse of the Strouhal number

$$\begin{cases} \hat{\mathbf{V}} = \hat{\mathbf{V}}_0 + \hat{St}^{-1}\hat{\mathbf{V}}_1 + \cdots \\ \hat{P} = \hat{St}(\hat{P}_0 + \hat{St}^{-1}\hat{P}_1 + \cdots), \end{cases} \tag{2.102}$$

based on the anticipated scales of pressure and velocity. At leading order, we find the linear equations

$$\nabla \cdot \hat{\mathbf{V}}_0 = 0, \quad \frac{\partial \hat{\mathbf{V}}_0}{\partial \hat{\tau}} = -\nabla \hat{P}_0, \tag{2.103}$$

to be integrated with the boundary condition

$$\hat{\mathbf{V}}_0 \to [-\sin\hat{\tau}, 0] \quad \text{as} \quad X \to -\infty \quad \text{for} \quad 0 \le Y \le 1. \tag{2.104}$$

The associated velocity field is potential (irrotational) and may possibly be determined for each geometrical configuration with use of conformal mapping techniques [81, 82]. Note that, since $\hat{P}_0 \propto \cos\hat{\tau}$, the time-averaged overpressure is identically zero at this order. The value of $\hat{P}_i$ can be obtained by taking the time-average of the momentum equation that emerges at the following order,

$$\frac{\partial \hat{\mathbf{V}}_1}{\partial \hat{\tau}} + \nabla \left(\hat{P}_1 + \frac{|\hat{\mathbf{V}}_0|^2}{2} \right) = 0, \tag{2.105}$$

which yields $\langle \hat{P}_1 \rangle + \langle |\hat{\mathbf{V}}_0|^2 \rangle / 2 =$ constant, which can be evaluated in the ambient gas to give $\langle \hat{P}_1 \rangle = -\langle |\hat{\mathbf{V}}_0|^2 \rangle / 2$ for the spatial distribution of time-averaged pressure. Upon evaluating $\langle \hat{P}_1 \rangle$ inside the slender film with use of (2.104), we finally obtain the limiting value

$$\hat{P}_i = -\frac{1}{2\pi} \int_0^{2\pi} \frac{1}{2} \sin^2 \hat{\tau} \, \mathrm{d}\hat{\tau} = -\frac{1}{4} \quad \text{for} \quad \hat{S}t \gg 1. \tag{2.106}$$

The asymptotic values (2.101) and (2.106) serve as bounds of the large–α^2 asymptotic behavior of $\hat{P}_e$. Both values are indicated using dashed lines in figure 2.6(b). It should be noted that these bounds do not apply for finite values of the Stokes number, for which the computation of $\hat{P}_e$ requires numerical integration of the problem formulated in § 2.7.1, yielding values of $-\hat{P}_e$ that may exceed 1/4, as seen in figure 2.6(b).

2.7.6 The bounding unsteady viscous limit $\hat{S}t \gg 1$

As discussed in § 2.7.3, the curves of $\hat{P}_e$ displayed in figure 2.6(a) seem to approach asymptotically a limiting form for increasing values of the rescaled Strouhal number $\hat{S}t$. To accelerate the estimation of the peripheral pressure drop for values of $\hat{S}t$ greater than approximately 5, it is of interest to solve the governing equations (2.77) and (2.78) in the limit $\hat{S}t \gg 1$.

Since, in the first approximation ($\hat{St}^{-1} = 0$), the associated problem is linear, it is necessary to express the relevant flow variables as perturbation expansions of the same form given in (2.102), whence the time-averaged quantities of interest can be found at a higher order. At leading order, the reduced equations

$$\nabla \cdot \hat{\mathbf{V}}_0 = 0 \quad \text{and} \quad \frac{\partial \hat{\mathbf{V}}_0}{\partial \hat{\tau}} = -\nabla \hat{P}_0 + \frac{1}{\alpha^2} \nabla^2 \hat{\mathbf{V}}_0 \tag{2.107}$$

must be integrated numerically as described in § 2.7.2, supplemented by the familiar velocity matching condition (2.82) for $X \to -\infty$ and the reduced advective relaxation condition $\partial \hat{\mathbf{V}}_0 / \partial \hat{\tau} = 0$ for $X^2 + Y^2 \to \infty$. Applying the method of separation of variables and presuming solutions of the form

$$\hat{\mathbf{V}}_0 = \mathrm{Re}\left\{\mathrm{i}\mathrm{e}^{\mathrm{i}\hat{\tau}}\, \tilde{\mathbf{V}}_0(X,Y)\right\} \quad \text{and} \quad \hat{P}_0 = \mathrm{Re}\left\{\mathrm{e}^{\mathrm{i}\hat{\tau}} \tilde{P}_0(X,Y)\right\} \tag{2.108}$$

eliminates the time dependence in the linear problem above and provides the reduced equations

$$\nabla \cdot \tilde{\mathbf{V}}_0 = 0 \quad \text{and} \quad -\tilde{\mathbf{V}}_0 = -\nabla \tilde{P}_0 + \frac{1}{\alpha^2} \nabla \tilde{\mathbf{V}}_0\,, \tag{2.109}$$

which must be supplemented by the reduced matching condition

$$\tilde{\mathbf{V}}_0 = \left[1 - \frac{\cosh\left[\frac{\alpha(1+\mathrm{i})}{2\sqrt{2}}(2Y-1)\right]}{\cosh\left[\frac{\alpha(1+\mathrm{i})}{2\sqrt{2}}\right]}, 0 \right] \quad \text{as} \quad X \to -\infty \quad \text{for} \quad 0 \le Y \le 1\,. \tag{2.110}$$

Since the leading-order flow variables vary harmonically with time and yield no steady contribution, the reduced leading-order velocity distribution $\tilde{\mathbf{V}}_0$ must be substituted into the time-averaged equations that emerge at the following order,

$$\nabla \cdot \langle \hat{\mathbf{V}}_1 \rangle = 0 \quad \text{and} \quad \langle \hat{\mathbf{V}}_0 \cdot \nabla \hat{\mathbf{V}}_0 \rangle = \frac{1}{2}\mathrm{Re}\left\{\tilde{\mathbf{V}}_0 \cdot \nabla \tilde{\mathbf{V}}_0^*\right\} = -\nabla \langle \hat{P}_1 \rangle + \frac{1}{\alpha^2} \nabla^2 \langle \hat{\mathbf{V}}_1 \rangle\,, \tag{2.111}$$

where the identity (2.54) has been used to rewrite the known convective term on the left-hand side

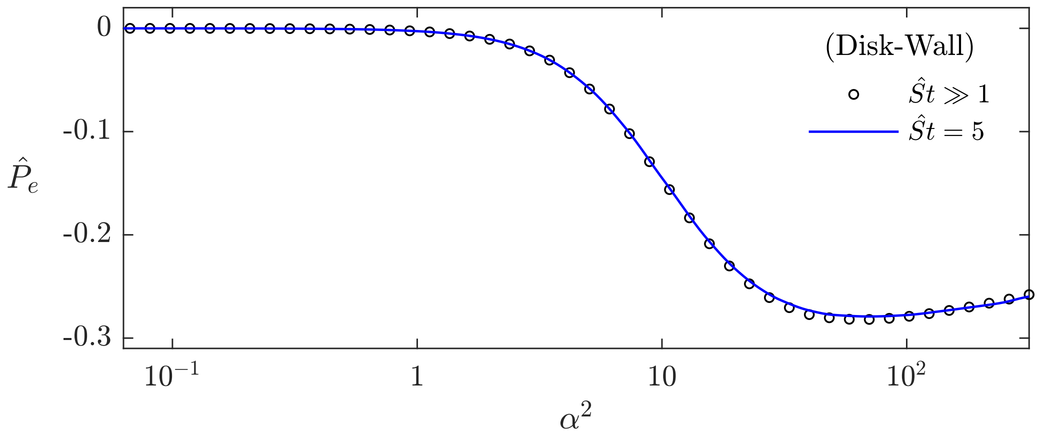

Figure 2.7. Variation with α^2 of the dimensionless steady peripheral pressure drop $\hat{P}_e$ for the "disk–wall" geometrical configuration in the unsteady viscous limit $\hat{S}t \gg 1$ (2.112), compared with the corresponding solution for $\hat{S}t = 5$.

of the momentum equation. Numerical integration of (2.111) using a trivial matching condition for time-averaged first-order velocity, $\langle \hat{\mathbf{V}}_1 \rangle = 0$ as $X \to -\infty$, and the familiar far-field relaxation conditions provides

$$\hat{P}_e(\alpha^2) = \langle \hat{P}_1 \rangle (X \to -\infty) \quad \text{for} \quad \hat{S}t \gg 1\,, \tag{2.112}$$

for the dimensionless peripheral pressure drop under the limit of large Strouhal numbers.

The resulting variation of $\hat{P}_e$ with α^2 is compared in figure 2.7 with that for $\hat{S}t = 5$, for the disk–wall geometry. In light of the similarity between the two curves, it must be mentioned that the total computational time required to solve the two reduced, time-independent linear problems (2.107) and (2.111), between 5 and 30 seconds, is substantially lower than that required to integrate the full nonlinear equations (2.77) and (2.78), between 20 and 30 minutes, with reasonable accuracy.

Note that, for moderately large values of the Stokes number $0 \leq \alpha^2 \lesssim 150$, all the curves shown for finite values of $\hat{S}t$ in figure 2.6 are bounded below by the curve for $\hat{S}t \gg 1$ shown in figure 2.7, which effectively denotes the maximum possible drop in the dimensionless steady pressure $\langle P \rangle$ across the peripheral region. The limiting solution above can thus supplement rapid computation of the greatest possible reduction in the repulsive force $\langle F_L \rangle$ associated with

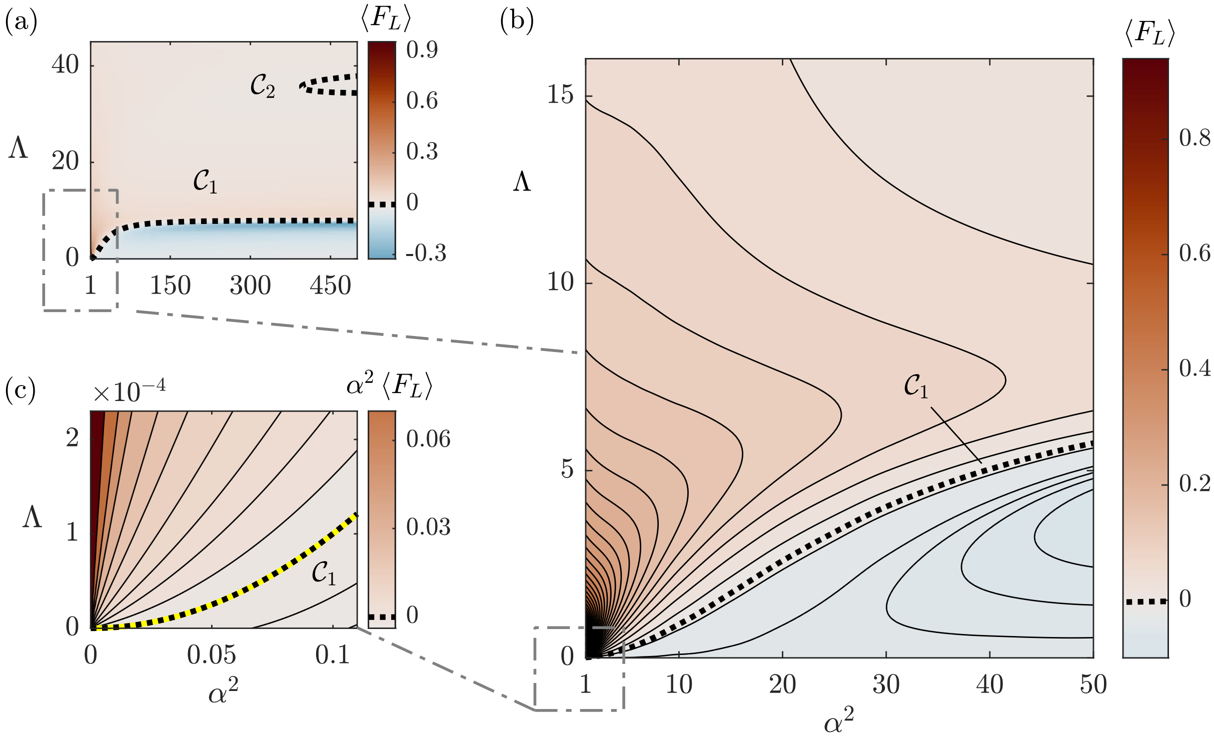

Figure 2.8. The variation with α^2 and Λ of the time-averaged force $\langle F_L \rangle$ defined in (2.56) and (2.57a,b), for $\hat{St} = 5$ and the "piston–wall" geometric configuration, with repulsive forces $\langle F_L \rangle > 0$ colored red and attractive forces $\langle F_L \rangle < 0$ colored blue. Computations are carried out using $\nu = 0.77$, $Pr = 0.7$ and $\gamma = 1.4$ (see § 2.3 for clarification). The dotted curves represent contours of zero force $\langle F_L \rangle = 0$.

pressure relaxation beyond the film edge $\xi = 1$, if needed, for a given value of α^2.

2.8 Discussion: Parametric dependences of the time-averaged squeeze-film levitation force

As revealed by (2.56), the normalized, time-averaged repulsive force $\langle F_L \rangle$ generated by an axisymmetric squeeze-film system has two distinct contributions, $\langle F_i \rangle$ and $\langle F_e \rangle$, whose definitions relate closely to the distinct flow regions identified in § 2.3. The first contribution, always positive, accounts for spatial deviations of the time-averaged pressure $\langle p \rangle$ along the gas film from that at the edge $\langle p \rangle(r = a)$. Its value, the variation of which is represented in figure 2.3(b) in a parametric domain spanned by the Stokes number α^2 (2.3) and the compressibility parameter Λ (2.4), can be evaluated using equation (2.59). The second contribution $\langle F_e \rangle = A^2 \hat{P}_e$, always negative, relates to the drop of the time-averaged pressure (from the ambient value p_a) across the small, peripheral region surrounding the edge of the squeeze film. Its value can be computed as the product of the square of the reduced stroke volume displaced by the oscillating disk/piston $A = |\Pi'(1)|$, given in equation (2.44) and plotted in figure 2.3(a) as a function of Λ and α^2, and the reduced pressure drop $\hat{P}_e$, represented in figure 2.6 as a function of α^2 and $\hat{St}$. Note that, while $\langle F_i \rangle$ and A can be calculated using the *explicit* expressions provided in § 2.10, the computation of $\hat{P}_e$ requires, in general, numerical integration of the nonlinear, incompressible Navier–Stokes equations (2.77) and (2.78).

Since the two competing contributions present in (2.56) have comparable orders of magnitude, their combined effect may, in principle, result in net forces that are either repulsive (if $\langle F_L \rangle > 0$) or attractive (if $\langle F_L \rangle < 0$) depending on the values of the controlling parameters. The typical dependence of $\langle F_L \rangle$ on α^2 and Λ is exemplified in figure 2.8 for the "piston–wall" geometry with $\hat{St} = 5$. Positive values of the force, corresponding to repulsion, are colored red, while negative values, representing attraction, are colored blue, with darker shades signifying larger magnitudes $|\langle F_L \rangle|$ in both cases. The dotted curves, across which $\langle F_L \rangle$ transitions in sign, are referred to in the proceeding discussion as "neutral contours".

It is natural to note from figure 2.8(a) that, under the classical lubrication limit $\alpha^2 \to 0$, which has been the subject of thorough investigation for well over half a century, the steady squeeze-film force $\langle F_L \rangle$ is repulsive for all Λ and unaffected by peripheral flow effects, as discussed in § 2.6.3. Figure 2.9(a) portrays the convergence of the viscoacoustic force, computed with $\hat{St} = 1$ for the piston–piston edge geometry, to the classical lubrication solution for decreasing values of α^2. The predominance of repulsive forces extends also to order-unity values of α^2, provided that the compressibility parameter remains above a critical value Λ_c, which rises for increasing values of α^2. The resulting function $\Lambda_c(\alpha^2)$ defines a neutral contour C_1 that marks a transition from repulsion to attraction.

Of particular interest is the limiting form of C_1 near the origin of the diagram, which

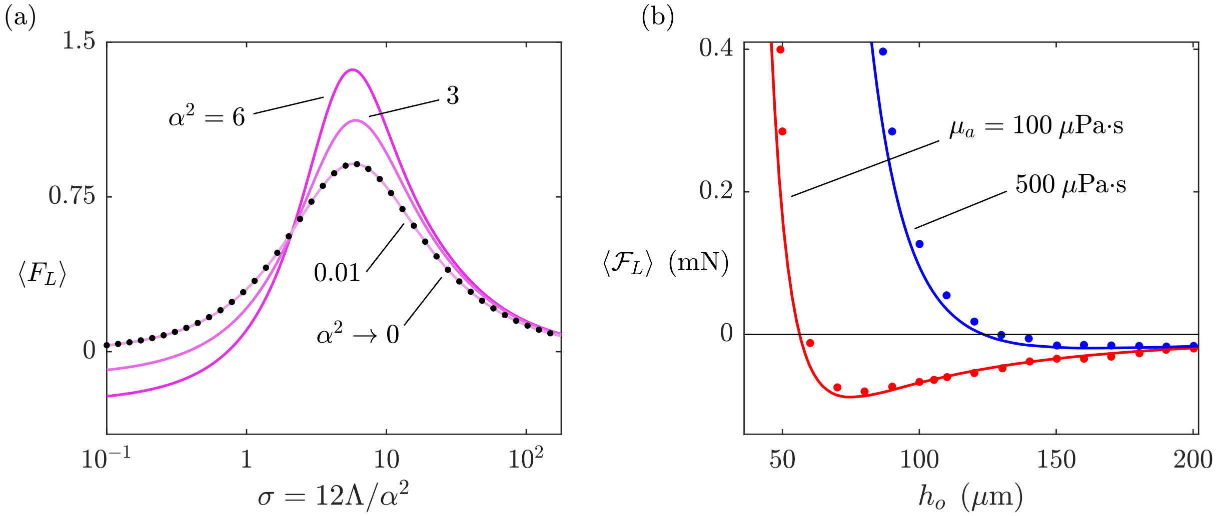

Figure 2.9. Verification of the predicted steady levitation force (denoted by solid curves) with (a) the classical limiting lubrication solution obtained from [5] and (b) time-dependent CFD simulations conducted by [6] (both denoted by dots). For the former case, the dimensionless force is plotted against the squeeze number and for the latter, the dimensional force is plotted against the mean gap width.

corresponds to weakly compressible systems operating near the lubrication limit. The associated behavior of the force $\langle F_L \rangle$ can be obtained by combining the explicit viscoacoustic forms of the inner contribution $\langle F_i \rangle(\alpha^2,\Lambda)$ and the stroke volume $A(\Lambda,\alpha^2)$ with the relevant limiting form of the peripheral pressure drop $\hat{P}_e = -\mathcal{P}\alpha^4$, where $-\mathcal{P} \simeq 2.68\times10^{-3}$ for all three geometrical configurations, as reported earlier below (2.97). The computed force is depicted in figure 2.8(c), whence it is apparent that C_1 approaches the origin as the parabola

$$\Lambda_c = k\alpha^4\,, \quad \text{with} \quad k \approx 0.01\,, \tag{2.113}$$

represented by the thick yellow line [1]. It is remarkable that this fundamental parametric relation, applicable to squeeze-film systems with relatively low oscillation frequencies $\omega \ll (\mu_a/\rho_a)/(h_o^2)$,

---

[1] In the publication where this result was originally communicated [60], the curvature k of the parabola (2.113) was miscalculated (as $k \approx 0.026$) due to the use of the weakly compressible lubrication approximations (2.71) for the quantities $\langle F_i \rangle$ and A, which do not account for departures of the Stokes number α^2 from zero. To write an equation that rigorously defines k, one would need to derive simplified forms of $\langle F_i \rangle$ and A in the distinguished limit $\Lambda/\alpha^2 \sim \alpha^2 \ll 1$, whose order of accuracy is consistent with that of the limiting form (2.97) of $\hat{P}_e$, and set the resulting expression for $\langle F_L \rangle$ equal to zero.

is independent of both the Strouhal number and—effectively—the specific geometry that pertain to the peripheral region. Using (2.113) together with the definitions of α^2 (2.3) and Λ (2.4) provides

$$h_c \approx 3.162\,\frac{(a\mu_a/\rho_a)^{1/2}}{(p_a/\rho_a)^{1/4}}\,, \tag{2.114}$$

for the critical value of the mean gap width at which the force switches from repulsion (for $h_o < h_c$) to attraction (for $h_o > h_c$). The above estimate (2.114) reveals that, for such systems, the conditions required for a transition are effectively independent of the oscillation frequency.

The region of the α^2–Λ parametric domain that lies below C_1, which encompasses the strictly incompressible case $\Lambda = 0$, consists entirely of weakly attractive forces. Interestingly, the dimensionless attractive force in the incompressible limit, to be computed from $\langle F_L\rangle = \langle F_i\rangle + A^2\hat{P}_e$ with use made of (2.63) and (2.61) to evaluate $\langle F_i\rangle$ and A^2, is seen to approach constant limiting values for $\alpha^2 \ll 1$ and $\alpha^2 \gg 1$. In the former case $\alpha^2 \ll 1$, with $\langle F_i\rangle = 33/560$, $A = 6/\alpha^2$, and $\hat{P}_e = \mathcal{P}\alpha^4$, the latter indicated in (2.97), it follows that

$$\langle F_L\rangle = \frac{33}{560} + 36\mathcal{P} \simeq -0.0375, \tag{2.115}$$

whereas in the latter case $\alpha^2 \gg 1$, with $\langle F_i\rangle = 1/32$, $A = 1/2$, and $\hat{P}_e$ approaching its inviscid value $\hat{P}_i(\hat{S}t)$, the solution reduces to

$$\langle F_L\rangle = \frac{1+8\hat{P}_i(\hat{S}t)}{32}\,, \tag{2.116}$$

a function of the Strouhal number that is necessarily negative since $\hat{P}_i$ lies in the range $-1/4 < \hat{P}_i < -1/8$, bounded by the limiting values given in (2.101) and (2.106). It must be noted that this limiting solution for $\Lambda = (\omega a)^2/(p_a/\rho_a) = 0$ may be used describe gaseous squeeze-film systems that operate with relatively low frequencies ω and/or small surface areas $\sim a^2$, but does not characterize systems that operate within a liquid [83]. Modeling, for instance, underwater ultrasonic SFL systems that display the familiar transition between repulsion and attraction [12]

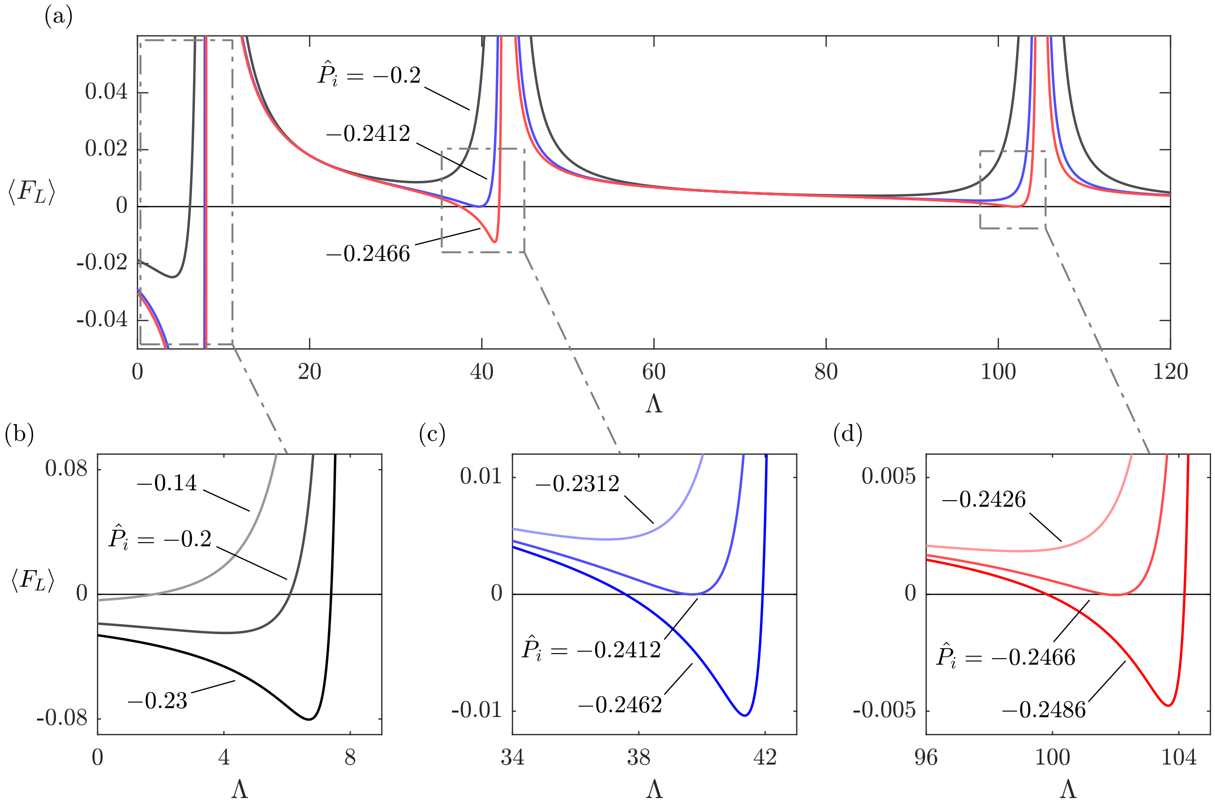

Figure 2.10. Variation with Λ of (a) the steady squeeze-film force in the inviscid limit (2.117) for different values of $\hat{P}_i(\hat{St})$, computed using $\gamma = 1.4$. Represented in the bottom row are (b) the first zero of the force, which exists for all $\hat{St}$ (i.e. any value of $\hat{P}_i$ in the range $-1/4 < \hat{P}_i < -1/8$), and (c,d) subsequent zeros, which emerge for increasing critical values of $\hat{St}$ (i.e. decreasing critical values of $\hat{P}_i$ given by $\hat{P}_i \simeq -0.2412, -0.2466, \cdots$).

requires re-formulation of the flow problem in the film (§ 2.4), perhaps with suitable descriptions of hydroacoustic wave propagation and cavitation [84], in place of the presently employed equation of state $p/p_a = (\rho/\rho_a)(T/T_a)$ for ideal gases.

As revealed by figure 2.8(a), the critical value Λ_c that defines the contour C_1 approaches a limiting value Λ_∞ as the Stokes number approaches infinity. Note that Λ_c denotes the inverse of the relative acoustic wave speed in the gas film for which the steady pressure variations along the film and near its edge provide cancelling contributions to the film force. Thus, the observed asymptotic behavior of Λ_c for $\alpha^2 \to \infty$ is consistent with the fact that, in the limit of nearly inviscid flow, the relative wave speed necessary to produce such a cancellation must cease to depend on viscosity, effects of which are confined to near-wall Stokes layers of small relative thickness $\delta_{SL} \sim \alpha^{-1} \ll 1$. The region of the parametric domain that lies above C_1 consists largely of repulsive forces, but is interrupted in figure 2.8(a) by a second neutral contour C_2, which encloses a peninsular region of attraction that develops for $\alpha^2 \gtrsim 400$ and $\Lambda \simeq 36$. To determine the value of Λ_∞ and explain the existence of this additional region of attraction, it is of interest to evaluate $\langle F_L \rangle = \langle F_i \rangle + A^2 \hat{P}_e$ in the inviscid limit $\alpha^2 \to \infty$. Using (2.74) and (2.76) gives

$$\langle F_L \rangle = \frac{1}{4K^2}\left[1 - \frac{2J_1(K)}{KJ_0(K)}\right] + \left(\hat{P}_i + \frac{1}{4}\right)\left[\frac{J_1(K)}{KJ_0(K)}\right]^2, \tag{2.117}$$

where $\hat{P}_i(\hat{St})$ is the inviscid value of $\hat{P}_e$, investigated in § 2.7.5, and $K = \sqrt{\Lambda/\gamma}$ is the relevant acoustic wavenumber (with γ being the ratio of specific heats). The above expression is plotted in figure 2.10 for selected values of $\hat{P}_i$. As can be seen, the number of zeros, which determines the number of parametric regions of attraction, depends on the value of $\hat{P}_i$, which in turn is a decreasing function of $\hat{St}$ that evolves from $\hat{P}_i = -1/8$ for $\hat{St} \ll 1$ to $\hat{P}_i = -1/4$ for $\hat{St} \gg 1$. Regardless of the value of $\hat{St}$ (i.e. for all values of $\hat{P}_i$ in the range $-1/4 < \hat{P}_i < -1/8$), there always exists at least one zero, corresponding to the asymptotic value Λ_∞ of Λ_c as $\alpha^2 \to \infty$. As suggested in figure 2.10(b), this asymptotic value approaches $\Lambda_\infty = 0$ for $\hat{St} \ll 1$ and $\Lambda_\infty \simeq 8.096$ for $\hat{St} \gg 1$, the latter coinciding with the location of the first singularity of (2.117), associated with the first zero of $J_0(\sqrt{\Lambda/\gamma})$ for $\gamma = 1.4$. As a result, the large-α^2 behavior of the principal neutral contour C_1 depicted in figure 2.8 can be expected to vary significantly as $\hat{St}$ approaches lower values. Specifically, for $\hat{St} \ll 1$, the contour will asymptotically approach the horizontal axis $\Lambda = 0$ as $\alpha^2 \to \infty$. In contrast, the shape of C_1 for small and moderate Stokes numbers $\alpha^2 \sim 1$ can be anticipated to vary weakly with $\hat{St}$, as indicated by the discussion surrounding (2.113).

As seen in figure 2.10(c), two more zeros, bounding the second neutral contour C_2, emerge when the value of $\hat{P}_i$ decreases below $\hat{P}_i \simeq -0.2412$. Additional zeros, corresponding to new regions of attraction, appear for decreasing values of $\hat{P}_i$ (i.e. increasing values of $\hat{St}$), so that, for instance, the existence of a third neutral contour requires $\hat{P}_i \lesssim -0.2466$, as revealed by figure 2.10(d). The number of zeros diverges as $\hat{P}_i \to -1/4$ (i.e. as $\hat{St} \to \infty$), creating an infinite cascade of peninsulas of attraction. In this connection, it is worth pointing out that, while the existence of the primary neutral contour C_1 for all relevant values of $\hat{P}_i$ (i.e. all finite $\hat{St}$ and all three geometries) is a key finding with important consequences for the operation of practical systems, the anticipated relevance of the additional neutral contours $C_2, C_3, \ldots$ and the corresponding regions of attraction is somewhat limited, since they only develop for very large values of α^2 and Λ.

Recently, time-dependent CFD simulations of the piston–piston squeeze-film problem have been conducted (using the COMSOL 'Multiphysics' software) by [6], who found that assuming adiabatic, constant-viscosity flow (corresponding to $Pr \to \infty$ and $\nu = 0$) yields reasonable accuracy relative to their experimental data. In their 2D axisymmetric computations, the dimensional steady squeeze-film force $\langle \mathcal{F}_L \rangle$ was quantified for various mean separation distances and fluid viscosities, while keeping all other dimensional parameters constant. In particular, in terms of the dimensionless governing parameters of our formulation, their operating conditions pertain to the case $0.05 \lesssim \varepsilon \lesssim 0.25$, $2 \lesssim \alpha^2 \lesssim 65$, $\Lambda \simeq 0.334$ and $0.07 \lesssim \hat{St} \lesssim 5.12$. Displayed in figure 2.9(b) is a comparison of their results with those of the present asymptotic formulation, the latter computed using $Pr = 10^4$ and $\nu = 0$, which demonstrates clearly the transition from strong repulsion to weak attraction when the mean separation width h_o is increased above its threshold value h_c. It must be noted that, although the agreement between our theoretical results and the numerical results of [6] is generally satisfactory, it deteriorates in the repulsive regime $h_o < h_c$ because the relative amplitude ε, the utilized perturbation parameter, is no longer small, compromising the accuracy of the asymptotic predictions.

2.9 Conclusions

A unifying quasi-analytical model of slender, gas-lubricated bearings was developed in this study to predict the steady squeeze-film force acting on an axisymmetric rigid body undergoing asymptotically small-amplitude time-harmonic axial oscillations in the vicinity of a parallel surface. Three geometrical configurations involving a disk or a piston as the oscillator and a piston or an infinite wall as the stationary surface were considered as part of the analysis (see figure 2.1). The method of matched asymptotic expansions was applied to relate the Navier–Stokes solutions describing the flow in two distinct regions: a slender region between the parallel surfaces featuring predominantly radial flow driven by the disk oscillations, and an asymptotically smaller non-slender peripheral region where the oscillatory gas motion is driven largely by said radial flow. The problem was solved in the general case in which the oscillation time is comparable to the three relevant fluid-mechanical times, namely, the characteristic time for radial acoustic-wave propagation, the characteristic viscous time across the gas layer, and the characteristic residence time of flow in the peripheral region.

Historically, a major obstacle to computing the viscoacoustic film force has been the determination of a proper boundary condition for the fluid pressure at the edge of the gas layer. The present formulation relies on the distinguished double limit $\varepsilon \sim \delta \ll 1$ defined by comparable small values of the dimensionless vibration amplitude ε and the aspect ratio δ, whence the time-averaged spatial pressure variations across the peripheral region are comparable to those found along the wall-bounded gas layer. The harmonic leading-order flow inside the slender film was solved analytically, providing a closed-form expression for the radial flow to be used as a matching boundary condition for the peripheral region. Upon computing first-order corrections, the radial departures of the time-averaged pressure inside the gas layer from its value at the edge were found to depend on the Stokes number α^2 and a compressibility parameter Λ, two order-unity parameters that respectively quantify the relative magnitudes of the viscous and acoustic timescales. Characterizing the peripheral flow required numerical integration of the local Navier–Stokes equations, shown to reduce to their incompressible, planar form at leading order, with α^2 and a modified local Strouhal number $\hat{St}$ entering as relevant controlling parameters. The dependence on the geometrical configuration was found to be relatively weak, with the magnitude of the pressure drop being slightly larger for wider angles of the near-edge opening of the bounding surfaces.

Our analysis illustrates that the time-averaged pressure decreases across the peripheral region from its value in the stagnant atmosphere and then principally increases along the air gap to reach a local maximum at the axis, in agreement with prior numerical results [4]. These two competing effects determine the sign of the steady dimensionless perpendicular force $\langle F_L \rangle$ felt by the oscillating body (and also by the stationary parallel surface), so that both attractive and repulsive forces can be generated. The resulting value of $\langle F_L \rangle$ was found to vary strongly with the Stokes number α^2 and the compressibility parameter Λ, but comparatively weakly with the peripheral Strouhal number and the geometrical configuration. The typical behavior of $\langle F_L \rangle$ for a fixed choice of $\hat{St}$ and geometry was depicted on a diagram (see figure 2.8) structured with the principal parameters α^2 and Λ as the bounding axes, showing that there is a critical separating contour C_1 in the associated parametric domain across which the steady squeeze-film force switches from positive to negative values, indicating a transition from repulsion to attraction. The accuracy of the present asymptotic analysis near this transition region was verified by means of comparison with the results of a time-dependent CFD simulation conducted recently by [6] (see figure 2.9(b)). It was proven that the contour C_1 exists for all values of $\hat{St}$ and different geometrical configurations, and that its shape near the origin is universal, resulting in an accompanying prediction (2.114) for the critical gap width h_c separating attraction from repulsion for relatively low-frequency squeeze-film systems. The accuracy of this theoretical prediction must be tested in future work by means of carefully monitored experiments. Also of interest in connection with the force diagram is that additional regions of attractive force, in the form of peninsulas, develop for large values of the Stokes number α^2 when the value of $\hat{St}$ is sufficiently large.

The explicit expressions provided for the time-averaged pressure distribution in the slender gas layer and the corresponding integral contribution to the steady force, as well as the reduced numerical description of the time-averaged pressure drop across the peripheral region surrounding the layer, both applicable for arbitrary values of the principal governing parameters α^2, Λ and $\hat{St}$, shed light on the fundamental flow physics and expedite the viscoacoustic evaluation of the force, potentially supplementing the design and operation of high-frequency squeeze-film systems that require real-time feedback control. It is worth pointing out that the analysis of the first-order corrections in the gas film can be readily extended to provide the steady film temperature $\langle \Theta_1 \rangle$ in closed form, if needed in future applications. Simplified expressions of the pressure distribution and force for limiting values of α^2 and Λ were provided in § 2.6.3 and § 2.8 to allow accelerated computation for systems that operate near the lubrication ($\alpha^2 \ll 1$), inviscid ($\alpha^2 \gg 1$) or incompressible ($\Lambda \ll 1$) limit.

The ability to controllably generate and transition between repulsive and attractive forces using a single squeeze-film system is of significant interest in contemporary applications including contactless levitation and soft robotics. The construction and assembly line transport of microelectronic components would be greatly assisted by levitation devices capable of suspending sensitive objects from various angles and releasing them on command [6]. A controllable transition to attraction is also desirable in the context of contactless locomotion of soft robots over diverse terrains [3]. Gaseous squeeze films may be preferable in this context over other adhesive mechanisms such as electromagnetic and dry fibrillar attraction due to reasons including weight requirements, complexity of manufacturing and limitations in the type of operational surface. The present theoretical study demonstrates that a rigid squeeze-film oscillator can alternate between repulsion and attraction through control of operational variables such as the oscillation frequency and the mean separation width. As previously noted, the closed-form expressions provided in this study may serve to improve the feedback control systems required for the stable operation of such devices.

Practical applicability of the present analysis is limited by the possibility of elastic deformations in the oscillating body that may be non-negligible in the analysis of the induced flow [7]. Of particular interest beyond this study is the characterization of axisymmetric squeeze-film systems involving radially non-uniform driving oscillations $h = h(r,t)$. In an appendix in their seminal paper, Taylor and Saffman [5] provided analytical expressions for the mean radial pressure distribution produced by piece-wise linear oscillations $h(r,t)$ of a squeeze-film system in the lubrication limit. Specifically, oscillations of the form $h/h_o = 1 + \varepsilon(1 - 2r/a)\cos(\omega t)$, where the mid-circle $r = a/2$ of the disk is fixed and the center $r = 0$ and edge $r = a$ oscillate out of phase, were shown to produce weak attractive squeeze-film forces for low frequencies ω, not found in the lubrication limit for *rigid* oscillators. Recent experiments [3, 49, 54] have demonstrated that highly flexible oscillators can be used to generate substantially stronger attractive forces that allow the levitation of hundreds and thousands of grams of payload. The physics of such 'flexural' squeeze-film systems is explored in Chapters 3 and 4 of this dissertation.

2.10 Appendix: Auxiliary expressions used in the evaluation of the gaseous film overpressure and its contribution to the steady squeeze-film force

The reduced asymptotic expressions provided in (2.55) and (2.59), respectively for deviations of steady pressure in the film from its value at the edge, $\langle P_1\rangle(\xi) - \langle P_1\rangle(1)$, and the associated contribution to the steady squeeze-film force, $\langle F_i\rangle$, involve the complex functions

$$X_1 = \Pi(\xi) = \frac{J_0\left(\xi\sqrt{C\Lambda}\right) - J_0\left(\sqrt{C\Lambda}\right)}{\left|\mathcal{G}_U(1)\sqrt{C\Lambda}\, J_0\left(\sqrt{C\Lambda}\right)\right|^2}, \tag{2.118}$$

$$X_2 = \frac{\left|J_1\left(\xi\sqrt{C\Lambda}\right)\right|^2 - \left|J_1\left(\sqrt{C\Lambda}\right)\right|^2 + \int_1^{\xi} \frac{1}{\xi} J_1\left(\xi\sqrt{C\Lambda}\right) J_1\left(\xi\sqrt{C^*\Lambda}\right)\, d\xi}{\left|\mathcal{G}_U(1)\sqrt{C\Lambda}\, J_0\left(\sqrt{C\Lambda}\right)\right|^2}, \tag{2.119}$$

$$X_3 = \frac{J_0^*\left(\sqrt{C\Lambda}\right) - J_0^*\left(\xi\sqrt{C\Lambda}\right)}{J_0^*\left(\sqrt{C\Lambda}\right)\left|\mathcal{G}_U(1)C\Lambda\right|^2} - \frac{\int_1^{\xi} J_0\left(\xi\sqrt{C\Lambda}\right) J_1^*\left(\xi\sqrt{C\Lambda}\right)\, d\xi}{\sqrt{C\Lambda}\left|\mathcal{G}_U(1)\sqrt{C\Lambda}\, J_0\left(\sqrt{C\Lambda}\right)\right|^2}, \tag{2.120}$$

and the complex constants

$$\mathcal{X}_1 = \frac{2J_1\left(\sqrt{C\Lambda}\right) \big/ J_0\left(\sqrt{C\Lambda}\right) - \sqrt{C\Lambda}}{\mathcal{G}_U(1)(C\Lambda)^{3/2}}, \tag{2.121}$$

$$\begin{aligned}\mathcal{X}_2 = \frac{-\mathrm{i}}{\left|\mathcal{G}_U(1)C\Lambda J_0\left(\sqrt{C\Lambda}\right)\right|^2}\Bigg\{ &\frac{C^*\Lambda}{\mathrm{Im}(C\Lambda)^2}\mathrm{Im}\left[\sqrt{C^*\Lambda}J_0\left(\sqrt{C\Lambda}\right) J_1^*\left(\sqrt{C\Lambda}\right)\right] \\ &+ \frac{\sqrt{C^*\Lambda}}{2\mathrm{Im}(C\Lambda)}\left[\sqrt{C^*\Lambda}\left|J_0\left(\sqrt{C\Lambda}\right)\right|^2 + \sqrt{C\Lambda}\left|J_1\left(\sqrt{C\Lambda}\right)\right|^2\right] \\ &+ \frac{J_0\left(\sqrt{C\Lambda}\right)}{\mathrm{i}\sqrt{C^*\Lambda}}\left[2J_1^*\left(\sqrt{C\Lambda}\right) - \sqrt{C^*\Lambda}J_0^*\left(\sqrt{C\Lambda}\right)\right]\Bigg\},\end{aligned} \tag{2.122}$$

$$\mathcal{X}_3 = -\frac{\left|J_1\left(\sqrt{C\Lambda}\right)\right|^2 + \mathrm{Im}\left[\sqrt{C\Lambda}J_0\left(\sqrt{C\Lambda}\right) J_1^*\left(\sqrt{C\Lambda}\right)\right] \big/ \mathrm{Im}(C\Lambda)}{\left|\mathcal{G}_U(1)\sqrt{C\Lambda}J_0\left(\sqrt{C\Lambda}\right)\right|^2} \tag{2.123}$$

and

$$\mathcal{H}_1 = 1 - \frac{\tan(\beta_U)}{\beta_U}, \tag{2.124}$$

$$\mathcal{H}_2 = 1 - \frac{\tan(\beta_U)}{\beta_U} - \frac{\tanh(\beta_\Theta)}{\beta_\Theta} + \frac{\beta_U \tan(\beta_U) + \beta_\Theta \tanh(\beta_\Theta)}{\beta_U^2 + \beta_\Theta^2}, \tag{2.125}$$

$$\begin{aligned}\mathcal{H}_3 = {} & \frac{2\beta_U - 2\tan(\beta_U)}{\beta_U} + \frac{2\beta_U}{\beta_U^2 + \beta_\Theta^2}\Bigg[\beta_\Theta \tan(\beta_U)\tanh(\beta_\Theta) \\ & - \beta_U + \frac{\left(\beta_U^2 - \beta_\Theta^2\right)\tan(\beta_U) + 2\beta_U\beta_\Theta \tanh(\beta_\Theta)}{\beta_U^2 + \beta_\Theta^2}\Bigg],\end{aligned} \tag{2.126}$$

$$\mathcal{H}_4 = \frac{-4\beta_U^3 + 15\left[\tan(\beta_U) - \tanh(\beta_U)\right] - 6\beta_U \tanh(\beta_U)\tan(\beta_U)}{24\beta_U^3}, \tag{2.127}$$

$$\begin{aligned}\mathcal{H}_5 = {} & \frac{1}{12\beta_U^3}\Big[\beta_U\left(15 - 2\beta_U^2\right) + \left(6\beta_U^2 - 9\right)\tan(\beta_U) \\ & - 6\tanh(\beta_U) - 3\beta_U \tanh(\beta_U)\tan(\beta_U)\Big],\end{aligned} \tag{2.128}$$

$$\begin{aligned}\mathcal{H}_6 = {} & -\frac{1}{6} + \frac{2\beta_U + \left(\beta_U^2 - 2\right)\tan(\beta_U)}{2\beta_U^3} + \frac{\beta_\Theta - \tanh(\beta_\Theta)}{2\beta_\Theta^3} \\ & - \frac{1}{2\beta_\Theta\left(\beta_U^2 + \beta_\Theta^2\right)}\Bigg[\beta_\Theta + \beta_U \tan(\beta_U)\tanh(\beta_\Theta) \\ & + \frac{\left(\beta_U^2 - \beta_\Theta^2\right)\tanh(\beta_\Theta) - 2\beta_U\beta_\Theta \tan(\beta_U)}{\beta_U^2 + \beta_\Theta^2}\Bigg],\end{aligned} \tag{2.129}$$

$$\mathcal{H}_7 = \frac{\beta_U\left(6 - \beta_U^2\right) + 3\left(\beta_U^2 - 2\right)\tan(\beta_U)}{6\beta_U^3}, \tag{2.130}$$

$$\mathcal{H}_8 = \frac{\left(\beta_U^2 + 1\right)\tanh(\beta_U) - \beta_U}{2\beta_U^3}. \tag{2.131}$$

The symbols Re, Im, and the asterisk $*$ represent respectively the real part, imaginary part and conjugate of a complex quantity. The definitions of β_U and β_Θ are given in (2.37) while those of C and $\mathcal{G}_U(1)$ are given in (2.41).

Equations (2.118)–(2.123) were obtained with use of the integrals tabulated in [85]. In particular, each $\mathcal{X}_i$ is available in *explicit* form, allowing rapid computation of $\langle F_i \rangle$ (2.57) [2].

---

[2] Equations (2.121)–(2.123) and (2.125) were printed with errors in the original publication of these results [60].

Chapter 2, in part, has been published in the *Journal of Fluid Mechanics* under the title "Viscoacoustic squeeze film force on a rigid disk undergoing small axial oscillations", by S. Ramanarayanan, W. Coenen and A. L. Sánchez, 933, A15, (2022). The dissertation author and his doctoral advisor were the primary authors and investigators of this paper.

Chapter 3

Enhancement of attractive load capacity by resonant flexural oscillation

3.1 Executive summary

In this chapter, numerical and asymptotic methods are used to investigate the fluid dynamics underlying the anomalously large attractive forces that were recently observed in squeeze-film levitation systems driven by axial vibrations of a flexible oscillator. Namely, in a recent experimental study, a thin plastic disk driven near one of its natural frequencies attractively levitated an object weighing several hundred grams. This behavior is in stark contrast with that of rigid-body systems, which produce attractive forces thousands of times weaker and only within a limited range of operating conditions. Flexural systems driven by standing-wave deformations of the oscillator are addressed in this chapter in a unifying matched-asymptotic analysis that accounts for effects of fluid viscosity, inertia and compressibility, as well as pressure variations beyond the outer boundary of the squeeze film. While the weak attractive forces produced by rigid-body systems are known to depend critically on the existence of a net pressure drop across this peripheral region, the present analysis reveals that the augmented attractive load capacity of resonant flexural systems is associated instead with local minima of film pressure near the nodal regions of the standing wave. Furthermore, the flexural wavenumber of the oscillating disk is found to correlate strongly with the attractive load capacity as well as the range of frequencies and disk surface areas for which attractive forces can be produced.

3.2 Introduction

As outlined in Chapter 1 of this dissertation, a typical squeeze-film levitation system involves two rigid objects whose parallel surfaces are separated by a thin film of air. One of the objects performs high-frequency time-harmonic oscillations along an axis perpendicular to the surfaces, perturbing the air in the slender film and its immediate outer periphery. The inherently nonlinear dynamics of the excited pulsating fluid flow gives rise to a pressure distribution along the film that varies non-harmonically with time, yielding a time-averaged normal force on the objects—the steady squeeze-film force (SSF), which is typically repulsive [7].

This phenomenon, first implemented within the context of gaseous lubrication [8, 9], has been applied in recent decades to design contactless levitation systems that can suspend and transport sensitive objects such as microelectronic components and glass substrates [1, 11–14]. This so-called "*squeeze-film levitation*" (SFL) is often preferable to (i) contact-based soft grippers that may deposit residual materials or produce electrostatic adhesion that prevents reliable detachment [6] and (ii) pneumatic grippers that require constant fluid pumping and thus significant electrical energy [86, 87].

The typically repulsive SSF, which enables levitation of several kilograms [19], has been shown to transition to attraction when the mean distance between the two surfaces is increased beyond a critical value. Until recently, such a transition had been observed only in systems with restrictively small oscillation frequencies or object surface areas, precluding aerial attractive levitation of more than a gram (see table 3.1) [4, 6, 36, 37, 48].

A remarkable patent published in 2015 [49] reported, for the first time, attractive squeeze-film levitation of over a hundred grams. An experimental study in 2021 levitated attractively loads of several hundred grams [3]. Another recent communication [54] reports a load of nearly 200 kilograms, all three studies displaying a substantial increase in energy efficiency over conventional pneumatic grippers [87]. The oscillators used by [3] were disks made of plastic shim stock, with small aspect ratios (thickness divided by radius) of order 10^{-2}. The greatest

Table 3.1. Tabulated below are the maximal *attractive* steady squeeze-film forces $\langle -\mathcal{F}_L \rangle$ (expressed in units of grams-force) reported in various experimental studies conducted since 1999, along with the operating conditions used by each. The final column of each row lists the value of the force normalized with the effective area of the squeeze film.

Oscillator description	Oscillator thickness t_d (mm)	Squeeze-film radius a (cm)	Oscillation frequency $\frac{\omega}{2\pi}$ (Hz)	Oscillation amplitude εh_o (μm)	Mean film thickness h_o (μm)	Dimensional levitation force $\langle -\mathcal{F}_L \rangle$ (gf)	Normalized levitation force $\frac{\langle -\mathcal{F}_L \rangle}{\pi a^2} \left(\frac{\text{gf}}{\text{cm}^2}\right)$
aluminum disk[a] [37]	10	3.5	1,600	2.6	220	0.196	5.09×10^{-3}
aluminum disk	10	3.5	200	187	760	0.52	13.5×10^{-3}
ultrasonic horn[b] [4]	—	0.2	26,630	4	—	$7.84{\times}10^{-3}$	0.06
ultrasonic horn [36]	—	0.15	21,000	4.9	39	0.013	0.18
ultrasonic horn [48]	—	0.3	28,000	2.5	50	0.127	0.45
ultrasonic horn [6]	—	≈ 0.13[c]	21,000	10	44	0.031	0.58
ultrasonic horn [12]	—	2.5	17,000	1.1	100	45[d]	2.29
plastic disk[e] [3]	0.254	6.93	200	—	≈ 2,800[f]	611.6	4.05
plastic disk	0.127	2.45	200	—	≈ 2,200[f]	407.7	21.62
aluminum plate[g] [53]	0.79	≈ 17.20[c]	15	—	—	18.6×10^3	20.01
aluminum plate [54]	1.02	≈ 34.39[c]	15	—	—	199.4×10^3	53.66

[a] Driven by an electrodynamic shaker (the EMIC 512A/D compact vibration generator)
[b] Appended to a bolt-clamped Langevin transducer
[c] Equivalent radius $a_e = \sqrt{\ell w/\pi}$ of an effectively rectangular squeeze film of length ℓ and width w
[d] Exceptional experiment conducted under water
[e] Driven by a small, centrally mounted eccentric-rotating-mass motor
[f] Central value $h_o(0)$ of the mean distribution of film thickness $h_o(r)$ for an oscillator experiencing significant fluid–structure coupling
[g] Driven by a powerful, centrally mounted vibration actuator

attractive forces are reported to have occurred at an operating frequency of ≈ 200 Hz, for which the authors report having observed a nodal circle on the disk, indicative allegedly of resonant standing-wave oscillations. (This observation is discussed further in Chapter 4 in the context of fluid–structure interactions.) As an illustrative comparison, these forces are a thousandfold larger than those reported in a prior experiment conducted under similar operating conditions (frequency and surface area) but with an effectively rigid oscillator [37] (see the second and ninth rows of table 3.1).

3.3 Preliminary simulations

To begin investigating the fluidic phenomena underlying this magnification, we performed preliminary numerical simulations of an axisymmetric squeeze-film system excited by standing-

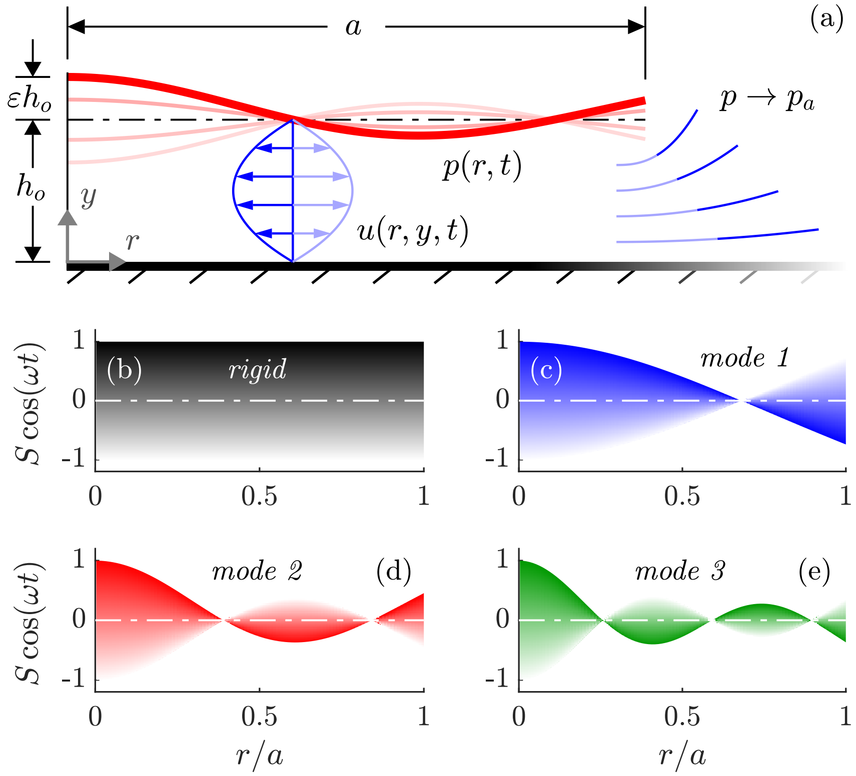

Figure 3.1. (a) Schematic of an axisymmetric squeeze-film levitation system involving an oscillating disk. Shaded below it are waveforms that represent (b) rigid-body and (c)–(e) resonant flexural oscillations of a disk with a Poisson's ratio of $\nu_d = 0.3$, the latter described below equation (3.4).

wave oscillations of a disk. As depicted in figure 3.1(a), a thin disk of radius a, submerged in a gas with ambient viscosity μ_a, density ρ_a and pressure p_a, oscillates near an infinite wall such that the thickness of the gaseous film separating the two, h, varies with time t as

$$y = h(r,t) = h_o\left[1 + \varepsilon S(r/a)\cos(\omega t)\right], \tag{3.1}$$

where r and y denote the radial and transverse coordinates, h_o is the mean film thickness and ε, $S(r/a)$ and ω represent respectively the relative characteristic amplitude, peak amplitude profile and angular frequency of the standing wave.

Systems such as those described in table 3.1 generally satisfy the assumption of slenderness, $\delta = h_o/a \ll 1$, such that axial variations of the local fluid pressure can be neglected, i.e. $\partial p/\partial y = 0$, and the repulsive SSF can be computed using the simplified integral

$$\langle \mathcal{F}_L \rangle = \int_0^a \langle p(r,t) - p_a \rangle \, 2\pi r \, \mathrm{d}r \,, \tag{3.2}$$

incurring only small relative errors of order δ. The angled brackets in (3.2) denote the cycle-averaging operator

$$\langle \star \rangle = \frac{\omega}{2\pi} \int_t^{t+2\pi/\omega} \star \, \mathrm{d}\bar{t} \,, \tag{3.3}$$

where $\bar{t}$ is a dummy integration variable.

The simulations involved a relevant form of the classical Reynolds equation [8], a partial differential equation that models viscous, compressible flow in thin films while neglecting fluid inertia and variations of the edge pressure $p(r = a,t) = p_a$ (see also § 3.4.9 for elaboration). Numerical integration was performed using a standard central-space, forward-Euler finite-difference scheme [88]. Motivation for considering this *Stokes limit* was found in the appendix of a seminal 1957 paper [5], where it is reported that the SSF generated by piece-wise linear standing-wave oscillations of a disk ($S = 1 - 2r/a$) becomes attractive for critically low values of the so-called *squeeze number* $\sigma = 12(\mu_a/p_a)(\omega a^2/h_o^2)$, i.e. for sufficiently low frequencies, small radii and/or large mean film thicknesses.

Here, we consider instead a family of axisymmetric standing waves that are resonant solutions to the Kirchhoff–Love equation, a linear partial differential equation that models small-amplitude, low-wavelength oscillations of thin plates [89]. The peak amplitude profile is given by

$$S_{KL}(r/a) = \frac{I_1(K)J_0(Kr/a) - J_1(K)I_0(Kr/a)}{I_1(K) - J_1(K)} \,, \tag{3.4}$$

where J and I are the regular and modified Bessel functions of the first kind, whose order is indicated by the subscript. Such solutions (3.4) exist only for discrete values of the relevant dimensionless wavenumber K (normalized with the inverse radius a^{-1}) that satisfy the characteristic

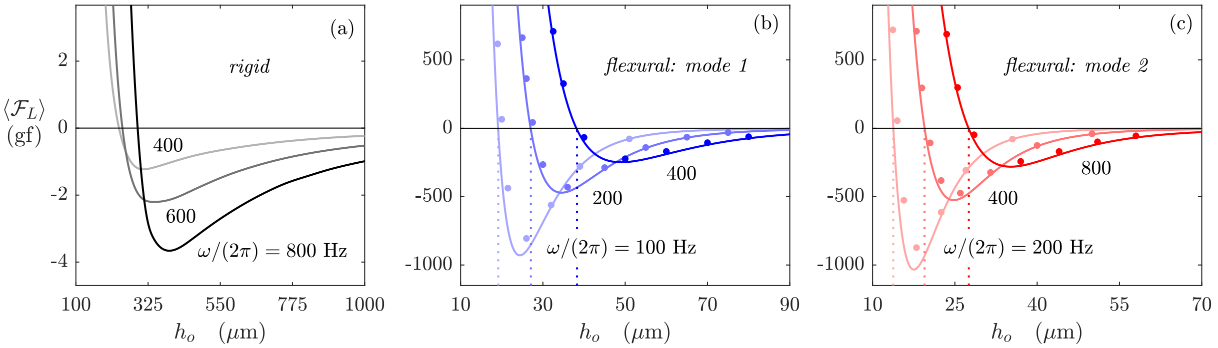

Figure 3.2. Variation of the computed steady squeeze-film force with the mean film thickness h_o and angular frequency ω, for a disk of radius $a = 7$ cm oscillating with central amplitude $\varepsilon h_o = 10\,\mu$m. Asymptotic predictions (solid curves) are displayed for (a) rigid-body and (b,c) resonant flexural oscillations (those depicted in figure 3.1), and compared for the latter with finite-difference solutions of the Reynolds equation (large dots). Vertical dotted lines mark critical transition thicknesses h_o^* calculated using (3.72).

equation

$$1 - \frac{K}{2}\left[\frac{J_0(K)}{J_1(K)} + \frac{I_0(K)}{I_1(K)}\right] = \nu_d\,, \tag{3.5}$$

where ν_d is the Poisson's ratio of the material. For instance, a disk with $\nu_d = 0.3$ achieves its first three resonant modes for $K \approx 3.0005, 6.2003$ and 9.3675. The standing waves associated with the listed modes are depicted in panels (c)–(e) of figure 3.1, to be considered for the remainder of this chapter. Note that mode 1, which exhibits a single nodal circle at $r/a \approx 0.68$, is qualitatively representative of the oscillations in the recent experiment [3], although the latter involved a non-uniform distribution of mean film thickness $\langle h \rangle = h_o(r)$, symptomatic of strong fluid–structure coupling. It must finally be noted that these resonant modes occur for corresponding natural frequencies

$$\omega = \frac{K^2}{a^2}\sqrt{\frac{E_d t_d^2}{12(1-\nu_d^2)\rho_d}}\,, \tag{3.6}$$

where $t_d \ll a$ is the thickness of the disk and E_d and ρ_d are its homogenous Young's modulus and density.

Our viscous-flow simulations, selected results of which are displayed in the form of dots in figures 3.2(b) and (c), appear to predict accurately the magnification of attractive load capacity that was observed in SFL systems involving pronounced disk flexure [3, 49]. Nevertheless, modeling the wider range of operating conditions used among common squeeze-film systems—in particular, ultrasonic frequencies ($\omega/(2\pi) \gtrsim 20$ kHz), which allow inaudible vibration—additionally necessitates rigorous quantification of (i) effects of fluid inertia in the thin gaseous film [90] and (ii) accompanying variations of pressure at its edge $p(r = a, t)$ [63, 68, 74], as done below.

3.4 Matched-asymptotic viscoacoustic formulation

In Chapter 2 of this dissertation, a theoretical formulation was outlined [60] that uses the method of *matched asymptotic expansions* [78] to solve the full viscoacoustic flow problem for ideal, rigid-body systems ($S = 1$) that oscillate with small relative amplitudes $\varepsilon \ll 1$. The analysis involved solving asymptotically reduced forms of the Navier–Stokes equations in two distinct flow regions of the squeeze-film system depicted in figure 3.1(a):

(i) a small, non-slender peripheral region extending for distances of order h_o in all directions from the edge $r = a$, and

(ii) a slender region of nearly unidirectional flow spanning the majority of the slender film but far removed from this periphery, $a \geq a - r \gg h_o$.

Performing a straightforward order-of-magnitude analysis of the reduced equations that describe fluid flow in each region revealed that (i) the flow speeds in both regions are of comparable magnitude $\sim \varepsilon\omega a$, (ii) the instantaneous pressure variations across the periphery are a factor of order $\delta = h_o/a \ll 1$ smaller than those along the film and (iii) the time-averaged pressure variations across the periphery differ by a factor of order δ/ε from those along the film. In pursuit of a formulation that accounts simultaneously for spatial variations of time-averaged pressure across both regions, the distinguished limit $\delta \sim \varepsilon \ll 1$ was selected for further analysis.

In this limit, when the flow variables local to the film are expanded in terms of the selected perturbation parameter ε,

$$\begin{cases} u(r,y,t) = u_0 + \varepsilon u_1 + \cdots , \\ p(r,t) - p_a = (p_0 - p_a) + \varepsilon(p_1 - p_a) + \cdots , \end{cases} \tag{3.7}$$

the leading-order pressure satisfies the straightforward boundary condition $p_0(r \to a) = p_a$, but yields no time-averaged contribution to the levitation force, i.e. $\langle p_0 - p_a \rangle = 0$. This is due to the fact that, in the limit of small amplitudes, the reduced conservation equations that describe airflow in the film are linear at leading order and driven by a harmonic boundary condition (3.1). The required first-order correction $\langle p_1 - p_a \rangle$ was determined using a process of conventional asymptotic matching: (i) the leading-order radial velocity component near the edge of the film $u_0(r \to a, y, t)$ was used as a boundary condition to drive the pulsating flow in the periphery, (ii) numerical simulation of the latter provided the condition $\langle p_1 \rangle(r \to a)$ needed to determine the steady first-order pressure distribution in the film $\langle p_1 \rangle(r)$ and (iii) substituting $\langle p_1 \rangle$ into equation (3.2) yielded the SSF with relative errors of order $\delta \sim \varepsilon \ll 1$.

Three principal governing parameters emerged in the reduced conservation equations:

$$\text{a Stokes number} \qquad \alpha^2 = \frac{h_o^2 \omega}{\mu_a/\rho_a} \sim 1\,, \tag{3.8}$$

$$\text{an acoustic wavenumber} \qquad \Lambda^{1/2} = \frac{a\omega}{\sqrt{p_a/\rho_a}} \sim 1 \tag{3.9}$$

$$\text{and a Strouhal number} \qquad St = \frac{\delta}{\varepsilon} \sim 1\,. \tag{3.10}$$

These nondimensional parameters represent ratios of the relevant fluidic timescales in the problem—those of viscous diffusion across the film $h_o^2/(\mu_a/\rho_a)$, pressure equilibration along the film $a/\sqrt{p_a/\rho_a}$ and flow residence in the periphery $h_o/(\varepsilon\omega a)$, respectively—to the period of driving oscillations $\sim \omega^{-1}$. Treating St as order unity is required to satisfy the selected distinguished limit $\delta \sim \varepsilon$, and doing the same for α and Λ ensures that fluid inertia and gaseous compressibility are rigorously taken into account.

We found that the steady levitation force can be expressed in the nondimensional form

$$\frac{\langle \mathcal{F}_L \rangle}{\varepsilon^2 \Lambda p_a \pi a^2} = \langle F_L \rangle = \langle F_i \rangle + A^2 \hat{P}_e\,, \tag{3.11}$$

involving two distinct contributions, each computed with small relative errors of order $\delta \sim \varepsilon \ll 1$,

$$\langle F_i \rangle(\alpha^2, \Lambda) = 2 \int_0^1 \frac{\langle p \rangle(r) - \langle p \rangle(a)}{\varepsilon^2 \Lambda p_a} \frac{r}{a} \mathrm{d}\left(\frac{r}{a}\right) \tag{3.12}$$

and

$$A^2(\alpha^2, \Lambda) \hat{P}_e(\alpha^2, \hat{St}) = \frac{\langle p \rangle(a) - p_a}{\varepsilon^2 \Lambda p_a}\,, \tag{3.13}$$

which account for variations of steady pressure along the film and across the periphery, respectively. In the expression for the latter, A is a dimensionless measure of the amplitude of the pulsating volume flux through the circumferential boundary $r = a$, and $\hat{P}_e$ is an appropriately normalized measure of the steady peripheral pressure drop that depends on a modified Strouhal number $\hat{St} = St/A$ and must be computed numerically. For rigid-body systems, $\langle F_i \rangle$ and $A^2 \hat{P}_e$ were found to be globally positive and negative, respectively, whence a transition to attractive forces $\langle F_L \rangle < 0$ required a sufficiently large peripheral pressure drop $A^2(-\hat{P}_e) > \langle F_i \rangle$ and occurred only for relatively low values of $\Lambda \propto (\omega a)^2$, consistent with the aforementioned experimental observations. (Further details of this formulation [60] can be found in Chapter 2.)

The results of this theory demonstrated reasonable agreement with prior CFD simulations [6], but its practical applicability is severely limited since common squeeze-film levitators are designed to oscillate at a natural frequency that corresponds to one of their flexural modes [7]. Such resonant operation enables greater amplitudes [13] but also causes noticeable elastic deformation, even for piston-type oscillators designed to bend minimally under stress [40]. Motivated by the results of our preliminary numerical simulation outlined in § 3.3, we will now extend this formulation to account for axisymmetric standing-wave deformations of an oscillator $S(r/a) \neq 1$. A detailed transcript of the modified derivation is provided below, and results are discussed later in § 3.5.

3.4.1 Foreword to the modified derivation

Prior to following the derivation below, the reader is strongly encouraged to peruse § 2.3 of this dissertation, where they can review further mathematical details of the matched-asymptotic formulation, including (i) the reduced conservation equations that govern each of the two distinct flow regions and (ii) corresponding characteristic scales of the local flow properties: velocity $[u,v]$ and deviations of the thermodynamic variables p,ρ,μ,κ and T (pressure, density, viscosity, thermal conductivity and temperature) from their respective ambient values $p_a,\rho_a,\mu_a,\kappa_a$ and T_a.

The following text mirrors sections 2.4–2.6 in describing the flow inside the slender squeeze film, in order to derive modified expressions for the dimensionless flux amplitude A and the inner contribution to the steady squeeze-film force $\langle F_i \rangle$. In the explored limit of small amplitudes, the numerical method for computing the dimensionless steady peripheral pressure drop $\hat{P}_e$, presented in § 2.7, requires no modification.

3.4.2 Parametrization of flexural oscillations

Consider the flexural axisymmetric squeeze-film system depicted in figure 3.1. A cylindrically symmetric object has a circular face of radius a that is separated from a nearby parallel wall by a distance $h \ll a$. The object undergoes time-harmonic oscillations along an axis perpendicular to the wall, deforming axisymmetrically such that the thickness of the air film separating the two, h, varies as given by the general expression

$$h(r,t) = h_o + \mathrm{Re}\left\{s(r)\mathrm{e}^{\mathrm{i}\omega t}\right\}, \tag{3.14}$$

where h_o is the mean film thickness and ω is the relevant angular frequency. It must be noted that the surface of the oscillator may experience radial displacement as well, which will be addressed shortly.

The appropriate nondimensional form of (3.14) is

$$H(\xi,\tau) = \frac{h}{h_o} = 1 + \varepsilon \mathrm{Re}\left\{S(\xi)\mathrm{e}^{\mathrm{i}\tau}\right\}, \quad \text{where} \quad \xi = \frac{r}{a}, \quad \tau = \omega t \quad \text{and} \quad S = \frac{s}{\varepsilon h_o} \sim 1, \qquad (3.15)$$

with εh_o specifying the local amplitude of oscillation at a radial location of interest (e.g. the location where the oscillations are driven).

If $S(\xi)$ is a real function, (3.15) reduces to $H(\xi,\tau) = 1 + \varepsilon S(\xi)\cos\tau$, describing standing-wave surface oscillations. If $S = 1$, (3.15) reduces to $H(\tau) = 1 + \varepsilon\cos\tau$ and the case of rigid-body oscillations is naturally recovered, with the result that each equation in the following development reduces to its counterpart in the original formulation presented in Chapter 2 [60].

3.4.3 Definition of the steady squeeze-film force

In modifying the original formulation to account for flexural oscillations, we will preserve the distinguished limit $\varepsilon \sim \delta \ll 1$, for which the relative amplitude ε and inverse aspect ratio $\delta = h_o/a$ are comparably small.

In order to ensure the applicability of slender-flow theory in the gaseous film, the characteristic wavelength λ associated with the surface waveform $s(r)$ is assumed to be comparable to the radius of the undeformed oscillator, i.e. $\lambda \sim a$. It then follows that $\lambda \gg h_o$, whence the characteristic transverse flow speed $v \sim \varepsilon\omega h_o$ is indeed asymptotically smaller by $O(\delta \sim \varepsilon)$ than its radial counterpart $u \sim u_c = \varepsilon\omega a$.

As the oscillator deforms, points on its surface experience radial displacements Δr whose magnitude depends on its structural characteristics, i.e. geometry, Young's modulus, etc. For the following analysis, we will assume that these time-harmonic, radial surface displacements are at most comparable to their transverse counterparts, i.e.

$$\Delta r \sim \varepsilon h_o \sim \varepsilon^2 a\,, \tag{3.16}$$

whence (i) temporal variations of the oscillator radius a and (ii) the radial component of the oscillator surface velocity $u \sim \Delta r/(\omega^{-1}) \sim \varepsilon u_c$ can be neglected in the following asymptotic analysis.

Thus, the expression for the repulsive steady squeeze-film force provided in (2.12) for a rigid oscillator, $\langle \mathcal{F}_L \rangle = \int_0^a \langle p(r) - p_a \rangle 2\pi r \, \mathrm{d}r$, can be readily applied here with small, relative errors of $O(\varepsilon \sim \delta \ll 1)$ [60].

3.4.4 Problem definition in the slender film

Based on the characteristic-scales analysis described in § 2.3, we begin by introducing the nondimensional variables $\tau = \omega t$, $\xi = r/a$, $Y = y/h_o$, $U = u/u_c$, $V = v/(\delta u_c)$, $P = (p - p_a)/(\varepsilon \Lambda p_a)$, $R = (\rho - \rho_a)/(\varepsilon \Lambda \rho_a)$ and $\Theta = (T - T_a)/(\varepsilon \Lambda T_a)$. The reduced Navier–Stokes equations that describe the flow in the slender film, given by (2.6)–(2.10), can then be expressed, with errors of $O(\delta^2 \sim \varepsilon^2)$, as

$$\Lambda \frac{\partial R}{\partial \tau} + \frac{1}{\xi}\frac{\partial}{\partial \xi}[(1 + \varepsilon \Lambda R)\xi U] + \frac{\partial}{\partial Y}[(1 + \varepsilon \Lambda R) V] = 0\,, \tag{3.17}$$

$$\frac{\partial P}{\partial Y} = 0\,, \tag{3.18}$$

$$(1 + \varepsilon \Lambda R)\left[\frac{\partial U}{\partial \tau} + \varepsilon \left(U \frac{\partial U}{\partial \xi} + V \frac{\partial U}{\partial Y}\right)\right] = -\frac{\partial P}{\partial \xi} + \frac{1}{\alpha^2}\frac{\partial}{\partial Y}\left[(1 + \varepsilon \Lambda \Theta)^{\nu} \frac{\partial U}{\partial Y}\right], \tag{3.19}$$

$$\begin{aligned}(1 + \varepsilon \Lambda R)\left[\frac{\partial \Theta}{\partial \tau} + \varepsilon \left(U \frac{\partial \Theta}{\partial \xi} + V \frac{\partial \Theta}{\partial Y}\right)\right] - \left(\frac{\gamma - 1}{\gamma}\right)\left(\frac{\partial P}{\partial \tau} + \varepsilon U \frac{\partial P}{\partial \xi}\right) = \\ \varepsilon \left(\frac{\gamma - 1}{\gamma}\right)\frac{(1 + \varepsilon \Lambda \Theta)^{\nu}}{\alpha^2}\left(\frac{\partial U}{\partial Y}\right)^2 + \frac{1}{Pr\,\alpha^2}\frac{\partial}{\partial Y}\left[(1 + \varepsilon \Lambda \Theta)^{\nu} \frac{\partial \Theta}{\partial Y}\right],\end{aligned} \tag{3.20}$$

$$P = R + \Theta + \varepsilon \Lambda R \Theta\,, \tag{3.21}$$

comprising continuity, momentum conservation in the transverse and radial directions, energy conservation and the ideal-gas equation of state. In addition to the small relative amplitude $\varepsilon \ll 1$, the problem above involves five parameters:

- the primary controlling parameters $\alpha^2 = h_o^2\omega/(\mu_a/\rho_a)$, the Stokes number that quantifies the relative importance of viscous diffusion, and $\Lambda = (a\omega)^2/(p_a/\rho_a)$, the squared acoustic wavenumber that quantifies the relative importance of gaseous compressibility,
- the relevant Prandtl number $Pr = c_p\mu_a/\kappa_a$, defined in terms of the specific heat at constant pressure c_p and the ambient viscosity μ_a and thermal conductivity κ_a,
- the ratio of specific heats $\gamma = c_p/c_v$, where c_v is the specific heat at constant volume
- and the coefficient ν, which describes the linearized variation of viscosity and thermal conductivity with small changes in temperature, i.e.

$$\frac{\mu}{\mu_a} = \frac{\kappa}{\kappa_a} = 1 + \varepsilon\nu\frac{T - T_a}{\varepsilon T_a} + O(\varepsilon^2), \tag{3.22}$$

  where ν depends on the chosen relation, such as a power law or Sutherland's law [91].

The values $Pr = 0.7$, $\gamma = 1.4$ and $\nu = 0.77$, suitable approximations for standard air [91, pp. 27,28], were used in generating the sample results shown later in § 3.5.

The system of equations (3.17)–(3.21) is subject to the non-slip, non-penetration and isothermal boundary conditions

$$\begin{cases} U = V = \Theta = 0 & \text{at} \quad Y = 0 \\ U - O(\varepsilon) = V - \mathrm{Re}\left\{S\mathrm{e}^{\mathrm{i}\tau}\right\} = \Theta = 0 & \text{at} \quad Y = H(\xi,\tau), \end{cases} \tag{3.23}$$

as well as the regularity condition at the central axis

$$U = \frac{\partial P}{\partial \xi} = \frac{\partial R}{\partial \xi} = \frac{\partial \Theta}{\partial \xi} = 0 \quad \text{at} \quad \xi = 0\,. \tag{3.24}$$

Note that the only modifications to the original formulation (2.16)–(2.21) are the new non-slip and non-penetration boundary conditions at the oscillator surface $[U,V]\big|_{Y=H}$.

Integrating the continuity equation (3.17) across the film and applying the well-known *Leibniz integral rule* gives, in place of (2.23),

$$\Lambda\frac{\partial}{\partial\tau}\left(\int_0^H R\,\mathrm{d}Y\right)+\frac{1}{\xi}\frac{\partial}{\partial\xi}\left[\xi\int_0^H(1+\varepsilon\Lambda R)U\,\mathrm{d}Y\right]+\mathrm{Re}\left\{S\mathrm{i}\mathrm{e}^{\mathrm{i}\tau}\right\}=0\,. \tag{3.25}$$

Integrating (3.25) in the radial direction and computing the time average yields, with errors of $O(\varepsilon^2)$,

$$\left\langle\int_0^H(1+\varepsilon\Lambda R)U\mathrm{d}Y\right\rangle=0, \tag{3.26}$$

which is formally identical to (2.24). To simplify further analytical development, we introduce the normalized transverse coordinate $\eta=Y/H(\xi,\tau)$, using the corresponding derivative transformations

$$\left[\frac{\partial}{\partial\xi},\frac{\partial}{\partial Y},\frac{\partial}{\partial\tau}\right]\to\left[\frac{\partial}{\partial\xi}-\varepsilon\eta\mathrm{Re}\left\{\frac{\mathrm{d}S}{\mathrm{d}\xi}\mathrm{e}^{\mathrm{i}\tau}\right\}\frac{\partial}{\partial\eta},\left(1-\varepsilon\mathrm{Re}\{S\mathrm{e}^{\mathrm{i}\tau}\}\right)\frac{\partial}{\partial\eta},\frac{\partial}{\partial\tau}-\varepsilon\eta\mathrm{Re}\{S\mathrm{i}\mathrm{e}^{\mathrm{i}\tau}\}\frac{\partial}{\partial\eta}\right], \tag{3.27}$$

in place of (2.26), each with errors of $O(\varepsilon^2)$. Temporal variations of the oscillator radius a due to elastic deformation need not be incorporated here as they are second-order corrections (see (3.16) and below).

The above problem is to be solved using perturbation methods, with the relative amplitude ε serving as the small parameter, in order to determine the time-averaged levitation force through the expression

$$\langle F_L\rangle=\frac{\langle\mathcal{F}_L\rangle}{\varepsilon^2\Lambda p_a\pi a^2}=\frac{2}{\varepsilon}\int_0^1\langle P\rangle\,\xi\mathrm{d}\xi\,, \tag{3.28}$$

the nondimensionalized form of (3.2). The fluid variables are expressed hereafter as regular perturbation expansions of the form

$$\begin{cases} U = U_0 + \varepsilon U_1 + \cdots, \quad V = V_0 + \varepsilon V_1 + \cdots, \\ P = P_0 + \varepsilon P_1 + \cdots, \quad R = R_0 + \varepsilon R_1 + \cdots, \quad \Theta = \Theta_0 + \varepsilon \Theta_1 + \cdots. \end{cases} \tag{3.29}$$

3.4.5 Leading-order solution in the slender film

Substituting (3.29) and the coordinate transformation (3.27) into the problem defined by (3.17)–(3.24) and collecting terms of order unity yields the leading-order linear system of equations

$$\Lambda \frac{\partial R_0}{\partial \tau} + \frac{1}{\xi}\frac{\partial}{\partial \xi}(\xi U_0) + \frac{\partial V_0}{\partial \eta} = 0, \tag{3.30}$$

$$\frac{\partial P_0}{\partial \eta} = 0, \tag{3.31}$$

$$\frac{\partial U_0}{\partial \tau} = -\frac{\partial P_0}{\partial \xi} + \frac{1}{\alpha^2}\frac{\partial^2 U_0}{\partial \eta^2}, \tag{3.32}$$

$$\frac{\partial \Theta_0}{\partial \tau} - \frac{\gamma - 1}{\gamma}\frac{\partial P_0}{\partial \tau} = \frac{1}{Pr\,\alpha^2}\frac{\partial^2 \Theta_0}{\partial \eta^2}, \tag{3.33}$$

$$P_0 = R_0 + \Theta_0, \tag{3.34}$$

subject to the boundary conditions

$$\begin{cases} U_0 = V_0 = \Theta_0 = 0 & \text{at} \quad \eta = 0 \\ U_0 = V_0 - \mathrm{Re}\left\{S\mathrm{i}e^{\mathrm{i}\tau}\right\} = \Theta_0 = 0 & \text{at} \quad \eta = 1 \\ U_0 = \dfrac{\partial P_0}{\partial \xi} = \dfrac{\partial R_0}{\partial \xi} = \dfrac{\partial \Theta_0}{\partial \xi} = 0 & \text{at} \quad \xi = 0 \\ P_0 = 0 & \text{at} \quad \xi = 1, \end{cases} \tag{3.35}$$

the last of which follows as a direct consequence of the fact that, in the limit $\delta \sim \varepsilon \ll 1$, pressure variations across the periphery are of $O(\varepsilon)$ smaller than those along the film, as discussed in section 2.3.

Following the method of *separation of variables* outlined below (2.32), the leading-order solution can be written as

$$\begin{cases} U_0 = \mathrm{Re}\left[\mathrm{i}\mathrm{e}^{\mathrm{i}\tau}\Pi'\mathcal{G}'_U(\eta)\right] \\ V_0 = \mathrm{Re}\left\{\mathrm{i}\mathrm{e}^{\mathrm{i}\tau}\left[S(\xi)\frac{\mathcal{G}_U(\eta)}{\mathcal{G}_U(1)} + \Lambda\Pi\left(C\mathcal{G}_U(\eta) + \frac{\gamma-1}{\gamma}\mathcal{G}_\Theta(\eta) - \eta\right)\right]\right\} \\ P_0 = \mathrm{Re}\left[\mathrm{e}^{\mathrm{i}\tau}\Pi(\xi)\right] \\ R_0 = \mathrm{Re}\left\{\mathrm{e}^{\mathrm{i}\tau}\Pi(\xi)\left[1 - \frac{\gamma-1}{\gamma}\mathcal{G}'_\Theta(\eta)\right]\right\} \\ \Theta_0 = \frac{\gamma-1}{\gamma}\mathrm{Re}\left[\mathrm{e}^{\mathrm{i}\tau}\Pi(\xi)\mathcal{G}'_\Theta(\eta)\right], \end{cases} \tag{3.36}$$

where the constant C in the expression for V_0, which replaces (2.42), is defined as

$$C = \frac{1 - \frac{\gamma-1}{\gamma}\mathcal{G}_\Theta(1)}{\mathcal{G}_U(1)}. \tag{3.37}$$

This solution contains two auxiliary transverse functions $\mathcal{G}_U(\eta) = \mathcal{G}(\beta_U;\eta)$ and $\mathcal{G}_\Theta(\eta) = \mathcal{G}(\beta_\Theta;\eta)$ and their derivatives, given respectively by the consolidated expressions

$$\mathcal{G}(\beta;\eta) = \eta - \frac{\sinh[\beta(2\eta-1)] + \sinh\beta}{2\beta\cosh\beta} \qquad \text{and} \qquad \mathcal{G}'(\beta;\eta) = 1 - \frac{\cosh[\beta(2\eta-1)]}{\cosh\beta}, \tag{3.38}$$

which involve reduced forms of the Stokes and Prandtl numbers

$$\beta_U = \frac{\alpha}{2}\frac{(1+\mathrm{i})}{\sqrt{2}} \qquad \text{and} \qquad \beta_\Theta = \sqrt{Pr}\frac{\alpha}{2}\frac{(1+\mathrm{i})}{\sqrt{2}}, \tag{3.39}$$

just as outlined below (2.35). The most important modification to the original solution concerns the auxiliary function $\Pi(\xi)$, which carries the radial dependence of the leading-order flow properties, and is now a solution to the forced Bessel equation

$$\frac{1}{\xi}\frac{\mathrm{d}}{\mathrm{d}\xi}\left(\xi\frac{\mathrm{d}\Pi}{\mathrm{d}\xi}\right)+\frac{1-\frac{\gamma-1}{\gamma}\mathcal{G}_{\Theta}(1)}{\mathcal{G}_{U}(1)}\Lambda\Pi=-\frac{S(\xi)}{\mathcal{G}_{U}(1)}, \tag{3.40}$$

in place of (2.39). Upon imposing the regularity condition at the axis $\Pi'(0)=0$ and the relaxation condition at the edge $\Pi(1)=0$, this differential equation can be solved using the method of *variation of parameters* [92, p. 15], in conjunction with *Abel's identity* for simplifying the associated Wronskian [92, pp. 8,9], to yield closed-form expressions for the reduced pressure

$$\begin{aligned}\Pi=\frac{\pi}{2\mathcal{G}_{U}(1)}\Bigg\{&J_0(\xi\sqrt{C\Lambda})\left[\frac{Y_0(\sqrt{C\Lambda})}{J_0(\sqrt{C\Lambda})}\int_0^1 xS(x)J_0(x\sqrt{C\Lambda})\mathrm{d}x-\int_\xi^1 xS(x)Y_0(x\sqrt{C\Lambda})\mathrm{d}x\right]\\&-Y_0(\xi\sqrt{C\Lambda})\int_0^\xi xS(x)J_0(x\sqrt{C\Lambda})\mathrm{d}x\Bigg\}\end{aligned} \tag{3.41}$$

and its radial derivative

$$\begin{aligned}\Pi'=\frac{\pi\sqrt{C\Lambda}}{2\mathcal{G}_{U}(1)}\Bigg\{&J_1(\xi\sqrt{C\Lambda})\left[-\frac{Y_0(\sqrt{C\Lambda})}{J_0(\sqrt{C\Lambda})}\int_0^1 xS(x)J_0(x\sqrt{C\Lambda})\mathrm{d}x+\int_\xi^1 xS(x)Y_0(x\sqrt{C\Lambda})\mathrm{d}x\right]\\&+Y_1(\xi\sqrt{C\Lambda})\int_0^\xi xS(x)J_0(x\sqrt{C\Lambda})\mathrm{d}x\Bigg\},\end{aligned} \tag{3.42}$$

where J_i and Y_i refer respectively to the Bessel functions of the first and second kinds, of order i. It can be shown that (3.41) and (3.42) reduce to the forms given in (2.40) when $S=1$. Finally, the edge value of the reduced pressure gradient is given by

$$\Pi'(1)=-\frac{\int_0^1 xS(x)J_0(x\sqrt{C\Lambda})\mathrm{d}x}{\mathcal{G}_{U}(1)J_0(\sqrt{C\Lambda})}, \tag{3.43}$$

in place of (2.44).

Note that the integrals present in (3.41)–(3.43) can be solved explicitly for certain types of waveforms $S(\xi)$. Namely, for resonant solutions of the Kirchhoff–Love thin-plate bending equation (3.4), S involves Bessel functions of its own, allowing analytical integration with use of known identities [85].

Since the leading-order pressure varies harmonically with time, it yields no time average (i.e. $\langle P_0 \rangle = 0$), and determining the steady levitation force (3.28) thus requires computing first-order corrections.

3.4.6 Undisturbed solution process in the non-slender periphery

The flow in the peripheral region, which extends for distances of $O(h_o)$ from the edge of the film $r = a$, is driven at leading order by the radial component of the pulsating edge velocity

$$U_0(\xi = 1, \eta, \tau) = \mathrm{Re}\left[\mathrm{i}e^{\mathrm{i}\tau}\Pi'(1)\mathcal{G}'_U(\eta)\right] = A\mathrm{Re}\left[\mathrm{i}e^{\mathrm{i}(\tau+\varphi)}\mathcal{G}'_U(\eta)\right], \tag{3.44}$$

written in terms of the phase shift $\varphi = \arg[\Pi'(1)]$ and the amplitude $A = |\Pi'(1)|$ of the oscillating edge pressure gradient given in (3.43). Note that A characterizes the volume flux of radial airflow due to disk oscillations.

The corresponding transverse component $V_0(\xi = 1)$ and the axial displacements of the oscillator both enter as boundary conditions only at the following order, since the transverse flow velocities in the non-slender periphery are of $O(\delta^{-1} \sim \varepsilon^{-1})$ larger than those in the film (see § 2.3). Radial deformations of the oscillator $u(y = h) \sim \varepsilon u_c$ are similarly negligible at leading order since they are of $O(\varepsilon)$ smaller than the radial velocities in the periphery $\sim u_c$ (see below (3.16) for clarification).

Dependence on the waveform $S(\xi)$ and the compressibility parameter Λ can be factored out of the peripheral-flow problem by means of a convenient nondimensionalization of the local flow variables,

$$\hat{P}(X, Y, \hat{\tau}) = \frac{p - p_a}{\varepsilon^2 \Lambda p_a A^2} \qquad \text{and} \qquad \hat{U}(X, Y, \hat{\tau}) = \frac{u}{A u_c}, \tag{3.45}$$

which are expressed in terms of the local coordinates $\hat{\tau} = \tau + \varphi$ and $(X, Y) = (r - a, y)/h_o$, as well as the local Strouhal number $\hat{St} = St/A = \delta/(\varepsilon A) \sim 1$. In that case, the only information needed here from the leading-order solution in the film is the transverse variation $\mathcal{G}_U'(\eta)$ of the driving velocity (3.44), which enters through the appropriate matching condition

$$\lim_{X\to-\infty} \hat{U} = \mathrm{Re}\left[\mathrm{i}e^{\mathrm{i}\hat{\tau}}\mathcal{G}_U'(Y)\right]. \tag{3.46}$$

As described in § 2.7, effects of gaseous compressibility and geometrical curvature do not enter at leading order in the equations governing peripheral flow, (2.77) and (2.78). However, viscous shear and local and convective acceleration are present, requiring numerical solution using conventional finite-element methods. Since the equations are nonlinear, the local pressure distribution exhibits a nonzero time-averaged component $\langle\hat{P}\rangle(X,Y)$, which approaches a limiting value at the matching boundary

$$\lim_{X\to-\infty}\langle\hat{P}\rangle = \hat{P}_e = \frac{\langle P_1\rangle(\xi=1)}{A^2}, \tag{3.47}$$

which will serve as a boundary condition for the first-order problem in the slender film (see § 2.7.3 for clarification).

Since the reduced boundary conditions considered here are identical to those developed in the rigid-body formulation (see § 2.7.1), the numerical solution for $\hat{P}_e(\alpha^2,\hat{St})$ that is detailed in § 2.7.2 needs no modification when $S \neq 1$.

3.4.7 First-order corrections in the slender film

Collecting terms of order ε in the integrated time-averaged continuity equation (3.26) gives

$$\int_0^1 \langle U_1\rangle\,\mathrm{d}\eta = -\int_0^1 \left\langle \mathrm{Re}\left\{Se^{\mathrm{i}\tau}\right\} U_0\right\rangle \mathrm{d}\eta - \Lambda\int_0^1 \langle R_0U_0\rangle\,\mathrm{d}\eta, \tag{3.48}$$

in place of (2.46). Doing the same for the momentum equations (3.18) and (3.19) and computing the time average provides

$$\frac{\partial\langle P_1\rangle}{\partial\eta}=0 \qquad \text{and} \qquad -\frac{\mathrm{d}\langle P_1\rangle}{\mathrm{d}\xi}+\frac{1}{\alpha^2}\frac{\partial^2\langle U_1\rangle}{\partial\eta^2}=f(\xi,\eta), \tag{3.49}$$

the latter of which is formally identical to (2.47). The known function f is now defined as

$$\begin{aligned} f=\Bigg\langle &\Lambda R_0\frac{\partial U_0}{\partial\tau}+U_0\frac{\partial U_0}{\partial\xi}+V_0\frac{\partial U_0}{\partial\eta}-\eta\mathrm{Re}\left\{S\mathrm{i}e^{\mathrm{i}\tau}\right\}\frac{\partial U_0}{\partial\eta} \\ &+\frac{1}{\alpha^2}\frac{\partial}{\partial\eta}\left[\left(2\mathrm{Re}\left\{Se^{\mathrm{i}\tau}\right\}-\nu\Lambda\Theta_0\right)\frac{\partial U_0}{\partial\eta}\right]\Bigg\rangle \end{aligned} \tag{3.50}$$

$$\begin{aligned} &=\frac{1}{\xi}\frac{\partial}{\partial\xi}\left(\xi\left\langle U_0^2\right\rangle\right)+\frac{\partial}{\partial\eta}\langle U_0V_0\rangle-\eta\left\langle\mathrm{Re}\left\{S\mathrm{i}e^{\mathrm{i}\tau}\right\}\frac{\partial U_0}{\partial\eta}\right\rangle \\ &\quad+\frac{2}{\alpha^2}\left\langle\mathrm{Re}\left\{Se^{\mathrm{i}\tau}\right\}\frac{\partial^2U_0}{\partial\eta^2}\right\rangle-\frac{\nu\Lambda}{\alpha^2}\frac{\partial}{\partial\eta}\left\langle\Theta_0\frac{\partial U_0}{\partial\eta}\right\rangle, \end{aligned} \tag{3.51}$$

expressed in nonconservative and conservative forms, respectively, in place of (2.48) and (2.49). Note that the waveform $S(\xi)$ now appears in the definition of f due to the modified coordinate transformations (3.27).

Integrating the radial momentum equation (3.49) thrice in the transverse direction, and combining the result with (3.48) to eliminate the steady flux $\int_0^1\langle U_1\rangle\,\mathrm{d}\eta$, yields the time-averaged pressure gradient inside the squeeze film

$$\frac{\mathrm{d}\langle P_1\rangle}{\mathrm{d}\xi}=\frac{12}{\alpha^2}\left[\int_0^1\left\langle\mathrm{Re}\left\{Se^{\mathrm{i}\tau}\right\}U_0\right\rangle\mathrm{d}\eta+\Lambda\int_0^1\langle R_0U_0\rangle\,\mathrm{d}\eta\right]-6\int_0^1\eta(1-\eta)f\,\mathrm{d}\eta, \tag{3.52}$$

in place of (2.52). Note that the boundary conditions $\langle U_1\rangle=0$ at $\eta=0,1$ were used for the transverse integration, since, although the radial surface speed $U(Y=H)\sim\varepsilon$ may, in principle, enter at this order, it varies harmonically with time and therefore yields *no time average*.

3.4.8 Time-averaged levitation force

Integrating (3.52) in the radial direction yields the steady pressure distribution

$$\langle P_1\rangle(\xi) = \langle P_1\rangle(1) - \int_\xi^1 \langle P_1\rangle'(x)\,\mathrm{d}x\,, \tag{3.53}$$

where $\langle P_1\rangle' = \mathrm{d}\langle P_1\rangle/\mathrm{d}\xi$. Integrating (3.53) with use of (3.28) gives the steady repulsive force

$$\langle F_L\rangle = 2\int_0^1 \langle P_1\rangle(x)\,x\mathrm{d}x\,. \tag{3.54}$$

As described below (2.56), it is useful to split the expression of the steady force into two distinct terms, in the form

$$\begin{gathered}\langle F_L\rangle = \langle F_i\rangle + \langle F_e\rangle, \quad \text{where} \\ \langle F_i\rangle = 2\int_0^1 [\langle P_1\rangle(x) - \langle P_1\rangle(1)]\,x\mathrm{d}x \quad \text{and} \quad \langle F_e\rangle = \langle P_1\rangle(1)\end{gathered} \tag{3.55}$$

represent, respectively, the value of the force devoid of peripheral flow effects and the steady pressure drop across the periphery. By design of this matched-asymptotic formulation, both the steady pressure distribution and the levitation force can be determined *in integral form* up to the constant

$$\langle P_1\rangle(1) = A^2\hat{P}_e\,, \tag{3.56}$$

where the flux amplitude $A(\alpha^2,\Lambda) = |\Pi'(1)|$, defined below (3.44), can be found using the integral expression in (3.43). The normalized steady peripheral pressure drop $\hat{P}_e(\alpha^2,\hat{St} = St/A)$ is thus the only quantity that must, in general, be found using a time-dependent numerical simulation, as explained in § 3.4.6. Note that the computation of $\hat{P}_e$ can be simplified using asymptotic reduction for limiting values of α^2 and $\hat{St}$, as outlined in § 2.7.4 – § 2.7.6.

Substituting the leading-order solution (3.36) into the expression for the steady pressure gradient (3.52) and integrating the result using equations (3.53) and (3.54) yields

$$\begin{aligned}\langle P_1\rangle(\xi)-\langle P_1\rangle(1) = 3\mathrm{Re}\bigg\{ &-\frac{2\mathrm{i}}{\alpha^2}\left(X_1^*+\Lambda X_2\right)\mathcal{H}_1+\frac{\mathrm{i}(\gamma-1)\Lambda}{\gamma\alpha^2}X_2(2\mathcal{H}_2+\nu\mathcal{H}_3)+X_3\mathcal{H}_4\\ &+\left[\frac{X_1^*}{\mathcal{G}_U(1)}+C\Lambda X_2\right]\mathcal{H}_5+\Lambda X_2\left(\frac{\gamma-1}{\gamma}\mathcal{H}_6-\mathcal{H}_7\right)-X_1\mathcal{H}_8\bigg\}\end{aligned} \tag{3.57}$$

and

$$\begin{aligned}\langle F_i\rangle = 3\mathrm{Re}\bigg\{ &-\frac{2\mathrm{i}}{\alpha^2}\left(\mathcal{X}_1^*+\Lambda\mathcal{X}_2\right)\mathcal{H}_1+\frac{\mathrm{i}(\gamma-1)\Lambda}{\gamma\alpha^2}\mathcal{X}_2(2\mathcal{H}_2+\nu\mathcal{H}_3)+\mathcal{X}_3\mathcal{H}_4\\ &+\left[\frac{\mathcal{X}_1^*}{\mathcal{G}_U(1)}+C\Lambda\mathcal{X}_2\right]\mathcal{H}_5+\Lambda\mathcal{X}_2\left(\frac{\gamma-1}{\gamma}\mathcal{H}_6-\mathcal{H}_7\right)-\mathcal{X}_1\mathcal{H}_8\bigg\},\end{aligned} \tag{3.58}$$

in place of (2.55) and (2.59), respectively, where a term superscripted with an asterisk is the conjugate of a complex quantity. The radial integrals involved in the above expressions are defined as

$$X_i = -\int_\xi^1 g_i(\xi)\mathrm{d}\xi \qquad \text{and} \qquad \mathcal{X}_i = 2\int_0^1 X_i\xi\mathrm{d}\xi = -\int_0^1 g_i(\xi)\xi^2\mathrm{d}\xi\,, \tag{3.59}$$

for $i = 1$–3, where

$$g_1 = S^*\Pi', \quad g_2 = \Pi\Pi'^* \qquad \text{and} \qquad g_3 = \frac{1}{\xi}\frac{\mathrm{d}}{\mathrm{d}\xi}(\xi\Pi'\Pi'^*), \tag{3.60}$$

in place of (2.118)–(2.123). The axial integrals $\mathcal{H}_i$ ($i = 1$–8) remain as defined in (2.124)–(2.131).

3.4.9 The Stokes limit: $\alpha^2 \to 0$ with $\Lambda \sim \alpha^2$

Since effects of fluid acceleration are absent in the limit of small Stokes numbers $\alpha^2 \ll 1$, the onset of time-averaged overpressure in the film will be seen to stem from (i) effects of fluid compressibility and (ii) interactions between the radial fluid velocity component and the dynamic flexure of the oscillator $H(\xi,\tau)$. We begin by introducing the appropriately rescaled variables $[\tilde{P},\tilde{R},\tilde{\Theta}] = \alpha^2[P,R,\Theta]$ to account for the dominant balance between the pressure gradient and the viscous diffusion term in the momentum equation (3.19). The energy, state and momentum equations respectively yield

$$\tilde{\Theta} = 0\,, \qquad \tilde{P} = \tilde{R} \qquad \text{and} \qquad U = \frac{\partial \tilde{P}}{\partial \xi}\frac{Y}{2}(Y - H)\,. \tag{3.61}$$

When the continuity equation (3.17) is then integrated across the film, we obtain, in place of (2.66),

$$\sigma \frac{\partial (H\tilde{P})}{\partial \tau} - \frac{1}{\xi}\frac{\partial}{\partial \xi}\left[\xi H^3 \frac{\partial \tilde{P}}{\partial \xi}\left(1 + \varepsilon \frac{\sigma}{12}\tilde{P}\right)\right] + 12\mathrm{Re}\left\{S\mathrm{i}\mathrm{e}^{\mathrm{i}\tau}\right\} = 0\,, \tag{3.62}$$

a reduced form of the Reynolds equation that features a single fluidic parameter, the squeeze number $\sigma = 12\Lambda/\alpha^2$ defined in (2.67). This partial differential equation was first solved in 1957 using perturbation methods by Taylor and Saffman for the case of rigid-body oscillations $S = 1$ [5]. In an appendix of the cited paper, the steady radial pressure distributions for certain linear piecewise oscillation modes ($S = 1 - \xi$, $S = 1 - 2\xi$ and $S = \xi$) are described for limiting values of σ. Presented below is a perturbative solution for arbitrary oscillation modes, valid for $\sigma \sim 1$.

Upon introducing the expansion $\tilde{P} = \tilde{P}_0 + \varepsilon \tilde{P}_1 + \cdots$, the above Reynolds equation (3.62) reduces at leading order to the Bessel equation

$$\tilde{\Pi}'' + \frac{\tilde{\Pi}'}{\xi} + \frac{\sigma}{\mathrm{i}}\tilde{\Pi} = 12\mathrm{i}S(\xi)\,, \quad \text{subject to} \quad \tilde{\Pi}'(\xi = 0) = \tilde{\Pi}(\xi = 1) = 0\,, \tag{3.63}$$

for the reduced pressure $\tilde{\Pi}$, which carries the radial dependence of $\tilde{P}_0 = \mathrm{Re}\{\tilde{\Pi}(\xi)\mathrm{e}^{\mathrm{i}\tau}\}$. Due to its similarity with the Bessel equation (3.40) derived in the full viscoacoustic problem above, the solution to this equation can be obtained by inspection, giving

$$\begin{aligned}\tilde{\Pi} = 6\mathrm{i}\pi \Bigg\{ & Y_0(\beta_\sigma^* \xi)\int_0^\xi x S(x) J_0(\beta_\sigma^* x)\mathrm{d}x \\ & + J_0(\beta_\sigma^* \xi)\left[\int_\xi^1 x S(x) Y_0(\beta_\sigma^* x)\mathrm{d}x - \frac{Y_0(\beta_\sigma^*)}{J_0(\beta_\sigma^*)}\int_0^1 x S(x) J_0(\beta_\sigma^* x)\mathrm{d}x\right]\Bigg\}\end{aligned} \tag{3.64}$$

and

$$\tilde{\Pi}' = -6\mathrm{i}\pi\beta_\sigma^* \Bigg\{ Y_1(\beta_\sigma^*\xi) \int_0^\xi x S(x) J_0(\beta_\sigma^* x) \mathrm{d}x + J_1(\beta_\sigma^*\xi) \left[\int_\xi^1 x S(x) Y_0(\beta_\sigma^* x) \mathrm{d}x - \frac{Y_0(\beta_\sigma^*)}{J_0(\beta_\sigma^*)} \int_0^1 x S(x) J_0(\beta_\sigma^* x) \mathrm{d}x \right] \Bigg\}, \qquad (3.65)$$

where $\beta_\sigma = (1+\mathrm{i})\sqrt{\sigma/2}$, as defined in (2.68). The rescaled flux amplitude is then given by

$$\alpha^2 \lim_{\alpha^2 \to 0} A = |\tilde{\Pi}'(1)| = \left| \frac{12 \int_0^1 x S(x) J_0(\beta_\sigma^* x) \mathrm{d}x}{J_0(\beta_\sigma^*)} \right| = g_A(\Lambda/\alpha^2). \qquad (3.66)$$

Collecting terms of order ε in (3.62), we obtain, following straight-forward manipulation, the rescaled steady pressure gradient,

$$\frac{\mathrm{d}\langle \tilde{P}_1 \rangle}{\mathrm{d}\xi} = -\left\langle \frac{\partial \tilde{P}_0}{\partial \xi} \left(3\mathrm{Re}\left\{ S \mathrm{e}^{\mathrm{i}\tau} \right\} + \frac{\sigma}{12}\tilde{P}_0 \right) \right\rangle, \qquad (3.67)$$

whence the rescaled inner contribution to the levitation force,

$$\alpha^2 \lim_{\alpha^2 \to 0} \langle F_i \rangle = -\frac{1}{2}\mathrm{Re}\left\{ 3\tilde{\mathcal{X}}_1 + \frac{\sigma}{12}\tilde{\mathcal{X}}_2 \right\} = g_F(\Lambda/\alpha^2), \qquad (3.68)$$

can be computed using the two integrals

$$\tilde{\mathcal{X}}_1 = -\int_0^1 \xi^2 S^* \tilde{\Pi}' \mathrm{d}\xi \qquad \text{and} \qquad \tilde{\mathcal{X}}_2 = -\int_0^1 \xi^2 \tilde{\Pi} \tilde{\Pi}'^* \mathrm{d}\xi. \qquad (3.69)$$

As demonstrated in § 2.7.4, the normalized steady peripheral pressure drop simplifies in this viscous limit to the expression $\hat{P}_e \to \mathcal{P}\alpha^4$, where the constant $\mathcal{P} \approx -0.0027$ is independent of the modified Strouhal number $\hat{St}$ defined below (3.45), and weakly dependent on the peripheral geometry. The net levitation force in the classical Stokes limit $\alpha^2 \to 0$ can thus be expressed,

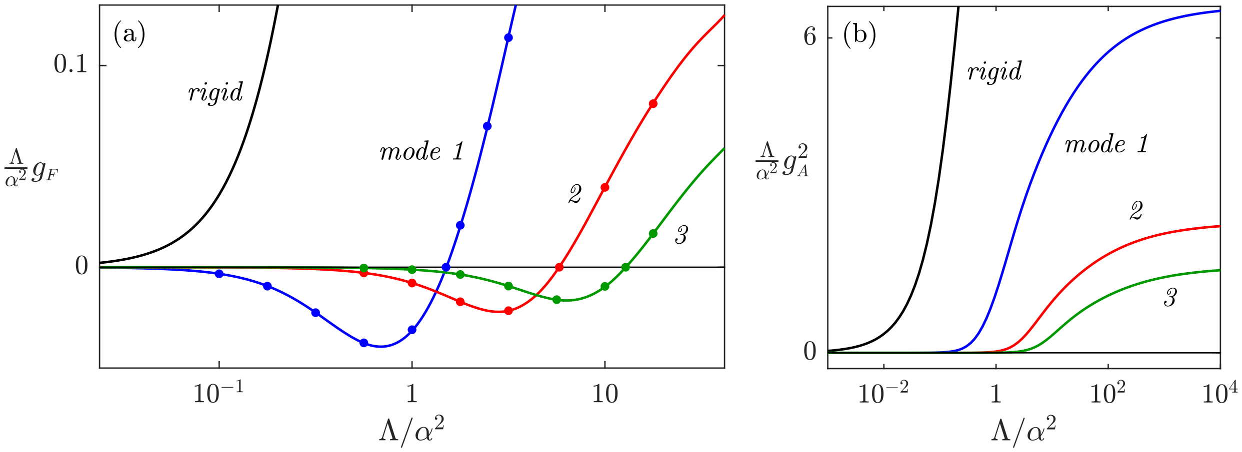

Figure 3.3. Variation with $\Lambda/\alpha^2 = \sigma/12$ of rescaled forms of (a) the inner contribution to the force (3.68), confirmed with finite-difference solutions of the Reynolds equation for $\varepsilon = 0.1$ (dots), and (b) the flux amplitude (3.66), in the Stokes limit $\alpha^2 \to 0$.

with small, relative errors of $O(\varepsilon \sim \delta \ll 1)$ and $O(\alpha^2 \ll 1)$, as

$$\frac{\langle \mathcal{F}_L \rangle}{\varepsilon^2 p_a \pi a^2} = \Lambda \langle F_L \rangle \to \frac{\Lambda}{\alpha^2} g_F \, . \tag{3.70}$$

The variation with $\Lambda/\alpha^2 = \sigma/12$ of the quantities $(\Lambda/\alpha^2)g_F$ and $(\Lambda/\alpha^2)g_A^2$ is depicted in figure 3.3, for rigid-body systems and also for the resonant flexural systems depicted in figures 3.1(c)–(e). Curves in panel (a) demonstrate that, when operating at a fixed small value of α^2, the greatest repulsive forces occur for relatively large values of Λ, whereas the transition to attractive forces occurs for relatively small values. Panel (b) demonstrates that the volume-flux amplitude of resonant flexural systems is smaller than that of rigid-body systems operating under identical conditions, progressively so for increasing values of the structural (elastic) wavenumber. As a result, one may anticipate that the role of the peripheral pressure drop in reducing the repulsive SSF—and eventually giving rise to attraction—is reduced substantially in flexural SFL systems. To confirm this conjecture, however, it is imperative to explore the results of the full viscoacoustic problem for which the Stokes number α^2 and the compressibility parameter Λ are of order unity.

3.5 Discussion of results

Asymptotic predictions of the dimensional levitation force $\langle \mathcal{F}_L \rangle$ (3.2), obtained using the viscoacoustic formulation derived above, are exemplified in figure 3.2. As shown in panels 3.2(b) and (c), reasonable agreement is obtained with finite-difference solutions of the Reynolds equation for moderately small values of the Stokes number, $\alpha^2 \lesssim 2.75$. (Note that accuracy deteriorates as the mean thickness h_o approaches the amplitude $\varepsilon h_o = 10\,\mu$m, since the perturbation parameter ε, a measure of the relative asymptotic error, grows in magnitude.) It is clear when comparing the curves in panels 3.2(a)–(c) that the attractive squeeze-film load capacity provided by a rigid-body oscillator is hundreds of times lower than that enabled by an oscillator undergoing resonant elastic deformations as defined by Kirchoff–Love theory, operating under otherwise identical conditions—most importantly, with the same central oscillation amplitude $S(0) = 1$ (3.1). For instance, at a frequency of 400 Hz, a rigid oscillator of radius 7 cm is capable of levitating approximately 1 gram by attraction, while a disk of equal radius (with $\nu_d = 0.3$) operating at its first or second resonant bending mode can levitate around 250 or 525 grams, respectively. It must be noted in this connection that, in order to produce a standing wave with a higher resonant wavenumber K at the same frequency ω, the flexural rigidity of the disk must be reduced carefully such that the resonance relation (3.6) remains satisfied. Estimates of $\langle \mathcal{F}_L \rangle$ for a wider range of ω (omitted from the figure to preserve clarity) reveal that the greatest load that can be attracted by a given oscillator, $\max[\langle -\mathcal{F}_L \rangle (h_o)]$ for $h_o > b$, varies non-monotonically with the frequency, reaching an extremum for a critical value of ω. It is important to note here that the enhanced attractive forces provided by standing-wave oscillation are accompanied by a drastic reduction of the repulsive load-bearing capacity, which can be seen by extrapolating the curves in figure 3.2(a) to small separation distances $\approx 20\,\mu$m and comparing with the curves in panels (b) and (c).

It is worth comparing this result with that of Da Silva [10], who found instead that flexural oscillation near resonance increases the repulsive load capacity. The disparity is readily explained by considering the fact that Da Silva utilized a bulky piezoelectric transducer to excite the oscillating plate, whence the optimal resonant frequencies of the assembly did not coincide with the native natural frequencies of the plate itself. The deforming oscillator thus exhibited large local amplitudes near its outer edge relative to the driving amplitude near its center, unlike the native resonant waveforms considered here, those depicted in figures 3.1(c)–(e). Note that Da Silva found good agreement between the measured waveforms and those predicted by Kirchhoff–Love theory for the non-native resonant frequencies utilized. This augmentation of the repulsive squeeze-film force due to wide flapping of the outer edge was also found in other studies that involved bulky external vibration sources, such as [93]. Realization of the native waveforms that afford an accentuated attractive load capacity requires the use of a vibration source that alters minimally the optimal frequencies of the oscillating assembly. The recent experiment by [3], which inspired the present investigation, seems to have involved such a configuration; a disk made of polyester plastic [94] was excited by a haptic feedback motor with mass $\lesssim 2$ g [95].

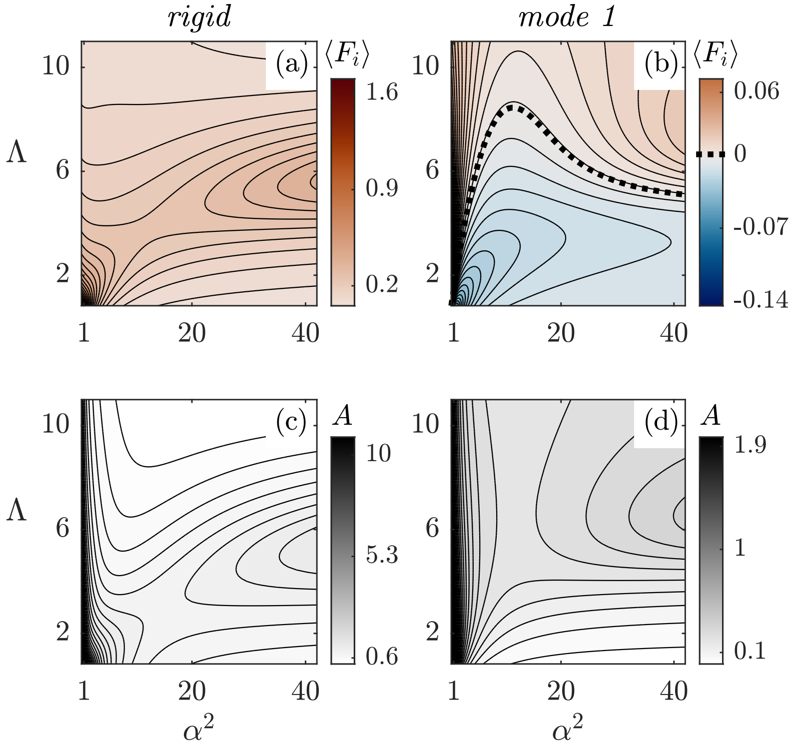

Figure 3.4. Variation with the Stokes number α^2 and the acoustic wavenumber Λ of (a,b) the dimensionless inner contribution to the levitation force $\langle F_i \rangle$ and (c,d) the flux amplitude A, both discussed below equation (3.11), for (a,c) rigid-body and (b,d) mode-1 flexural oscillations.

While the transition to attractive forces for rigid-body systems is known to depend heavily on the peripheral pressure drop [4, 6, 60], as discussed below (3.13), the results of our modified asymptotic formulation suggest that the transition for flexural systems occurs primarily due to nonlinear flow dynamics inside the slender film. As seen from figures 3.4(c) and (d), the amplitude A of the volume rate of airflow through the film edge, whose square serves as a weightage factor for the peripheral pressure drop $A^2\hat{P}_e$, generally exhibits lower values for a

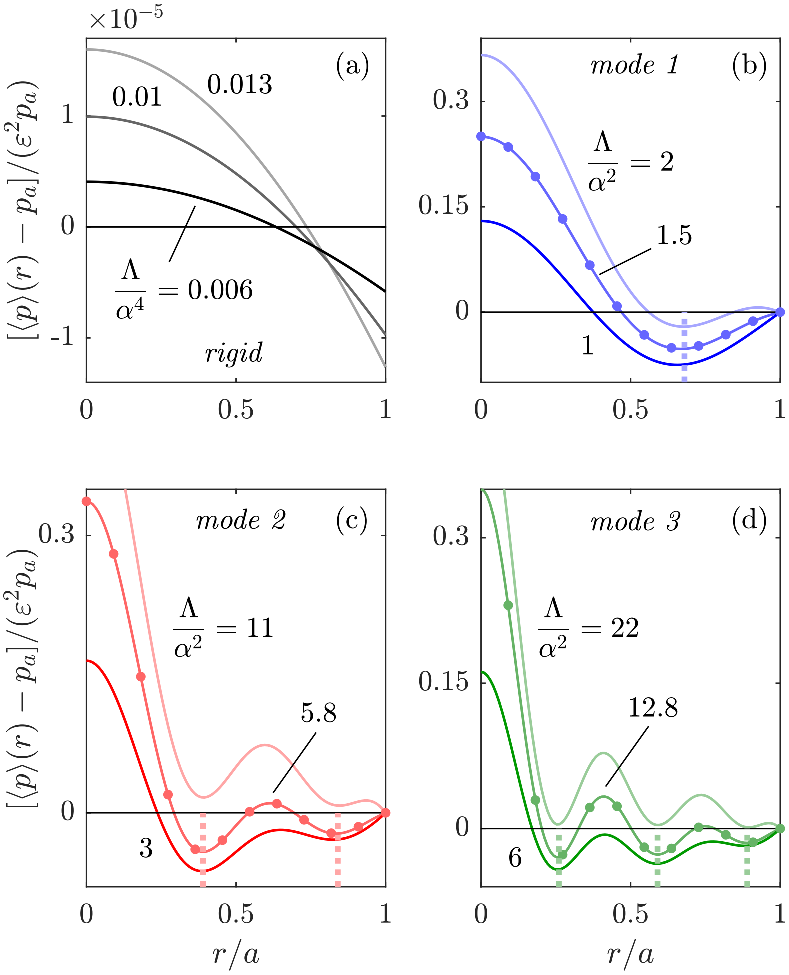

Figure 3.5. Profiles of steady pressure in the squeeze film for $\alpha^2 = 0.1$ (with small relative errors of order $\varepsilon \sim \delta \ll 1$) for (a) rigid-body and (b)–(d) resonant flexural oscillations. Dotted lines mark the nodal locations of the associated standing waves. The middle curve in each panel, confirmed in (b)–(d) with finite-difference solutions of the Reynolds equation for $\varepsilon = 0.1$ (large dots), corresponds to $\langle F_L \rangle = 0$, and the curves above and below represent states of repulsion and attraction, respectively.

flexural oscillator at any given operating condition defined by the Stokes number α^2 and the acoustic wavenumber $\Lambda^{1/2}$. This is consistent with the intuitive notion that, while the airflow excited by a rigid oscillator can be expected to exhibit substantial discharge and entrainment through the film edge, the precise flow rate being dependent on the degree of compressibility Λ, the flow induced by flexural oscillations of the type pictured in figures 3.1(c)–(e) would feature much less edge flux and, instead, predominantly oscillate along the film about the nodal regions. As seen in figures 3.4(a) and (b), the inner contribution to the time-averaged levitation force $\langle F_i \rangle$, globally positive when $S = 1$, exhibits negative values when $S = S_{KL}$ (3.4) in a substantial region of the α^2–Λ parametric domain, that being a secondary consequence of the nonlinear dynamics—i.e. the time-asymmetrical nature—of this oscillatory airflow.

This distinction in the cause of attractive forces can be investigated in greater detail by examining the distribution of time-averaged overpressure along the film, exemplified in figure 3.5. The curve in each panel with the highest value at the axis $r = 0$ corresponds to a positive SSF (steady squeeze-film force), the one with the lowest corresponds to a negative SSF and the middle curve is computed at the critical condition where $\langle F_L \rangle = 0$. The transition to attraction for the rigid oscillator occurs as a result of an increase in the magnitude of the peripheral pressure drop $p_a - \langle p \rangle(a)$ relative to the central overpressure $\langle p \rangle(0) - p_a$. However, that for resonant flexural systems is seen to correlate to a surge in local minima of film pressure, whose radial locations seem to coincide with those of the nodal regions of the deforming oscillator (for the small Stokes number $\alpha^2 = 0.1$ considered in the figure).

As a consequence of this distinction, the parametric region of attraction ($\langle F_L \rangle < 0$) is observed to be significantly larger for flexural systems than for rigid-body systems, as illustrated in figure 3.6. For each resonant flexural mode, this region lies below a separating contour that displays a linear limiting behavior for small values of the Stokes number. The slope of this line, $(\Lambda/\alpha^2)_c$, is seen to grow for increasing values of the wavenumber K. As shown in § 3.4.9, in the corresponding Stokes limit $\Lambda \sim \alpha^2 \to 0$, the expressions needed to compute the nondimensional

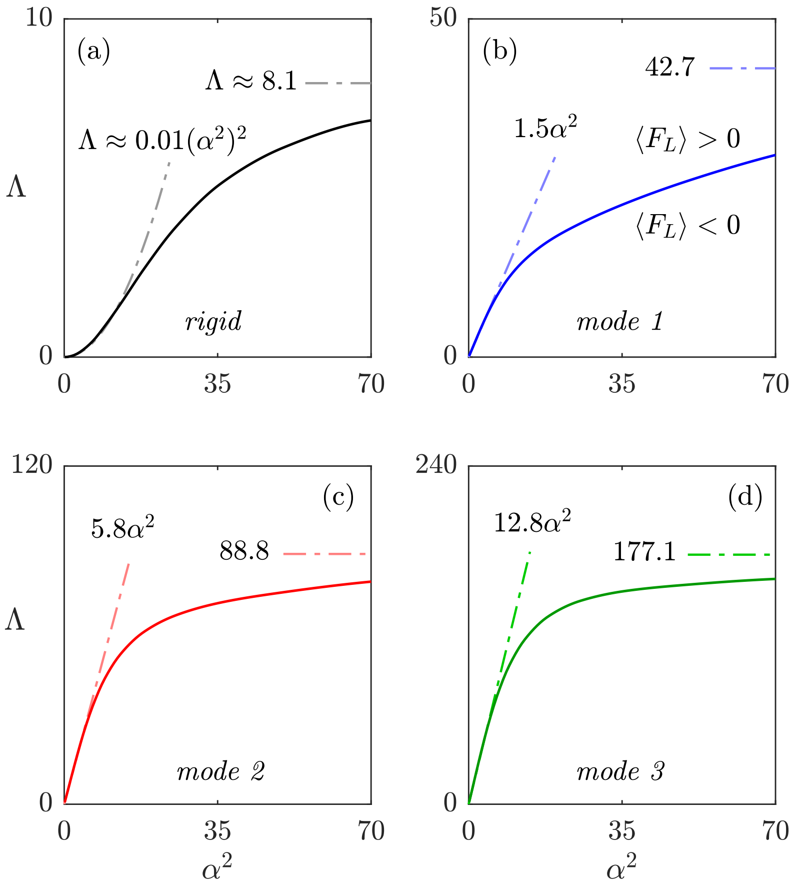

Figure 3.6. Principal contours in the α^2–Λ parametric plane (for $\hat{St} \gg 1$) across which the typically repulsive levitation force (above) transitions to attraction (below). Limiting behaviors of these contours for extreme values of α^2 are denoted with dashed lines. The pressure profiles in figure 3.5 that correspond to $\langle F_L\rangle = 0$ are evaluated for limitingly small values of (α^2,Λ) that lie on these prinicipal contours.

levitation force (3.11)–(3.13) reduce in the first approximation to

$$\begin{aligned} \alpha^2\langle F_i\rangle &\rightarrow g_F\left(\Lambda/\alpha^2\right) \sim 1, \\ \alpha^2 A &\rightarrow g_A\left(\Lambda/\alpha^2\right) \sim 1 \quad \text{and} \\ \alpha^{-4}\hat{P}_e &\rightarrow \mathcal{P} \sim 1, \end{aligned} \tag{3.71}$$

where $\mathcal{P} < 0$ is a constant. The inner contribution $\langle F_i\rangle$ effectively depends on the similarity parameter $\Lambda/\alpha^2 \sim 1$, which is, aside from a numerical factor of 12, the aforementioned squeeze number σ that appears in the Reynolds equation [5]. The peripheral pressure drop $A^2\hat{P}_e$ is asymptotically smaller by a factor of order $\alpha^2 \ll 1$, such that, for flexural squeeze-film systems operating near the Stokes limit, the root $(\Lambda/\alpha^2)_c$ of the function g_F essentially specifies the critical operating condition for which $\langle \mathcal{F}_L \rangle = 0$. One may confirm qualitatively that these roots, visualized in figure 3.3, indeed correspond to the limiting slopes labeled in figure 3.6. As a result, the critical separation distance h_o^* at which the transition to attraction occurs can be written a priori as

$$h_o^* = a\sqrt{\frac{\omega\mu_a/p_a}{(\Lambda/\alpha^2)_c}}, \tag{3.72}$$

predictions of which are verified in figures 3.2(b) and (c).

It was shown in Chapter 2 that, for rigid-body systems, in contrast, g_F is universally positive [60]. As discussed in § 2.8, the transition seems to occur instead in the sub-limit $\Lambda/\alpha^2 \sim \alpha^2 \to 0$, where $\langle F_i \rangle$ reduces back to order unity and is cancelled by the peripheral pressure drop for a critical value of the ratio Λ/α^4, as reflected by the pressure profiles in figure 3.5(a). The associated separating contour correspondingly exhibits a parabolic limiting behavior $\Lambda \propto (\alpha^2)^2$ as it approaches the origin, as displayed in figure 3.6(a). Therefore, when operating near the Stokes limit with a given frequency and squeeze-film radius, i.e. a fixed value of $\Lambda \ll 1$, the transition to attraction occurs at a relatively greater distance $h_o^* \propto (\alpha^2)^{1/2}$ for rigid-body systems, beyond which the relative amplitude $\varepsilon \propto h_o^{-1}$, and thus, the maximal attractive load capacity $\langle -\mathcal{F}_L \rangle \propto \varepsilon^2$, are severely reduced, as seen in figure 3.2(a).

It must be noted that, while the separating contours in figure 3.6 display universal behaviors in the Stokes limit $\alpha^2 \to 0$, the values Λ_i that they approach in the inviscid limit $\alpha^2 \to \infty$ lower significantly with decreasing values of the modified Strouhal number. As seen in the figure, for $\hat{St} \gg 1$, $\Lambda_i \approx [8.1, 42.7, 88.8, 177.1]$ respectively for rigid-body, mode-1, mode-2 and mode-3 oscillations, but for $\hat{St} \ll 1$, $\Lambda_i \approx [0, 6.1, 32.6, 82.8]$. Nevertheless, an expansion of the parametric region where $\langle F_L \rangle < 0$ necessarily loosens the restrictions on $\Lambda \propto (\omega a)^2$ required for a transition from repulsive to attractive forces. In other words, flexural oscillations of increasing wavenumber allow attractive levitation for a progressively wider range of frequencies and/or oscillator surface areas, those for which rigid-body oscillations would not.

3.6 Conclusions

In summary, we have offered in this chapter a theoretical explanation for the unprecedentedly strong attractive load capacities observed in recently designed squeeze-film levitation systems [3,49]. The key innovation introduced in the recent designs seems to be the use of a very thin oscillator that performs pronounced, flexural oscillations in response to localized excitation with relatively low frequency, as opposed to the bulky and stiff oscillators operated conventionally at ultrasonic frequencies. Our mathematical formulation, verified against finite-difference solutions of the classical Reynolds equation, rigorously accounts for effects of fluid inertia, pressure variations in a small region surrounding the edge of the film and elastic deformations of the oscillator. While the weak attractive forces produced by rigid-body oscillations are known to occur purely due to a drop in the time-averaged pressure near the film edge, the much larger forces enabled by resonant flexural oscillations are found to correlate with local minima of pressure that emerge within the film. For sufficiently low frequencies, these minima occur at lateral locations near the nodal regions of the standing elastic wave. Semi-analytical solutions of this formulation for resonant oscillations, modeled using the Kirchhoff–Love theory of thin-plate bending, reveal that the maximal attractive load capacity, as well as the range of operating conditions under which attractive forces can be produced, grows substantially for increasing values of the relevant flexural wavenumber—that is, for increasingly flexible disks.

The results of this theoretical study pose significant implications for future developments in squeeze-film levitation. For instance, recently developed ultrasonic pick-and-place devices [6] could, in principle, suspend objects of greater surface area and mass if the oscillator is modified carefully to exhibit appropriate elastic deformation. Practical applicability of this formulation may be further improved by modeling the fluid–structure interactions that may occur for highly flexible oscillators, symptoms of which have been observed in recent experiments [3].

Chapter 3 has been published in *AIP Advances* under the title “On the enhanced attractive load capacity of resonant flexural squeeze-film levitators”, by S. Ramanarayanan and A. L. Sánchez, 12(10), 105126, (2022). The dissertation author was the primary investigator and author of this paper.

Chapter 4

Effects of fluid–structure coupling in systems with highly flexible oscillators

4.1 Executive summary

The results of Ch. 3 are extended here to account for two-way-coupling between the dynamic bending of the oscillator and the pulsatile gas flow in the squeeze film. Accounting rigorously for such fluid–structure interactions is found to provide improved agreement between experimental data [3] and theoretical predictions regarding the behavior of a highly flexural SFL system—in particular, (i) the scale of the attractive levitation force for small separation distances between the oscillator and opposite wall and (ii) the nature of the time-averaged pressure distribution within the air layer.

4.2 Introduction

In 2015, Dr. David Colasante communicated an interesting experiment where a thin plate was oscillated rapidly along its normal axis and brought near a parallel wall, the two being separating by a thin layer of air [49]. A strong, steady attractive force was seen to emerge, pulling the oscillating plate toward the wall. In one case the force grew sufficiently large to steadily levitate a device with a total mass of ≈ 2.6 kg below a horizontal wall [50]. A recently constructed device of larger scale generated an attractive force of nearly 200 kgf (kilograms-force) with a

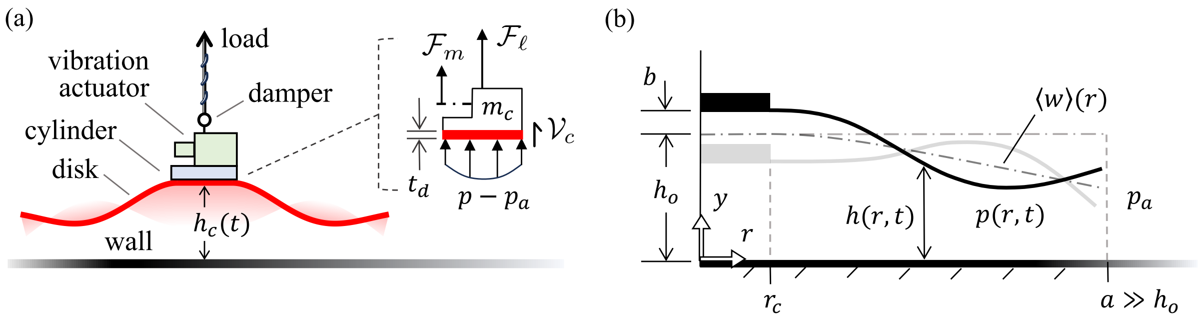

Figure 4.1. (a) Cartoon and free-body diagram of a load-bearing squeeze-film-levitation system enabled by the flexural oscillations of a thin, locally excited disk and (b) a formal schematic of the axisymmetric system geometry used in the problem definition § 4.3.

supplied power of 200 watts [54]. A similar phenomenon had been demonstrated previously by [96] and [97], who showed that normal vibration of a standard suction cup improves its performance by lowering further the sub-ambient air pressure inside the cavity [98]. However, this method involved physical contact between the cup and the adjacent wall, as evidenced by an apparent resistance to translational motion and rotation. The levitated devices in the experiments of Dr. Colasante showed no palpable resistance [99], indicating the presence of a lubricating air layer. In 2021, [3] appear to have discovered independently the same phenomenon of vibration-induced gaseous lubrication, designing a load-carrying robotic device capable of traveling underneath horizontal surfaces and up vertical walls with use of a standard wheel base and a thin, oscillating plastic disk. The device produced ≈ 610 gf (grams-force) using a power input of $\lesssim$ 0.29 W (watts) [95], thereby achieving an impressive operating efficiency of over 2000 gf/W. Subsequently, [100] designed an upgraded mobile robot that travelled and rotated beneath a horizontal surface without the use of wheels, eliminating all physical contact. The required propulsive/rotary aerodynamic shear force/torque on the oscillating plate was achieved by generating traveling-wave deformations of the plate with use of multiple vibration actuators excited with appropriate mutual phase shifts.

The phenomenon observed by [49], [3] and [100] is commonly referred to in literature as ‘squeeze-film levitation’ (SFL) [7], a method of gaseous lubrication discovered seemingly in the mid 1950s, whereby the required overpressure inside a wall-bounded gas layer is effectively provided by relative perpendicular oscillation of the walls [5]. In contrast to aerodynamic and aerostatic lubrication which directly provide (quasi-)steady overpressure due to relative translational motion of the walls or external pumping of air, respectively, the unsteady oscillatory airflow in squeeze-film lubrication provides a cycle-averaged overpressure as a result of the nonlinear effects of gaseous compressibility and convective fluid acceleration [60, 74]. The resulting time-averaged pressure difference across the oscillating plate provides an effectively steady load-bearing capacity. Typical SFL systems involve highly stiff oscillators that are driven by bulky piezoelectric transducers at ultrasonic frequencies, producing large *repulsive* forces that render them suitable for conventional bearing lubrication. For example, [19] measured a steady, repulsive force of $\approx 11{,}700$ gf by oscillating a cylindrical oscillator of diameter 5 cm at a frequency of 20,000 Hz (hertz). Prior to the experiment of [49], attractive forces had been found to occur only under a limited range of operating conditions, the corresponding load capacities being thousands of times weaker [6, 37, 101]. For example, a maximal attractive force of just ≈ 0.5 gf was measured by [37] using a cylindrical oscillator of diameter 7 cm and frequency 200 Hz. As a result, throughout history, levitation and transportation/rotation systems enabled by repulsive forces have garnered considerable theoretical attention [2, 7, 19, 33–35], while fewer studies have addressed the emergence of the much weaker attractive forces [4, 6, 60].

A recent study [101] posited that the unprecedented magnification of attractive load capacity observed in the recent experiments by [49] and [3] can be attributed to the pronounced elastic deformations experienced by the highly flexible oscillators utilized. With use of a matched-asymptotic description of the airflow in the slender air layer as well as a small peripheral region extending beyond its edge, the authors proved that the steady attractive force provided by resonant flexural oscillations of a thin plate may be thousands of times larger than those provided by a rigid-body oscillator operating under otherwise identical conditions—specifically, with the same central displacement amplitude. However, fundamental disagreements remain between crucial aspects of the theoretical predictions of [101] and the experimental observations

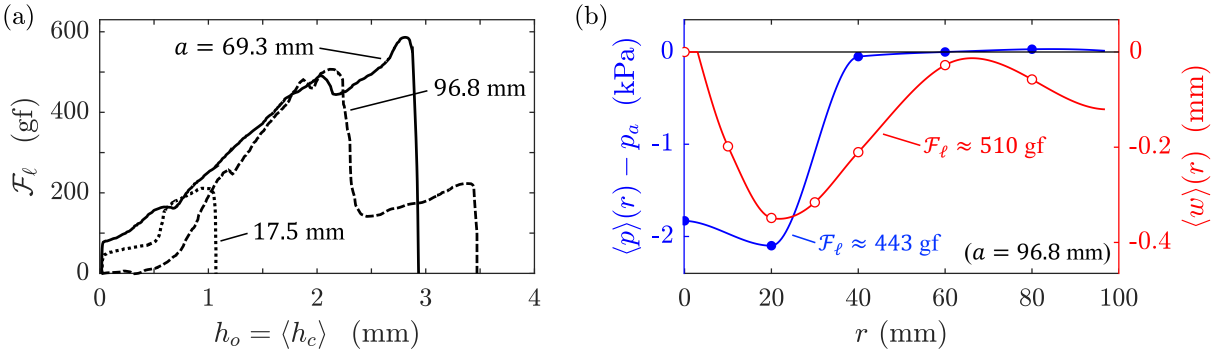

Figure 4.2. Approximate recreation of selected experimental measurements by [3]: (a) variation of the applied pulling load with the mean central separation distance and (b) time-averaged radial distributions of the gauge pressure in the air layer and the accompanying oscillator displacement. See fig. 4.1 for clarification.

of [3]. On the one hand, the theory predicts the onset of the maximal attractive force for a mean separation distance of less than 50 μm between the center of the oscillating plate and the opposite wall, while the data shows a gradual rise of the force to its maximal value that occurs at much larger distances of order 1–3 mm, as exemplified in figure 4.2(a). On the other hand, the predicted distribution of the time-averaged pressure within the air layer differs substantially from that measured, the latter depicted in figure 4.2(b); in particular, the predicted central gauge pressure is always positive.

We argue in this chapter that these differences may be attributed to the neglect of two-way-coupled fluid–structure interactions whereby the motion of the flexible oscillator is affected non-negligibly by the overpressure generated in the thin air layer. The effects of coupling are demonstrably negligible in the case of the much stiffer oscillators used in earlier studies [93]. In contrast, they are palpable in the experiments of [3], as evidenced by the observed time-averaged deformation of the oscillating disk, shown in figure 4.2(b), which correlates closely with the pictured pressure distribution. Two-way coupling has been explored before in repulsive SFL configurations where a rigid body is levitated above an oscillating plate/piston. The influence of film pressure on the Newtonian dynamics of the levitated body has been studied in the case of rigid oscillators [102] and those undergoing prescribed standing-wave deformations [103]. [104]

additionally explored effects of coupling on the displacement amplitude of a rigid oscillator. [105] and [106] elucidated the damping effect of viscous squeeze-film airflow on the resonant dynamic bending of a compliant plate. To the best of our knowledge, a theoretical investigation is yet to be conducted into the effects of two-way coupling on the time-averaged repulsive/attractive load capacity of an SFL system equipped with a flexible oscillator, that being the objective of the present study.

We formulate below in § 4.3 a reduced mathematical description of the compressible gas flow in a squeeze-film system driven by the flexural oscillation of a compliant plate, by application of the nonlinear theory of elastohydrodynamic lubrication [107–111]. The equations governing the fluid–structure dynamics are coupled with a statement of Newton's second law involving the sinusoidal excitation force exerted by the vibration actuator. The resulting system of equations is solved approximately in § 4.4 under the asymptotic limit of small oscillations, allowing explicit relation of the known excitation amplitude and the consequent displacement amplitude of material points on the oscillating plate. The nonlinear problem that emerges at the following asymptotic order is solved in § 4.5 to provide a concise analytical expression for the operating efficiency of a flexural squeeze-film system: the ratio of the generated time-averaged levitation force to the supplied excitation amplitude. The asymptotic solution is verified in § 4.6 by comparison to finite-difference computations, and shown to provide improved agreement with salient aspects of the experimental data provided by [3]. Finally, recommendations are provided in § 4.7 for theoretical research that may inspire, inform and supplement future practical innovations that exploit this emerging technology.

4.3 Problem definition

Consider the diagram displayed in figure 4.1(a), which represents the basic mechanical configuration involved in recent experimental studies that demonstrated strongly attractive squeeze-film levitation (SFL) [3, 112]. A thin, flexible disk of radius a and uniform thickness

$t_d \ll a$ is located near a parallel wall. Glued coaxially to the opposite surface of the disk is a rigid, circular cylinder of radius $r_c < a$, on top of which a vibration actuator is affixed. The actuator exerts on the cylinder an oscillatory force that varies sinusoidally with time with a frequency of $\omega/(2\pi)$, where ω denotes the associated angular frequency, causing the disk to undergo dynamic bending. The nonlinear dynamics of the oscillatory gas flow excited in the air layer separating the disk and the wall [60], the 'squeeze film', gives rise to an associated cycle-averaged pressure field that provides a steady force attracting the disk toward the wall. Under appropriate conditions, this attractive time-averaged pressure force can support the application of a steady pulling load, as pictured.

While the cited studies used haptic feedback motors of the eccentric-rotating-mass (ERM) type, which generate forces in all directions orthogonal to the axis of rotation, earlier experiments by [49, 50] employed sound exciters that provide a force that acts purely along the cylinder axis of symmetry. In pursuit of an elegant theoretical description of the fluid–structure dynamics in SFL, purely axial oscillations are considered below. In that case, application of Newton's second law for the rigid cylinder and the central portion of the disk to which it is glued provides

$$\langle \mathcal{F}_L \rangle + \mathcal{F}_m \cos(\omega t + \phi) + 2\pi \int_0^{r_c} (p - p_a) r \,\mathrm{d}r + 2\pi r_c \mathcal{V}_c = (\pi r_c^2 \rho_d t_d + m_c) \frac{\partial^2 h_c}{\partial t^2}, \tag{4.1}$$

where t and r denote respectively the time and the radial distance from the axis of symmetry, $\langle \mathcal{F}_L \rangle$ is the constant pulling force (steadied by a vibration damper at the point of application), $\mathcal{F}_m$ denotes the amplitude of the sinusoidal excitation force, $p(r,t) - p_a$ denotes the distributed gauge pressure acting on the disk surface (with p_a denoting the ambient pressure), $\mathcal{V}_c$ represents the axial structural stress resultant within the disk at the critical radius r_c, m_c quantifies the collective mass of the cylinder and other structures involved in the transfer of the vibrational force to the disk, ρ_d denotes the uniform density of the disk and $h_c(t)$ represents the time-varying distance between the wall and the central portion of the disk. (The phase shift ϕ included in the argument of the excitation force is introduced to facilitate the analysis, and will be discussed later.) In writing (4.1), the gravitational acceleration (of magnitude $g \approx 9.81$ m/s^2) is assumed to be negligibly small relative to that induced by the high-frequency actuator. This assumption is substantiated by [3], whose SFL system operated at $\omega/(2\pi) \approx 200$ Hz with a characteristic disk displacement of $\Delta h_c \approx 200\,\mu$m, which provides $g/(\Delta h_c \omega^2) \approx 0.03 \ll 1$. Also of importance below is to note that the weight of the oscillating device in the experiment, $W_d = (m_c + \pi a^2 \rho_d t_d)g \approx 12.6$ gf (grams-force), was negligibly small relative to the applied pulling loads $\langle \mathcal{F}_L \rangle \approx 500$ gf, i.e. $W_d/\langle \mathcal{F}_L \rangle \approx 0.025 \ll 1$.

Experimental data suggests that the central separation distance h_c fluctuates periodically about a constant mean value h_o if the imposed load $\langle \mathcal{F}_L \rangle$ is steady. This effective 'levitation height' h_o grows as the load is quasi-statically increased, till a critical value is reached beyond which the attractive force becomes insufficient and the disk detaches abruptly from the wall, as depicted in figure 4.2(a) [3]. It is of great interest to devise a solution of (4.1) that allows prediction of the 'load capacity' of an SFL system, the maximal pulling force $\max[\langle \mathcal{F}_L \rangle (h_o)]$ beyond which it experiences such failure. In practical applications, known quantities are limited to structural properties of the oscillator, thermodynamic properties of the operating fluid and the amplitude $\mathcal{F}_m$ and angular frequency ω of the excitation force; for instance, those of an ERM motor can be calculated using the mass, eccentric radius and expected rotational speed of the spinning head for a given applied voltage [113]. Solution of (4.1) thus requires determining simultaneously the evolving height $h_c(t)$ of the oscillating central assembly and the reactive aerodynamic and structural forces affecting its dynamics. The problem is complicated especially because of the nonlinear fluid–structure interactions involved, due to which the periodic cylinder motion may exhibit multiple harmonics in addition to the excitation frequency ω.

As shown in the following derivation, the problem simplifies in the case of small axial displacements of the disk relative to the levitation height, allowing approximate solution of (4.1) with use of classical perturbation methods. Under the limit of a small relative amplitude, the rigid cylinder may be assumed in the first approximation to oscillate sinusoidally along its axis of symmetry with a given amplitude $b \ll h_o$ and an angular frequency equal to that of the vibration actuator, ω, so that

$$h_c = h_o + b\cos(\omega t). \tag{4.2}$$

Secondary frequencies arising from weak nonlinear dynamics will enter as asymptotic corrections of order $(b/h_o)^2 \ll 1$ and smaller, to be discussed later. The cylinder displacement (4.2) can be expected to exhibit a phase lag ϕ—with respect to the sinusoidal excitation—that is affected non-negligibly by elastohydrodynamic damping, the combined dissipative effects of viscous stresses in the gas layer and material friction within the disk [114]. This phase lag has been accounted for when writing in (4.1) the forcing term $\mathcal{F}_m \cos(\omega t + \phi)$.

In general, we may express the width $h(r,t)$ of the thin film of air separating the disk and wall, depicted in figure 4.1(b), in terms of the function

$$w(r,t) = h - h_o, \tag{4.3}$$

which denotes the evolving position of the film-adjacent disk surface. Since the central portion of the disk is affixed to the cylinder, it follows from (4.2) that, in the first approximation,

$$w = b\cos(\omega t) \quad \text{for} \quad 0 \le r \le r_c\,. \tag{4.4}$$

In pursuit of quantifying the reactive aerodynamic and structural forces that modulate the value of b, we introduce below a reduced theoretical description of the relevant fluid–structure dynamics, which couples the Reynolds lubrication equation governing the variation of air pressure p in the squeeze film with the Kirchhoff–Love equation governing the dynamic displacement w of the flexible annular portion of the disk $r_c \le r \le a$. We show that, when $b/h_o \ll 1$, the coupled equations can be solved with use of (4.4) as the driving kinematic boundary condition to provide analytical expressions for the reactive forces in terms of b. Substituting these expressions in (4.1) allows straightforward computation of the value of b with relative errors of $O(b/h_o \ll 1)$. Solving the nonlinear system of equations that emerges at the following asymptotic order provides an analytical expression for the load $\langle \mathcal{F}_L \rangle$ with the same level of accuracy.

This asymptotic formulation will be shown below to allow efficient characterization of the dynamics and performance of highly flexural SFL systems, and provide promising agreement with experimental measurements of the pull-off curve $\langle \mathcal{F}_L \rangle (h_o)$, the steady overpressure $\langle p \rangle - p_a$ in the squeeze film and the accompanying steady deformation of the disk $\langle w \rangle (r)$ (see figures 4.1(b) and 4.2 for clarification), both expressed here with use of the cycle-averaging operator $\langle * \rangle = (2\pi/\omega)^{-1} \int_t^{2\pi/\omega} * \, \mathrm{d}t$.

4.3.1 Description of the squeeze-film gas dynamics

In modeling the gas flow, it will be assumed that the squeeze film is slender, $h_o \ll a$, that the characteristic wavelength λ of disk undulation is comparable to the disk radius a, and that the levitation height is sufficiently small—i.e. $h_o^2 \ll \mu_a/\rho_a/\omega$, where μ_a and ρ_a denote respectively the ambient dynamic viscosity and density of the gas—for the flow to be dominated by viscous forces with negligible effects of fluid inertia. Since the Prandtl number of air at room temperature is about 0.71 [115, p. 2.4], the assumption of small Stokes numbers $\alpha^2 = h_o^2/(\mu_a/\rho_a/\omega) \ll 1$ implies that transverse heat conduction dominates the energy balance, so that, in the first approximation, one can neglect the departures of the gas temperature in the film from the value found on both bounding surfaces, assumed here to be equal to the ambient gas temperature [60]. In the associated limit of classical, isothermal lubrication theory [8], the compressible flow of an ideal gas is governed, with small relative errors of orders $(h_o/\lambda)^2 \sim (h_o/a)^2 \ll 1$ and $\alpha^2 \ll 1$, by the equations

$$\frac{\partial \rho}{\partial t} + \frac{1}{r}\frac{\partial(\rho r u)}{\partial r} + \frac{\partial(\rho v)}{\partial y} = 0, \quad \frac{\partial p}{\partial r} = \mu_a \frac{\partial^2 u}{\partial y^2}, \quad \frac{\partial p}{\partial y} = 0, \quad \text{and} \quad \frac{p}{\rho} = \frac{p_a}{\rho_a}, \qquad (4.5a\text{–}d)$$

representing the conservation of mass, the conservation of momentum in the radial and transverse directions, respectively, and the isothermal equation of state. In the above equations, y is the normal distance to the wall, u and v denote respectively the radial and axial components of the flow velocity, and ρ and p denote respectively the variable gas density and pressure, the subscript "a" denoting ambient values found in the unperturbed surroundings. (Note that convective acceleration is neglected in the radial momentum balance since the Strouhal number of the flow, h_o/b, is always greater than unity.)

The velocity in the gas film must satisfy the non-slip and non-penetration conditions at the bounding surfaces

$$\begin{cases} u = v = 0 & \text{at} \quad y = 0 \\ u = v - \partial w/\partial t = 0 & \text{at} \quad y = h = h_o + w(r,t), \end{cases} \tag{4.6}$$

where the condition $u = 0$ at $y = h$ ignores the negligibly small radial displacements of material points on the disk, which are of order $(b/h_o)^2(h_o/a)^2 a \ll a$.

The gas pressure must satisfy the conditions of regularity at the axis of symmetry and relaxation at the film edge,

$$\begin{cases} \partial p/\partial r = 0 & \text{at} \quad r = 0 \\ p = p_a & \text{at} \quad r = a\,. \end{cases} \tag{4.7}$$

the latter of which implicitly neglects the pressure variations $p - p_a$ existing across the small peripheral region of gas flow that extends for distances of order h_o in all directions from the film edge $r = a$. These variations, which have been shown to provide a non-negligible contribution to the levitation force in configurations with order-unity Stokes numbers $\alpha^2 = \omega h_o^2/(\mu_a/\rho_a) \sim 1$ [4,60], can be neglected in the lubrication limit $\alpha^2 \ll 1$ considered here. For a proof, we begin by noting that the disk oscillations induce radial flow of characteristic speed $u \sim u_c = (b/h_o)\omega a$ in the film, as follows from the balance of volumetric dilation rates in the continuity equation (4.5a). A similar analysis of the radial momentum equation (4.5b) then provides $(p - p_a) \sim (\Delta p)_f = (b/h_o)(\mu_a \omega a^2)/(p_a h_o^2)$ for the characteristic value of the pressure variations along the film. The nature of the flow induced in the small, non-slender periphery depends on the local Reynolds number $Re_p = \rho_a u_c h_o/\mu_a = \alpha^2/St_p$, defined here in terms of the associated Strouhal number $St_p = h_o^2/(ba)$. One the one hand, though the flow in the film is dominated by viscous forces since $\alpha^2 \ll 1$, inertial forces can dominate in the periphery if $St_p \ll \alpha^2$. In that case, the associated pressure drop across the periphery $(p - p_a) \sim (\Delta p)_p$ can be expected to scale with the dynamic pressure $(\Delta p)_p = \rho_a u_c^2$, which is negligibly small compared with the pressure variations along the film, i.e. $(\Delta p)_p/(\Delta p)_f = \alpha^2(b/h_o) \ll 1$. On the other hand, in the opposite limit $Re_p \ll 1$, the peripheral flow is also dominated by viscous forces, whence $(\Delta p)_p = \mu_a u_c/h_o$, such that $(\Delta p)_p/(\Delta p)_f = h_o/a \ll 1$. Thus, regardless of the value of Re_p, the pressure drop across the periphery can be neglected when analyzing the flow in the film.

The lubrication problem defined in (4.5*a*–*d*)–(4.7) affords reduction to a single differential equation involving the pressure $p(r,t)$, independent of y as follows from (4.5*c*), and the disk deformation $w(r,t)$. The derivation begins by substituting $\rho = \rho_a(p/p_a)$, obtained by rearranging the equation of state (4.5*d*), into the continuity equation (4.5*a*) and integrating the result across the film with use of the non-penetration conditions given in (4.6) to provide $\partial(hp)/\partial t + (1/r)\partial(rp\int_0^h u\,\mathrm{d}y)/\partial r = 0$, after use is made of the Leibniz integral rule. Substituting into this equation the Poiseuille radial velocity $u = -(\partial p/\partial r)y(h-y)/(2\mu_a)$, which follows from integration of the radial momentum equation (4.5*b*) with the non-slip conditions given in (4.6), yields the relevant form of the Reynolds lubrication equation [8]

$$\frac{\partial}{\partial t}[(h_o + w)p] - \frac{1}{12\mu_a r}\frac{\partial}{\partial r}\left[(h_o + w)^3 pr\frac{\partial p}{\partial r}\right] = 0, \tag{4.8}$$

where we have subsituted for the film thickness $h(r,t)$ the expression $h_o + w(r,t)$, consistent with (4.3). The evolving pressure in the gas film $p(r,t)$ is to be obtained by integration of the above equation with the boundary conditions given in (4.7). The solution depends on the disk position w, whose value for $0 \le r \le r_c$ is determined by the prescribed cylinder motion, as stated in (4.4), while its unknown value for $r_c < r \le a$ is to be determined from an analysis of the structural dynamics, as described below.

4.3.2 Description of the disk structural dynamics

In analyzing the oscillations of the annular portion of the disk $r_c \leq r \leq a$, it will be assumed that the disk is made of a homogeneous, isotropic material, and that its axial deflections, comparable in magnitude to the central amplitude b, are much smaller than its uniform thickness t_d, which in turn is much smaller than its radius a, i.e. $b \ll t_d \ll a$. The excitation frequency is assumed to be sufficiently low for the characteristic flexural wavelength λ of the disk to be comparable to the disk radius a, consistent with the slender-flow assumption drawn in § 4.3.1. Under these conditions the disk can be assumed to undergo pure bending [116, pp. 47–49], whence its dynamic deformations, influenced non-negligibly by the squeeze-film overpressure $p(r,t) - p_a$, can be described with use of the Kirchhoff–Love equation [117, 118]

$$\mathcal{D}\bar{\nabla}^4 w + \rho_d t_d \frac{\partial^2 w}{\partial t^2} = p - p_a, \quad \text{where} \quad \mathcal{D} = \frac{E_d t_d^3}{12(1-\nu_d^2)}, \tag{4.9}$$

involving the axisymmetric Laplacian operator $\bar{\nabla}^2 = [\partial^2/\partial r^2 + (1/r)\partial/\partial r]$ and the flexural rigidity $\mathcal{D}$ of the disk, the latter defined in terms of the disk Young's modulus E_d, mass density ρ_d and Poisson's ratio ν_d. Correspondingly, the axial stress resultant $\mathcal{V}_c$ affecting the dynamics of the central assembly (4.1) can be expressed as

$$\mathcal{V}_c = -\mathcal{D}\left[\partial(\bar{\nabla}^2 w)/\partial r\right]_{r=r_c}. \tag{4.10}$$

Note that the displacement of the neutral plane of the disk has been substituted in (4.9) and (4.10) with that of its film-adjacent surface w (4.3), introducing negligible relative errors of order $(b/h_o)(t_d h_o/a^2) \ll 1$. Also, in-plane stresses induced due to fluid shear acting on this surface [116, pp. 378–380] are smaller than the expected overpressure by a factor of order $(b/h_o)(h_o/a)^2 \ll 1$ [119, 120] and, hence, neglected when writing (4.9).

Equation (4.9) must be integrated for $r_c \leq r \leq a$ with the four boundary conditions

$$\begin{cases} w - b\cos(\omega t) = \dfrac{\partial w}{\partial r} = 0 & \text{at} \quad r = r_c \\ \left(\dfrac{\partial^2}{\partial r^2} + \dfrac{\nu_d}{r}\dfrac{\partial}{\partial r}\right) w = \dfrac{\partial}{\partial r}\left(\bar{\nabla}^2 w\right) = 0 & \text{at} \quad r = a, \end{cases} \tag{4.11}$$

which state that the annular portion of the disk is cantilevered at its inner edge $r = r_c$, where it follows the driving motion of the cylinder (4.4), and that neither bending moments nor axisymmetric axial stresses are supported at its free outer edge $r = a$ ([116, pp. 83–84]; [89, pp. 840–841]).

4.3.3 The case of central forcing and a universal measure of efficiency

Of particular interest from a theoretical perspective is the canonical configuration of a disk that is forced dynamically at its center, i.e. $r_c = 0$. In principle, the reactive structural stresses that develop within such a disk grow unboundedly ($\propto r^{-1}$) near its axis of symmetry. Interestingly, an explicit theoretical solution can be found for the case of a disk under static central loading while supported at its edge [117], where the disk displacement near the axis $r = 0$ varies as $w \propto r^2 \ln(r)$. Since this solution relies on the assumption of pure bending, it is prone to inaccuracy for radial distances comparable to the plate thickness $r \sim t_d$, for which the precise stress distribution in the locality of the axis must be considered carefully [116, pp. 67–78].

Contrary to the case of static loading, the singular case of a disk subject to dynamic forcing with prescribed amplitude at its center $r = 0$ does not have a straightforward solution. As shown by [121], one can treat this limiting case by considering instead a disk with a small central cavity able to support finite stresses. An expression for the disk flexure can be obtained simply by considering the limit of a vanishing cavity. Similarly, for the present fluid–structure problem, the ideal case of central forcing $r_c = 0$ presents a singular limit that is unamenable to straightforward solution. The general formulation to be developed here for $r_c \sim a$ can, however, be exploited to derive a limiting solution that describes systems with a vanishing clamp radius

$r_c \ll a$, as done below following the strategy devised by [121]. Note that the primary equation of motion (4.1) simplifies in this limit, the terms describing system inertia, aerodynamic pressure and structural shear vanishing with the square of r_c. The simplified equation will be shown below to allow straightforward computation of the ratio $\langle \mathcal{F}_L \rangle / \mathcal{F}_m$, a metric that can be used to compare readily the levitation 'efficiency' of SFL systems (for which $r_c \ll a$) with arbitrary displacement amplitudes b.

4.3.4 Dimensionless formulation and governing parameters

In pursuit of a rigorous understanding of the fluid–structure system described by the two equations (4.8) and (4.9) and their respective boundary conditions (4.7) and (4.11), it is of interest to reformulate the mathematical problem in terms of appropriate dimensionless variables, beginning with the independent temporal and spatial variables $\tau = \omega t$ and $\xi = r/a$. The disk deformation is scaled with the central amplitude b to give $W(\xi,\tau) = w/b$. It follows then from (4.3) that $h/h_o = 1 + \varepsilon W$, where

$$\varepsilon = b/h_o \tag{4.12}$$

defines the relative central oscillation amplitude. With this definition, it follows from (4.4) that $W = \cos\tau$ for $\xi \leq \xi_c$, where

$$\xi_c = r_c/a \tag{4.13}$$

is the dimensionless radial distance up to which the disk is clamped to the cylinder. The characteristic value $(\Delta p)_f$ of the overpressure $p - p_a$ in the squeeze film, deduced below (4.7), is used to define the dimensionless variable $P = 12(p - p_a)/(\varepsilon\sigma p_a)$, where

$$\sigma = \frac{12\mu_a \omega a^2}{p_a h_o^2} \tag{4.14}$$

is the classical 'squeeze number', a dimensionless parameter that quantifies the degree of gaseous compressibility in the squeeze film due to viscous retardation of radial airflow [8, p. 143].

In terms of the dimensionless variables listed above, the Reynolds lubrication equation (4.8) can be written in the form

$$\sigma\frac{\partial}{\partial\tau}\left[(1+\varepsilon W)P\right]-\frac{1}{\xi}\frac{\partial}{\partial\xi}\left[(1+\varepsilon W)^3\left(1+\frac{\varepsilon\sigma}{12}P\right)\xi\frac{\partial P}{\partial\xi}\right]+12\frac{\partial W}{\partial\tau}=0, \tag{4.15}$$

while the Kirchhoff–Love equation (4.9) takes the form

$$\nabla^4 W+K^4\frac{\partial^2 W}{\partial\tau^2}=C^6 P, \tag{4.16}$$

involving the dimensionless axisymmetric Laplacian operator $\nabla^2=[\partial^2/\partial\xi^2+(1/\xi)\partial/\partial\xi]$. As can be seen in (4.16), consideration of the disk dynamics introduces the two additional dimensionless parameters K and C, with

$$K^4=a^4\omega^2\frac{12\rho_d(1-\nu_d^2)}{E_d t_d^2} \qquad \text{and} \qquad C^6=a^6\frac{12\mu_a\omega(1-\nu_d^2)}{E_d(t_d h_o)^3} \tag{4.17a,b}$$

representing the characteristic magnitudes of the disk inertia and the squeeze-film overpressure, respectively, relative to that of the axial structural stresses. Note that C quantifies in (4.16) the degree to which the dynamic flexure of the annular portion of the disk is affected by the squeeze-film overpressure, and K represents the elastic wavenumber characterizing the bending of the isolated disk, i.e. for $C=0$ [101].

As follows from (4.7) and (4.11), equation (4.15) must be integrated with the boundary conditions

$$\partial P/\partial\xi=0 \text{ at } \xi=0 \qquad \text{and} \qquad P=0 \text{ at } \xi=1, \tag{4.18}$$

while (4.16) must be integrated with

$$\begin{cases} W-\cos\tau=\partial W/\partial\xi=0 & \text{at} \quad \xi=\xi_c \\ \left(\dfrac{\partial^2}{\partial\xi^2}+\dfrac{\nu_d}{\xi}\dfrac{\partial}{\partial\xi}\right)W=\dfrac{\partial}{\partial\xi}\left(\nabla^2 W\right)=0 & \text{at} \quad \xi=1\,. \end{cases} \tag{4.19}$$

The system of equations comprising (4.15) and (4.16) and their respective boundary conditions (4.18) and (4.19) determines the evolution of the film pressure P for $0 \le \xi \le 1$ together with the coupled deflection W of the annular portion of the flexible disk $\xi_c < \xi \le 1$. The problem is to be addressed below for order-unity values of the dimensionless parameters ξ_c, σ, K, C and ν_d, with use of asymptotic methods that exploit the presence of small relative oscillation amplitudes $\varepsilon = b/h_o \ll 1$.

4.4 Leading-order solution for small relative amplitudes

We begin by expressing the dimensionless pressure and disk displacement as expansions in increasing integer powers of the perturbation parameter $\varepsilon \ll 1$:

$$\begin{cases} W = W_0 + \varepsilon W_1 + \cdots \\ P = P_0 + \varepsilon P_1 + \cdots \,. \end{cases} \tag{4.20}$$

Substituting (4.20) into the governing equations (4.15) and (4.16) and their boundary conditions (4.18) and (4.19) and collecting terms of order unity provides the leading-order system of equations

$$\frac{\partial}{\partial \tau}(\sigma P_0 + 12 W_0) - \nabla^2 P_0 = 0 \quad \begin{cases} \xi = 0: \quad \partial P_0/\partial \xi = 0 \\ \xi = 1: \quad P_0 = 0 \end{cases} \tag{4.21}$$

and

$$\nabla^4 W_0 + K^4 \frac{\partial^2 W_0}{\partial \tau^2} = C^6 P_0 \quad \begin{cases} \xi = \xi_c: \quad W_0 - \cos\tau = \partial W_0/\partial \xi = 0 \\ \xi = 1: \quad \left(\dfrac{\partial^2}{\partial \xi^2} + \dfrac{\nu_d}{\xi}\dfrac{\partial}{\partial \xi}\right) W_0 = \dfrac{\partial}{\partial \xi}\left(\nabla^2 W_0\right) = 0 \,. \end{cases} \tag{4.22}$$

Since the motion of the central portion of the disk is prescribed by the sinusoidal function $W = \cos\tau$, as per (4.4), in seeking time-periodic solutions of the above equations it is convenient to consider separately the pressure fields existing for $0 \le \xi \le \xi_c$ and $\xi_c \le \xi \le 1$ with use of the *ansatz*

$$\begin{cases} P_0 = \mathrm{Re}\{\bar{\Pi}(\xi)\mathrm{e}^{\mathrm{i}\tau}\} \quad \text{and} \quad W_0 = \mathrm{Re}\{\mathrm{e}^{\mathrm{i}\tau}\} \qquad \text{for} \quad 0 \le \xi \le \xi_c \\ P_0 = \mathrm{Re}\{\Pi(\xi)\mathrm{e}^{\mathrm{i}\tau}\} \quad \text{and} \quad W_0 = \mathrm{Re}\{\Omega(\xi)\mathrm{e}^{\mathrm{i}\tau}\} \quad \text{for} \quad \xi_c \le \xi \le 1\,, \end{cases} \tag{4.23}$$

where the complex spatial functions $\bar{\Pi}$, Π, and Ω are to be determined below.

In the central portion of the disk, where $W_0 = \mathrm{Re}\{\mathrm{e}^{\mathrm{i}\tau}\}$, the Reynolds equation (4.21) reduces to the inhomogeneous Bessel equation

$$\bar{\Pi}'' + \frac{1}{\xi}\bar{\Pi}' + \frac{\sigma}{\mathrm{i}}\bar{\Pi} = 12\mathrm{i}\,, \qquad \text{for} \qquad 0 \le \xi \le \xi_c\,, \tag{4.24}$$

where a prime superscript denotes the derivative of a radial function, i.e. $f'(\xi) = \mathrm{d}f/\mathrm{d}\xi$. Integrating the above equation subject to the regularity condition $\bar{\Pi}'(0) = 0$ leads to

$$\bar{\Pi} = \frac{12\mathrm{i}}{\varsigma^2}\left[1 + \bar{A}J_0(\varsigma\xi)\right], \quad \text{with} \quad \varsigma = (1-\mathrm{i})\sqrt{\frac{\sigma}{2}}\,, \tag{4.25}$$

where J_0 represents the Bessel function of the first kind of zeroth order and ς and $\bar{A}$ are complex coefficients, the latter to be determined from patching [122, pp. 335–336] with the pressure distribution in the surrounding annular region.

To determine the solution in the annular outer region $\xi_c \le \xi \le 1$, we begin by using (4.22) and (4.23) to write

$$\Pi = C^{-6}\left(\nabla^4 - K^4\right)\Omega\,. \tag{4.26}$$

Substituting this result into (4.21) yields the sixth-order homogeneous equation

$$\nabla^6\Omega - \sigma\mathrm{i}\nabla^4\Omega - K^4\nabla^2\Omega + \mathrm{i}(\sigma K^4 - 12C^6)\Omega = 0\,, \tag{4.27}$$

the relevant ‘thin-film’ equation of elastohydrodynamic lubrication [110, 123], which can be alternatively written in the factorized form

$$\left(\nabla^2+\gamma_1^2\right)\left(\nabla^2+\gamma_2^2\right)\left(\nabla^2+\gamma_3^2\right)\Omega=0\,, \tag{4.28}$$

involving the constant roots γ_1^2,γ_2^2 and γ_3^2, defined collectively by

$$\gamma_n^2=-\frac{\mathrm{i}}{3}\left[\sigma+\mathrm{e}^{2\mathrm{i}\pi(n-1)/3}Q^{1/3}+\left(\sigma^2-3K^4\right)\mathrm{e}^{2\mathrm{i}\pi(1-n)/3}Q^{-1/3}\right],\quad \text{for}\ \ n=1:3\,, \tag{4.29}$$

where

$$Q=\sigma^3+9\sigma K^4-162C^6-3\left[3K^4\left(\sigma^2+K^4\right)^2+36C^6\left(81C^6-9\sigma K^4-\sigma^3\right)\right]^{1/2}. \tag{4.30}$$

The general solution to (4.28) can be written as a linear combination of Bessel functions of the first and second kinds of zeroth order, i.e.

$$\Omega=\sum_{n=1}^{3}\left[A_nJ_0(\gamma_n\xi)+B_nY_0(\gamma_n\xi)\right], \tag{4.31}$$

whence the reduced pressure (4.26) assumes the form

$$\Pi=\frac{1}{C^6}\sum_{n=1}^{3}\left(\gamma_n^4-K^4\right)\left[A_nJ_0(\gamma_n\xi)+B_nY_0(\gamma_n\xi)\right]. \tag{4.32}$$

The expressions (4.25), (4.31) and (4.32) involve seven complex constants, $\bar{A}$ and A_n and B_n for $n=1:3$, which must be determined by application of the five reduced boundary conditions

$$\begin{cases}\Omega-1=\Omega'=0 & \text{at}\quad \xi=\xi_c\\[2ex] \Pi=\Omega''+\nu_d\Omega'=\Omega'''+\Omega''-\Omega'=0 & \text{at}\quad \xi=1\,,\end{cases} \tag{4.33}$$

consistent with those stated in (4.21) and (4.22), and the two additional conditions

$$\bar{\Pi} - \Pi = \bar{\Pi}' - \Pi' = 0 \quad \text{at} \quad \xi = \xi_c\,, \tag{4.34}$$

which enforce continuity of the pressure and its gradient, respectively, at $\xi = \xi_c$. The last condition is needed to satisfy continuity of the radial flow velocity, defined above (4.8), and involves the reduced pressure gradients in the central and annular regions,

$$\bar{\Pi}' = -\frac{12\mathrm{i}}{\varsigma}\bar{A}J_1(\varsigma\xi) \quad \text{and} \quad \Pi' = \sum_{n=1}^{3} \frac{\gamma_n\left(K^4 - \gamma_n^4\right)}{C^6}\left[A_n J_1(\gamma_n\xi) + B_n Y_1(\gamma_n\xi)\right], \tag{4.35a,b}$$

respectively. The solution of the system of linear equations displayed in (4.33) and (4.34) can be expressed in the compact form

$$\begin{bmatrix} \bar{A} & A_1 & B_1 & A_2 & B_2 & A_3 & B_3 \end{bmatrix} = \begin{bmatrix} 1 & 0 & 12\mathrm{i}C^6/\varsigma^2 & 0 & 0 & 0 & 0 \end{bmatrix}\mathbf{M}^{-1}, \tag{4.36}$$

$\mathbf{M}^{-1}$ representing the inverse of the square matrix

$$\mathbf{M} =$$
$$\begin{bmatrix}
0 & 0 & \dfrac{12C^6 J_0(\varsigma\xi_c)}{\mathrm{i}\varsigma^2} & \dfrac{12\mathrm{i}C^6 J_1(\varsigma\xi_c)}{\varsigma} & 0 & 0 & 0 \\
J_0(\gamma_1\xi_c) & \gamma_1 J_1(\gamma_1\xi_c) & \Phi_J(\gamma_1,\xi_c) & \Psi_J(\gamma_1,\xi_c) & \Phi_J(\gamma_1,1) & \Theta_J(\gamma_1,1) & \gamma_1^3 J_1(\gamma_1) \\
Y_0(\gamma_1\xi_c) & \gamma_1 Y_1(\gamma_1\xi_c) & \Phi_Y(\gamma_1,\xi_c) & \Psi_Y(\gamma_1,\xi_c) & \Phi_Y(\gamma_1,1) & \Theta_Y(\gamma_1,1) & \gamma_1^3 Y_1(\gamma_1) \\
J_0(\gamma_2\xi_c) & \gamma_2 J_1(\gamma_2\xi_c) & \Phi_J(\gamma_2,\xi_c) & \Psi_J(\gamma_2,\xi_c) & \Phi_J(\gamma_2,1) & \Theta_J(\gamma_2,1) & \gamma_2^3 J_1(\gamma_2) \\
Y_0(\gamma_2\xi_c) & \gamma_2 Y_1(\gamma_2\xi_c) & \Phi_Y(\gamma_2,\xi_c) & \Psi_Y(\gamma_2,\xi_c) & \Phi_Y(\gamma_2,1) & \Theta_Y(\gamma_2,1) & \gamma_2^3 Y_1(\gamma_2) \\
J_0(\gamma_3\xi_c) & \gamma_3 J_1(\gamma_3\xi_c) & \Phi_J(\gamma_3,\xi_c) & \Psi_J(\gamma_3,\xi_c) & \Phi_J(\gamma_3,1) & \Theta_J(\gamma_3,1) & \gamma_3^3 J_1(\gamma_3) \\
Y_0(\gamma_3\xi_c) & \gamma_3 Y_1(\gamma_3\xi_c) & \Phi_Y(\gamma_3,\xi_c) & \Psi_Y(\gamma_3,\xi_c) & \Phi_Y(\gamma_3,1) & \Theta_Y(\gamma_3,1) & \gamma_3^3 Y_1(\gamma_3)
\end{bmatrix}, \tag{4.37}$$

where the auxiliary functions Φ, Ψ and Θ are defined respectively by

$$\begin{aligned}
\Phi_{\mathcal{B}}(\gamma_n, \xi) &= \left(\gamma_n^4 - K^4\right) \mathcal{B}_0(\gamma_n \xi), \\
\Psi_{\mathcal{B}}(\gamma_n, \xi) &= \frac{\partial \Phi_{\mathcal{B}}}{\partial \xi} = \gamma_n \left(K^4 - \gamma_n^4\right) \mathcal{B}_1(\gamma_n \xi) \quad \text{and} \\
\Theta_{\mathcal{B}}(\gamma_n, \xi) &= \gamma_n^2 \left[\mathcal{B}_0(\gamma_n \xi) - \frac{1 - \nu_d}{\gamma_n \xi} \mathcal{B}_1(\gamma_n \xi)\right],
\end{aligned} \tag{4.38}$$

with $\mathcal{B}_m$ representing a Bessel function of the first or second kind (J_m or Y_m) of mth order.

4.4.1 The limit $\xi_c \to 0$

As mentioned in § 4.3.3, it is of interest to investigate the nature of the solution for small values of the dimensionless clamp radius ξ_c. For $\xi_c = 0$, the singular Bessel functions $Y_0(\gamma_n \xi)$ in the expressions for the disk motion and pressure distribution (4.23) must be eliminated in pursuit of a physically valid description, and solutions can exist only for specific eigen-wavenumbers γ_n for which the relevant matrix, analogous to (4.37), has a zero determinant. For the one-way-coupled problem where $C = 0$, these solutions represent states of structural resonance of the disk, but for any finite value of C, representing aerodynamically damped oscillations, γ_n is a null set and no solutions exist. However, progress can be made by considering the limit of a vanishing clamp radius $\xi_c \to 0$. The reduced leading-order pressure in the annular region $\Pi(\xi)$ exhibits a vanishing gradient at $\xi = \xi_c$, consistent with a central pressure gradient (4.35*a*) that grows linearly for small radial distances $\xi \ll 1$. Upon applying the familiar boundary conditions (4.33)—which govern the disk motion and impose relaxation of pressure at the film edge—in conjuction with a modified regularity condition $\Pi'(\xi_c \ll 1) = 0$, the latter in place of (4.34), the constant coefficients that determine at leading order the annular pressure distribution (4.32) and disk flexure (4.31) can be expressed as

$$\lim_{\xi_c \to 0} \begin{bmatrix} A_1 & B_1 & A_2 & B_2 & A_3 & B_3 \end{bmatrix} = \begin{bmatrix} 1 & 0 & 0 & 0 & 0 & 0 \end{bmatrix} \mathbf{M}_0^{-1}, \tag{4.39}$$

$\mathbf{M}_0^{-1}$ representing the inverse of the reduced square matrix

$$\mathbf{M}_0 = \begin{bmatrix} 1 & 0 & 0 & \Phi_J(\gamma_1,1) & \Theta_J(\gamma_1,1) & \gamma_1^3 J_1(\gamma_1) \\ 2\ln(\gamma_1)/\pi & 1 & \gamma_1^4 & \Phi_Y(\gamma_1,1) & \Theta_Y(\gamma_1,1) & \gamma_1^3 Y_1(\gamma_1) \\ 1 & 0 & 0 & \Phi_J(\gamma_2,1) & \Theta_J(\gamma_2,1) & \gamma_2^3 J_1(\gamma_2) \\ 2\ln(\gamma_2)/\pi & 1 & \gamma_2^4 & \Phi_Y(\gamma_2,1) & \Theta_Y(\gamma_2,1) & \gamma_2^3 Y_1(\gamma_2) \\ 1 & 0 & 0 & \Phi_J(\gamma_3,1) & \Theta_J(\gamma_3,1) & \gamma_3^3 J_1(\gamma_3) \\ 2\ln(\gamma_3)/\pi & 1 & \gamma_3^4 & \Phi_Y(\gamma_3,1) & \Theta_Y(\gamma_3,1) & \gamma_3^3 Y_1(\gamma_3) \end{bmatrix}, \tag{4.40}$$

where the small-argument behaviors of the Bessel functions [124] have been employed to eliminate ξ_c.

4.4.2 Solving for the presumed displacement amplitude b

Based on the leading-order solution derived above, the reactive aerodynamic and structural forces affecting the dynamics of the oscillating central assembly can be expressed, with relative errors of $O(\varepsilon \ll 1)$, in the respective dimensionless forms

$$\frac{\int_0^{r_c}(p-p_a)r\mathrm{d}r}{\varepsilon p_a a^2} = -\mathrm{Re}\left\{F_c\,\mathrm{e}^{\mathrm{i}\tau}\right\}, \quad \text{where} \quad F_c = \xi_c\left[\frac{\xi_c}{2} + \frac{\bar{A}}{\varsigma}J_1\left(\varsigma\xi_c\right)\right], \tag{4.41}$$

and

$$\frac{r_c\mathcal{V}_c}{\mathcal{D}b/a^2} = -\mathrm{Re}\left\{V_c\,\mathrm{e}^{\mathrm{i}\tau}\right\}, \quad \text{where} \quad V_c = \xi_c\sum_{n=1}^{3}\gamma_n^3\left[A_nJ_1(\gamma_n\xi_c) + B_nY_1(\gamma_n\xi_c)\right]. \tag{4.42}$$

Substituting into the governing equation of motion (4.1) the presumed central displacement (4.4), the central pressure force (4.41) and the structural impedance (4.42) reveals a linear relationship between the unknown displacement amplitude b and the (generally) known excitation amplitude

$\mathcal{F}_m$, given by

$$\frac{b}{\mathcal{F}_m} = |\mathcal{X}|^{-1}, \quad \text{where} \quad \mathcal{X} = 2\pi\left(\frac{a^2}{h_o} p_a F_c + \frac{\mathcal{D}}{a^2} V_c\right) - \omega^2\left(m_c + \pi r_c^2 \rho_d t_d\right). \tag{4.43}$$

The associated phase lag, defined below (4.2), is given by $\phi = \arg(\mathcal{X})$. Note that this estimate for the value of b, accurate with relative errors of order $\varepsilon \ll 1$, does not require knowledge of the pulling load $\langle \mathcal{F}_L \rangle$ which enters in (4.1) only as a higher-order correction.

In the limit of a vanishing clamp radius $\xi_c \to 0$ (and, correspondingly, a massless central assembly $m_c = 0$), (4.1) reduces at leading order to a balance between the applied excitation and the reactive structural impedance, i.e. $\mathcal{F}_m \cos(\omega t + \phi) + 2\pi r_c \mathcal{V}_c = 0$, whence the dimensionless impedance amplitude $|V_c|$ can be expressed in the limiting form

$$\lim_{\xi_c \to 0} |V_c| = \lim_{\xi_c \to 0} \frac{\mathcal{F}_m}{2\pi \mathcal{D} b / a^2} = \frac{2}{\pi} \sum_{n=1}^{3} B_n \gamma_n^2 . \tag{4.44}$$

Correspondingly, the central displacement amplitude $b = \mathcal{F}_m / |\mathcal{X}|$ and phase lag $\phi = \arg(\mathcal{X})$ can be computed using the limiting form $\lim_{\xi_c \to 0} \mathcal{X} = -4(\mathcal{D}/a^2) \sum_{n=1}^{3} B_n \gamma_n^2$ of the complex constant $\mathcal{X}$ defined in (4.43).

4.5 Nonlinear interactions at first order

W_0, the displacement of the disk at leading order, and P_0, the associated pressure distribution in the thin film, are both sinusoidal functions of time and thus exhibit a zero time average, i.e. $\langle W_0 \rangle = \langle P_0 \rangle = 0$. Determination of the steady pressure distribution and the steady deformation of the disk thus requires solving the problem that emerges at the following asymptotic order. Collecting terms of order ε in the expanded forms of the governing equations (4.15) and (4.16) and their boundary conditions (4.18) and (4.19), and computing the time average thereof, provides the nonlinear system of equations

$$\frac{\partial}{\partial \xi}\left[\xi\left(3\left\langle W_0 \frac{\partial P_0}{\partial \xi}\right\rangle + \frac{\sigma}{24}\frac{\partial \langle P_0^2\rangle}{\partial \xi} + \frac{\partial \langle P_1\rangle}{\partial \xi}\right)\right] = 0 \quad \begin{cases} \xi = 0: & \partial\langle P_1\rangle/\partial\xi = 0 \\ \xi = 1: & \langle P_1\rangle = 0 \end{cases} \tag{4.45}$$

and

$$\nabla^4\langle W_1\rangle = C^6\langle P_1\rangle \quad \begin{cases} \xi = \xi_c: & \langle W_1\rangle = \mathrm{d}\langle W_1\rangle/\mathrm{d}\xi = 0 \\ \xi = 1: & \left(\dfrac{\mathrm{d}^2}{\mathrm{d}\xi^2} + \dfrac{\nu_d}{\xi}\dfrac{\mathrm{d}}{\mathrm{d}\xi}\right)\langle W_1\rangle = \dfrac{\mathrm{d}}{\mathrm{d}\xi}\left(\nabla^2\langle W_1\rangle\right) = 0, \end{cases} \tag{4.46}$$

where the value of $\langle W_1\rangle$ vanishes at the clamp radius $\xi = \xi_c$ since the driving motion of the cylinder is periodic in time, as elaborated below (4.1). In this connection, note from (4.45) and (4.46) that any secondary frequencies exhibited by $W_1(\xi,\tau)$ due to the nonlinear interactions at first order are irrelevant for the purpose of determining the time-averaged quantities of present interest, $\langle W_1\rangle(\xi)$ and $\langle P_1\rangle(\xi)$.

It must be noted that the relaxation condition provided in (4.45) for the steady, first-order overpressure $\langle P_1\rangle$ at the film edge follows from a rigorous comparison of the characteristic pressure variation along the film, $(\Delta p)_f$, with that occurring across a small, peripheral region surrounding the film edge, $(\Delta p)_p$, their ratio being dependent on the local Reynolds number Re_p characterizing the peripheral flow, as explained below (4.7). For $Re_p \gg 1$, $(\Delta p)_p/(\Delta p)_f \sim \varepsilon\omega h_o^2/(\mu_a/\rho_a)$, so that, in the lubrication limit $\alpha^2 = \omega h_o^2/(\mu_a/\rho_a) \ll 1$ considered here, the peripheral pressure variations can be neglected when analyzing both the leading-order solution and its first-order corrections in the film. On the other hand, in the viscous limit $Re_p \ll 1$, the flow in the periphery involves small spatial pressure variations satisfying $(\Delta p)_p/(\Delta p)_f \sim h_o/a \ll 1$, which can clearly be neglected when analyzing the leading-order solution in the film, as done in (4.21). The associated variations of density are relatively small, i.e., $(\rho-\rho_a)/\rho_a \sim (\Delta p)_p/p_a \sim \varepsilon\sigma(h_o/a)$, such that the nonlinear effects of gaseous compressibility on the peripheral flow are negligible in the first approximation. Since for $Re_p \ll 1$ the problem in either flow region is thus linear at leading order, the time-averaged pressure drop, obtained by considering higher-order corrections, exhibits characteristic values that are of order $\varepsilon(\Delta p)_f$ and $\varepsilon(\Delta p)_p$ along the film and across the periphery, respectively, their ratio remaining therefore of order $h_o/a \ll 1$. As a result, regardless of the value of Re_p, use of the steady relaxation condition $\langle P_1 \rangle(\xi = 1) = 0$ introduces asymptotic errors consistent with those involved in the general formulation outlined in § 4.3.1. For a detailed treatment of this matter, the interested reader is referred to [60].

4.5.1 Time-averaged squeeze-film overpressure and disk deformation

The steady pressure distribution $\langle P_1 \rangle(\xi)$, independent of the steady disk deformation $\langle W_1 \rangle(\xi)$ under the present perturbative formulation, can be determined by straightforward integration of (4.45) to give

$$\langle P_1 \rangle(\xi) = 3 \int_{\xi}^{1} \left\langle W_0 \frac{\partial P_0}{\partial \xi} \right\rangle (x) \, \mathrm{d}x - \frac{\sigma}{24} \langle P_0^2 \rangle , \tag{4.47}$$

where x serves as a dummy integration variable. Substitution of the expressions given in (4.23) provides

$$\langle P_1 \rangle = \begin{cases} \dfrac{1}{2} \mathrm{Re} \left\{ 3 \left[\bar{\Pi}(\xi_c) - \bar{\Pi}(\xi) + \int_{\xi_c}^{1} \Pi'^{*}(\tilde{\xi}) \Omega(\tilde{\xi}) \mathrm{d}\tilde{\xi} \right] - \dfrac{\sigma}{24} \bar{\Pi} \bar{\Pi}^{*} \right\}, & 0 \le \xi \le \xi_c \\ \dfrac{1}{2} \mathrm{Re} \left\{ 3 \int_{\xi}^{1} \Pi'^{*}(\tilde{\xi}) \Omega(\tilde{\xi}) \mathrm{d}\tilde{\xi} - \dfrac{\sigma}{24} \Pi \Pi^{*} \right\}, & \xi_c \le \xi \le 1 , \end{cases} \tag{4.48}$$

having made use of the identity $\left\langle \mathrm{Re}\{\mathcal{G} \mathrm{e}^{\mathrm{i}\tau}\} \mathrm{Re}\{\mathcal{H} \mathrm{e}^{\mathrm{i}\tau}\} \right\rangle = \mathrm{Re}\{\mathcal{G}^{*} \mathcal{H}\}/2$, where $\mathcal{G}$ and $\mathcal{H}$ are complex spatial functions and an asterisk denotes a complex conjugate. Note that, in the limit $\xi_c \to 0$, the second branch of the piecewise-defined equation (4.48) can be readily used to compute the steady pressure everywhere in the film except the axis of symmetry, i.e. for positive radial distances $0 < \xi \le 1$.

Integration of (4.46) provides the accompanying time-averaged deformation of the disk,

$$\begin{aligned}\langle W_1\rangle = C^6\Bigg(&\mathcal{I}_1(\xi_c)\ln\left(\frac{\xi_c}{\xi}\right)+\frac{1}{64}\int_{\xi_c}^{\xi}x^4[4\ln(x)-5]\langle P_1\rangle'(x)\mathrm{d}x-\frac{\ln(\xi)}{16}\int_{\xi_c}^{\xi}x^4\langle P_1\rangle'(x)\mathrm{d}x\\&+\mathcal{I}_2(\xi)\Big|_{\xi_c}^{\xi}+\frac{{\xi_c}^2[1+2\ln(\xi/\xi_c)]-\xi^2}{2\left[{\xi_c}^2-1+2/(1-\nu_d)\right]}\left[\mathcal{I}_1(\xi_c)+\frac{1}{16}\int_{\xi_c}^{1}x^4\langle P_1\rangle'(x)\mathrm{d}x\right]\Bigg),\end{aligned}\qquad(4.49)$$

expressed here in terms of the radial pressure gradient

$$\langle P_1\rangle'=\frac{\mathrm{d}\langle P_1\rangle}{\mathrm{d}\xi}=\begin{cases}-\dfrac{1}{2}\mathrm{Re}\left\{\bar{\Pi}'^*\left(3+\dfrac{\sigma}{12}\bar{\Pi}\right)\right\}, & 0\le\xi\le\xi_c\\[2ex] -\dfrac{1}{2}\mathrm{Re}\left\{\Pi'^*\left(3\Omega+\dfrac{\sigma}{12}\Pi\right)\right\}, & \xi_c\le\xi\le 1\end{cases}\qquad(4.50)$$

and the auxiliary integral functions

$$\begin{cases}\mathcal{I}_1(\xi)= & \dfrac{\xi^2}{4}\left[\dfrac{\xi^2}{4}\langle P_1\rangle+\ln(\xi)\int_{\xi}^{1}x^2\langle P_1\rangle'(x)\mathrm{d}x-\int_{\xi}^{1}x^2\ln(x)\langle P_1\rangle'(x)\mathrm{d}x\right]\\[2ex] \mathcal{I}_2(\xi)= & \dfrac{\xi^2}{16}\left[\dfrac{\xi^2}{4}\langle P_1\rangle+[2\ln(\xi)-1]\int_{\xi}^{1}x^2\langle P_1\rangle'(x)\mathrm{d}x-2\int_{\xi}^{1}x^2\ln(x)\langle P_1\rangle'(x)\mathrm{d}x\right].\end{cases}\qquad(4.51)$$

The general expression for the disk deformation (4.49) is seen to simplify in the limit of small clamp radii to give

$$\begin{aligned}\lim_{\xi_c\to 0}\langle W_1\rangle = C^6\Bigg(&\frac{1}{64}\int_{0}^{\xi}x^4[4\ln(x)-5]\langle P_1\rangle'(x)\mathrm{d}x-\frac{\ln(\xi)}{16}\int_{0}^{\xi}x^4\langle P_1\rangle'(x)\mathrm{d}x\\&+\mathcal{I}_2(\xi)-\frac{\xi^2(1-\nu_d)}{32(1+\nu_d)}\int_{0}^{1}x^4\langle P_1\rangle'(x)\mathrm{d}x\Bigg).\end{aligned}\qquad(4.52)$$

4.5.2 An analytical expression for the levitation force

Consistent with the simplified description of gas dynamics presented in § 4.3.1, the attractive levitation force that supports the applied pulling load is given by the expression

$$\langle\mathcal{F}_L\rangle=-2\pi\int_0^a\langle p-p_a\rangle\,r\mathrm{d}r\,,\qquad(4.53)$$

which follows from a cycle-averaged statement of Newton's 2nd law for the periodically oscillating system shown in figure 4.1(a), comprising both the central assembly and the annular portion of the disk. This definition may also be obtained by integrating the Kirchhoff–Love equation (4.9) across the annular portion of the disk $r_c \leq r \leq a$, substituting the resulting expression for the stress resultant $\mathcal{V}_c$ (4.10) into the equation of motion (4.1) and taking the time average thereof. The force (4.53) can be expressed in the suitable dimensionless form

$$\langle F_L \rangle = \frac{\langle \mathcal{F}_L \rangle}{\varepsilon^2 (\sigma/12) p_a \pi a^2} = -2 \int_0^1 \langle P_1 \rangle \xi \mathrm{d}\xi \,, \tag{4.54}$$

based on the scalings introduced in § 4.3.4. Integration by parts to yield the alternative expression $\langle F_L \rangle = \int_0^1 \xi^2 \big(\mathrm{d}\langle P_1 \rangle / \mathrm{d}\xi\big) \mathrm{d}\xi$, followed by substitution of the steady pressure gradient (4.50), finally provides

$$\begin{aligned} \langle F_L \rangle = -\frac{1}{2} \mathrm{Re} \Bigg\{ & \frac{12}{\sigma} \bar{A}^* \left(\frac{2\xi_c}{\varsigma^*} \left[2J_1(\varsigma^* \xi_c) - \varsigma^* \xi_c J_0(\varsigma^* \xi_c) \right] - \varsigma^* \bar{A} \mathcal{I}_{JJ}(\varsigma, \varsigma^*, \xi_c) \right) \\ & + \sum_{n=1}^{3} \sum_{m=1}^{3} \frac{\gamma_n^* \left(K^4 - \gamma_n^{*4} \right)}{C^6} \left[3 + \frac{\sigma \left(\gamma_m^4 - K^4 \right)}{12 C^6} \right] \mathcal{I}_L(\xi) \Bigg|_{\xi_c}^{1} \Bigg\} , \end{aligned} \tag{4.55}$$

involving the auxiliary function

$$\begin{aligned} \mathcal{I}_L(\xi) = {} & A_m A_n^* \mathcal{I}_{JJ}(\gamma_m, \gamma_n^*, \xi) + A_m B_n^* \mathcal{I}_{JY}(\gamma_m, \gamma_n^*, \xi) \\ & + B_m A_n^* \mathcal{I}_{YJ}(\gamma_m, \gamma_n^*, \xi) + B_m B_n^* \mathcal{I}_{YY}(\gamma_m, \gamma_n^*, \xi) \,, \end{aligned} \tag{4.56}$$

where the governing parameters σ, K and C are defined respectively in (4.14), (4.17*a*) and (4.17*b*), the coefficients $\bar{A}$, A_n and B_n (for $n = 1 : 3$) are defined compactly in (4.36), the complex constants ς and γ_n are given respectively in (4.25) and (4.29), and the four integral operators

$\mathcal{I}_{JJ}, \mathcal{I}_{JY}, \mathcal{I}_{YJ}$ and $\mathcal{I}_{YY}$ are defined collectively by

$$\begin{aligned}\mathcal{I}_{FG}(\alpha,\beta,\xi) &= \int^{\xi} \tilde{\xi}^2 F_0(\alpha\tilde{\xi}) G_1(\beta\tilde{\xi})\,\mathrm{d}\tilde{\xi} \\ &= \frac{2\beta\xi}{\left(\alpha^2-\beta^2\right)^2}\left[\beta F_0(\alpha\xi)G_1(\beta\xi) - \alpha F_1(\alpha\xi)G_0(\beta\xi)\right] \\ &\quad + \frac{\xi^2}{\alpha^2-\beta^2}\left[\beta F_0(\alpha\xi)G_0(\beta\xi) + \alpha F_1(\alpha\xi)G_1(\beta\xi)\right], \end{aligned} \tag{4.57}$$

where F_m and G_m each represents a Bessel function of the first or second kind (J_m or Y_m) of mth order [85, p. 301]. Note that, as before, an asterisk denotes a complex conjugate. The effective operating efficiency $\langle \mathcal{F}_L \rangle / \mathcal{F}_m$ of an SFL system can thus be expressed here in the appropriately normalized form $\langle \mathcal{F}_L \rangle / (\varepsilon \mathcal{F}_m) = \pi \mu_a \omega a^4 \langle F_L \rangle / (h_o^3 |\mathcal{X}|)$, involving the complex constant $\mathcal{X}$ defined in (4.43).

For a vanishing clamp radius $\xi_c \to 0$, the expression for the steady levitation force (4.55) simplifies to

$$\lim_{\xi_c \to 0} \langle F_L \rangle = -\frac{1}{2}\mathrm{Re}\left\{ \sum_{n=1}^{3}\sum_{m=1}^{3} \frac{\gamma_n^*\left(K^4 - \gamma_n^{*4}\right)}{C^6}\left[3 + \frac{\sigma\left(\gamma_m^4 - K^4\right)}{12C^6}\right]\left[\mathcal{I}_L(1) - \mathcal{I}_c\right]\right\}, \tag{4.58}$$

where

$$\mathcal{I}_c = \lim_{\xi_c \to 0} \mathcal{I}_L(\xi_c) = \frac{4/\pi}{\gamma_m^2 - \gamma_n^{*2}}\left[\frac{\gamma_n^*(B_m A_n^* - A_m B_n^*)}{\gamma_m^2 - \gamma_n^{*2}} + \frac{B_m B_n^*}{\pi\gamma_n^*}\left(1 - \frac{2\ln(\gamma_m/\gamma_n^*)}{(\gamma_m/\gamma_n^*)^2 - 1}\right)\right]. \tag{4.59}$$

Combining (4.58) with the reduced expression (4.44) for the structural impedance amplitude $|V_c|$ yields a simple formula for the quantity

$$\lim_{\xi_c \to 0} \frac{\langle \mathcal{F}_L \rangle}{\varepsilon \mathcal{F}_m} = \frac{C^6}{2}\frac{\lim_{\xi_c \to 0}\langle F_L \rangle}{\lim_{\xi_c \to 0}|V_c|}, \tag{4.60}$$

a dimensionless measure of the efficiency of an SFL system for which $\xi_c = r_c/a \ll 1$.

4.6 Discussion of results

The fluid–structure problem addressed above involves five principal dimensionless parameters, as defined in § 4.3.4: the small perturbation parameter $\varepsilon = b/h_o \ll 1$, which compares the central displacement amplitude of the oscillating disk with the time-averaged central width of the gas layer, the relative clamp radius $\xi_c = r_c/a$, which specifies the radial distance r_c beyond which the disk is allowed to undergo flexure (see figure 4.1(b) for clarification), the squeeze number σ, which quantifies the strength of viscous wall friction retarding airflow in the thin layer and give rise to compressibility, an elastic wavenumber K, which measures the disk inertia relative to its flexural rigidity, and a coupling parameter C, which controls the degree of influence of aerodynamic forcing on the disk bending. In the asymptotic limit $\varepsilon \ll 1$ considered here the perturbation parameter ε does not appear explicitly in the formulation. It enters only as a scale factor for the pressure in the gas layer. Variability of the clamp radius ξ_c lends this formulation applicable to a wide range of practical configurations, as exemplified by the sample calculations to be carried out in section 4.6.4. Of greatest interest here are the final parameters σ, K and C which govern the fundamental fluid–structure dynamics, to be investigated below by focusing mainly on centrally excited configurations (i.e. $\xi_c \to 0$).

The variation with $\sigma \propto \omega a^2/h_o^2$ and K of the typically repulsive, steady pressure force generated by SFL systems has been explored thoroughly in prior literature. In particular, an increase in $\sigma \propto h_o^{-2}$, realized typically by reducing the mean central distance h_o between the oscillating disk and the opposite surface, results in a magnification of the repulsive force proportionally with the inverse square of h_o [5, 19]. This growth of repulsion is found to occur for sufficiently small distances h_o regardless of the flexibility of the oscillator [93], the latter quantified by the parameter K. Defined with use of both the forcing frequency of vibration ω and the stiffness of the disk based on its geometric and material properties, the parameter K denotes the relevant elastic wavenumber, i.e. the characteristic wavelength of flexure scales as aK^{-1} for a disk of radius a. A transition to attractive forces is found to occur for systems with sufficiently low frequency ω [37] and/or oscillator size a [4, 6]. For these systems, attraction emerges only beyond a critical distance h_o, i.e. below a critical value of $\sigma \propto \omega a^2/h_o^2$.

The range of operating conditions ω and a for which attraction can be found, as well as the resulting attractive load capacity, is found to depend critically on the waveform exhibited by the oscillating disk [101]. In the case of an infinitely stiff oscillator, for which $K = 0$, the disk/piston moves as a rigid body and produces repulsive forces for nearly all values of σ [19]. In contrast, for critical values of K that correspond to the natural frequencies of a thin oscillator, the disk performs resonant flexural oscillations, such as those depicted in figure 4.3(a), and produces powerful attractive forces for a substantial range of values of σ [101]. The precise values of these critical elastic wavenumbers K, weakly dependent on the Poisson's ratio ν_d of the disk material, are exemplified in table 4.1 of Appendix 4.8 for $\nu_d = 0.3$, the value selected to produce the dimensionless results presented below. It must be mentioned here that rigid-body oscillation can provide attraction as well under a limited range of operating conditions, characterization of which requires consideration of fluid inertia [4, 60] which is neglected in the lubrication limit considered in the present study. However, the corresponding load capacities are severely limited in comparison to those enabled by resonant flexural oscillation—a thousandfold smaller in practical systems [101]. It is also worth noting the great importance of the precise excitation method. Excitation of the oscillator with use of a bulky external transducer may alter substantially the natural frequencies of the oscillating assembly, resulting in modified resonant waveforms that feature large local relative amplitudes $w(r)/w(r_c)$ near the outer edge of the oscillator $r = a$ [10]. The overall magnification of the peak amplitude profile due to this near-edge 'flapping' is found only to increase the repulsive load capacity of the system [93]. Of interest here, instead, are systems excited with use of light, localized excitation sources that alter minimally the natural frequencies of a thin oscillator and thus give rise to significant attractive forces [3, 49].

Motion of a centrally excited disk ($\xi_c \to 0$) at its second resonant mode ($K = 6.2$) is visualized in figure 4.3(a) for a value of the squeeze number $\sigma = 20$ that gives rise to an attractive force. The coupling parameter C is assigned a value of zero to represent the limit of one way

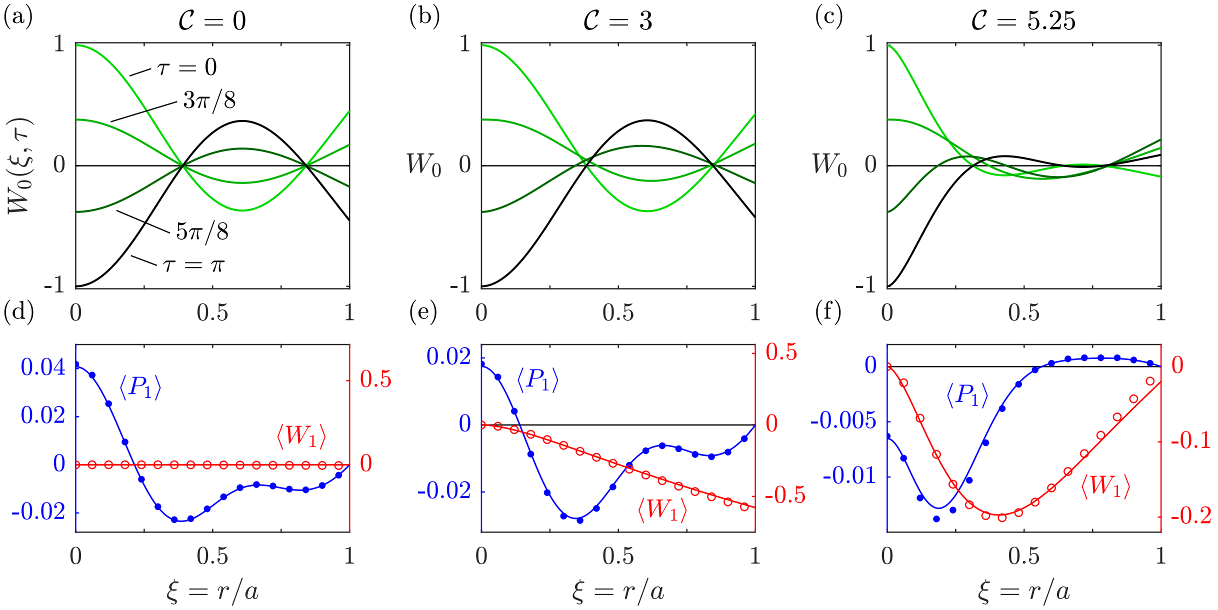

Figure 4.3. Behavior of a two-way-coupled SFL system operating with an elastic wavenumber of $K = 6.2$ and a squeeze number of $\sigma = 20$. Represented in panels (a)–(c) are the flexural disk oscillations for increasing values of the coupling parameter C, and shown below (d)–(f) are the associated radial distributions of time-averaged pressure and disk displacement.

coupling, a state for which the disk motion is unaffected by the airflow that it excites in the squeeze film (see Appendix 4.8 for mathematical details). As seen from the blue curve in figure 4.3(d), the distribution of steady pressure along the gas layer features two local minima whose radial locations correspond closely with those of the two nodal circles in the standing flexural wave, $r/a \approx 0.4$ and 0.8. In the absence of aerodynamic forcing, the disk oscillates sinusoidally about an undeformed mean position, as indicate by the red line in figure 4.3(d). This one-way-coupled description has been shown in prior literature [101] to successfully predict the large attractive load capacities observed in flexural SFL systems [3, 49], but fails to capture certain salient aspects of the underlying physics. In particular, experimental measurements of the mean pressure distribution show no signs of such near-nodal minima and instead display a drop of pressure from its ambient value at the edge of the air layer to a lower value at its central axis, as depicted in figure 4.2(b). As shown in the same figure, the disk correspondingly exhibits a measurable time-averaged deformation that features a valley at a critical radial location

$r/a \approx 0.2$ [3]. Accounting for two-way fluid–structure coupling by considering nonzero values of C yields greatly improved agreement with these observations, as described below.

Increasing the value of the coupling parameter to $C = 3$ yields but minor modifications to the one-way-coupled results, as seen in figures 4.3(b) and 4.3(e). Namely, the two nodal points are slightly disturbed and give way to localized regions of minimal amplitude, symptomatic of a damped oscillator [125]. The corresponding pressure distribution is slightly skewed, and the disk oscillates about a deformed mean shape that slopes monotonically toward the wall for increasing radial distances. As suggested above, pressure variations in the squeeze film arising from highly viscous gas flow serve to dampen the disk oscillations when $C > 0$, although the degree of damping seems to be limited for an operating condition where $C = 3$ and $K = 6.2$. When the strength of aerodynamic damping is further increased, by setting $C = 5.25$, the centrally excited disk appears to undergo traveling-wave-type oscillations whose amplitude is severely restricted for $r/a \gtrsim 0.3$, as shown in figure 4.3(c). As shown below in 4.3(f), under such strongly coupled conditions, the steady overpressure assumes a negative value at the central axis $r = 0$ and the steady disk deformation varies non-monotonically with radial distance, both in qualitative congruence with the recent experimental measurements by [3]. Furthermore, the apparent absence of the first nodal region in the predicted disk waveform suggests that the collection of sand observed at $r/a \approx 0.3$ does not constitute a classical Chladni pattern and owes instead to the gravity-driven transport of particles toward the valley formed by the mean disk deformation. In this connection, it is worth noting that the sand pattern formed in the experiment for smaller mean separation distances h_o is markedly non-axisymmetric, indicative of eccentric excitation.

For each of the three cases considered above, asymptotic predictions of the time-averaged pressure distribution and disk deformation are confirmed with use of a finite-difference solution of the governing equations (4.15) and (4.16), results of which are visualized in the form of dots and circles in figures 4.3(d)–(f). As can be seen, for the moderately small relative amplitude $\varepsilon = 0.1$ used in the integration, the numerical solutions display satisfactory agreement with the asymptotic predictions. The governing equations were discretized with use of second-order central-space finite-difference approximations and marched in time asynchronously, the Reynolds equation with a forward-Euler scheme and the Kirchhoff–Love equation with use of a second-order central-difference scheme [88, 126]. Initializing the system with uniform disk displacement $w(r) = b$ and zero velocity $\partial w/\partial t = 0$ was found to yield convergent results, except for the case of one-way coupling, which required substituting the uniform initial displacement with the known analytical expression for the anticipated peak amplitude profile (see appendix 4.8). This is due to the absence of damping for $C = 0$ that prevents the dissipation of secondary frequency content that may arise in the initial stages of oscillation. Accurate characterization of the disk motion for $C \neq 0$ required a sufficiently fine spatial discretization $\Delta\xi = \Delta r/a$ and, in turn, stable convergence to periodicity of the film pressure required a sufficiently small time step $\Delta\tau = \omega\Delta t$. For instance, the solution for $C = 3$ represented in figure 4.3(e) was obtained using $\Delta\xi = 0.01$ and $\Delta\tau = 6.3 \times 10^{-4}$. The restriction on the time step for numerical stability generally loosens when increasing the degree of damping; for instance, the solution for $C = 5.25$ represented in figure 4.3(f) was obtained using $\Delta\tau = 8.4 \times 10^{-4}$. Note finally that the precise shape of the steady disk deformation $\langle W \rangle$ continued to fluctuate noticeably even after the associated levitation force had converged with a convergence ratio of less than 0.5%.

Motivated by the preliminary results presented above, the following discussion explores the influence of aerodynamic damping on the performance of a flexural squeeze-film system—in particular, the attractive load capacity $\max(\langle \mathcal{F}_L \rangle)$ that is enabled by a sinusoidal excitation force of given amplitude $\mathcal{F}_m$.

4.6.1 Parametric dependence of the levitation force

Visualized in figures 4.4(a)–(c) is the variation with the principal governing parameters—the squeeze number σ, the elastic wavenumber K and the coupling parameter C—of the levitation force produced by a centrally excited disk ($\xi_c \to 0$). The force is computed in the dimensionless form $\langle \mathcal{F}_L \rangle/(\varepsilon^2 p_a \pi a^2)$, normalized with the square of the relative central displacement amplitude $\varepsilon = b/h_o$. In practical systems, the value of K is typically determined by the selection of an

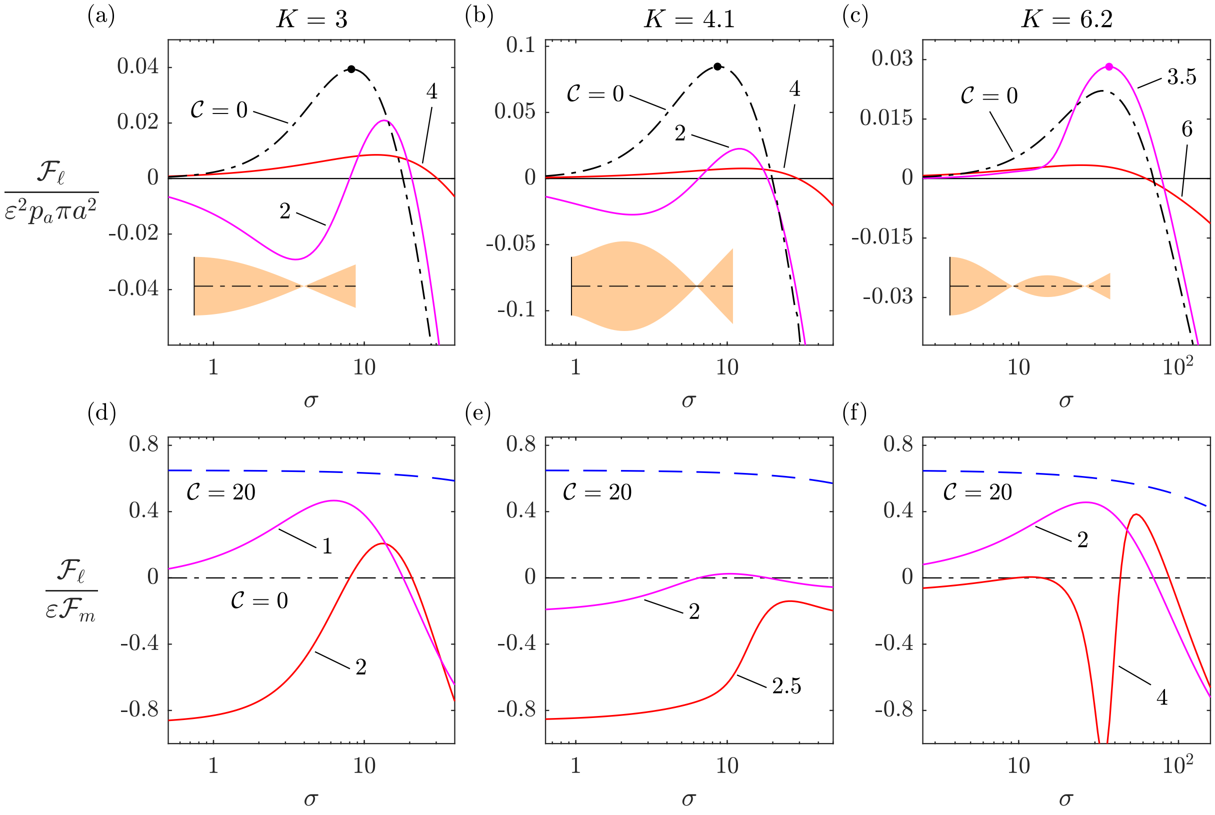

Figure 4.4. Variation with the squeeze number σ and coupling parameter C of the dimensionless levitation force (a)–(c) and (d)–(f) the associated efficiency for three values of the elastic wavenumber K.

oscillator and an optimal operating frequency, while those of $\sigma \propto h_o^{-2}$ and $C \propto h_o^{-1/2}$ are subject to strong dependence on the separation distance h_o, which varies during the pull-off process as explained in section 4.3. The curves shown in each panel of figures 4.4(a)–(c) may thus be interpreted to represent the variation of the attractive force with separation distance, for a disk with given structural properties oscillating at a fixed frequency. The wavenumbers $K = 3$ and 6.2 represented respectively in panels 4.4(a) and (c) correspond to the first and second natural frequencies of an undamped disk with $\nu_d = 0.3$, while the intermediate wavenumber $K = 4.1$ represented in panel (b) corresponds to a non-modal frequency. The broken curve in each panel represents the one-way-coupled solution where $C = 0$ [101]. For all curves shown, attraction persists till a critical value of σ is reached, beyond which the force transitions to growing

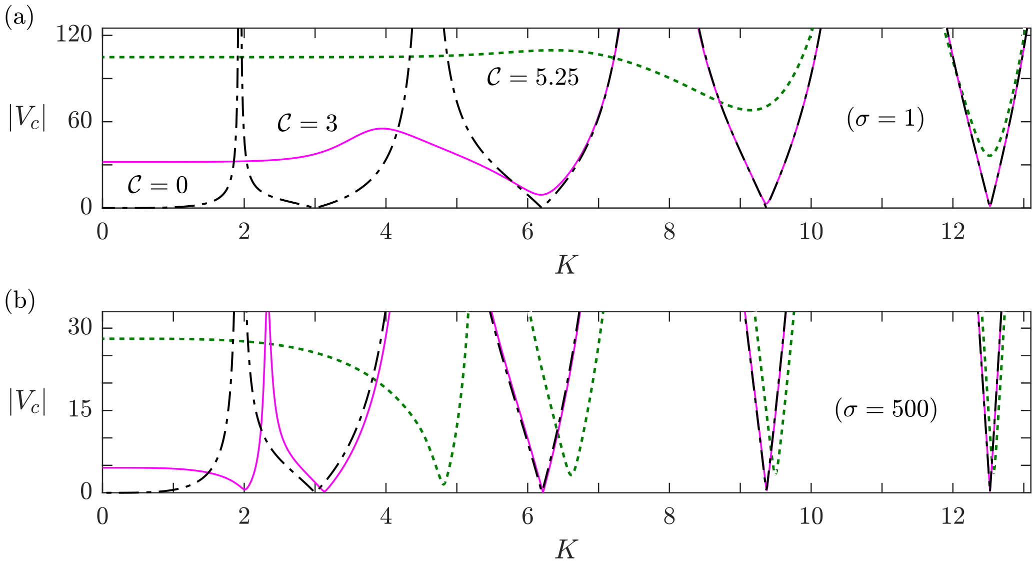

Figure 4.5. Variation with the elastic wavenumber K and the squeeze number σ of the dimensionless amplitude of the forces resisting disk oscillation. Curves are shown for three values of the coupling parameter $\mathcal{C}$.

repulsion, as explained earlier. Inside the parametric domain of attraction, the dimensionless force achieves a maximum that varies strongly with the degree of coupling. For $K = 3$ and 4.1, the greatest load capacity appears to occur when $\mathcal{C} = 0$, and for $K = 6.2$, when $\mathcal{C} \approx 3.5$. In the limit of highly damped oscillations $\mathcal{C} \gg 1$, the normalized levitation force $\langle \mathcal{F}_L \rangle / (\varepsilon^2 p_a \pi a^2)$ diminishes toward zero.

Among the elastic wavenumbers K represented in figures 4.4(a)–(c), the dimensionless force clearly exhibits the greatest values for $K = 4.1$, owing to an anomalous magnification of local relative amplitudes $w(r)/b$ as seen from the shaded waveforms. However, this apparent magnification is accompanied by the cost of augmented resistance to the disk oscillation arising from internal bending forces. In practical SFL systems, the structural resistance under such off-resonant operating conditions reduces substantially the central displacement amplitude b and thus also the energy efficiency [93]. In the present case of central forcing, the simplified formula (4.44) can be used to compute a dimensionless amplitude $|V_c|$ of the time-periodic structural impedance, which is influenced non-negligibly by the squeeze-film overpressure when $\mathcal{C} > 0$.

Represented in figures 4.5(a) and 4.5(b) by the broken curve is the variation of $|V_c|$ with K for one-way-coupled systems. The curves for $\sigma = 1$ and 500 are identical due to the absence of fluidic damping for $C = 0$, and exhibit roots for values of the wavenumber $K \approx 3.0, 6.2, 9.4, \cdots$ that represent the natural frequencies of the disk (beside the non-resonant rigid-body mode $K = 0$). As shown in panel 4.5(a), increasing the value of C homogenizes the impedance for a range of wavenumbers K, washing out the first few resonant modes. The affected range of K and the number of suppressed modes grow with the value of C. For sufficiently large values of K that satisfy $K^4 \sim C^6$, the variation of impedance with K gradually returns, in accordance with a restored three-term balance in the Kirchhoff–Love equation (4.16). Noting that $K^4/C^6 \propto \omega$, this result agrees well with the observed decrease of the effective damping ratio of a flexural squeeze-film bearing for increasing values of the near-resonant operating frequency ω [106]. It must be emphasized here that, although $|V_c|$ exhibits local minima of decreasing value as K grows, it never becomes identically zero for $C > 0$—the presence of damping, however weak, precludes the onset of ideal resonance. Finally, the curves in panel 4.5(b) reveal that an increase in the squeeze number σ mitigates modal suppression, but the reappearing minima of $|V_c|$ are substantially shifted along the frequency spectrum, the latter in agreement with the findings of [105]. Interestingly, the non-resonant 'zeroth' mode $K = C = 0$ is shifted to $K \approx 2$ when $C = 3$.

4.6.2 A measure of efficiency of levitation

As discussed earlier, the levitation force represented in figures 4.4(a)–(c) is computed for a constant value of the relative displacement amplitude $\varepsilon = b/h_o$, with no account taken of the required amplitude $\mathcal{F}_m$ of the excitation force. For a centrally forced disk, $\mathcal{F}_m$ can be deduced directly from the impedance amplitude $|V_c|$ as explained in section 4.4.2, allowing straightforward computation of the ratio $\langle\mathcal{F}_L\rangle/(\varepsilon\mathcal{F}_m)$, a measure of the efficiency of an SFL system, as defined in (4.60). The parametric dependences of this levitation efficiency are represented in figures 4.4(d)–(f), illustrating the conditional benefit of operating near a natural frequency. Note first that the efficiency, which scales with C^6 as per (4.60), vanishes in the limit of one-way coupling

$\mathcal{C} = 0$ for all values of K and σ. However, for any order-unity value of the coupling parameter $\mathcal{C}$, representing a moderate level of viscous aerodynamic damping, the maximal efficiency of attractive levitation obtained by varying the squeeze number σ is substantially lower for the non-modal wavenumber $K = 4.1$ than for the resonant wavenumbers $K = 3$ and 6.2. Interestingly, this advantage of near-resonant operation disappears in the case of strong coupling $\mathcal{C} \gg 1$. For $\mathcal{C} = 20$, the variation with σ is weak and nearly identical for all three values of K, well in agreement with the phenomenon of modal suppression found in figure 4.5. In contrast with the results shown in figures 4.4(a)–(c), accounting for the required excitation force $\mathcal{F}_m$ reveals that the levitation force $\langle \mathcal{F}_L \rangle$ does not collapse under strong damping—in fact, the maximal attractive load enabled by a given excitation force is substantial and appears to be independent of the elastic wavenumber K and the squeeze number σ.

Upon inspection of the curves in figure 4.4(d), it is apparent that the peak efficiency

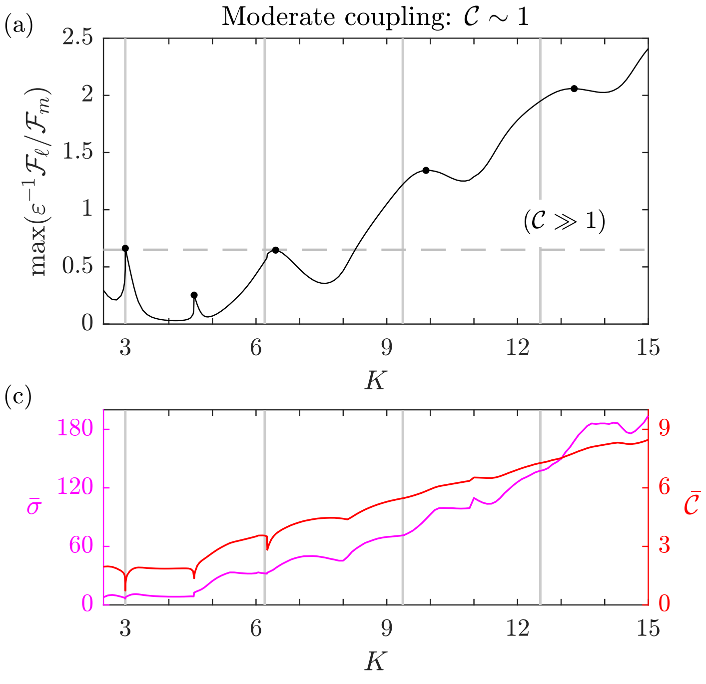

Figure 4.6. Variation with the elastic wavenumber K of (a) the observed local maximum in efficiency and (c) the order-unity values of the squeeze number $\bar{\sigma}$ and the coupling parameter $\bar{\mathcal{C}}$ for which it occurs. Depicted in panels (b) and (d) are the periodic disk deformations and steady pressure distribution, respectively, in the limit of strong coupling $\mathcal{C} \gg 1$.

exhibits a non-monotonic dependence on C, first increasing from zero to 0.4 as C rises from zero to 1, then halving when $C = 2$. This indicates the presence of a local maximum in efficiency that occurs for a critical operating condition defined by $\sigma = \bar{\sigma}$ and $C = \bar{C} \sim 1$. Represented in figure 4.6(a) by the solid curve is the value of this local maximum, $\max(\varepsilon^{-1}\langle\mathcal{F}_L\rangle/\mathcal{F}_m)$, for wavenumbers K up to 15. Displayed below in panel 4.6(c) are the associated critical parametric values $\bar{\sigma}$ and $\bar{C} \sim 1$. For wavenumbers $K \lesssim 8.3$, such as those represented in figures 4.4(d)–(f), the local maximum appears to be generally lower than the universal peak efficiency of ≈ 0.65 approached in the limit of strong coupling $C \gg 1$, the latter indicated by a dashed horizontal line in figure 4.6(a). This behavior is found to reverse, however, for larger values of $K \gtrsim 8.3$ representing disks with lower stiffness and/or oscillations with higher excitation frequency. More importantly, the sensitivity of the local maximum to the wavenumber K, and thus the degree of advantage earned by near-resonant operation, appears to diminish as K increases. Subsequent peaks of efficiency which appear for increasing critical values of K, indicated by dots on the curve, are less accentuated. As discussed earlier, these critical values of K are noticeably displaced from the corresponding resonant wavenumbers of the undamped disk (for which $C = 0$), the latter represented in panel 4.6(a) by grey vertical lines.

4.6.3 Universal limiting behavior for strong coupling

It was shown earlier that, for large values of the coupling parameter C, asymptotic predictions of the time-averaged pressure in the air layer and the associated steady disk deformation exhibit improved agreement with the recent experimental observations of [3]. The performance of an SFL system for such states of strong fluid–structure coupling was found in figures 4.6(d)–(f) to exhibit a diminishing dependence on the squeeze number and the elastic wavenumber. We explore below the formal limit $C \gg 1$ with $\sigma \sim K \sim 1$, mathematical details of which are included in Appendix 4.8. Most notably, the problem in this limit is found to be independent of the parameters σ and K and of the Poisson's ratio ν_d, due to which the appropriately rescaled limiting expressions describing the disk motion (4.69a) and the steady film pressure (4.72) are universal (i.e. parameter-free).

For large values of C, the disk motion is greatly suppressed by aerodynamic damping beyond a small radial distance, as shown in figure 4.3(c). Furthermore, while for states of weak or moderate coupling $C \lesssim 1$, the disk oscillations resemble a standing wave as seen in figures 4.3(a) and 4.3(b), under the action of strong viscous damping with $C \gg 1$, the disk undergoes pronounced traveling-wave deformations. The limiting curves depicted in figure 4.6(b) represent the components of this wave that are in phase (solid) and out of phase (broken) with the driving oscillations. The rapid disk undulations exhibit a large flexural wavenumber that scales linearly with $C \gg 1$, in place of the elastic wavenumber K found for C of order unity.

The associated time-averaged overpressure in the squeeze film assumes a diminishing value that scales as $C^{-2} \ll 1$ for a constant relative amplitude $\varepsilon = b/h_o$, explaining the collapsing levitation forces seen in figures 4.4(a)–(c) for large values of C. As shown in figure 4.6(d), the steady pressure in the limit $C \gg 1$ drops monotonically from the film edge to its center. As observed by [3] during pull-off tests, decreasing the degree of coupling widens the apparent region of radial pressure relaxation $0 \leq r/a \lesssim 5C^{-1}$. The associated efficiency of levitation (4.60), which normalizes the levitation force $\langle \mathcal{F}_L \rangle$ with the needed excitation amplitude $\mathcal{F}_m$, converges in this limit to a constant value of $\langle \mathcal{F}_L \rangle / (\varepsilon \mathcal{F}_m) \approx 0.6495$, in accordance with the weakly varying curves for $C = 20$ drawn in figures 4.4(d)–(f).

An interesting consequence of this universal behavior for $C \gg 1$ is that, for strongly coupled systems, one may anticipate a diminishing dependence of system behavior on the size of the oscillator. If the disk radius a is sufficiently large such that $C^6 \gg K^4$, increasing a further while preserving all other operating parameters will not increase the load capacity. This anomalous conclusion is exemplified below by way of sample calculations for a practical SFL system.

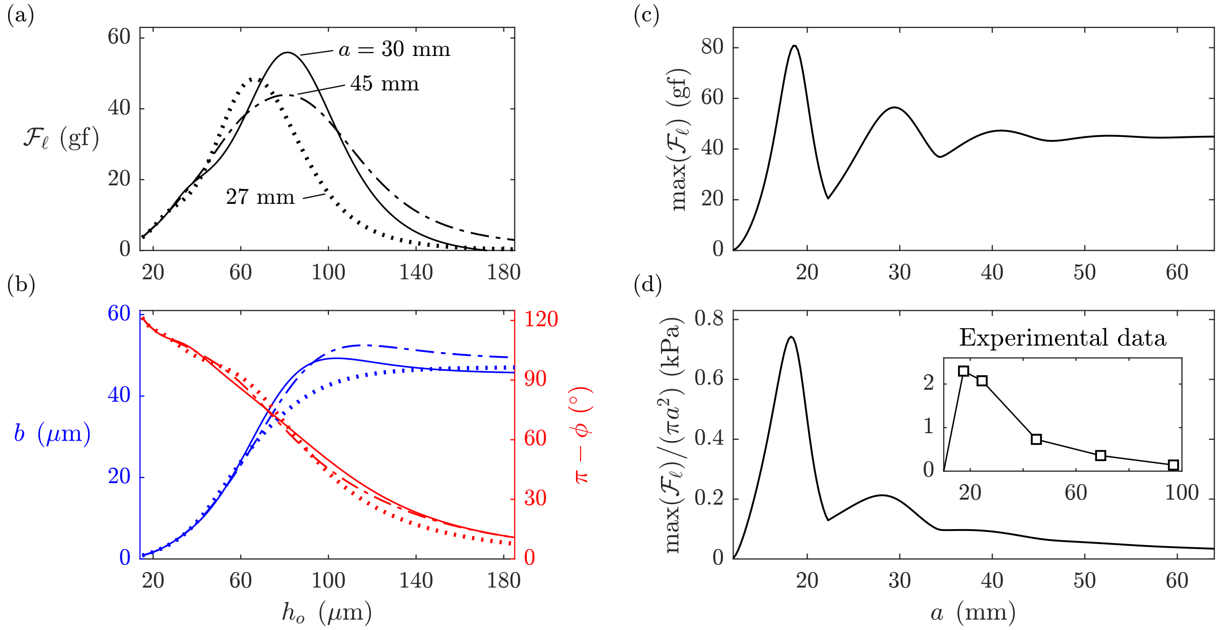

Figure 4.7. Variation with separation distance of (a) the attractive force and (b) the amplitude and phase lag of central disk displacement, and (c,d) variation with disk radius of the load capacity and its ratio to disk area, the latter compared with measurements by [3].

4.6.4 Prediction of load capacity for practical systems

In figure 4.4, variation of the levitation force $\langle \mathcal{F}_L \rangle$ with the mean central separation distance h_o was studied by investigating a dimensionless parametric domain spanned by the squeeze number σ and the coupling parameter C. While these two parameters are formally independent in the present theoretical formulation, in practical SFL systems they evolve together as dictated by their respective dependences on the distance: $\sigma \propto h_o^{-2}$ and $C \propto h_o^{-1/2}$. Thus, the actual load capacity $\max[\langle \mathcal{F}_L \rangle(h_o)]$ may fall short of the idealistic value predicted in figure 4.6(a), warranting a system-specific calculation as done below.

Displayed in figure 4.7(a) is the predicted pull-off curve $\langle \mathcal{F}_L \rangle(h_o)$, computed using the asymptotic formulation derived in § 4.3–§ 4.5, for an SFL system operating under conditions similar to those used in the recent experiment by [3]. A motor with a forcing amplitude of $\mathcal{F}_m = 74.5$ gf and frequency of $\omega/(2\pi) = 200$ Hz is mounted to a cylinder of radius $r_c = 10$ mm. The oscillating assembly, weighing $m_c = 10$ g, is mounted concentrically to a disk of variable radius a and fixed thickness $t_d = 150\,\mu$m. The disk is made of polyester plastic with Young's modulus $E_d = 3.65$ GPa, mass density $\rho_d = 1.38$ g/cm^3 and Poisson's ratio $\nu_d = 0.48$ [94, 127]. The system operates in standard air with ambient pressure $p_a = 101325$ pa, density $\rho_a = 1.225$ kg/m^3 and viscosity $\mu_a = 1.81 \times 10^{-5}$ kg/(m·s). The separation distance h_o is varied from 15 to 185 μm.

The attractive levitation force is seen to initially increase, reaching a maximal value $\max(\langle \mathcal{F}_L \rangle)$ for a critical distance $h_o = \bar{h}_o$ beyond which it decays gradually. Note that, in practical systems, displacing the disk beyond $\bar{h}_o$ requires exerting a force greater than the maximal load capacity, yielding instead an abrupt failure of levitation [3]. In principle, use of the present asymptotic formulation introduces in the computation relative errors that scale with b/h_o, h_o/a and $h_o^2/(\mu_a/\rho_a/\omega)$, the latter of which is of order unity when $h_o \gtrsim 75\,\mu$m. Nevertheless, the scale of forces $\langle \mathcal{F}_L \rangle$ seen in the rising portion of the curves $h_o \lesssim 75\,\mu$m compares favorably with that reported in the experiment [3] for small distances of order 100 μm, as seen from figure 4.2(a), in stark contrast with the theoretical predictions produced previously with use of a one-way coupled formulation [101]. It can be anticipated that description of the observed gradual rise of $\langle \mathcal{F}_L \rangle$ to larger values ≈ 500 gf at greater distances $h_o \approx 2500\,\mu$m requires generalizing the present formulation to account for effects of fluid inertia that are non-negligible when $h_o^2 \sim \mu_a/\rho_a/\omega$.

On the other hand, when the separation distance is reduced, the attractive levitation force is found to collapse toward zero, in contrast with the transition to dramatically large repulsive forces observed in experiments with much stiffer oscillators [6, 37]. While in such cases the oscillator may be subject to negligible aerodynamic coupling, in the present example the augmented degree of coupling $C \propto 1/\sqrt{h_o}$ at small distances h_o results in the substantial suppression of disk motion, as revealed by figure 4.7(b). Depicted in panel (b) is the variation with h_o of the amplitude b and phase lag ϕ of the driving cylinder oscillations. As the disk is pulled away from the wall, b generally increases due to a weakening of the viscous aerodynamic impedance and ϕ approaches 180°, as expected for a forced harmonic oscillator [114].

The dependence of the load capacity $\max(\langle \mathcal{F}_L \rangle)$ on the disk radius a is elaborated in figure 4.7(c), showing rapid variation for small values of $a \sim r_c$ but converging asymptotically for larger radii, just as predicted in § 4.6.3. As a result, the associated value of the area-normalized load capacity $\max(\langle \mathcal{F}_L \rangle)/(\pi a^2)$ collapses beyond $a \approx 20$ mm, as shown in figure 4.7(d). As seen from the inset in panel 4.7(d), this prediction agrees well with the observations of [3], who alluded to the possible benefit of increasing the number of oscillators rather than their size when upscaling an SFL system.

4.7 Conclusions and recommendations for future work

Developed in this chapter is a reduced theoretical description of the pulsatile airflow excited in a slender air layer by the normal oscillations of a compliant bounding surface. The associated problem of elastohydrodynamic lubrication is relevant to the study of squeeze-film levitation (SFL) systems that are driven by highly flexible oscillators, which were shown in recent experiments to exhibit steady attractive load-bearing capacities a thousandfold larger than those driven by stiffer oscillators. Consideration of two-way-coupled fluid–structure interactions is found in this study to provide significantly improved accuracy in the theoretical characterization of such highly flexural SFL systems.

The present theory constitutes an extension of prior work that addressed the airflow excited by prescribed modal oscillations of a disk, a one-way-coupled problem that is governed by two distinct parameters—an elastic wavenumber K characterizing the flexibility of the disk and the squeeze number σ measuring the level of gaseous compressibility induced due to viscous wall friction [101]. Identified here is a third parameter of importance, C, which quantifies the degree to which the disk oscillations are dampened by the coupled pressure variations in the film. While the prior theory, for which $C = 0$, successfully predicted the scale of the time-averaged attractive forces seen in experiments by [3], it failed to capture accurately the causal distribution of pressure in the air layer and the measured deformations of the disk, those which are closely reproduced in the present solution for sufficiently large values of C. The solution exhibits a universal behavior in the limit $C \gg 1$ describing a state of strong coupling, whence we find that the load capacity provided by an oscillating disk fails to grow when the disk radius is increased beyond a critical value, just as observed by [3].

Further observations by the BRD lab [3] and Dr. Colasante [49] motivate generalization of the present formulation to describe (i) large deformations of the oscillator that are comparable to its thickness [116, 128], (ii) possible contact between a highly flexible oscillator and the opposite wall for small separation distances [3, 96, 129], (iii) nonlinear effects of fluid inertia in the gas layer and its periphery that are no longer negligible under the large separation distances for which the highest attractive forces are measured [60, 74, 101], (iv) possible aerodynamic instabilities for large-scale systems [54], (v) dissipative effects of structural damping that may be important in describing near-resonant oscillation [125], (vi) oscillators made of non-homogeneous and anisotropic materials [129] and (vii) hysteresis in the pull-off process due to abrupt application of the pulling load. The development of high- and multi-fidelity models that address these effects and thus predict system behavior accurately for a wide range of operating conditions would greatly assist the design and realization of robust SFL devices—for example, by supplementing active control mechanisms that mitigate the substantial stochasticity observed in devices driven by highly flexible oscillators [3]. The avenues of future research recommended above apply also for non-axisymmetric SFL configurations that are found in emerging applications such as mobile robots and contactless grippers [99, 100].

4.8 Appendix: Limiting behavior for extreme values of the coupling parameter C

4.8.1 One-way coupling $C = 0$ for arbitrary clamp radius $0 < \xi_c < 1$

We begin by noting that computation of the levitation force $\langle F_L \rangle$ with use of the integral identity (4.57) may yield unreliable, divergent results for critically small values of C. In such cases, it is recommended to confirm the computed value of $\langle F_L \rangle$ with use of direct numerical integration in (4.55) (or, for vanishingly small clamp radii, (4.58)). Fortunately, such numerical issues are seen to arise only after the computed value effectively converges to the limiting solution corresponding to $C = 0$. The associated limiting problem of one-way coupling, considered earlier for the case $\xi_c = 0$ [101], is described below for arbitrary clamp radii $0 < \xi_c < 1$.

When $C = 0$, the disk motion is unaffected by the aerodynamic force, whence the function W can be found by integrating the unforced Kirchhoff–Love equation

$$\left(\frac{\partial^2}{\partial \xi^2} + \frac{1}{\xi}\frac{\partial}{\partial \xi}\right)^2 W + K^4 \frac{\partial^2 W}{\partial \tau^2} = 0, \tag{4.61}$$

obtained by setting $C = 0$ in (4.16). The solution to (4.61) that satisfies the appropriate boundary conditions (4.19) can be written in the form $W = S(\xi)\cos\tau$, with

$$S = \begin{cases} 1 & , \quad 0 \le \xi \le \xi_c \\ \dfrac{J_0(K\xi) + C_1 Y_0(K\xi) + C_2 I_0(K\xi) + C_3 K_0(K\xi)}{J_0(K\xi_c) + C_1 Y_0(K\xi_c) + C_2 I_0(K\xi_c) + C_3 K_0(K\xi_c)} & , \quad \xi_c \le \xi \le 1, \end{cases} \tag{4.62}$$

where I_m and K_m represent respectively the mth-order modified Bessel functions of the first and second kinds, and the three constant coefficients C_i $(i = 1:3)$ can be written in the compact vectorial form

$$\begin{bmatrix} C_1 \\ C_2 \\ C_3 \end{bmatrix} = - \begin{bmatrix} Y_1(K\xi_c) & -I_1(K\xi_c) & K_1(K\xi_c) \\ Y_1(K) & I_1(K) & -K_1(K) \\ \Xi_Y^-(K) & -\Xi_I^-(K) & -\Xi_K^+(K) \end{bmatrix}^{-1} \begin{bmatrix} J_1(K\xi_c) \\ J_1(K) \\ \Xi_J^-(K) \end{bmatrix}, \tag{4.63}$$

involving the auxiliary function

$$\Xi_{\mathcal{B}}^{\pm}(x) = \mathcal{B}_0(x) \pm \frac{1-\nu_d}{x}\mathcal{B}_1(x), \tag{4.64}$$

where $\mathcal{B}_m$ represents a Bessel/modified Bessel function of order m.

The solution $W = S\cos\tau$ can now be substituted into the Reynolds equation (4.15),

Table 4.1. The first four resonant wavenumbers $K^{(n)}$ ($n = 1:4$) of an annular plate that is clamped at its oscillating inner radius $\xi_c = r_c/a < 1$, found using (4.65), for select values of ξ_c.

ξ_c	$K^{(1)}$	$K^{(2)}$	$K^{(3)}$	$K^{(4)}$
0	3.0005	6.2003	9.3675	12.5227
0.1	3.0702	6.4563	9.8732	13.3126
0.3	3.5944	7.9699	12.4189	16.8871
0.5	4.8155	11.0314	17.3008	23.5778

integration of which provides the squeeze-film pressure $P(\xi,\tau)$. Expressions for the steady pressure distribution $\langle P_1\rangle$ and the levitation force $\langle F_L\rangle$ provided by arbitrary standing-wave oscillations $S(\xi)$ can be found using the general formulas provided by [101]. Curves labeled '$C = 0$' in figures 4.3–4.5 of the main text were verified using this method.

When the disk described above oscillates at a natural frequency, the driving cylinder experiences no structural resistance to its motion, i.e. the transverse stress vanishes at the clamp radius $\xi_c = r_c/a$ [121]. Upon imposing this additional boundary condition, the critical elastic wavenumbers K that specify these resonant frequencies can be found by solving the equation

$$\det\left(\begin{bmatrix} J_1(K\xi_c) & Y_1(K\xi_c) & -I_1(K\xi_c) & K_1(K\xi_c) \\ J_1(K) & Y_1(K) & I_1(K) & -K_1(K) \\ \Xi_J^-(K) & \Xi_Y^-(K) & -\Xi_I^-(K) & -\Xi_K^+(K) \\ J_1(K\xi_c) & Y_1(K\xi_c) & I_1(K\xi_c) & -K_1(K\xi_c) \end{bmatrix}\right) = 0\,. \tag{4.65}$$

Note that the resonant wavenumbers and mode shapes for a circular disk [89,101] can be recovered respectively from (4.65) and (4.62) by taking the limit of a vanishing clamp radius $\xi_c \to 0$. The first few critical wavenumbers K for select values of ξ_c are exemplified in table 4.1 for a disk with Poisson's ratio $\nu_d = 0.3$. The precise values of the critical K vary weakly with ν_d in the range of interest—for most plastic and metallic materials, $0.3 \lesssim \nu_d \lesssim 0.5$ [130,131].

4.8.2 Strong fluid–structure coupling $C \gg 1$

The limit of strong fluid–structure coupling $C \gg 1$ is considered below for the canonical case of a vanishing clamp radius $\xi_c \to 0$. For values of C much larger than unity, the disk bends with a small characteristic wavelength that scales with the inverse of C, as can be seen from an order-of-magnitude analysis of the dominant terms in (4.27). Correspondingly, the scale of pressure variations in the air layer reduces by an order C^2, as follows from the balance of radial momentum (4.5*b*). When $C \gg 1$, the Kirchhoff–Love equation (4.16) reduces to

$$\hat{\nabla}^4 W = \hat{P}, \quad \text{with} \quad \hat{\nabla}^2 = \frac{\partial^2}{\partial X^2} + \frac{1}{X}\frac{\partial}{\partial X}, \tag{4.66}$$

where $X = C\xi$ is the appropriately rescaled spatial variable that accounts for the high-wavenumber disk undulations and $\hat{P} = C^2 P$ represents the correspondingly rescaled overpressure, and the Reynolds equation (4.15) reduces to

$$-\frac{1}{X}\frac{\partial}{\partial X}\left[(1+\varepsilon W)^3 X \frac{\partial \hat{P}}{\partial X}\right] + 12\frac{\partial W}{\partial \tau} = 0\,. \tag{4.67}$$

Substituting into (4.66) and (4.67) the familiar truncated perturbation expansion for the disk displacement $W = W_0 + \varepsilon W_1$ and that for the newly rescaled pressure $\hat{P} = \hat{P}_0 + \varepsilon \hat{P}_1$, and collecting terms of order unity provides $\hat{\nabla}^4 W_0 = \hat{P}_0$ and $\hat{\nabla}^2 \hat{P}_0 = 12\partial W_0/\partial\tau$, respectively. Introducing an ansatz of the form $W_0 = \mathrm{Re}\{\hat{\Omega}\mathrm{e}^{\mathrm{i}\tau}\}$ and $\hat{P}_0 = \mathrm{Re}\{\hat{\Pi}\mathrm{e}^{\mathrm{i}\tau}\}$, and combining the two reduced governing equations provides $(\hat{\nabla}^2 + \hat{\gamma}_1^2)(\hat{\nabla}^2 + \hat{\gamma}_2^2)(\hat{\nabla}^2 + \hat{\gamma}_3^2)\hat{\Omega} = 0$, involving the rescaled wavenumbers

$$\hat{\gamma}_n = \lim_{C \gg 1} C^{-1}\gamma_n = \left(2^{1/3}\right)\left(3^{1/6}\right)\mathrm{e}^{\mathrm{i}[\pi/4 + (n-1)\pi/3]} \quad \text{for} \quad n = 1:3\,, \tag{4.68}$$

which can also be obtained directly by taking the limit $C \gg 1$ in (4.29). The spatial variations of disk displacement and squeeze-film pressure at leading order can then be expressed respectively as

$$\hat{\Omega} = \sum_{n=1}^{3} [A_n J_0(\hat{\gamma}_n X) + B_n Y_0(\hat{\gamma}_n X)] \quad \text{and} \quad \hat{\Pi} = \sum_{n=1}^{3} \hat{\gamma}_n^4 [A_n J_0(\hat{\gamma}_n X) + B_n Y_0(\hat{\gamma}_n X)], \qquad (4.69a,b)$$

where the six coefficients A_n and B_n are to be determined by application of appropriate boundary conditions, analogous to those listed in (4.21) and (4.22), those at the disk edge $\xi = 1$ now being imposed correspondingly for $X \to \infty$. Use of the limiting forms of the Bessel (and Hankel) functions for large complex arguments [124, pp. 355–389] provides $\begin{bmatrix} A_1 & B_1 & A_2 & B_2 & A_3 & B_3 \end{bmatrix} = \begin{bmatrix} 1 & 0 & 0 & 0 & 0 & 0 \end{bmatrix} \mathbf{M}_\infty^{-1}$, where

$$\mathbf{M}_\infty = \begin{bmatrix} 1 & 0 & 0 & \hat{\gamma}_1^{3/2} & \hat{\gamma}_1^{5/2} & \hat{\gamma}_1^{7/2} \\ 2/\pi \ln(\hat{\gamma}_1) & 1 & \hat{\gamma}_1^4 & \mathrm{i}\hat{\gamma}_1^{3/2} & \mathrm{i}\hat{\gamma}_1^{5/2} & \mathrm{i}\hat{\gamma}_1^{7/2} \\ 1 & 0 & 0 & \hat{\gamma}_2^{3/2} & \hat{\gamma}_2^{5/2} & \hat{\gamma}_2^{7/2} \\ 2/\pi \ln(\hat{\gamma}_2) & 1 & \hat{\gamma}_2^4 & \mathrm{i}\hat{\gamma}_2^{3/2} & \mathrm{i}\hat{\gamma}_2^{5/2} & \mathrm{i}\hat{\gamma}_2^{7/2} \\ 1 & 0 & 0 & \hat{\gamma}_3^{3/2} & \hat{\gamma}_3^{5/2} & \hat{\gamma}_3^{7/2} \\ 2/\pi \ln(\hat{\gamma}_3) & 1 & \hat{\gamma}_3^4 & \mathrm{i}\hat{\gamma}_3^{3/2} & \mathrm{i}\hat{\gamma}_3^{5/2} & \mathrm{i}\hat{\gamma}_3^{7/2} \end{bmatrix}. \qquad (4.70)$$

Note that the problem is thus fundamentally parameter-free in the limit of large C, with σ, K and the disk Poisson's ratio ν_d—the latter of which enters for order-unity C through a free-edge boundary condition in (4.22)—all being absent in the solution.

The amplitude of the disk structural impedance at the rescaled, vanishing clamp radius $X = X_c = C\xi_c \ll 1$ scales in this limit with the square of C, as follows from the definitions given in (4.42) and (4.44). The appropriately rescaled amplitude is found to approach the constant value $C^{-2}|V_c| \to (2/\pi)\left|\sum_{n=1}^{3} B_n \hat{\gamma}_n^2\right| \approx 3.7867$.

Collecting terms of order ε in (4.67) and calculating the time average thereof provides

$$\frac{\mathrm{d}}{\mathrm{d}X}\left[X\left(\frac{\mathrm{d}\langle\hat{P}_1\rangle}{\mathrm{d}X}+3\left\langle W_0\frac{\partial\hat{P}_0}{\partial X}\right\rangle\right)\right]=0\,. \tag{4.71}$$

Integrating this equation twice with application of the modified regularity conditions $\partial\hat{P}_0/\partial X = \partial\hat{P}_1/\partial X = 0$ at the vanishing clamp radius $X_c \ll 1$ provides the rescaled, time-averaged squeeze-film pressure distribution

$$\langle\hat{P}_1\rangle(X) = -\int_X^\infty \frac{\mathrm{d}\langle\hat{P}_1\rangle}{\mathrm{d}X}\mathrm{d}X\,, \tag{4.72}$$

valid for $X > 0$ and expressed in terms of the associated steady pressure gradient $\mathrm{d}\langle\hat{P}_1\rangle/\mathrm{d}X = -(3/2)\mathrm{Re}\{\hat{\Omega}\,\mathrm{d}\hat{\Pi}^*/\mathrm{d}X\}$. The characteristic scale of the corresponding levitation force reduces in this limit by a factor of C^4, as can be deduced from the original definition (4.54), and the appropriately rescaled force is found to converge to the constant value $C^4\langle F_L\rangle \approx 4.919$. Interestingly, the associated efficiency of levitation (4.60) reduces in this limit to a constant value $\langle\mathcal{F}_L\rangle/(\varepsilon\mathcal{F}_m) \approx 4.919/3.7867/2 = 0.6495$.

Chapter 4 is currently being prepared for submission for publication along with A. L. Sánchez, under the title “The role of fluid–structure coupling in the generation of attractive squeeze-film forces”. The dissertation author was the primary investigator and author of this draft.

Chapter 5

Transportation of levitated objects using asymmetrical flexural oscillations

5.1 Executive summary

Developed in this chapter is a theoretical description of the fluid flow involved in contactless transport systems that operate using squeeze-film levitation. Regular perturbation methods are employed to solve the appropriate Reynolds equation that governs the viscous, compressible flow of air in the slender film separating the oscillator and the opposite surface. The reduced mathematical formulation allows efficient computation of the time-averaged levitation force and moment induced by the gas overpressure in the squeeze film, as well as the accompanying quasistatic thrust force that accounts additionally for shear stresses. Investigated, in particular, is the possibility of combining two distinct methods of thrust generation that have been experimentally demonstrated in previous studies—(i) inclination of the levitated body and (ii) generation of asymmetrical flexural deformations, such as traveling waves, on the oscillator surface—the latter of which is shown to allow a transition from the typically repulsive levitation force to one that is attractive. Computations reveal that systematic control of the inclination angle can provide significant performance benefits for squeeze-film transport systems. In the case of attractive levitation, the amount of improvement that can be obtained appears to correlate closely with the degree of lateral asymmetry exhibited by the flexural oscillations.

Contactless transportation using squeeze-film levitation is potentially of great use in

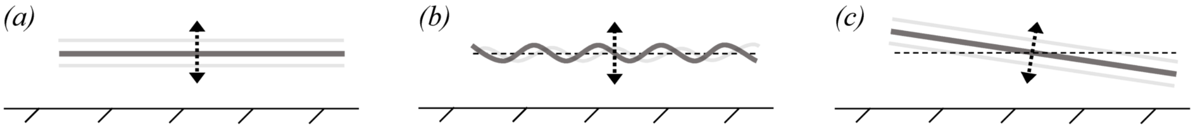

Figure 5.1. (a) A conventional squeeze-film levitation system can be modified to generate thrust by (b) excitation of propagating-wave surface deformations or (c) inclination of the oscillator surface.

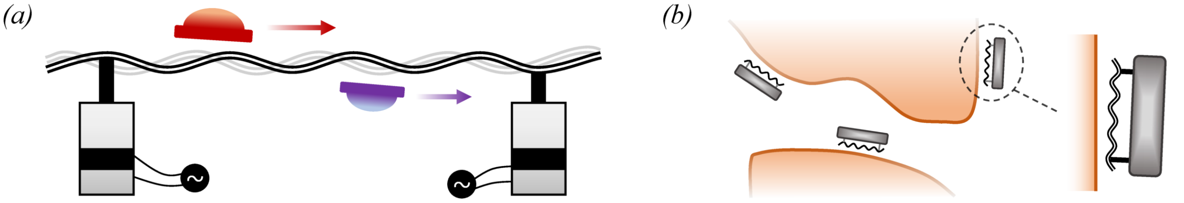

Figure 5.2. Proposed applications of squeeze-film transport: (a) contactless assembly line conveyance using both repulsion (red) and attraction (blue), and (b) soft-robotic locomotion over complex terrain.

applications such as the assembly line handling of touch-sensitive objects and soft-robotic locomotion over complex terrain. Achieving lateral mobility in levitation systems has typically required incorporation of multiple oscillation sources, which consume substantial energy while generating thrust forces and transport speeds that are inadequate for large-scale, practical application. The results of the present analysis demonstrate that much greater thrust can be generated by controlling systematically the inclination angle of an object levitated by repulsive *or attractive* pressure forces, for instance, through active control of the center of mass of a self-levitating robot. The generality and computational efficiency of this mathematical formulation make it a versatile tool for guiding the design, optimization and closed-loop control of next-generation squeeze-film transport systems.

5.2 Introduction

A typical squeeze-film levitation (SFL) system, as cartooned in figure 5.1(a), consists of two rigid objects with parallel surfaces that are separated by a slender layer of air, the ‘squeeze film’. High-frequency oscillation of either object along an axis perpendicular to the surfaces generates pulsating airflow in the film that yields a strong, steady, repulsive pressure force between the two objects. This phenomenon has been exploited to design gas-lubricated bearings [7, 9] and levitation devices that exhibit large load capacities, as demonstrated, for example, by Zhao [19], who used an ultrasonic oscillator with a small surface diameter of 5 cm to generate 115 N ($\approx$ 11.7 kgf) of repulsion.

SFL systems are typically operated at a frequency that corresponds to one of the resonant bending modes of the oscillating assembly. Active feedback control of the excitation signal has been implemented to account for slight, unpredictable drifts of the natural frequency [132]. The drastic increase in the amplitude of oscillations near resonance magnifies substantially the repulsive levitation force [10, 40, 93]. The effective flexural amplitude can be improved by reducing the stiffness of the oscillator through careful selection of material(s) [133, 134] and geometry [135].

Under a limited range of operating conditions—namely, for surfaces with millimetric characteristic dimensions or oscillation frequencies as low as several hundred hertz—this steady force has been observed to transition from strong repulsion to weak attraction of less than 1 gf [4, 6, 36, 37]. Recent experiments have shown that this minor attractive load capacity is magnified a thousand fold when the stiffness of the oscillator is reduced substantially to provide pronounced flexural deformations that may be subject to non-negligible fluid–structure coupling [3, 49]. A preliminary theoretical analysis [101] (see Ch. 3) indicated that the range of operating conditions under which attraction occurs, as well as the magnitude of the resulting forces, grows substantially with the wavenumber of oscillation—or, practically speaking, with the degree of flexibility of the oscillator.

Proposed applications of SFL include, primarily, assembly line handling and transport of touch-sensitive items, such as surface-mount devices for circuit boards [6] and glass substrates to be installed in liquid-crystal displays [12], and load-carrying ‘soft’ robots that can travel over multifarious terrains [3]; see figure 5.2 for a rudimentary visualization of each. Pursuant of these applications, a number of methods have been proposed to modify the basic SFL configuration to produce also lateral forces, as reviewed in the following paragraphs.

The earliest of these is the excitation of traveling-wave deformations of the oscillator, as diagrammed in figure 5.1(b), which generates steady, asymmetrical fluid shear on the bounding surfaces of the squeeze film. This method has been applied to develop rail-transport systems that levitate repulsively objects with masses of order $10-100$ grams and displace them with speeds of order 10 cm/s [14, 37, 136]. Experimenters have also designed self-levitating mobile robots with comparable masses that can produce thrust forces of order 10 mN [32, 33]. The wave-generation methods employed in these experiments involve two spatially separated oscillators attached to a platform [137]. Of great concern has been the purity of the traveling wave generated on the finite platform—which is limited practically by wave reflection at free boundaries and points of attachment, since the resulting interference may critically reduce the thrust force [33]. Ameliorative solutions include ‘impedance matching’, where one of the oscillators acts as a passive absorber through piezoelectric energy dissipation [37, 138], and ‘two-mode excitation’, where the two oscillators operate out of phase at a critical frequency that results in a favorable superposition of two consecutive resonant bending modes of the platform [13, 139]. Active feedback control using the latter method has been claimed to provide nearly perfect traveling waves [140, 141].

Three prominent alternative methods of transport have been proposed in recent years. The first relies on the steady shear force caused by the asymmetrical fluid streaming that occurs when a levitated object is misaligned with a *finite* parallel surface [142]. This so-called ‘restoring force’ is exploited by assembling an array of oscillators and controlling carefully the amplitude of each such that fluid shear conveys a levitated object along the array. (Note that a propulsive pressure force resulting from tilting of the levitated object with respect to the oscillating platforms, as described in a later paragraph, may also be involved in this method.) Notable limitations of this method include the need for multiple oscillators, whose number and/or size must grow with the desired transport distance, and the apparent inapplicability to robotic locomotion.

[34] proposed a remarkable method more amenable to such robotic applications: simultaneous generation of linear and rotational oscillations of a platform using a pair of independently excited piezoelectric elements, the resonant frequencies of the two oscillation modes matched using computer-aided design. In principle, if the modes are driven exactly out of phase, the oscillations should resemble a traveling wave with very large wavelength. The authors report an optimal phase shift of $\approx 25°$, which allowed a roughly 20-gram robot to travel at 2.25 cm/s and generate 30 mN of static thrust.

The third and most recent alternative, proposed by [45], involves inclination of the levitated object, as exemplified in figure 5.1(c), which would tilt the levitative steady pressure force to provide a relatively small lateral component. This method seems particularly attractive for implementation on mobile robots, simply through active control of the on-board mass distribution. Although the robustness and stability of steady-state transport are yet to be investigated rigorously for this method, [45] claims that it may yield substantial improvement in versatility, load capacity and controllability.

A unifying factor among the literature cited above is the focus on repulsive levitation. To the best of our knowledge, controlled transportation using attraction is yet to be studied theoretically. (Following the publication of the contents in this chapter, an experimental demonstration of transport and rotation with attractive levitation was communicated by the Bioinspired Robotics and Design Lab at UC San Diego [100].) Explored in this chapter is the prospect of combining the distinct thrust-generation mechanisms of (i) traveling-wave deformations and (ii) controlled surface inclination. Results of a rigorous fluid-flow analysis indicate that, while thrust-generating inclination reduces the maximal repulsive load capacity, the attractive load capacity of flexural SFL systems can be improved substantially through methodical adjustment of the tilting angle.

The remainder of this chapter is organized as follows. Outlined in Section 5.3 is the proposed fluid-dynamic problem that represents a generic squeeze-film system involving arbitrary flexural oscillations and a variable tilt angle. The reduced conservation equations governing fluid

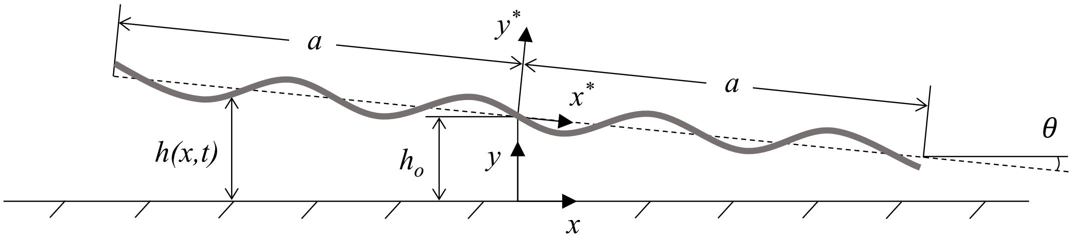

Figure 5.3. A generic squeeze-film transport system: a levitated plate undergoing flexural oscillation is tilted at an angle θ with respect to a nearby wall and propelled to the right by fluid stresses beneath.

flow in the slender air layer are presented, followed by the introduction of appropriately rescaled dimensionless variables. An asymptotic solution is derived in § 5.4 and integral expressions are provided for the steady thrust force, the levitation force and the associated center of pressure. These levitation metrics are visualized in § 5.5 for a variety of relevant transport configurations. The chapter concludes with a discussion of possible applications of the developed formulation in system design, optimization and control.

5.3 Problem definition

5.3.1 Preliminary considerations

Consider, as a relevant canonical configuration, the planar SFL system represented in figure 5.3, where a plate of undeformed length $2a$ levitates and translates above an infinitely long horizontal wall. In its undeformed state, the plate is tilted at an angle θ with respect to the wall, and its center is separated from the wall by a time-averaged distance h_o. The plate undergoes time-harmonic, flexural oscillations that are described by the equation $y^* = b\mathrm{Re}\{W(x^*/a)\mathrm{e}^{\mathrm{i}\omega t}\}$, where (x^*, y^*) specifies the depicted rotated coordinate system attached to the plate center, b and ω denote, respectively, the characteristic amplitude and angular frequency of oscillation, and W is a dimensionless function that defines the waveform. For instance, the cases $W = \cos(2\pi x^*/a)$ and $W = \exp(-2\mathrm{i}\pi x^*/a)$ represent, respectively, standing and forward-traveling waves of wavelength a.

The local pressure, temperature, density and viscosity of the oscillating gas inside the film are denoted respectively by p,T,ρ and μ. The corresponding values of those properties in the unperturbed surroundings are denoted with the subscript ‘a’; for instance, p_a denotes the ambient pressure.

In pursuit of modeling typical SFL systems [4, 19, 40], it is assumed here that

(i) the squeeze film is slender, $h_o \ll a$, whence the tilt angle is small: $\theta \sim h_o/a \ll 1$,

(ii) the characteristic wavelength of the flexural oscillations is comparable to a, whence

(iii) any lateral displacement Δx^* of points on the deforming plate surface is negligible, and

(iv) the transport speed u_t is negligibly small [136] compared to the characteristic speed u_s of steady gaseous streaming in the film: $u_t \ll u_s \sim (b/h_o)^2 \omega a$ [60].

Assumptions (i) and (ii) allow application of the slender-flow approximation [60] to model gas flow in the film. Due to (iii) and (iv), the only nontrivial boundary condition to be imposed for the flow velocity stems from the transverse motion of the plate surface, which can now be expressed with use of the simplified equation

$$y = h(x,t) = h_o - x\theta + b\mathrm{Re}\left\{W(x/a)\mathrm{e}^{\mathrm{i}\omega t}\right\}, \quad \text{for} \quad -a \le x \le a, \tag{5.1}$$

where (x, y) denotes a coordinate system whose origin travels along the wall (see figure 5.3), with x coincident to the wall and y denoting the perpendicular distance to the plate center. The assumption of small angles $\theta \ll 1$ introduces relative errors of order θ^2 for the terms in (5.1) representing steady tilt and unsteady flexure.

The levitation force, defined as the vertical component of the time-averaged aerodynamic force acting on the plate (per unit length perpendicular to the plane of motion), can then be expressed as

$$\langle \mathcal{F}_L \rangle = \int_{-a}^{a} \langle p - p_a \rangle \mathrm{d}x, \tag{5.2}$$

and the associated thrust force—the horizontal component—can be expressed as

$$\langle \mathcal{F}_T \rangle = \int_{-a}^{a} \left(\langle p - p_a \rangle \theta - \langle \mu \, \partial u / \partial y \rangle \big|_{y=h} \right) \mathrm{d}x , \tag{5.3}$$

both with relative errors of order $(h_o/a)^2 \sim \theta^2$. The angled brackets in the definitions above denote the time average of a time-dependent quantity over one period of oscillation, $\langle \star \rangle = (\omega/2\pi) \int_{t^*}^{t^*+2\pi/\omega} \star \, \mathrm{d}t$.

In addition, the levitation moment about the plate center and the associated center of steady pressure can be expressed as

$$\langle \mathcal{M} \rangle = \int_{-a}^{a} \langle p - p_a \rangle x \mathrm{d}x \qquad \text{and} \qquad x_{csp} = \frac{\langle \mathcal{M} \rangle}{\langle \mathcal{F}_L \rangle} , \tag{5.4}$$

with the same level of accuracy. Note that, due to the simplifications employed, the general quasistatic transport problem defined above also describes systems such as those depicted in figure 5.2(a), where a rigid object with a flat surface (of length $2a$) is transported over a flexurally oscillating rail.

5.3.2 The lubrication approximation

As shown by [74] and later by [60], the flow dynamics in the thin air layer of a squeeze-film system is characterized by three principal timescales—that of the driving oscillations $t_o = \omega^{-1}$, viscous diffusion across the film $t_v = h_o^2/(\mu_a/\rho_a)$, and acoustic pressure equilibration along the film $t_a = a/\sqrt{p_a/\rho_a}$—which enter in the theoretical description through two nondimensional parameters: the relevant Stokes number $\alpha^2 = t_v/t_o$ (or, equivalently, the associated Womersley number α) and a compressibility number $\Lambda = t_a/t_o$. As shown by G.I. Taylor and P.G. Saffman [5], the description simplifies in configurations for which $t_v \ll t_o$, where inertial forces are negligibly weak compared to viscous shear. In the associated lubrication limit $\alpha^2 \ll 1$, the three timescales are found to enter through a single parameter

$$\sigma = \frac{12\Lambda}{\alpha^2} = \frac{12t_a^2}{t_o t_v} = \frac{12\mu_a \omega a^2}{p_a h_o^2} \sim 1\,, \tag{5.5}$$

where the factor of 12 is included for consistency with the classical definition. Often referred to as the ‘squeeze number’, σ effectively represents the combined effects of gaseous compressibility and viscous shear within the film. Solution for the case of parallel walls ($\theta = 0$) with uniform oscillation amplitude ($W = 1$) has revealed that the air near the center of the film is entrapped due to viscous resistance, and its nonlinear response to sinusoidal compression and expansion provides the steady repulsive pressure force $\langle \mathcal{F}_L \rangle$ [8, 9]. The extent of this central region and, hence, the magnitude of the force, grows monotonically with increasing values of σ. On the other hand, as $\sigma \longrightarrow 0$ and the system becomes weakly nonlinear, the force vanishes, proportional to σ^2 [60].

While quantifying the effects of local and convective fluid acceleration affords higher accuracy in the computation of the levitation force for a wider range of operating parameters [63, 68, 74], the lubrication approximation has been shown to provide excellent agreement with experimental measurements for systems with small mean distances $h_o \ll \sqrt{\mu_a/(\rho_a \omega)}$, those that satisfy $t_v \ll t_o$ [9, 19]. In the following analysis, the classical compressible lubrication limit ($t_v/t_o \sim t_a^2/t_o^2 \ll 1$) will be employed to describe rigorously the family of transport systems schematized in figure 5.3. The mathematical formulation derived below may be readily extended in the future to address the general viscoacoustic limit ($t_v/t_o \sim t_a/t_o \sim 1$) by following the methods of [60], although quantification of inertial effects would severely limit the degree of analytical development possible.

The fluid flow in asymmetrical SFL systems has been studied previously for two limiting cases that correspond to the canonical transport mechanisms drawn in figures 5.1(b) and (c). For the latter case, where $W = 1$ and $\theta \neq 0$, [59] outlined an asymptotic computation of the time-dependent film pressure under the assumption of a known, non-negligible transport speed. A verified numerical model developed by [45] using the ANSYS CFX software provided preliminary insights regarding the contribution to the thrust force from steady shear stresses acting on the levitating body, those arising from streaming in the air layer bounded by non-parallel surfaces. For the former case, where $\theta = 0$ and $W = W(\xi)$, [143] computed analytically the quasistatic thrust force generated by pure traveling-wave oscillations with variable wavenumber. [33] presented a numerical investigation of the problem for imperfect traveling waves, demonstrating the adverse effect of impurity on the thrust force. The utilized model accounted rigorously for effects of local fluid acceleration and estimated the additional drag force induced by fluid shear on the exposed plate surface.

Two notable treatments of the generic problem depicted in figure 5.3 must be mentioned here. [144] presented a formulation similar to that of [33] but computed additionally the contribution of steady overpressure to the thrust in the presence of inclination, quantifying the adverse effect of the impurity of traveling waves on the terminal transport velocity. [145] addressed the stability of transport systems to disturbances in the tilt angle θ, using a model that accounts for fluid inertia but neglects the fundamental role of gaseous compressibility. They discovered a steady restoring moment that increases in magnitude with the inclination angle. However, (i) systematic modulation of thrust by controlling the inclination and (ii) achievement of transport with attractive levitation were beyond the scopes of these studies, and are explored below.

5.3.3 Conservation equations governing airflow in the squeeze film

Under the limit $t_v \ll t_o$, the Navier–Stokes equations (continuity and conservation of momentum in the lateral and transverse directions) and the thermal equation of state for an ideal gas reduce respectively to

$$\frac{\partial \rho}{\partial t} + \frac{\partial(\rho u)}{\partial x} + \frac{\partial(\rho v)}{\partial y} = 0, \qquad \mu_a \frac{\partial^2 u}{\partial y^2} = \frac{\partial p}{\partial x}, \qquad \frac{\partial p}{\partial y} = 0, \qquad \text{and} \qquad \frac{p}{p_a} = \frac{\rho}{\rho_a}, \tag{5.6}$$

with relative errors of order $(h_o/a)^2$. In deriving the above equations, it has been assumed for simplicity that both the plate and wall surfaces are held at the ambient temperature T_a, whence the conservation of energy for viscous flow implies that $T = T_a$ everywhere in the film [60]. As a result, the dynamic viscosity can be considered uniform as well, $\mu(T) = \mu_a$ [77]. Detailed discussions of these equations, which comprise the *isothermal* compressible lubrication limit, are presented by [5], [8] and [60].

In pursuit of a reduced dimensionless formulation of the problem, we introduce the appropriately rescaled flow variables $\xi = x/a$, $Y = y/h_o$, $\tau = \omega t$, $U = u/(\varepsilon\omega a)$, $V = v/(\varepsilon\omega h_o)$, and $P = (p - p_a)/(\varepsilon\sigma p_a/12) = (\rho - \rho_a)/(\varepsilon\sigma\rho_a/12)$, where the quantity σ is defined in (5.5). Note that the characteristic scales for the variations of pressure and density follow from straightforward order-of-magnitude analyses of the lateral momentum equation and the equation of state, respectively. Upon defining additionally a rescaled inclination angle $\varphi = \theta/(h_o/a)$, the plate position (5.1) can be rewritten as

$$\frac{h}{h_o} = H(\xi,\tau) = 1 - \varphi\xi + \varepsilon \mathrm{Re}\left\{W(\xi)\mathrm{e}^{\mathrm{i}\tau}\right\}, \quad \text{where} \quad \left|\varphi = \frac{\theta}{h_o/a}\right| \leq 1 - \varepsilon, \tag{5.7}$$

with relative errors of order θ^2 and $\varepsilon\theta^2$ stemming respectively from the terms describing tilt and flexure.

Substituting these definitions into the lateral momentum and continuity equations provides

$$\frac{\partial^2 U}{\partial Y^2} = \frac{\partial P}{\partial \xi} \qquad \text{and} \qquad \frac{\sigma}{12}\frac{\partial P}{\partial \tau} + \frac{\partial}{\partial \xi}\left[\left(1 + \varepsilon\frac{\sigma}{12}P\right)U\right] + \frac{\partial}{\partial Y}\left[\left(1 + \varepsilon\frac{\sigma}{12}P\right)V\right] = 0, \tag{5.8}$$

respectively, where $P = P(\xi,\tau)$ due to the transverse momentum equation. The above system of equations is subject to non-slip and non-penetration conditions on the bounding walls,

$$U = V = 0 \quad \text{at} \quad Y = 0 \qquad \text{and} \qquad U = V - \varepsilon^{-1}\partial H/\partial\tau = 0 \quad \text{at} \quad Y = H, \tag{5.9}$$

expressed here with errors of order θ^2. Upon integrating the lateral momentum equation twice in the Y direction and applying the conditions $U(Y=0)=U(Y=H)=0$, we obtain the quasisteady Poiseuille velocity profile

$$U(\xi,Y,\tau)=\frac{1}{2}\frac{\partial P}{\partial \xi}Y(Y-H), \tag{5.10}$$

involving the time-varying lateral pressure gradient $\partial P/\partial\xi$. Substituting this result into the continuity equation, integrating across the film, applying the conditions $V(Y=0)=V(Y=H)-\mathrm{Re}\left\{W(\xi)\mathrm{i}e^{\mathrm{i}\tau}\right\}=0$ and simplifying with use of the Leibniz integral rule yields the relevant Reynolds equation [8]

$$\sigma\frac{\partial(PH)}{\partial\tau}-\frac{\partial}{\partial\xi}\left[H^3\left(1+\varepsilon\frac{\sigma}{12}P\right)\frac{\partial P}{\partial\xi}\right]+12\mathrm{Re}\left\{W(\xi)\mathrm{i}e^{\mathrm{i}\tau}\right\}=0\,. \tag{5.11}$$

Two boundary conditions for $P(\xi,\tau)$ are required to close the problem defined by (5.7), (5.10) and (5.11).

Previous studies have shown that the pressure in the squeeze film relaxes to its ambient value across small, non-slender peripheral regions that extend distances $|\Delta\mathbf{x}|$ of order $h_o \ll a$ beyond the edges $\xi=\pm1$ [4,60]. Due to the associated disparity of spatial scales, the characteristic variations of pressure across these peripheries are smaller than those along the film by a factor of order h_o/a. For arbitrary *order-unity* values of the relative amplitude $\varepsilon \lesssim 1$, equation (5.11) can therefore be readily solved using numerical methods when supplemented by the simple boundary conditions $P(\xi=\pm1)=0$, which introduce small relative errors of $O(h_o/a \ll 1)$. Finite-difference solutions of the strongly nonlinear Reynolds equation have displayed excellent agreement with experimental results for operating conditions that fall under the lubrication limit $t_v \ll t_o$ [9,19]. In the present study, numerical integration of (5.11) was performed using a straightforward central-space, forward-Euler scheme for the purpose of verifying the asymptotic solution derived below. Instructions for implementing the algorithm, as well as discussions regarding its stability, accuracy and computational efficiency, are provided by [88].

5.4 Asymptotic solution

To allow efficient analytical reduction of the problem at hand, it will be assumed that the oscillation amplitude $\Delta y^* = b$ is small relative to the mean thickness of the air layer, i.e. $b \ll h_o$, which allows asymptotic solution using the relative amplitude

$$\varepsilon = \frac{b}{h_o} \ll 1 \tag{5.12}$$

as the small perturbation parameter. Despite operating near resonance, typical SFL systems exhibit diminutive amplitudes of order $b = 10\ \mu$m [6, 19, 136], whence an asymptotic solution can provide reasonable accuracy as long as the film thickness h_o is relatively large [101]. On the other hand, the strongly repulsive forces that are generated at close range ($h_o \gtrsim b$) are best quantified using a numerical solution of the Reynolds equation [19], as described in § 5.3.3, or a computational simulation using the full Navier–Stokes equations [4, 6].

Under the limit of small relative amplitudes $\varepsilon \ll 1$, the required boundary conditions for the fluid pressure at the film edges must be developed carefully. We begin by introducing perturbation expansions for the pressure and lateral flow velocity component,

$$\begin{cases} P = P_0 + \varepsilon P_1 + \cdots \\ U = U_0 + \varepsilon U_1 + \cdots . \end{cases} \tag{5.13}$$

As shall be shown in § 5.4, substitution of this expansion into (5.11) leads to an equation that is *linear* at leading order. Thus, the first term in each expansion varies sinusoidally with time and yields no contribution to the time-averaged levitation forces and moment, whose evaluation consequently requires the computation of first-order corrections. Due to the disparity of spatial scales between the slender film and the small non-slender regions surrounding its edges, discussed below (5.11), the leading-order pressure accepts simple relaxation conditions: $P_0(\xi = \pm 1) = 0$. However, determining the corresponding conditions for P_1 requires, in principle, establishing a formal asymptotic relationship between the two small parameters ε and h_o/a, and systematically matching [78] with the local asymptotic expansions for the pressure in the two non-slender peripheries [60]. Fortunately, for $\varepsilon \ll 1$, the reduced conservation equations that govern the peripheral flow under the lubrication limit are linear in the first approximation [60]. The peripheral pressure variations at leading order thus exhibit a zero time average, whence relaxation conditions can be imposed for the *time-averaged* first-order pressure at the film edge, $\langle P_1\rangle(\xi = \pm 1) = 0$. While these conditions do not allow computation of the time dependence of $P_1(\xi,\tau)$, they are sufficient to solve for the desired steady levitation metrics (5.2)–(5.4).

Substituting the expression for $H(\xi,\tau)$ given in (5.7) along with the first two terms of the pressure expansion (5.13) into the Reynolds equation (5.11) yields

$$\begin{aligned}&\sigma\frac{\partial}{\partial\tau}\left[(P_0+\varepsilon P_1)\left(1-\varphi\xi+\varepsilon\mathrm{Re}\left\{W\mathrm{e}^{\mathrm{i}\tau}\right\}\right)\right]+12\mathrm{Re}\left\{W\mathrm{i}\mathrm{e}^{\mathrm{i}\tau}\right\}\\ &-\frac{\partial}{\partial\xi}\left[\left(1-\varphi\xi+\varepsilon\mathrm{Re}\left\{W\mathrm{e}^{\mathrm{i}\tau}\right\}\right)^3\left[1+\varepsilon\frac{\sigma}{12}(P_0+\varepsilon P_1)\right]\frac{\partial}{\partial\xi}(P_0+\varepsilon P_1)\right]=0,\end{aligned}\tag{5.14}$$

which is to be solved to determine $P(\xi,\tau)$ with small errors of $O(\varepsilon^2)$ and $O(h_o^2/a^2 \sim \theta^2)$.

The horizontal velocity distribution $U(\xi,Y,\tau)$ can, in turn, be found with the same level of accuracy using the expanded form of (5.10),

$$U_0+\varepsilon U_1=\frac{1}{2}\frac{\partial}{\partial\xi}(P_0+\varepsilon P_1)Y\left[Y-\left(1-\varphi\xi+\varepsilon\mathrm{Re}\left\{W\mathrm{e}^{\mathrm{i}\tau}\right\}\right)\right].\tag{5.15}$$

5.4.1 Leading-order solution

Collecting terms of order unity in (5.14) leads to the linear equation

$$\sigma(1-\varphi\xi)\frac{\partial P_0}{\partial\tau}-\frac{\partial}{\partial\xi}\left[(1-\varphi\xi)^3\frac{\partial P_0}{\partial\xi}\right]+12\mathrm{Re}\left\{W(\xi)\mathrm{i}\mathrm{e}^{\mathrm{i}\tau}\right\}=0,\tag{5.16}$$

which can be solved using the method of separation of variables. Upon substituting the ansatz

$$P_0 = \mathrm{Re}\left\{\Pi(\xi)\mathrm{e}^{\mathrm{i}\tau}\right\}, \tag{5.17}$$

equation (5.16) reduces to the equidimensional ordinary differential equation

$$\frac{\mathrm{d}^2\Pi}{\mathrm{d}\xi^2} - \frac{3\varphi}{1-\varphi\xi}\frac{\mathrm{d}\Pi}{\mathrm{d}\xi} - \frac{\sigma\mathrm{i}}{(1-\varphi\xi)^2}\Pi = 12\mathrm{i}\frac{W(\xi)}{(1-\varphi\xi)^3}, \quad \text{with} \quad \Pi(\xi = \pm 1) = 0\,. \tag{5.18}$$

Solution by the method of variation of parameters gives the reduced pressure distribution

$$\Pi(\xi) = \frac{6\mathrm{i}}{\zeta\varphi(1-\varphi\xi)}\left[L(\xi) - \frac{1-[(1+\varphi)/(1-\varphi\xi)]^{2\zeta}}{1-[(1+\varphi)/(1-\varphi)]^{2\zeta}}\left(\frac{1-\varphi\xi}{1-\varphi}\right)^{\zeta} L(1)\right], \tag{5.19}$$

expressed in terms of the parameter

$$\zeta = \sqrt{1+\frac{\sigma\mathrm{i}}{\varphi^2}}, \tag{5.20}$$

and the integral operator

$$L(\xi) = \frac{\int_{-1}^{\xi} W(\tilde{\xi})(1-\varphi\tilde{\xi})^{\zeta-1}\,\mathrm{d}\tilde{\xi}}{(1-\varphi\xi)^{\zeta}} - (1-\varphi\xi)^{\zeta}\int_{-1}^{\xi}\frac{W(\tilde{\xi})}{(1-\varphi\tilde{\xi})^{\zeta+1}}\,\mathrm{d}\tilde{\xi}, \tag{5.21}$$

where $\tilde{\xi}$ is a dummy integration variable. The reduced pressure gradient $\Pi' = \mathrm{d}\Pi/\mathrm{d}\xi$ is given by

$$\Pi'(\xi) = \frac{6\mathrm{i}}{\zeta\varphi(1-\varphi\xi)^2}\left[\tilde{L}(\xi) + \frac{1-\zeta-(1+\zeta)[(1+\varphi)/(1-\varphi\xi)]^{2\zeta}}{1-[(1+\varphi)/(1-\varphi)]^{2\zeta}}\left(\frac{1-\varphi\xi}{1-\varphi}\right)^{\zeta} L(1)\right], \tag{5.22}$$

involving the additional integral operator

$$\tilde{L}(\xi) = (1-\zeta)(1-\varphi\xi)^{\zeta}\int_{-1}^{\xi}\frac{W(\tilde{\xi})}{(1-\varphi\tilde{\xi})^{\zeta+1}}\,\mathrm{d}\tilde{\xi} - (1+\zeta)\frac{\int_{-1}^{\xi} W(\tilde{\xi})(1-\varphi\tilde{\xi})^{\zeta-1}\,\mathrm{d}\tilde{\xi}}{(1-\varphi\xi)^{\zeta}}\,. \tag{5.23}$$

Finally, collecting terms of order unity in (5.15) gives the leading-order horizontal velocity distribution

$$U_0 = \frac{\partial P_0}{\partial \xi}\frac{Y(Y-1+\varphi\xi)}{2}, \tag{5.24}$$

expressed here in terms of the gradient of the known leading-order pressure P_0, given in (5.17).

Since P_0 varies sinusoidally with time and thus exhibits a zero time average, i.e. $\langle P_0\rangle = 0$, evaluation of the steady levitation metrics (5.2)–(5.4) requires computation of first-order corrections.

5.4.2 First-order corrections

Collecting terms of order ε in (5.14) and taking the time average gives

$$3(1-\varphi\xi)^2\left\langle \operatorname{Re}\left\{W\mathrm{e}^{\mathrm{i}\tau}\right\}\frac{\partial P_0}{\partial \xi}\right\rangle + \frac{\sigma}{12}(1-\varphi\xi)^3\left\langle P_0\frac{\partial P_0}{\partial \xi}\right\rangle + (1-\varphi\xi)^3\left\langle \frac{\partial P_1}{\partial \xi}\right\rangle = 0, \tag{5.25}$$

which can be integrated subject to the boundary conditions $\langle P_1\rangle(\xi = \pm 1) = 0$ to give

$$\langle P_1\rangle(\xi) = \frac{(1-\varphi)^2}{4\varphi}\left[\left(\frac{1+\varphi}{1-\varphi\xi}\right)^2 - 1\right]\int_{-1}^{1} G(\xi)\,\mathrm{d}\xi - \int_{-1}^{\xi} G(\tilde{\xi})\,\mathrm{d}\tilde{\xi}, \tag{5.26}$$

where

$$G(\xi) = \left\langle \frac{\partial P_0}{\partial \xi}\left(\frac{3}{1-\varphi\xi}\operatorname{Re}\{W\mathrm{e}^{\mathrm{i}\tau}\} + \frac{\sigma}{12}P_0\right)\right\rangle. \tag{5.27}$$

Upon substituting the definition of the leading-order pressure (5.17) and applying the identity

$$\left\langle \operatorname{Re}\left\{\mathcal{A}(\xi)\mathrm{e}^{\mathrm{i}\tau}\right\}\operatorname{Re}\left\{\mathcal{B}(\xi)\mathrm{e}^{\mathrm{i}\tau}\right\}\right\rangle = \frac{\operatorname{Re}\{\mathcal{A}^*\mathcal{B}\}}{2}, \tag{5.28}$$

where $\mathcal{A}$ and $\mathcal{B}$ are complex spatial functions and the asterisk denotes a complex conjugate, the function G can be rewritten as

$$G(\xi) = \frac{1}{2}\operatorname{Re}\left\{\Pi'^*\left(\frac{3W}{1-\varphi\xi} + \frac{\sigma}{12}\Pi\right)\right\}, \tag{5.29}$$

in terms of the reduced leading-order pressure Π and its gradient Π', given respectively in (5.19) and (5.22). Straightforward differentiation of (5.26) yields

$$\frac{\mathrm{d}\langle P_1\rangle}{\mathrm{d}\xi} = \frac{(1-\varphi^2)^2}{2(1-\varphi\xi)^3}\int_{-1}^{1} G(\xi)\,\mathrm{d}\xi - G(\xi), \tag{5.30}$$

for the time-averaged pressure gradient. Finally, collecting terms of order ε in (5.15) and taking the time average gives the steady horizontal velocity

$$\langle U_1\rangle = \frac{\mathrm{d}\langle P_1\rangle}{\mathrm{d}\xi}\frac{Y(Y-1+\varphi\xi)}{2} - \frac{Y}{4}\mathrm{Re}\{\Pi'^{*}W\}, \tag{5.31}$$

where the identity (5.28) has been employed to simplify the second term.

5.4.3 Nondimensionalized levitation metrics

Once P_0, $\langle P_1\rangle$ and $\langle U_1\rangle$ are determined, the time-averaged aerodynamic forces and moment can be expressed in the following rescaled forms, each with small asymptotic errors of $O(\varepsilon, h_o/a \sim \theta)$. Using integration by parts, one can rewrite the steady levitation force (5.2) as

$$\langle F_L\rangle = \frac{12\langle\mathcal{F}_L\rangle}{\varepsilon^2\sigma p_a a} = \int_{-1}^{1}\langle P_1\rangle\,\mathrm{d}\xi = -\int_{-1}^{1}\xi\frac{\mathrm{d}\langle P_1\rangle}{\mathrm{d}\xi}\,\mathrm{d}\xi, \tag{5.32}$$

and the steady moment about the plate center (5.4) as

$$\langle M\rangle = \frac{12\langle\mathcal{M}\rangle}{\varepsilon^2\sigma p_a a^2} = \int_{-1}^{1}\xi\langle P_1\rangle\mathrm{d}\xi = -\frac{1}{2}\int_{-1}^{1}\xi^2\frac{\mathrm{d}\langle P_1\rangle}{\mathrm{d}\xi}\mathrm{d}\xi, \tag{5.33}$$

both expressed in terms of the steady pressure gradient $\mathrm{d}\langle P_1\rangle/\mathrm{d}\xi$. Substituting the definition of the latter, given in (5.30), one may rewrite these expressions as

$$\langle F_L\rangle = \int_{-1}^{1}\xi G(\xi)\mathrm{d}\xi - \varphi\int_{-1}^{1}G(\xi)\mathrm{d}\xi \tag{5.34}$$

and

$$\langle M\rangle = \left[\frac{1}{2\varphi^2} - 1 + \frac{1}{\varphi}\left(\frac{1-\varphi^2}{2\varphi}\right)^2 \ln\left(\frac{1-\varphi}{1+\varphi}\right)\right]\int_{-1}^{1} G(\xi)\mathrm{d}\xi + \frac{1}{2}\int_{-1}^{1} \xi^2 G(\xi)\mathrm{d}\xi\,, \tag{5.35}$$

in terms of the known function G (5.29), with the associated dimensionless center of pressure given by

$$\xi_{csp} = \frac{x_{csp}}{a} = \frac{\langle M\rangle}{\langle F_L\rangle}\,. \tag{5.36}$$

The thrust force (5.3) can be expressed in the normalized form

$$\langle F_T\rangle = \frac{12\langle \mathcal{F}_T\rangle}{\varepsilon^2\sigma p_a h_o} = \langle F_T\rangle_P + \langle F_T\rangle_S\,, \tag{5.37}$$

as the sum of the distinct contributions of pressure and shear stress,

$$\langle F_T\rangle_P = \int_{-1}^{1} \varphi\langle P_1\rangle\,\mathrm{d}\xi = \varphi\langle F_L\rangle \qquad \text{and} \qquad \langle F_T\rangle_S = -\int_{-1}^{1} \left.\frac{\partial\langle U_1\rangle}{\partial Y}\right|_{Y=H}\mathrm{d}\xi\,, \tag{5.38}$$

respectively. Substituting the definition of $\langle U_1\rangle$, given in (5.31), provides

$$\langle F_T\rangle_S = -\frac{\varphi}{2}\langle F_L\rangle - \frac{1}{4}\mathrm{Re}\left\{\int_{-1}^{1} \Pi'^{*} W\,\mathrm{d}\xi\right\}, \tag{5.39}$$

where (5.32) has been used in rewriting the first term, which leads to

$$\langle F_T\rangle = \frac{\varphi}{2}\langle F_L\rangle - \frac{1}{4}\mathrm{Re}\left\{\int_{-1}^{1} \Pi'^{*} W\,\mathrm{d}\xi\right\} \tag{5.40}$$

for the thrust, upon addition to the first equation in (5.38). Note that, while the sign of $\langle F_T\rangle_P$ is determined strictly by the direction of levitation, effects of tilt and flexure compete to determine the sign of $\langle F_T\rangle_S$ and thus also that of $\langle F_T\rangle$.

5.4.4 Limiting cases of interest

For SFL systems with nonparallel surfaces undergoing arbitrary flexural oscillations, the integrals required to compute the steady pressure distribution (5.26), levitation force (5.34), moment (5.35) and thrust force (5.40), must be solved numerically. Results for this general problem are presented later, obtained using vectorized global adaptive quadrature [146] by way of the "*integral*" function built into the MATLAB software [147].

Discussed below are three special cases that allow analytical determination of the levitation metrics, namely, systems that involve (I) parallel rigid surfaces, (II) parallel surfaces undergoing a specific class of flexural oscillations and (III) nonparallel rigid surfaces. Note that these three cases correspond to the simplified levitation systems represented in figures 5.1(a), (b) and (c), respectively.

Case I) $\varphi = 0$ **,** $W = 1$

For an SFL system with parallel surfaces that undergo no elastic deformation, i.e. $H(\tau) = 1 + \varepsilon \cos \tau$, the reduced leading-order pressure is given by

$$\Pi(\xi) = \frac{12\mathrm{i}}{\beta^2}\left[\frac{\cosh(\beta\xi)}{\cosh\beta} - 1\right], \qquad \text{where} \qquad \beta = \sqrt{\sigma}\frac{1+\mathrm{i}}{\sqrt{2}}. \tag{5.41}$$

The steady pressure distribution and levitation force are given respectively by

$$\langle P_1\rangle(\xi) = \frac{3}{\sigma}\left[5 - \left|\frac{\cosh(\beta\xi)}{\cosh\beta}\right|^2 - 4\mathrm{Re}\left\{\frac{\cosh(\beta\xi)}{\cosh\beta}\right\}\right] \quad \text{and} \quad \langle F_L\rangle = \frac{30}{\sigma}\left(1 - \mathrm{Re}\left\{\frac{\tanh\beta}{\beta}\right\}\right), \tag{5.42}$$

the latter of which is demonstrably identical to the solution found by [143].

Due to the lateral symmetry of H (about $\xi = 0$), the thrust and levitation moment vanish, and the center of steady pressure is correspondingly located at the plate center, i.e. $\langle F_T\rangle = \langle M\rangle = \xi_{csp} = 0$.

Case II) $\varphi = 0$ **,** $W(\xi) = \sum_i C_i \xi^{n_i} \mathrm{e}^{m_i \xi}$ $\left\{C_i, m_i \in \mathbb{C}\text{ , } n_i \in \mathbb{Z}_{\geq 0}\right\}$

For systems with parallel surfaces undergoing flexural oscillation, where $H(\xi,\tau) = 1 + \varepsilon \mathrm{Re}\{W(\xi)\mathrm{e}^{\mathrm{i}\tau}\}$,

$$\Pi(\xi) = \frac{6\mathrm{i}}{\beta}\left[L(\xi) - \frac{\sinh[\beta(1+\xi)]}{\sinh(2\beta)}L(1)\right], \quad \text{where} \quad \beta = \sqrt{\sigma}\frac{1+\mathrm{i}}{\sqrt{2}}, \tag{5.43}$$

and the integral function L is defined as

$$L(\xi) = \mathrm{e}^{\beta\xi}\int_{-1}^{\xi} W(\tilde{\xi})\mathrm{e}^{-\beta\tilde{\xi}}\,\mathrm{d}\tilde{\xi} - \mathrm{e}^{-\beta\xi}\int_{-1}^{\xi} W(\tilde{\xi})\mathrm{e}^{\beta\tilde{\xi}}\,\mathrm{d}\tilde{\xi}\,. \tag{5.44}$$

The steady pressure distribution is then given by

$$\langle P_1\rangle(\xi) = \frac{1+\xi}{2}\int_{-1}^{1} G(\xi)\mathrm{d}\xi - \int_{-1}^{\xi} G(\tilde{\xi})\mathrm{d}\tilde{\xi}, \quad \text{where} \quad G = \frac{1}{2}\mathrm{Re}\left\{\Pi'^{*}\left(3W + \frac{\sigma}{12}\Pi\right)\right\}, \tag{5.45}$$

and the levitation force and moment are defined respectively by the simplified integrals

$$\langle F_L\rangle = \int_{-1}^{1} \xi G(\xi)\mathrm{d}\xi \qquad \text{and} \qquad \langle M\rangle = \frac{1}{2}\int_{-1}^{1} \xi^2 G(\xi)\mathrm{d}\xi - \frac{1}{6}\int_{-1}^{1} G(\xi)\mathrm{d}\xi\,. \tag{5.46}$$

First-order corrections to the pressure give no contribution to the thrust force due to the absence of tilt ($\varphi = 0$), whence $\langle F_T\rangle_P = 0$ and $\langle F_T\rangle_S = \langle F_T\rangle = -(1/4)\mathrm{Re}\left\{\int_{-1}^{1} \Pi'^{*}(\xi)W(\xi)\mathrm{d}\xi\right\}$.

In their asymptotic study, [143] computed $\langle F_T\rangle$ analytically for the case of pure traveling-wave oscillations, and utilized finite-difference methods for computing first-order pressure corrections. The generalized formulation above provides integral expressions for the thrust, as well as the accompanying levitation force and moment, for arbitrary waveforms $W(\xi)$. Fully analytical computation is possible for waves of the type $W(\xi) = \sum_i C_i \xi^{n_i} \mathrm{e}^{m_i \xi}$, where each C_i and m_i are complex numbers and each n_i is a whole number, which allow explicit integration in (5.44)–(5.46). Such waves can be found, for instance, in the form of solutions to the Euler–Bernoulli equation which governs the dynamic bending of beams [89, 125].

Case III) $\varphi \neq 0$ **,** $W = 1$

For rigid-body systems with non-parallel surfaces, where $W = 1$ and $H(\xi,\tau) = 1 - \varphi\xi + \varepsilon\cos\tau$, the reduced leading-order pressure assumes the form

$$\Pi(\xi) = \frac{12\mathrm{i}}{\varphi^2\zeta^2}\frac{1}{1-\varphi\xi}\left[\frac{(1-\varphi^2)^\zeta(1-\varphi\xi)^{-\zeta} + (1-\varphi\xi)^\zeta}{(1+\varphi)^\zeta + (1-\varphi)^\zeta} - 1\right], \tag{5.47}$$

with ζ defined in (5.20). Analytical expressions for the steady levitation metrics can be found through tedious but straightforward algebra. Most notably, the contribution to the thrust force from shear stresses is opposite in direction and half in magnitude relative to that from film pressure. This can be shown simply by substituting $W = 1$ into (5.39), which gives $\langle F_T\rangle_S = -\varphi\langle F_L\rangle/2 = -\langle F_T\rangle_P/2$. The net thrust force is thus given simply by $\langle F_T\rangle = \varphi\langle F_L\rangle/2$.

Of practical interest is the behavior of the solution for very small separation distances h_o, for which the greatest repulsive levitation forces are found to occur [19]. In the associated limit $\sigma \to \infty$, the steady overpressure distribution simplifies to $\langle P_1\rangle(\xi) = 15/\left[\sigma(1-\varphi\xi)^2\right]$, not accounting for the rapid relaxation of pressure to its ambient value at the film edges $\xi = \pm 1$ [59]. The corresponding levitation force and moment assume the simplified forms

$$\lim_{\sigma\to\infty}\langle F_L\rangle = \frac{30}{\sigma(1-\varphi^2)} \qquad \text{and} \qquad \lim_{\sigma\to\infty}\langle M\rangle = \frac{15}{\sigma\varphi^2}\left[\ln\left(\frac{1-\varphi}{1+\varphi}\right) + \frac{2\varphi}{1-\varphi^2}\right]. \tag{5.48}$$

5.5 Discussion of results

5.5.1 Time-averaged squeeze-film pressure

Exemplified in figure 5.4 are normalized distributions of the time-averaged first-order film pressure $\langle P_1\rangle(\xi)$ for the three limiting cases discussed above and represented in figures 5.1(a)–(c): (a) a rigid oscillator, (b) an oscillator undergoing traveling-wave deformations of the form $W = \exp(-2\mathrm{i}\pi\xi)$ and (c) a tilted, rigid oscillator with an inclination angle $\varphi = \theta/(h_o/a) = 0.2$. For

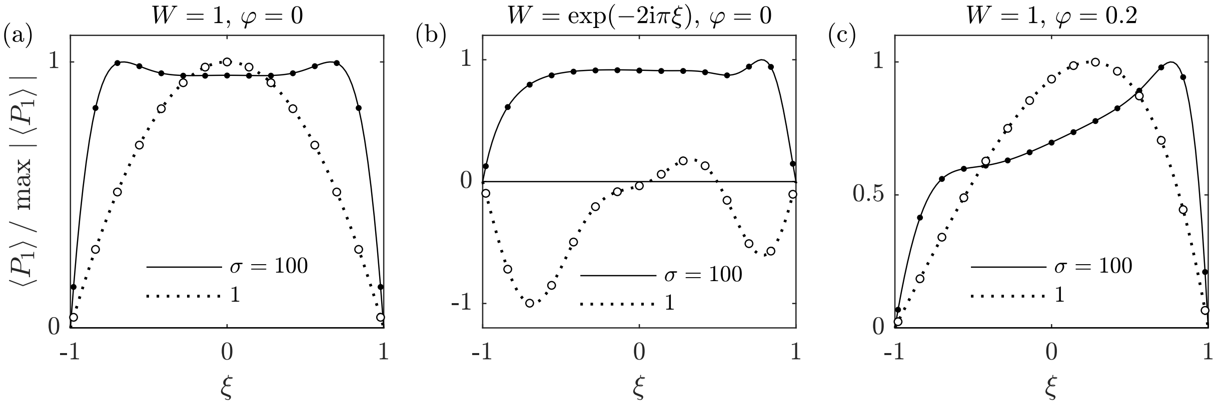

Figure 5.4. Sample profiles of the normalized time-averaged film pressure for SFL systems with (a) zero flexure and zero tilt, (b) pure traveling-wave flexure and (c) nonzero tilt. Asymptotic results (continuous and dotted curves) are verified with numerical solutions of (5.11) for $\varepsilon = 0.01$ (dots and circles).

all three cases displayed, $\langle P_1 \rangle(\xi)$ depends strongly on the squeeze number $\sigma = 12\mu_a \omega a^2/(p_a h_o^2)$. In particular, when $\sigma \gg 1$ and effects of gaseous compressibility are correspondingly augmented, as discussed below (5.5), the overpressure varies gradually within the film and relaxes sharply near its edges, in agreement with prior results [9, 59, 60].

For a flexible plate undergoing traveling-wave deformations, the steady overpressure distribution becomes largely negative for critically small values of σ, in agreement with prior results that demonstrate a strong correlation between flexural oscillations and the emergence of attractive SFL forces ($L < 0$) [101]. It is of interest to understand the behavior of such systems because of their ability to provide controlled transportation with attractive levitation, a phenomenon that was only recently demonstrated practically [100].

For a rigid plate with a positive inclination angle, the steady pressure distribution is skewed such that $\langle P_1 \rangle$ assumes larger values near the lowered leading edge $\xi = 1$. Correspondingly, while the steady film pressure yields a positive contribution $\varphi \langle F_L \rangle$ to the thrust, the steady shear force caused by first-order streaming acts in the opposite direction, reducing $\langle F_T \rangle$ by a factor of two, as noted below (5.47).

5.5.2 Visualization of levitation metrics

In pursuit of a practical understanding of the generic SFL transport system outlined in figure 5.3, it is of interest to delineate clearly—i.e. in a manner amenable to physical interpretation—the parametric dependences of the steady levitation metrics on the tilt ratio $\varphi = \theta/(h_o/a)$, flexural waveform $W(\xi)$ and squeeze number $\sigma = 12\mu_a\omega a^2/(p_a h_o^2)$.

Although these three governing parameters are considered to be independent under the present formulation, variations in σ can, in practice, affect W. In particular, since SFL oscillators typically operate near resonance [132], altering their excitation frequency ω or length $2a$ may disturb substantially the amplitude b and wavelength of their flexural deformations. Therefore, it seems most appropriate to interpret the variation with σ of the levitation forces and moment as a variation with the levitation height h_o. The latter is typically a 'dependent' variable that responds freely to changes in the applied load $\langle \mathcal{F}_L \rangle$, such as the change in apparent weight of a mobile robot as it travels along a curved path as in figure 5.2(b) [3]. (Note that, for oscillators with sufficiently low mass or flexural rigidity, b and W may be affected significantly by variations in h_o and the tilt angle θ [3, 103]; such consequences of two-way-coupled fluid–structure interactions are not considered below.)

Correspondingly, in representing the present asymptotic results, it is convenient to renormalize the steady levitation and thrust forces according to

$$L = \left(\frac{\sigma}{12}\right)^2 \langle F_L \rangle = \frac{\langle \mathcal{F}_L \rangle}{b^2 p_a^2/(\mu_a\omega a)} \quad \text{and} \quad T = \left(\frac{\sigma}{12}\right)^{3/2} \langle F_T \rangle = \frac{\langle \mathcal{F}_T \rangle}{b^2 p_a^{3/2} / \left(a\sqrt{\mu_a\omega}\right)}, \tag{5.49}$$

where multiplication by an appropriate power of σ has eliminated h_o. Upon introducing also a normalized height

$$\bar{h}_o = \frac{1}{\sqrt{\sigma}} = \frac{h_o}{2a\sqrt{3\mu_a\omega/p_a}}, \tag{5.50}$$

the dimensionless functions $L(\bar{h}_o)$ and $T(\bar{h}_o)$ can be interpreted to represent the variations of the levitation and thrust forces with the mean levitation height, for a given tilt ratio and flexural

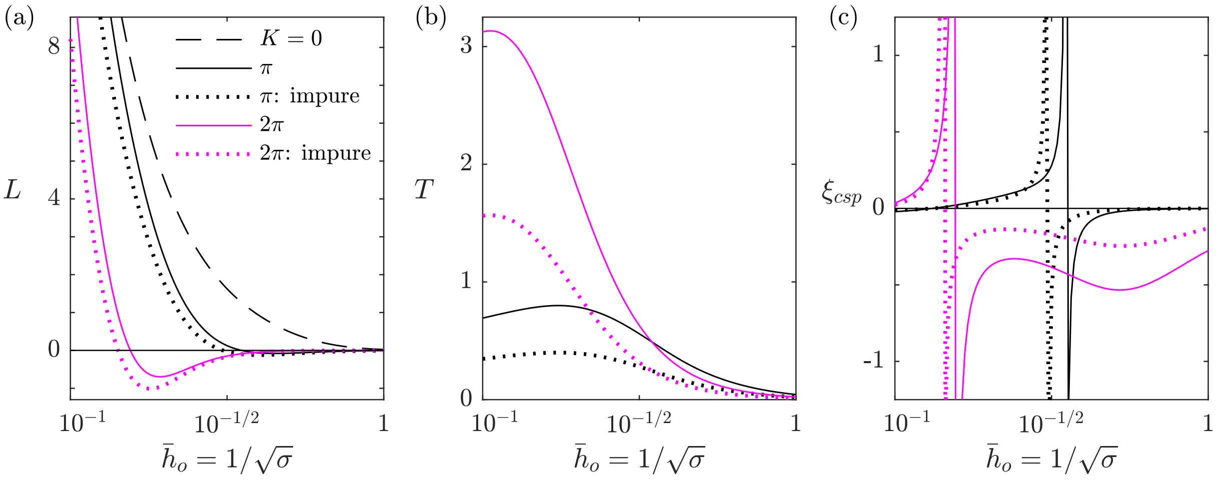

Figure 5.5. Variation with the normalized levitation height $\bar{h}_o$ (5.50) of the dimensionless (a) levitation and (b) thrust forces (5.49) and (c) the center of steady pressure (5.36), for a traveling-wave-driven system with varying wavenumber K. Curves labeled 'impure' are computed for a wave purity of $\mathcal{P} = 0.5$ (5.51).

waveform.

Displayed in figures 5.5 and 5.6 are the variations with $\bar{h}_o$ of L, T and the center of steady pressure ξ_{csp} for the canonical transport systems pictured in figures 5.1(b) and (c), respectively. It may be readily noted from both figures that the limiting behaviors of L for small and large values of $\bar{h}_o = 1/\sqrt{\sigma}$ are consistent with prior knowledge concerning the role of gaseous compressibility in SFL systems, the latter elucidated below (5.5). The behavior of the solution for intermediate levitation heights $\bar{h}_o \sim 1$, however, differs substantially between the two cases and will be discussed below.

5.5.3 Transport by traveling-wave oscillations

The solid curves in figure 5.5 represent the levitation metrics for systems with parallel surfaces ($\varphi = 0$) driven by pure traveling-wave deformations of the form $W = \mathrm{e}^{-\mathrm{i}K\xi}$, where K is the relevant flexural wavenumber that has been normalized with the inverse of the semi-length a.

As seen respectively in panels (a) and (b), the levitation force is significantly reduced by flexure within the displayed range of heights $\bar{h}_o$, and the thrust force exhibits a finite maximum at a critical height that varies with K. Investigation of the limit $\bar{h}_o \to 0$ (or, equivalently, $\sigma \to \infty$)

reveals that curves of L for all values of K eventually converge in the case of pure traveling waves, in agreement with the findings of [143], who noted that optimization of these systems for repulsive operation warrants compromising between a levitation force that increases for decreasing values of $\bar{h}_o$ and a thrust force that varies non-monotonically.

Furthermore, as seen in panel 5.5(c), the center of steady pressure ξ_{csp} varies strongly with $\bar{h}_o$, indicative of a high sensitivity to levitation height that must be taken into account when designing and controlling a mobile robot or a rail-transport system. Interestingly, ξ_{csp} exhibits a singularity at a critical height that corresponds to a state of zero levitation. Beyond this critical height, L assumes negative values, corresponding to attractive levitation (see the associated distribution of steady film pressure exemplified in figure 5.4(c)). Both the attractive load capacity and the maximum thrust rise with increasing values of the wavenumber K.

As noted previously, generation of pure traveling-wave deformations of a finite body is hindered by the reflection of propagating waves at open boundaries and points of actuation. The resulting *impure* traveling waves can be modeled approximately with use of the modified waveform

$$W = \cos(K\xi) - \mathrm{i}\mathcal{P}\sin(K\xi), \quad \text{with} \quad 0 \leq \mathcal{P} \leq 1, \tag{5.51}$$

where $\mathcal{P}$ constitutes a coefficient of purity. Namely, when $\mathcal{P} = 1$, W parametrizes the classical traveling wave $\mathrm{e}^{-\mathrm{i}K\xi}$, and when $\mathcal{P} = 0$, a perfect standing wave of equal wavenumber and amplitude [33, 144]. Note that the inverse of $\mathcal{P}$ is often referred to in literature as the 'standing-wave ratio'. As exemplified by the dotted curves in figures 5.5(a) and (b), introduction of impurity in a traveling-wave-driven SFL system seems to improve the attractive load capacity, but reduces drastically the maximum thrust force that can be produced.

5.5.4 Effects of surface inclination

Represented in figure 5.6 are the levitation metrics for a rigid-body system ($W = 1$) with various tilt ratios $\varphi = \theta/(h_o/a)$. Recall that φ is a dimensionless representation of the amount of

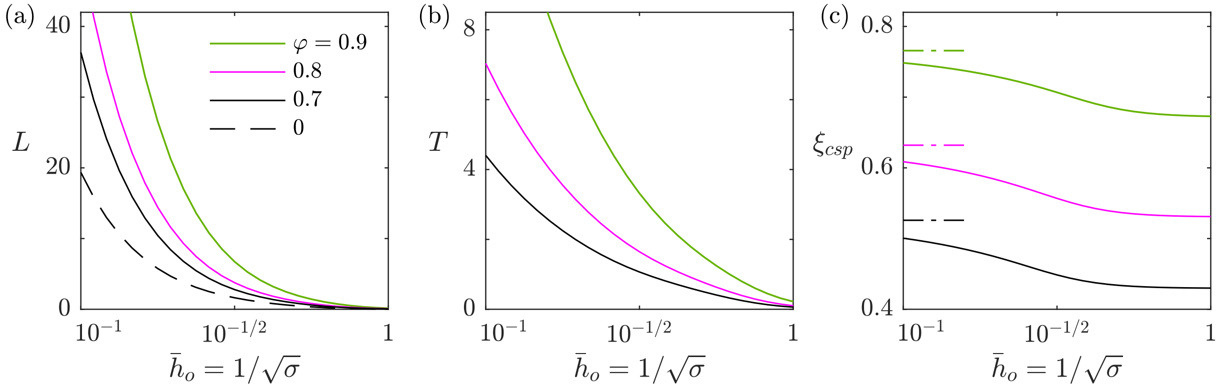

Figure 5.6. Variation with the normalized levitation height $\bar{h}_o$ of the dimensionless (a) levitation and (b) thrust forces and (c) the center of steady pressure ξ_{csp} for a rigid-body SFL system, for various values of the tilt ratio φ (5.7). Limiting values of ξ_{csp} for $\bar{h}_o \to 0$ (broken lines) are found using (5.36) and (5.48).

tilt where, for any given levitation height h_o, $\varphi = 0$ denotes parallel surfaces and $\varphi = \pm(1-\varepsilon)$ denotes maximum tilt in either direction—i.e. the leading or trailing edge of the plate comes into contact with the opposite wall during the closing stroke of each oscillation cycle.

It is clear from panels 5.6(a) and (b) that tilting the plate about its center substantially increases the levitation and thrust forces produced at any given central levitation height $\bar{h}_o$. Both appear to increase unboundedly as $\bar{h}_o \to 0$, assuming substantially greater values than those produced by flexure-driven systems for the range of $\bar{h}_o$ displayed. Indeed, in the associated limit of large σ (5.48), L becomes proportional to the inverse square of the levitation height $\bar{h}_o^{-2}$, well in agreement with prior research [5], and $T \propto \bar{h}_o^{-1}$. Of course, both are physically limited since h_o cannot decrease below the oscillation amplitude b [19]. Finally, panel 5.6(c) demonstrates that the center of steady pressure ξ_{csp} moves toward the leading edge with increasing forward tilt and varies rather weakly with $\bar{h}_o$. The associated steady moment acts to reduce the angle of inclination, in agreement with the restoring moment found by [145].

A note on load and thrust capacities

A cautionary note must be provided here regarding the effect of tilt on the load and thrust *capacities* of an SFL system. Tilting about the center increases both L and T for any given levitation height $h_o \propto \bar{h}_o$, as noted previously, but also limits the minimum possible h_o physically attainable by the system for a given amplitude b (such that neither edge of the plate makes contact with the wall). It is then unclear from figures 5.6(a) and (b) alone whether tilting increases or decreases the *maximum* possible levitation and thrust forces producible by an SFL system.

This question can be addressed by considering, for simplicity, the large-σ (small-h_o) behavior of the problem under an appropriate reformulation—shifting the spatial domain from $-1 \leq \xi \leq 1$ to $-2 \leq \xi \leq 0$. Under this reference frame, the leading edge of the plate is the point of rotation h_o, whence the minimum possible levitation height $h_o = b$ is constant for all positive tilt angles $\theta > 0$. The spatial pressure variation along the squeeze-film is then given at leading order by

$$\Pi(\xi) = \frac{12\mathrm{i}}{\varphi^2\zeta^2}\frac{1}{1-\varphi\xi}\left(\frac{(1+2\varphi)^{\zeta}-1}{(1+2\varphi)^{2\zeta}-1}\left[(1-\varphi\xi)^{\zeta}+\left(\frac{1+2\varphi}{1-\varphi\xi}\right)^{\zeta}\right]-1\right), \tag{5.52}$$

in place of (5.47), and the steady pressure variation at first order can be computed as

$$\langle P_1\rangle(\xi) = \int_{\xi}^{0} G(\tilde{\xi})\mathrm{d}\tilde{\xi} - \frac{(1-\varphi\xi)^{-2}-1}{(1+2\varphi)^{-2}-1}\int_{-2}^{0} G(\tilde{\xi})\mathrm{d}\tilde{\xi}, \tag{5.53}$$

where the auxiliary function G, defined originally in (5.29), is given here by $G = 1/2\mathrm{Re}\{\Pi'(\sigma\Pi^*/12 + 3/(1-\varphi\xi))\}$. (Recall that an asterisk denotes a complex conjugate.) It can be shown by plotting (5.53) that the steady pressure everywhere inside the film ($-2 < \xi < 0$) reduces when the plate is tilted forward ($\varphi > 0$) about its leading edge. It is then obvious that inclination actually reduces the repulsive load capacity, but the effect on the maximal thrust is unclear *a priori*.

In the limit of large σ, (5.53) reduces to the same expression given above (5.48), whence the levitation and thrust forces simplify respectively to $\sigma\langle F_L\rangle = 30/(1+2\varphi)$ and $\sigma\langle F_T\rangle = 15\varphi/(1+2\varphi)$. Fortunately, the thrust $T = (\sigma/12)^{3/2}\langle F_T\rangle$ for any large value of σ does grow monotonically with φ, approaching an asymptotic value of $3^{-3/2}(15/16)\sqrt{\sigma}$ as $\varphi \to \infty$.

Thus, for practical SFL systems, increasing inclination provides greater lateral forces while reducing the repulsive load capacity. For instance, tilting by an amount $\varphi = \theta/(h_o/a) = 1/2$

provides a thrust capacity equal to half the asymptotic value approached for $\varphi \to \infty$, but at the cost of reducing the repulsive load capacity by 50% from its value for zero tilt. Note finally that this question of capacities is of lesser concern for flexural systems performing attractive levitation, for which the maximal forces are achieved for finite critical levitation heights h_o, as elaborated below [1].

* * *

It is of interest to investigate the effects of surface inclination on systems with nonuniform oscillations, for which $\mathrm{d}W/\mathrm{d}\xi \neq 0$. We begin by noting, based on the curves shown in figure 5.5(c), that the sensitivity of ξ_{csp} to perturbations in the levitation height h_o can be expected to increase in the presence of oscillator flexure, accompanying a possible transition to attractive levitation forces [101]. For systems with lateral symmetry, i.e. when $W(-\xi) = W(\xi)$ for $0 < \xi \leq 1$, inclination in either direction is expected to (i) provide significant thrust and (ii) increase substantially the existing repulsive levitation force for a given levitation height, based on the results shown in figure 5.6. Systems undergoing asymmetrical oscillations require further investigation.

Visualized using solid curves in figure 5.7, for example, are the levitation metrics of a system driven by pure traveling-wave oscillations, for various values of the tilt ratio φ. As seen in panel (a), positive and negative inclination increase substantially the repulsive and attractive levitation forces, respectively. Displayed in panel (c) are the aptly rescaled steady pressure distributions that correspond to the state of maximal attraction for $\varphi = \theta/(h_o/a) = 0$ and -0.5, indicated in panel (a) by the solid triangles. Panel (b) reveals that inclination in either direction increases also the thrust force T for a wide range of levitation heights $\bar{h}_o$, due to the combined contributions of fluid shear (stemming from wave propagation) and pressure (from surface tilt). The dotted curves in panels (a)–(c) indicate, however, that the degree of purity of the traveling wave significantly impacts the extent to which these benefits may be realized practically. Panel (d), where only pure traveling waves are considered for purposes of visual clarity, confirms

---

[1] This nuance was not adequately addressed in the original publication where the results of this chapter were communicated [148].

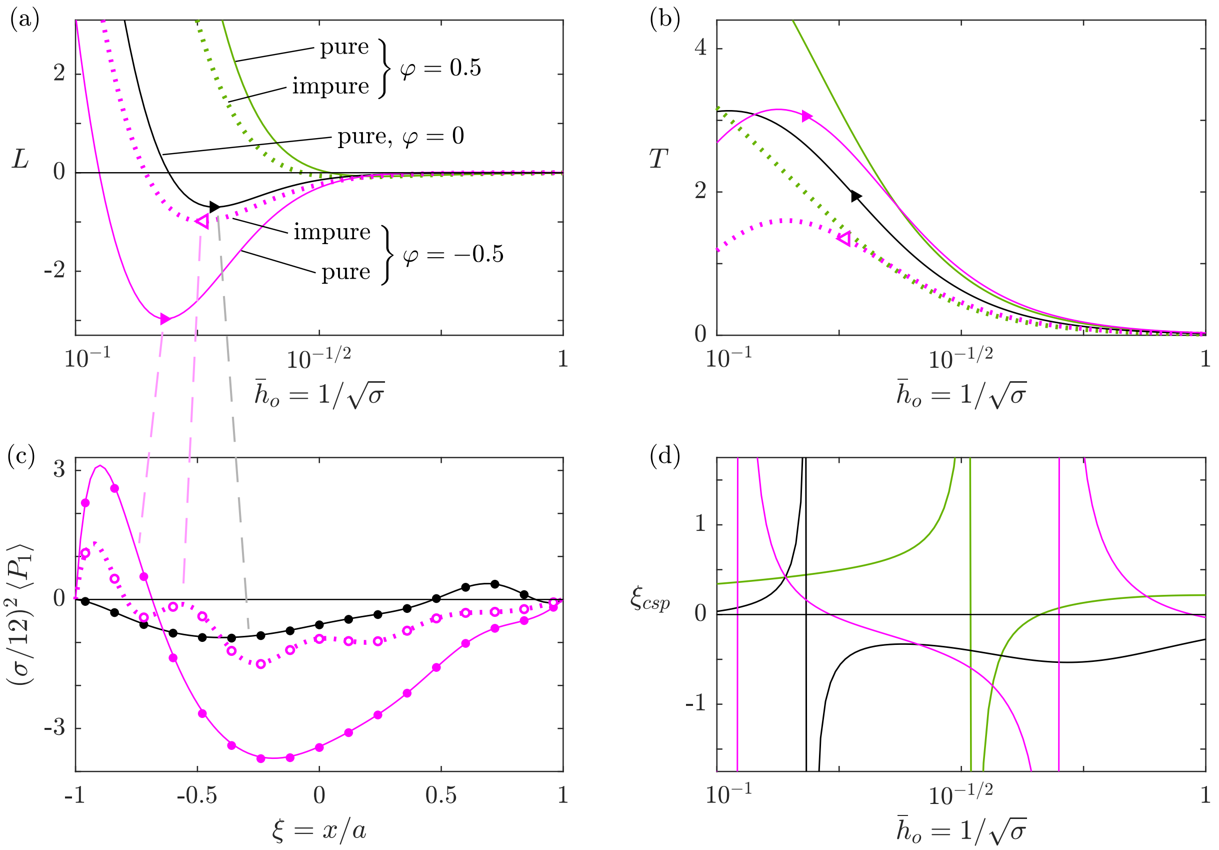

Figure 5.7. Variation with the normalized levitation height $\bar{h}_o$ (5.50) of the rescaled (a) levitation force (5.49), (b) thrust and (d) center of steady pressure (5.36), for a flexural system with wavenumber $K = 2\pi$. Curves are shown for various tilt ratios φ (5.7) and wave purities $\mathcal{P}$ (5.51); curves labeled 'impure' are computed for $\mathcal{P} = 0.5$. Plotted in (c), and verified numerically for $\varepsilon = 0.01$ (dots and circles), are profiles of steady pressure for states where the system produces maximal attraction, marked with triangles in (a) and (b).

the anticipated high sensitivity of ξ_{csp} to h_o that accompanies the transition from repulsion to attraction for flexural systems.

5.5.5 Optimization of traveling-wave-driven systems with variable inclination

Based on the preliminary results above, it appears that controllability of the inclination angle of the levitated object can improve the effectiveness of transport systems driven by traveling-wave deformations of the oscillator, for purposes of both repulsive and attractive squeeze-film levitation. To quantify precisely the extent of improvement that may be gained, we conclude this chapter with a rigorous investigation of the associated generalized problem ($\varphi \neq 0$, $0 \leq \mathcal{P} \leq 1$).

As discussed in § 5.2, the purity $\mathcal{P}$ of a traveling wave is limited by the effectiveness of the wave-generation method, and the wavenumber K is typically determined by the chosen natural frequency and geometric properties of the oscillator. Active feedback control is often employed to ensure that the resulting waveform W remains constant during operation. In contrast, the levitation height $\bar{h}_o$ and tilt ratio φ are free to respond to (i) perturbation by external forces and/or (ii) active adjustments to the mass or center of mass of the levitated object. In pursuit of quantifying the maximal capabilities of traveling-wave-driven SFL systems that feature controllable inclination, we therefore explore the parametric domain spanned by $\bar{h}_o$ and φ, for a fixed wavenumber $K = 2\pi$ and select values of $\mathcal{P}$.

Two important distinctions must be drawn at this point between the mobile robot depicted in figure 5.2(b) and the rail-transport system schematized in figure 5.2(a). In the case of the former, the oscillator is attached to the levitated object, such that the waveform W is invariant as the object travels. In contrast, for rail-transport systems, the wave is subject to a phase shift that evolves as the object translates, whence stationary components in the wave can cause fluctuations in the levitation forces and moment. The resulting operational instabilities may be especially pronounced for traveling waves with lower purity $\mathcal{P}$ and relative wavenumber K [37, 149, 150]. Secondly, the mass distribution of a self-levitating mobile robot may be adjusted actively to control the inclination φ, but that of a levitated object in a rail-transport system is typically fixed. Both of these distinctions must be considered carefully when interpreting and applying practically the following results.

The performance objective(s) for an SFL system will vary with the desired transportation path, for instance, translation (i) above a horizontal surface, (ii) below a horizontal surface, (iii) upward or downward along a vertical surface, or otherwise (see figure 5.2 for clarificatory illustrations).

For transport above a horizontal surface, a possible objective may be maximizing the thrust T while incurring the least possible loss of repulsive load capacity L. Based on the

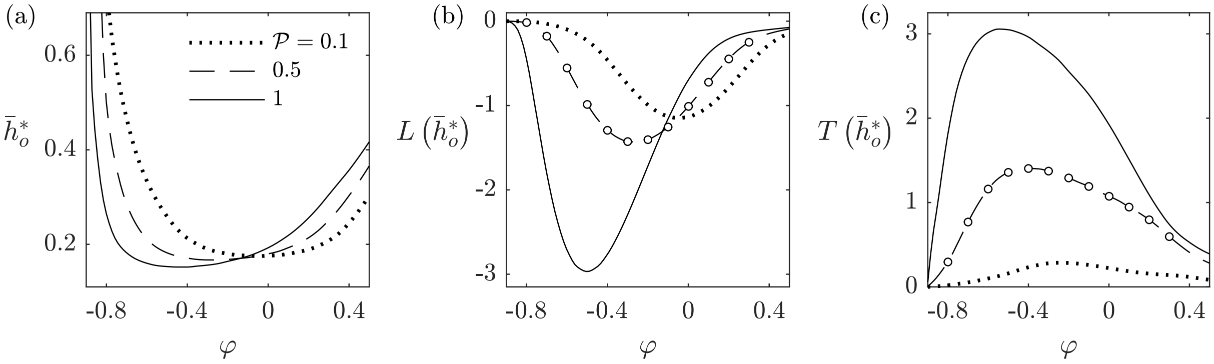

Figure 5.8. Variation with the tilt ratio φ of (a) the normalized critical levitation height at which a traveling-wave-driven system with wavenumber $K = 2\pi$ generates maximal attraction, and the corresponding values of (b) the levitation force L and (c) the thrust T, for three values of the wave purity $\mathcal{P}$ (5.51). For the case $\mathcal{P} = 0.5$, L and T are verified with numerical solutions computed for $\varepsilon = 0.01$ (circles).

discussion provided in § 5.5.4 and the results shown in figures 5.5–5.7, it is clearly beneficial to increase the traveling wave purity as much as physically possible while modulating carefully the inclination angle to balance the required gain in thrust with the inevitable, accompanying reduction in load capacity.

For transport below a horizontal surface, it may be of interest to maximize the attractive levitation force ($-L$) and/or the thrust T. As seen for example in figures 5.5 and 5.7, L may exhibit a negative global minimum for a critical levitation height $\bar{h}_o = \bar{h}_o^*$. Plotted in figure 5.8 are the *non-monotonic* variations with φ of this maximal attractive force $L(\bar{h}_o^*)$ and the corresponding thrust $T(\bar{h}_o^*)$ for various values of $\mathcal{P}$, demonstrating that there is a critical range of tilt ratios for which the performance of such a system is maximized. For instance, when $\mathcal{P} = 0.5$, an inclination of $-0.45 \lesssim \varphi \lesssim -0.2$ is most desirable. Note that the benefits of controlled inclination are greater for purer traveling waves. Of practical concern is the fact that systems operating at this critical height are unstable to positive perturbations in $\bar{h}_o$, i.e. $\partial L/\partial \bar{h}_o > 0$ for $\bar{h}_o > \bar{h}_o^*$. For this reason, operating below the maximum capacity, at a height $\bar{h}_o < \bar{h}_o^*$, is recommended for avoiding catastrophic failure during attractive levitation.

Finally, for vertical transport along an upright surface, the thrust force must be maximized

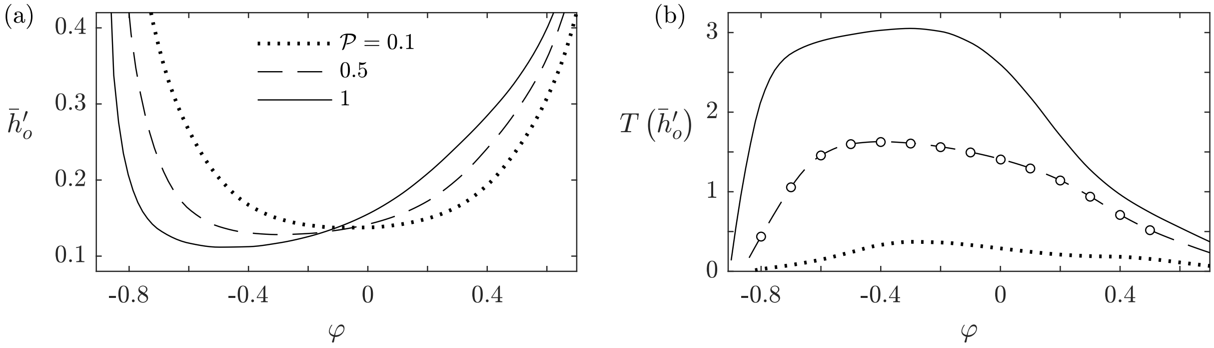

Figure 5.9. Variation with the tilt ratio φ of (a) the normalized critical levitation height at which a traveling-wave-driven system with wavenumber $K = 2\pi$ generates zero levitation force and (b) the corresponding value of the thrust force T, for three values of the wave purity $\mathcal{P}$ (5.51). For the case $\mathcal{P} = 0.5$, asymptotic results for T are verified with numerical solutions computed for $\varepsilon = 0.01$ (circles).

while the levitation force L must be identically zero. As seen for example in figures 5.5 and 5.7, the function $L(\bar{h}_o)$ may vanish at a critical height $\bar{h}_o'$, corresponding to a transition from repulsive to attractive levitation. A system that operates at this height is necessarily stable to positive and negative perturbations in $\bar{h}_o$, i.e. $\partial L/\partial \bar{h}_o < 0$ for $\bar{h}_o = \bar{h}_o'$. Plotted in figure 5.9 is the variation with the tilt ratio φ of the corresponding thrust force $T(\bar{h}_o')$ for various values of the wave purity $\mathcal{P}$. Once again, there appears to be a desirable range of tilt ratios for which performance is maximized, with greater benefits obtained for purer oscillations.

These analyses may be readily extended to address more complex design problems, those that may require inclined transport paths and involve performance criteria that concern simultaneously the levitation force $\langle \mathcal{F}_L \rangle$, thrust $\langle \mathcal{F}_T \rangle$ and stability to perturbations in the tilt angle θ.

5.6 Conclusions

Developed in this chapter is a theoretical description of the planar, viscous, compressible airflow in contactless transport systems that operate using squeeze-film levitation. The reduced asymptotic formulation, which addresses the flexural oscillation of a plate near a non-parallel surface, provides fundamental insights into the fluidic mechanisms that underlie thrust generation in squeeze-film systems, and enables rapid computation of their performance characteristics using integral expressions.

Particular attention is dedicated to studying the effects of inclination of the levitated body for transport systems that are driven by impure traveling-wave deformations of the oscillator (see figures 5.2 and 5.3 and equation (5.51) for clarification). Results demonstrate that controlled modulation of the tilting angle can improve substantially the maximal load capacity as well as the associated thrust force generated by systems that operate using attractive levitation. The amount of improvement that can be gained is found to depend strongly on the purity of the traveling wave or, more generally, presumably on the degree of lateral asymmetry in the flexural oscillations. This is in stark contrast to the behavior of repulsive levitation systems, for which inclination to provide thrust necessarily reduces the maximal load capacity.

Sample computations are provided to display the potential of the present formulation in serving as an efficient tool to supplement the design, optimization and active control of mobile robots. The accuracy and versatility of this theoretical model must be improved in the future by modeling appropriately the effects of non-negligible transport speeds [59], free vibrations of the levitated object [39, 103], fluid–structure coupling by which the flexural waveform of the oscillator may alter in response to changes in levitation height and tilt angle [3], fluid inertia and the accompanying variations of steady pressure beyond the boundaries of the squeeze film [60], and surface roughness which can substantially reduce the levitation force and transport speed [3, 34].

Chapter 5 has been published in *Flow* under the title “Benefits of controlled inclination for contactless transport by squeeze-film levitation”, by S. Ramanarayanan and A. L. Sánchez, 3, E26, (2023). The dissertation author was the primary investigator and author of this paper.

Chapter 6

Suggested future work

Provided below are recommendations for specific avenues of theoretical and experimental research that, together, may further enhance our understanding of vibration-driven squeeze-film (SF) systems and bring them closer to the point of practical application.

6.1 Open practical challenges

(i) **Sensitivity to surface roughness:** The most limiting feature of contemporary SF systems seems to be the need for smooth bounding surfaces [34], with complete failure of levitation observed when using materials such as stone, bricks and open-cell foam [3]. Despite their high energy efficiency, SF levitators are inferior in this respect to Bernoulli grippers, which can lift objects with a wide range of surface texture and structural compliance. An elegant but revolutionary development is required in solving this problem, presumably with the aid of theoretical modeling of surface asperities to investigate in detail the fundamental cause(s) of failure [151, 152].

(ii) **Systemic stochasticity:** In a recent study of squeeze-film levitation with highly flexible oscillators [3], the experimenters report having observed "large variation across trials" when measuring the maximal attractive load capacity, and state that such variability is expected due to the "randomness inherent in a vibration-based actuation method". This element of operational stochasticity may owe in large part to the substantial flexibility of the oscillator, which is needed to produce strong attraction (see Chapter 3). Active control techniques must be developed to improve the reliability and robustness of such flexural SF systems.

(iii) **Sound levels:** The first studies of highly flexural SF systems [3, 49] utilized sound exciters and eccentric-rotating-mass motors, resulting in non-negligible levels of sound emanating from both the vibration source and the flapping oscillator. A more recent study [100] utilized linear resonant actuators, which provided nearly silent operation but also a substantial reduction in attractive load capacity due to a weak forcing amplitude. Langevin transducers driven by piezoelectric ceramics readily enable ultrasonic frequencies which are inaudible to humans, but such high frequencies do not appear to be amenable to the generation of strong attraction, based on the results presented in Chapter 3. Development of low-frequency, low-noise, large-amplitude vibration actuators may render flexural SF systems more readily applicable commercially, especially for devices meant to operate in homes, office spaces, etc.

(iv) **Non-planar surfaces of attachment:** The three main surface geometries studied in the history of repulsive force generation are planar, cylindrical and spherical, with the latter two requiring cambered oscillators. It may be of interest to design cambered flexural oscillators that produce strong attractive forces for non-planar surface geometries. If realized, such systems may compete with modified Bernoulli grippers that have been designed with deformable lifting surfaces [153], for instance, in applications involving the contactless handling of food items to avoid contamination. Note that attractive levitation of compliant oscillators beneath slightly curved surfaces has been demonstrated successfully [3].

(v) **Bidirectional levitation:** Assembly-line transport of sensitive items such as silicon wafers or glass substrates (used in the design of digital displays) is an important proposed application of SF levitation. The ability to transition reliably between repulsive and attractive levitation would render SF devices highly suitable for this task and enable complex handling procedures. The salient limitation of SF systems in this respect is that their maximal load capacity in either direction depends critically on the operating frequency and oscillator stiffness: lower frequency and stiffness provide weaker repulsion and stronger attraction, in general (see Ch. 3). The ability to modulate either parameter—without adversely affecting the oscillation amplitude—may provide for a versatile gripper with high bidirectional load capacity. For example, one may develop an oscillator that is specially designed to enable active alteration of its flexural rigidity, possibly through control of its internal structure. It must be noted in this connection that, in previous studies a 'holding force' has been observed that stabilizes the levitated object to lateral perturbation (displacement perpendicular to the oscillation axis) [4]. This restorative, time-averaged aerodynamic force can be enhanced by utilizing multiple oscillators oriented in different directions around the levitated object [154–156]. It may be benificial to integrate into such configurations highly flexible oscillators that can provide strong attractive levitation forces.

6.2 Possible theoretical investigations

(i) **Hysteresis during pull-off:** In this dissertation, the attractive load capacity of an SF system was computed by seeking a unique, periodic solution to the relevant differential equation(s) governing the fluid–structure dynamics. Such an analysis does not account for possible hysteresis in the pull-off process whereby the system performance at any given stage of the process may depend on its operating conditions at a previous stage. Hysteresis may be caused by (i) physical contact between the oscillator and the opposite surface during early stages of pull-off, akin to a suction cup [96], and (ii) abrupt application of the pulling load over a small timescale that is comparable to the period of the sinusoidal excitation. For a discussion of the former, see § 6.3. As evidence of the latter, [3] demonstrated the ability of a robot levitating underneath a horizontal surface to remain suspended when a heavy payload was attached impulsively. It is of great interest to investigate rigorously the effects of these factors on the pull-off force—the maximal attractive force supported by the system.

(ii) **Other mechanical configurations:** It may be of practical interest to extend the results derived herein to describe squeeze-film systems with more complex configurations, such as those involving non-circular oscillators and/or non-planar surfaces of attachment, and those requiring transportation of a levitated object/device. In particular, the formulations developed in Chapters 4 and 5 must be combined to assess the impact of fluid–structure coupling (and structural impedance to localized excitation) on the general conclusion drawn in Ch. 5—that controlled modulation of the tilting angle of an attractively levitated object/device can improve its transport performance.

(iii) **Multi-fidelity computation:** While the reduced theoretical descriptions presented in this dissertation provide new insights into the physical dynamics of SF systems, their quantitative accuracy is fundamentally limited by the various enabling approximations drawn. Computational simulations must be conducted for appropriately generalized fluid–structure problems in order to provide greater accuracy for specific design purposes. The distinct advantages of the two approaches—the speed of reduced mathematical formulae and the precision of computational solutions—may be synthesized with use of multi-fidelity modeling to supplement design optimization and feedback control for future SF systems.

(iv) **Flow stability analysis:** The theoretical analyses in this dissertation assume laminar flow, in congruence with the asymptotic limit of small oscillator displacement. However, in practical systems the local Reynolds number, which rises linearly with radial distance along the air layer (for an axisymmetric geometry), may grow sufficiently large to induce a transition to turbulence that may affect the performance of larger-scale systems, such as those developed by Dr. Colasante (see § 1.3). In this connection, the stability of an oscillatory base flow in a squeeze film must be studied rigorously. It may be of use to additionally consider the effects of a compliant bounding surface [157, 158], in pursuit of explaining the systemic stochasticity observed in the case of highly flexible oscillators [3].

6.3 Other instances of vibration-induced attraction

(i) **Underwater squeeze-film effect:** The first study of SF levitation to report attractive forces seems to be from 1999 [12], where 45 grams of force were supported under water by a piston of diameter $2a = 5$ cm oscillating at a frequency of $f = 17$ kHz. The results of this dissertation clearly indicate that there is a critical maximum frequency f_c beyond which an SF system cannot generate attraction, and that the value of f_c grows with the flexibility of the oscillator. Nevertheless, a frequency of 17,000 Hz is several orders of magnitude larger than those for which such strong attractive forces have been found in air (see table 3.1), warranting dedicated exploration of the unique dynamics of underwater SF operation. Two recent theoretical studies notably investigated hydrodynamic SF lubrication [83, 159], the latter of which claims that effects of compressibility are non-negligible. (This claim may be relevant with respect to the 1999 experiment due to the fact that, for an approximate value of $c_w = 1500$ m/s for the underwater acoustic wave speed [160], the anticipated timescale for lateral pressure equilibration, $a/c_w \approx 17\,\mu$s, is not too small relative to that of the driving oscillations, $1/f \approx 59\,\mu$s.) However, neither study explained the observed transition to attractive forces, characterization of which may require a rigorous theoretical description of hydroacoustic wave propagation [84] (and, possibly, cavitation [161]).

(ii) **Alternating-flow Bernoulli gripper:** The large attractive SF levitation forces enabled by highly flexible oscillators seems to have been first observed by Dr. David Colasante [49]. In earlier experiments, he explored a related method for contactless attractive levitation, namely, an alternating-flow Bernoulli gripper (or aerostatic bearing). A standard Bernoulli gripper blows a jet of air on a nearby object, creating a local overpressure. The air diverges through the slender film between the gripper and the object, creating an area of low pressure that can provide a net attractive force under appropriate conditions [87]. Dr. Colasante replaced the continuous air pump with a speaker whose diaphragm oscillated at about 65 Hz and provided oscillatory airflow. His device levitated an object weighing 126 grams, with a power input of about 50 watts [162]. As Bernoulli grippers are already utilized commercially, there is great practical interest to compare by means of a unified fluid-flow analysis the performance of continuous- and alternating-flow grippers. The aerodynamics giving rise to the attractive force in the latter configuration may be related in some respects to the problem of rigid-body SF levitation explored in Chapter 2 of this dissertation.

(iii) **Vibrating suction cup and the effects of physical contact:** A technique closely related to flexural SF levitation has been investigated before, namely, vibration-induced enhancement of suction cup attachment. In the communication where this technique was first introduced [96], a wall-climbing robotic device equipped with six suction cups, each with a diameter of 2.5 cm, was oscillated by a powerful eccentric-rotating-mass motor at a very low frequency of 8 Hz. The device attached successfully to a *rough* vertical surface whose asperities prevented regular (non-oscillatory) attachment. Unlike ideal SF levitation, this technique seems to involve physical contact between the oscillator and wall, as evidenced by the observed resistance to translational and rotational motion. The maximal pulling force, translational force and twisting moment supported by the cup increase substantially when it is axially oscillated [97]. This method inspired the later development of ‘biomimetic’ wall-climbing robots [163, 164] with various configurations.

Note in this connection that, while the analyses of SF levitation contained in this dissertation assume the presence of a complete lubrication layer, i.e. $h > 0$ for $0 \leq r \leq a$, it appears based on the experiments of [3] and [129] that a highly flexible oscillator performing attractive SF levitation may come into contact with the opposite surface when the applied pulling load—and, correspondingly, the separation distance $h(r,t)$—is sufficiently small (as noted from personal communication with the authors of both references). The onset of physical contact is evidenced by (i) an increased resistance to translational motion shown by the oscillator and (ii) an increased operational sound level due to the transfer of mechanical vibrations to the opposite surface.

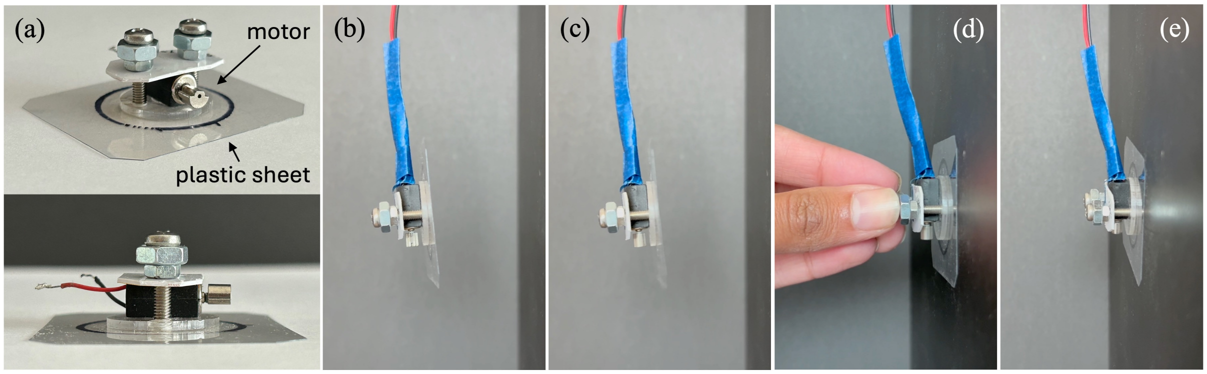

Figure 6.1. (a) An eccentric-rotating-mass motor (6 x 12 mm, rated for: 3 V, 85 mA, 12000 rpm) is affixed to a 0.007-inch-thick polyester plastic plate. (b) The device is hung by the motor wires, (c) the motor is activated, (d) the device is pressed against a wall and (e) clings to the wall until the motor is deactivated.

To illustrate these potentially adverse effects of physical contact in attractive SF levitation, consider the simple, inexpensive experiment[1] depicted in figure 6.1. The experiment requires (i) a small vibration actuator such as a sound exciter, a linear resonant actuator or an eccentric-rotating-mass motor, and (ii) a small rectangular plate cut out of a business card, a Manilla folder, polyester plastic, posterboard, or a similarly flexible material.

Mount the motor near the center of the plate with a strong glue joint that allows efficient transfer of vibrations. Activate the motor and note the noise level of the device. Hold the device without touching the oscillating plate, and bring the plate close to a parallel glass window, a whiteboard, a piece of sheet metal or plexiglass, or a similarly smooth surface. Press the device against the surface. When you remove your hand from the device, it should cling to the surface and possibly drift around slowly. Note that the noise may have increased due to surface vibrations. Try using surfaces with various orientations: vertical, horizontal and inclined. Performance may vary based on the strength of the motor, the flexibility of the plate and the cumulative mass of the device and wires. Repeat this process with the motor turned off, to confirm that there is no natural adhesion and insufficient vacuum generation between the static plate and the opposite surface.

---

[1] A video recording of the experiment is available through the following link: https://youtu.be/9XWjjLyw9_o

If you pull on the device as it clings to the wall, you should feel a slight resistance before it detaches, indicative of the attractive squeeze-film force. If you nudge the device laterally, you should feel a strong resistive force. In the case of levitation below a horizontal surface, the magnitude of this resistive lateral force may vary based on the weight of the levitating device, i.e. the effective pulling load. It is very important to note here that such lateral resistance was not observed in the similar experiments conducted by Dr. Colasante [49] and the BRD lab [3] when the device weight—i.e the effective pulling load—was increased to several hundred or thousand grams-force.

In pursuit of characterizing accurately and thoroughly the ‘pull-off’ process in attractive SF levitation, it is of great interest to formulate a theoretical description of squeeze-film lubrication that considers the possibility of physical contact between parts of the deforming oscillator and the opposite surface, that which may occur in the initial stages of the process where the applied pulling load is small. The required theory may involve aspects of the viscoacoustic description of flexural SF levitation presented in Chapter 3 of this dissertation as well as the fluid–structure formulation describing ‘elastohydrodynamic lubrication’ outlined in Ch. 4. Based on the results of [96–98], one may choose to account additionally for the presence of a significantly cambered oscillator, a correspondingly non-slender air layer and possible surface roughness.

Bibliography

[1] Sadayuki Ueha, Yoshiki Hashimoto, and Yoshikazu Koike. Non-contact transportation using near-field acoustic levitation. *Ultrasonics*, 38(1-8):26–32, 2000.

[2] Solomon Davis, Ran Gabai, and Izhak Bucher. Realization of an automatic, contactless, acoustic levitation motor via degenerate mode excitation and autoresonance. *Sensors and Actuators A: Physical*, 276:34–42, 2018.

[3] William P Weston-Dawkes, Iman Adibnazari, Yi-Wen Hu, Michael Everman, Nick Gravish, and Michael T Tolley. Gas-lubricated vibration-based adhesion for robotics. *Adv. Intell. Syst.*, 3(7):2100001, 2021.

[4] Shigeka Yoshimoto, Tomohiro Shou, and Kei Somaya. Vertical attractive force generated in a noncontact chuck using ultrasonic vibration. *Precision Engineering*, 37(4):805–811, 2013.

[5] Sir Geoffrey Taylor and PG Saffman. Effects of compressibility at low reynolds number. *Journal of the Aeronautical Sciences*, 24(8):553–562, 1957.

[6] Marco AB Andrade, Tiago S Ramos, Julio C Adamowski, and Asier Marzo. Contactless pick-and-place of millimetric objects using inverted near-field acoustic levitation. *Applied Physics Letters*, 116(5):054104, 2020.

[7] Minghui Shi, Kai Feng, Junhui Hu, Jiang Zhu, and Hailong Cui. Near-field acoustic levitation and applications to bearings: a critical review. *International Journal of Extreme Manufacturing*, 1(3):032002, 2019.

[8] WE Langlois. Isothermal squeeze films. *Q. Appl. Math.*, 20(2):131–150, 1962.

[9] EOJ Salbu. Compressible squeeze films and squeeze bearings. *J. Basic Eng.*, 86(2):355–364, 1964.

[10] Fernando Antonio Pina Da Silva. *Squeeze film air bearings with flexible supports*. PhD thesis, Imperial College, 1980.

[11] Yoshiki Hashimoto, Yoshikazu Koike, and Sadayuki Ueha. Acoustic levitation of planar objects using a longitudinal vibration mode. *Journal of the Acoustical Society of Japan (E)*, 16(3):189–192, 1995.

[12] Toru Hatanaka, Koike Yoshikazu, Nakamura Kentaro, Ueha Sadayuki, and Hashimoto Yoshiki. Characteristics of underwater near-field acoustic radiation force acting on a planar object. *Japanese journal of applied physics*, 38(11A):L1284, 1999.

[13] Byoung-Gook Loh and Paul I Ro. An object transport system using flexural ultrasonic progressive waves generated by two-mode excitation. *IEEE transactions on ultrasonics, ferroelectrics, and frequency control*, 47(4):994–999, 2000.

[14] Yanbo Yin. *Non-Contact Object Transportation Using Near-Field Acoustic Levitation Induced By Ultrasonic Flexural Waves*. PhD thesis, North Carolina State, Univ., Diss., 2008.

[15] B Popper and M Reiner. The application of the centripetal effect in air to the design of a pump. *Br. J. Appl. Phys.*, 7(12):452, 1956.

[16] D J Acheson. *Elementary fluid dynamics*. Oxford University Press, New York, 1990.

[17] K Stewartson. On the flow between two rotating coaxial disks. In *Mathematical Proceedings of the Cambridge Philosophical Society*, volume 49, pages 333–341. Cambridge University Press, 1953.

[18] K Weissenberg. A continuum theory of rheological phenomenon. *Nature*, 159(4035):310–311, 1947.

[19] Su Zhao. *Investigation of non-contact bearing systems based on ultrasonic levitation*. PhD thesis, Paderborn University, 2010.

[20] Jim McHugh. Albert kingsbury: His life and times. *SV Sound and vibration*, 37(10):12–20, 2003.

[21] Luigi Lentini, Mona Moradi, and Federico Colombo. A historical review of gas lubrication: From Reynolds to active compensations. *Tribology in Industry*, 40(2):165, 2018.

[22] Duncan Dowson. Men of tribology: Gustav Adolph Hirn (1815–1890) and Nikolay Pavlovitch Petrov (1836–1920). *Journal of Lubrication Technology*, 100(3):311–315, 07 1978. URL: https://doi.org/10.1115/1.3453178.

[23] V N Constantinescu. On hydrodynamic instability of gas-lubricated journal bearings. *Journal of Basic Engineering*, 87(3):579–587, 1965.

[24] Edgar J Gunter Jr. Rotor-bearing stability. In *Proceedings of the 1st Turbomachinery Symposium*. Texas A&M University. Gas Turbine Laboratories, 1972.

[25] Qiang Gao, Wanqun Chen, Lihua Lu, Dehong Huo, and Kai Cheng. Aerostatic bearings design and analysis with the application to precision engineering: State-of-the-art and future perspectives. *Tribology International*, 135:1–17, 2019.

[26] Haruo Mori. A theoretical investigation of pressure depression in externally pressurized gas-lubricated circular thrust bearings. *Journal of Basic Engineering*, 83(2):201–208, 1961.

[27] Mohamed E Eleshaky. CFD investigation of pressure depressions in aerostatic circular thrust bearings. *Tribology International*, 42(7):1108–1117, 2009.

[28] Karl Bücks and Hans Müller. Über einige beobachtungen an schwingenden piezoquarzen und ihrem schallfeld. *Zeitschrift für Physik*, 84(1):75–86, 1933.

[29] Ahmed Almurshedi. *Alternative plate deformation phenomenon for squeeze film levitation*. PhD thesis, Brunel University London, 2018.

[30] Seki Inoue, Shinichi Mogami, Tomohiro Ichiyama, Akihito Noda, Yasutoshi Makino, and Hiroyuki Shinoda. Acoustical boundary hologram for macroscopic rigid-body levitation. *The Journal of the Acoustical Society of America*, 145(1):328–337, 2019.

[31] Hillary W St. Clair. Agglomeration of smoke, fog, or dust particles by sonic waves. *Industrial & Engineering Chemistry*, 41(11):2434–2438, 1949.

[32] Daisuke Koyama, Kentaro Nakamura, and Sadayuki Ueha. A stator for a self-running, ultrasonically-levitated sliding stage. *IEEE transactions on ultrasonics, ferroelectrics, and frequency control*, 54(11):2337–2343, 2007.

[33] Kai Feng, Yuanyuan Liu, and Miaomiao Cheng. Numerical analysis of the transportation characteristics of a self-running sliding stage based on near-field acoustic levitation. *The Journal of the Acoustical Society of America*, 138(6):3723–3732, 2015.

[34] Keyu Chen, Shiming Gao, Yayue Pan, and Ping Guo. Self-running and self-floating two-dimensional actuator using near-field acoustic levitation. *Applied Physics Letters*, 109(12):123503, 2016.

[35] Ping Guo and Han Gao. An active non-contact journal bearing with bi-directional driving capability utilizing coupled resonant mode. *CIRP Annals*, 67(1):405–408, 2018.

[36] Masaya Takasaki, Daisuke Terada, Yasuhiro Kato, Yuji Ishino, and Takeshi Mizuno. Non-contact ultrasonic support of minute objects. *Physics Procedia*, 3(1):1059–1065, 2010.

[37] Ueha Sadayuki. Phenomena, theory and applications of near-field acoustic levitation. *Revista de Acústica*, 33(3-4):21–25, 2002.

[38] ZY Hong, W Zhai, N Yan, and B Wei. Measurement and simulation of acoustic radiation force on a planar reflector. *The Journal of the Acoustical Society of America*, 135(5):2553–2558, 2014.

[39] S Yoshimoto. Floating characteristics of squeeze-film gas bearings with vibration absorber for linear motion guide. *J. Lubr. Technol.*, 119, 1997.

[40] E Matsuo, Y Koike, K Nakamura, S Ueha, and Y Hashimoto. Holding characteristics of planar objects suspended by near-field acoustic levitation. *Ultrasonics*, 38(1-8):60–63, 2000.

[41] Yanzhong Wang and Bin Wei. Mixed-modal disk gas squeeze film theoretical and experimental analysis. *International Journal of Modern Physics B*, 27(25):1350168, 2013.

[42] Jin Li, Pinkuan Liu, Han Ding, and Wenwu Cao. Design optimization and experimental study of acoustic transducer in near field acoustic levitation. In *2011 IEEE International Conference on Robotics and Automation*, pages 4353–4358. IEEE, 2011.

[43] Pinkuan Liu, Jin Li, Han Ding, and Wenwu Cao. Modeling and experimental study on near-field acoustic levitation by flexural mode. *IEEE transactions on ultrasonics, ferroelectrics, and frequency control*, 56(12):2679–2685, 2009.

[44] ZY Hong, P Lü, DL Geng, W Zhai, N Yan, and B Wei. The near-field acoustic levitation of high-mass rotors. *Review of Scientific Instruments*, 85(10):104904, 2014.

[45] Bin Wei, Ran Shaham, and Izhak Bucher. Theoretical investigation and prototype design for non-parallel squeeze film movement platform driven by standing waves. *Tribology International*, 119:539–548, 2018.

[46] Minghui Shi, Xuejiang Liu, Kai Feng, and Kai Zhang. Experimental and numerical investigation of a self-adapting non-contact ultrasonic motor. *Tribology International*, 153:106624, 2021.

[47] Junichi Saito, James Robert Friend, Kentaro Nakamura, and Sadayuki Ueha. Resonant mode design for noncontact ultrasonic motor with levitated rotor. *Japanese journal of applied physics*, 44(6S):4666, 2005.

[48] Masaya Takasaki, Shota Chino, Yasuhiro Kato, Yuji Ishino, and Takeshi Mizuno. Actuation force measurement mechanism for non-contact ultrasonic suspension. In *Key Eng. Mater.*, volume 523, pages 727–732. Trans Tech Publ. Ltd., 2012.

[49] David A Colasante. Apparatus and method for orthosonic lift by deflection, Mar. 2015. U.S. Patent No. 08967965 B1. URL: https://patentscope.wipo.int/search/en/detail.jsf?docId=US130909010.

[50] David A Colasante. OL9: Orthosonic lift in stereo!, Jun. 2016. URL: https://youtu.be/kG6vXGidQbo.

[51] David A Colasante. OL8: “Souped up” hoverboard, Jun. 2016. URL: https://www.youtube.com/watch?v=H-88gsWLTac.

[52] Cobra CM-2820/16 multirotor motor, Kv=740, 2020. Innov8tive Designs. Online: accessed 2024-02-02. URL: https://innov8tivedesigns.com/cobra-cm-2820-16-multirotor-motor-kv-740.html.

[53] David A Colasante. 12in sq Al BK 25w 15Hz 80min. quiet!, 2023. Online: accessed 2024-02-14. URL: https://drive.google.com/file/d/1W2G5iCc4pNyLkVXOVt_uwoc5aQjlxRAr.

[54] David A Colasante. 24in x24in AL LFE 15Hz 200w 436 lbs. net, 2023. Online: accessed 2024-02-14. URL: https://drive.google.com/file/d/1_2n9Pg3h0cDz-4TFnFCxAi3IVVEM2pTA.

[55] Albert Kingsbury. Experiments with an air-lubricated journal. *Journal of the American Society for Naval Engineers*, 9(2):267–292, 1897.

[56] Osborne Reynolds. IV. On the theory of lubrication and its application to Mr. Beauchamp Tower's experiments, including an experimental determination of the viscosity of olive oil. *Philos. Trans. R. Soc. Lond.*, 177:157–234, 1886.

[57] W. J. Harrison. The hydrodynamical theory of lubrication with special reference to air as a lubricant. *Trans. Cambridge Philos. Soc.*, 22(3):39–54, 1913.

[58] John D. Anderson. *Fundamentals of Aerodynamics*. McGraw-Hill, New York, NY, sixth edition, 2017.

[59] Richard C DiPrima. Asymptotic methods for an infinitely long slider squeeze-film bearing. *J. Lubr. Technol.*, 90(1):173–183, 1968.

[60] S Ramanarayanan, W Coenen, and AL Sánchez. Viscoacoustic squeeze-film force on a rigid disk undergoing small axial oscillations. *Journal of Fluid Mechanics*, 933:A15, 2022.

[61] Lord Rayleigh. Xxxiv. On the pressure of vibrations. *Lond. Edinb. Dubl. Phil. Mag. J. Sci.*, 3(15):338–346, 1902.

[62] Boa-Teh Chu and Robert E Apfel. Acoustic radiation pressure produced by a beam of sound. *J. Acoust. Soc. Am.*, 72(6):1673–1687, 1982.

[63] A. Minikes and I. Bucher. Comparing numerical and analytical solutions for squeeze-film levitation force. *J. Fluids Struct.*, 22(5):713–719, 2006.

[64] C H T Pan. The gaseous squeeze-film at moderately large squeeze numbers. *Journal of Basic Engineering*, 92(4):766–781, 1970.

[65] Xin Li and Toshiharu Kagawa. Theoretical and experimental study of factors affecting the suction force of a bernoulli gripper. *Journal of Engineering Mechanics*, 140(9):04014066, 2014.

[66] EC Kuhn and CC Yates. Fluid inertia effect on the film pressure between axially oscillating parallel circular plates. *ASLE Transactions*, 7(3):299–303, 1964.

[67] RM Terrill. The flow between two parallel circular disks, one of which is subject to a normal sinusoidal oscillation. *Journal of Lubrication Technology*, 91(1):126–131, 1969.

[68] Jin Li, Wenwu Cao, Pinkuan Liu, and Han Ding. Influence of gas inertia and edge effect on squeeze film in near field acoustic levitation. *Applied Physics Letters*, 96(24):243507, 2010.

[69] Yukio Hori. *Hydrodynamic lubrication*. Springer Science & Business Media, 2006.

[70] SR Turns. Annular squeeze films with inertial effects. *J. Lubr. Technol.*, 105, 1983.

[71] Hideyuki Nomura, Tomoo Kamakura, and Kazuhisa Matsuda. Theoretical and experimental examination of near-field acoustic levitation. *The Journal of the Acoustical Society of America*, 111(4):1578–1583, 2002.

[72] Kevin W Thompson. Time dependent boundary conditions for hyperbolic systems. *Journal of computational physics*, 68(1):1–24, 1987.

[73] Thomas Hagstrom. Radiation boundary conditions for the numerical simulation of waves. *Acta numerica*, 8:47–106, 1999.

[74] Ivan Melikhov, Sergey Chivilikhin, Alexey Amosov, and Romain Jeanson. Viscoacoustic model for near-field ultrasonic levitation. *Phys. Rev. E*, 94(5):053103, 2016.

[75] Björn Engquist and Andrew Majda. Absorbing boundary conditions for numerical simulation of waves. *Proceedings of the National Academy of Sciences*, 74(5):1765–1766, 1977.

[76] Hermann Schlichting and Klaus Gersten. *Boundary-Layer Theory*. Springer, 2016.

[77] Sydney Chapman and Thomas George Cowling. *The mathematical theory of non-uniform gases: an account of the kinetic theory of viscosity, thermal conduction and diffusion in gases*. Cambridge university press, 1990.

[78] P. A. Lagerstrom. *Matched asymptotic expansions: ideas and techniques*. Springer-Verlag, 1988.

[79] F. Hecht. New development in FreeFEM++. *J. Numer. Math.*, 20((3-4)):251–266, 2012.

[80] Jaime Carpio, Juan Luis Prieto, and Marcos Vera. A local anisotropic adaptive algorithm for the solution of low-mach transient combustion problems. *Journal of Computational Physics*, 306:19–42, 2016.

[81] Garrett Birkhoff and E. H. Zarantonello. *Jets, Wakes and Cavities*. Academic Press, 1957.

[82] Mikhail I Gurevich. *The Theory of Jets in an Ideal Fluid*. Pergamon Press, 1966.

[83] Mostafa A Atalla, Ron AJ van Ostayen, Aimée Sakes, and Michaël Wiertlewski. Incompressible squeeze-film levitation. *Applied Physics Letters*, 122(24), 2023.

[84] Lawrence E Kinsler, Austin R Frey, Alan B Coppens, and James V Sanders. *Fundamentals of acoustics*. John wiley & sons, 2000.

[85] W. Rosenheinrich. *Tables of some indefinite integrals of Bessel functions of integer order*. University of Applied Sciences, Jena, 2019.

[86] Xin Li and Toshiharu Kagawa. Development of a new noncontact gripper using swirl vanes. *Robot Comput. Integr. Manuf.*, 29(1):63–70, 2013.

[87] M Rahul, S P Sivapirakasam, B R Vishnu, S L Aravind, and Sreejith Mohan. Experimental investigation on gripper force of electrically activated non-contact swirl vane gripper. *Mater. Today Proc.*, 46:9636–9640, 2021.

[88] W A Michael. Approximate methods for time-dependent gas-film lubrication problems. *J. Appl. Mech.*, 30(4):509–517, 1963.

[89] Bingen Yang. 16 - free vibration of membranes and plates. In Bingen Yang, editor, *Stress, Strain, and Structural Dynamics*, pages 807–851. Academic Press, Burlington, 2005. URL: https://www.sciencedirect.com/science/article/pii/B9780127877679500179.

[90] TA Stolarski and Wei Chai. Inertia effect in squeeze film air contact. *Tribology international*, 41(8):716–723, 2008.

[91] Paco Axel Lagerstrom. *Laminar flow theory*. Princeton University Press, Princeton, New Jersey, 1996.

[92] C. M. Bender and S. A. Orszag. *Advanced mathematical methods for scientists and engineers I: Asymptotic methods and perturbation theory*, volume 1. Springer Science & Business Media, 1999.

[93] Jin Li, Pinkuan Liu, and Han Ding. Dynamic coupling and experimental study on flexural transducer used in near field acoustic levitation. *Journal of Advanced Mechanical Design, Systems, and Manufacturing*, 8(3):JAMDSM0038–JAMDSM0038, 2014.

[94] Overview of materials for polyester film, n.d. Online: accessed 2024-01-01. URL: https://www.matweb.com/search/datasheet.aspx?matguid=40559706b4fd4aa0a43f5739799728f5.

[95] Product data sheet: Model No. 306-114. https://catalogue.precisionmicrodrives.com/product/306-114-6mm-vibration-motor-10mm-type, 2021. Online: accessed 2024-01-31.

[96] Tao Zhu, Rong Liu, Xu D Wang, and Kun Wang. Principle and application of vibrating suction method. In *2006 IEEE International Conference on Robotics and Biomimetics*, pages 491–495. IEEE, 2006.

[97] Qingfeng Hong, Rong Liu, Hao Yang, and Xudong Zhai. Wall climbing robot enabled by a novel and robust vibration suction technology. In *2009 IEEE International Conference on Automation and Logistics*, pages 331–336. IEEE, 2009.

[98] Wei Wang, Kun Wang, Guang-Hua Zong, and Da-Zhai Li. Principle and experiment of vibrating suction method for wall-climbing robot. *Vacuum*, 85(1):107–112, 2010.

[99] D.A. Colasante. OL5: Orthosonic flying saucer. https://youtu.be/RWUWKx0N_rg, Jun. 2016. Online: accessed 2024-02-06.

[100] Chengzhe Jia, Sankaran Ramanarayanan, Antonio L. Sanchez, and Michael T. Tolley. Controlling the motion of gas-lubricated adhesive disks using multiple vibration sources. *Frontiers in Robotics and AI*, 10:1231976, 2023.

[101] Sankaran Ramanarayanan and A L Sánchez. On the enhanced attractive load capacity of resonant flexural squeeze-film levitators. *AIP Advances*, 12(10):105126, 2022.

[102] N. Brunetière, A. Blouin, and G. Kastane. Conditions of lift-off and film thickness in squeeze film levitation. *J. Tribol.*, 140(3):031705, 2018.

[103] D Ilssar and I Bucher. The effect of acoustically levitated objects on the dynamics of ultrasonic actuators. *Journal of Applied Physics*, 121(11):114504, 2017.

[104] Dotan Ilssar, Izhak Bucher, and Henryk Flashner. Modeling and closed loop control of near-field acoustically levitated objects. *Mechanical Systems and Signal Processing*, 85:367–381, 2017.

[105] C. Zhang, G. Xu, and Q. Jiang. Characterization of the squeeze film damping effect on the quality factor of a microbeam resonator. *J. Micromech. Microeng.*, 14(10):1302, 2004.

[106] A.K. Pandey and R. Pratap. Effect of flexural modes on squeeze film damping in MEMS cantilever resonators. *J. Micromech. Microeng.*, 17(12):2475, 2007.

[107] K. Sim and D. Kim. Thermohydrodynamic analysis of compliant flexure pivot tilting pad gas bearings. *J. Eng. Gas Turbine. Power*, 130(3):032502, 2008.

[108] J.A. Greenwood. Elastohydrodynamic lubrication. *Lubricants*, 8(5):51, 2020.

[109] Y. Wu, L. Yang, T. Xu, and W. Wu. Thermo-elasto-hydrodynamic characteristics analysis of journal microbearing lubricated with rarefied gas. *Micromachines*, 11(11):955, 2020.

[110] S. Poulain, A. Carlson, S. Mandre, and L. Mahadevan. Elastohydrodynamics of contact in adherent sheets. *J. Fluid Mech.*, 947:A16, 2022.

[111] B. Rallabandi. Fluid-elastic interactions near contact at low Reynolds number. *Annu. Rev. Fluid Mech.*, 56, 2024.

[112] I. Omodia, K.S. Das, and L. Mahadevan. Vibration-induced elasto-hydro-dynamic adhesion of thin elastic sheet. Poster communication, 2022. University of Maryland Eastern Shore and Harvard University.

[113] M. Burroughs. Why is vibration amplitude in g?, Nov 2021. Online: accessed 2023-12-07. URL: https://www.precisionmicrodrives.com/why-is-vibration-amplitude-in-g.

[114] A. Bettini. *A Course in Classical Physics 1–Mechanics*. Springer International Publishing, Switzerland, 2016.

[115] W. M. Rohsenow, J. P. Hartnett, and Y. I. eds. Cho. *Handbook of Heat Transfer*. McGraw-Hill, New York, NY, third edition, 1998.

[116] S. Timoshenko and S. Woinowsky-Krieger. *Theory of plates and shells*. McGraw-Hill, Inc., New York, NY, 1959.

[117] P. A. Kelly. Solid mechanics part II: Engineering solid mechanics – small strain, 2013. Online: accessed 2023-09-21.

[118] M. Ducceschi. *Nonlinear Vibrations of Thin Rectangular Plates: A Numerical Investigation with Application to Wave Turbulence and Sound Synthesis*. PhD thesis, ENSTA ParisTech, Palaiseau, FR, 2014.

[119] M. Watanabe and F. Hara. Theoretical instability analysis of a rotating flexible disk subjected to swirling fluid flow. In *Int. Mech. Eng. Congress Expo.*, volume 2 of *4th International Symposium on Fluid-Structure Interactions, Aeroelasticity, Flow-Induced Vibration and Noise*, pages 57–66. ASME, 1997.

[120] A. Tulchinsky and A.D. Gat. Transient dynamics of an elastic Hele-Shaw cell due to external forces with application to impact mitigation. *J. Fluid Mech.*, 800:517–530, 2016.

[121] A.G. Warren. LXXXIII. The free and forced symmetrical oscillations of thin bars, circular diaphragms, and annuli. *Lond. Edinb. Dubl. Phil. Mag. J. Sci.*, 9(60):881–901, 1930.

[122] C.M. Bender and S. Orszag. *Advanced mathematical methods for scientists and engineers I: Asymptotic methods and perturbation theory*. Springer, New York, 1999.

[123] J.C. Flitton and J.R. King. Moving-boundary and fixed-domain problems for a sixth-order thin-film equation. *Eur. J. Appl. Math.*, 15(6):713–754, 2004.

[124] M. Abramowitz and I.A. eds. Stegun. *Handbook of Mathematical Functions with Formulas, Graphs, and Mathematical Tables*, volume 55 of *Applied Mathematics Series*. National Bureau of Standards, Washington, D.C., 1972.

[125] B Geist and J R McLaughlin. The effect of structural damping on nodes for the Euler-Bernoulli beam: a specific case study. *Applied Mathematics Letters*, 7(3):51–55, 1994.

[126] P. Moin. *Fundamentals of Engineering Numerical Analysis*. Cambridge University Press, New York, NY, 2 edition, 2010.

[127] F. Sasmita, T.A. Candra, H. Judawisastra, and T.A. Priambodo. Young's modulus determination of polyester and epoxy by means of ultrasonic pulse echo testing. In *IOP Conf. Ser. Mater. Sci. Eng.*, volume 547 of *Design and application of engineering materials*, page 012045. IOP Publishing, 2019.

[128] S.M. Soedel and W. Soedel. On the free and forced vibration of a plate supporting a freely sloshing surface liquid. *J. Sound Vib.*, 171(2):159–171, 1994.

[129] David A Colasante. 20in ply CT 34Hz 60w quiet 40.5lbs!!, 2022. Online: accessed 2024-02-14. URL: https://drive.google.com/file/d/1QPp-9drnPlWl5W4wge4eeMbNE_XyzBu_.

[130] Poisson's ratio, 2008. Online: accessed 2024-01-01. URL: https://www.engineeringtoolbox.com/poissons-ratio-d_1224.html#google_vignette.

[131] Modulus of elasticity and Poisson's coefficient of polymeric materials, n.d. Online: accessed 2024-01-01. URL: https://www.engineeringtoolbox.com/poissons-ratio-d_1224.html#google_vignette.

[132] Dotan Ilssar, Izhak Bucher, and Henryk Flashner. Modeling and closed loop control of near-field acoustically levitated objects. *Mechanical Systems and Signal Processing*, 85:367–381, 2017.

[133] Chao Wang and YH Joe Au. Comparative performance of squeeze film air journal bearings made of aluminium and copper. *The International Journal of Advanced Manufacturing Technology*, 65:57–66, 2013.

[134] Minghui Shi, Lin An, Kai Feng, Zhiyang Guo, and Wanhui Liu. Numerical and experimental study on the influence of material characteristics on the levitation performance of squeeze-film air bearing. *Tribology International*, 126:307–316, 2018.

[135] Tadeusz Adam Stolarski, Rafał Gawarkiewicz, and Krzysztof Tesch. Acoustic journal bearing—a search for adequate configuration. *Tribology International*, 92:387–394, 2015.

[136] Takeshi Ide, James Friend, Kentaro Nakamura, and Sadayuki Ueha. A non-contact linear bearing and actuator via ultrasonic levitation. *Sensors and Actuators A: Physical*, 135(2):740–747, 2007.

[137] Skriptyan Noor Hidayatullah Syuhri. *Fluid flow induced by travelling waves in beam-like structures: modelling, simulation and experimental validation*. PhD thesis, University of Glasgow, 2022.

[138] Hassan Hariri, Yves Bernard, and Adel Razek. A traveling wave piezoelectric beam robot. *Smart Materials and Structures*, 23(2):025013, 2013.

[139] Yoshiro Tomikawa, Kazunari Adachi, Hiroshi Hirata, Takanori Suzuki, and Takehiro Takano. Excitation of a progressive wave in a flexurally vibrating transmission medium. *Japanese Journal of Applied Physics*, 29(S1):179, 1990.

[140] Frédéric Giraud, Christophe Giraud-Audine, Michel Amberg, and Betty Lemaire-Semail. Vector control method applied to a traveling wave in a finite beam. *IEEE Transactions on Ultrasonics, Ferroelectrics, and Frequency Control*, 61(1):147–158, 2014.

[141] Sofiane Ghenna, Frédéric Giraud, Christophe Giraud-Audine, Michel Amberg, and Betty Lemaire-Semail. Modelling and control of a travelling wave in a finite beam, using multi-modal approach and vector control method. In *2015 Joint Conference of the IEEE International Frequency Control Symposium & the European Frequency and Time Forum*, pages 509–514. IEEE, 2015.

[142] Ryuto Yano, Manabu Aoyagi, Hideki Tamura, and Takehiro Takano. Novel transfer method using near-field acoustic levitation and its application. *Japanese Journal of Applied Physics*, 50(7S):07HE29, 2011.

[143] Adi Minikes, Izhak Bucher, and Shimon Haber. Levitation force induced by pressure radiation in gas squeeze films. *The Journal of the Acoustical Society of America*, 116(1):217–226, 2004.

[144] Adi Minikes and Izhak Bucher. Noncontacting lateral transportation using gas squeeze film generated by flexural traveling waves–numerical analysis. *The Journal of the Acoustical Society of America*, 113(5):2464–2473, 2003.

[145] J Li, CJ Liu, and WJ Zhang. Pressure potential and stability analysis in an acoustical noncontact transportation. *Acoustical Physics*, 63:125–131, 2017.

[146] Lawrence F Shampine. Vectorized adaptive quadrature in MATLAB. *Journal of Computational and Applied Mathematics*, 211(2):131–140, 2008.

[147] Numerical integration and differentiation, 2023. URL: https://www.mathworks.com/help/matlab/ref/integral.html.

[148] Sankaran Ramanarayanan and Antonio L Sánchez. Benefits of controlled inclination for contactless transport by squeeze-film levitation. *Flow*, 3:E26, 2023.

[149] Yoshiki Hashimoto, Yoshikazu Koike, and Sadayuki Ueha. Near-field acoustic levitation of planar specimens using flexural vibration. *The Journal of the Acoustical Society of America*, 100(4):2057–2061, 1996.

[150] Yan De Liang, Hong Ling, and Yuan Zhang. Study on the conditions of near-field acoustic levitation. In *Manufacturing Science and Engineering I*, volume 97 of *Advanced Materials Research*, pages 4135–4140. Trans Tech Publications Ltd, 2010.

[151] D. Lo Jacono, F. Plouraboué, and A. Bergeon. Weak-inertial flow between two rough surfaces. *Phys. Fluids*, 17(6):063602, 2005.

[152] R. Guibert, F. Plouraboué, and A. Bergeon. Steady streaming confined between three-dimensional wavy surfaces. *J. Fluid Mech.*, 657:430–455, 2010.

[153] Anders Petterson, Thomas Ohlsson, Darwin G Caldwell, Steven Davis, John O Gray, and Tony J Dodd. A Bernoulli principle gripper for handling of planar and 3d (food) products. *Industrial Robot: An International Journal*, 37(6):518–526, 2010.

[154] Takafumi Amano, Yoshikazu Koike, Nakamura Kentaro, Ueha Sadayuki, and Hashimoto Yoshiki. A multi-transducer near field acoustic levitation system for noncontact transportation of large-sized planar objects. *Japanese Journal of Applied Physics*, 39(5S):2982, 2000.

[155] Jin Li, Pinkuan Liu, Han Ding, and Wenwu Cao. Nonlinear restoring forces and geometry influence on stability in near-field acoustic levitation. *Journal of Applied Physics*, 109(8), 2011.

[156] Kohei Aono, Manabu Aoyagi, Hidekazu Kajiwara, Hideki Tamura, and Takehiro Takano. Increase of holding force in near-field acoustic levitation of tabular object inserted between opposing vibration sources. *Japanese Journal of Applied Physics*, 58(SG):SGGD11, 2019.

[157] Konstantinos Tsigklifis and Anthony D Lucey. Asymptotic stability and transient growth in pulsatile poiseuille flow through a compliant channel. *Journal of Fluid Mechanics*, 820:370–399, 2017.

[158] Smail Lebbal, Frédéric Alizard, and Benoît Pier. Linear instabilities of pulsatile plane channel flow between compliant walls. *Journal of Fluid Mechanics*, 948:A15, 2022.

[159] Yuanyuan Liu, Zilong Zhao, and Wenjie Chen. Theoretical investigation of the levitation force generated by underwater squeeze action. *Japanese Journal of Applied Physics*, 62(3):034001, 2023.

[160] Sound speed profile, 2023. URL: https://en.wikipedia.org/wiki/Sound_speed_profile.

[161] Shinfuku Nomura, Thomas J Matula, Jun Satonobu, and Lawrence A Crum. Noncontact transportation in water using ultrasonic traveling waves. *The Journal of the Acoustical Society of America*, 121(3):1332–1336, 2007.

[162] David A Colasante. OL1: DC & AC lift by radial deflection, Jun. 2016. URL: https://www.youtube.com/watch?v=I3g0CcLzC6I.

[163] HX Zhang, J Gonzalez-Gomez, SY Chen, W Wang, R Liu, D Li, and JW Zhang. A novel modular climbing caterpillar using low-frequency vibrating passive suckers. In *2007 IEEE/ASME international conference on advanced intelligent mechatronics*, pages 1–6. IEEE, 2007.

[164] Rui Chen, Leilei Fu, Yilin Qiu, Ruizhou Song, and Yan Jin. A gecko-inspired wall-climbing robot based on vibration suction mechanism. *Proceedings of the Institution of Mechanical Engineers, Part C: Journal of Mechanical Engineering Science*, 233(19-20):7132–7143, 2019.